ISSN 1881-7831 Online ISSN 1881-784X

DD&T

Drug Discoveries & Therapeutics

Volume 17, Number 4
August, 2023

IRCA BSSA

IACMHR

www.ddtjournal.com

DD&T
Drug Discoveries & Therapeutics

ISSN: 1881-7831
Online ISSN: 1881-784X
CODEN: DDTRBX
Issues/Year: 6
Language: English
Publisher: IACMHR Co., Ltd.

Drug Discoveries & Therapeutics is one of a series of peer-reviewed journals of the International Research and Cooperation Association for Bio & Socio-Sciences Advancement (IRCA-BSSA) Group. It is published bimonthly by the International Advancement Center for Medicine & Health Research Co., Ltd. (IACMHR Co., Ltd.) and supported by the IRCA-BSSA.

Drug Discoveries & Therapeutics publishes contributions in all fields of pharmaceutical and therapeutic research such as medicinal chemistry, pharmacology, pharmaceutical analysis, pharmaceutics, pharmaceutical administration, and experimental and clinical studies of effects, mechanisms, or uses of various treatments. Studies in drug-related fields such as biology, biochemistry, physiology, microbiology, and immunology are also within the scope of this journal.

Drug Discoveries & Therapeutics publishes Original Articles, Brief Reports, Reviews, Policy Forum articles, Case Reports, Communications, Editorials, News, and Letters on all aspects of the field of pharmaceutical research. All contributions should seek to promote international collaboration in pharmaceutical science.

Editorial Board

Editorial and Head Office:

Pearl City Koishikawa 603,
2-4-5 Kasuga, Bunkyo-ku,
Tokyo 112-0003, Japan
E-mail: office@ddtjournal.com

Drug Discoveries & Therapeutics

Editorial and Head Office

Pearl City Koishikawa 603, 2-4-5 Kasuga, Bunkyo-ku,
Tokyo 112-0003, Japan

E-mail: office@ddtjournal.com
URL: www.ddtjournal.com

Review

220-229 **Drug resistance and new therapies in gallbladder cancer.**
Yuxin Sun, Xiaoxuan Li, Haihong Cheng, Shouhua Wang, Di Zhou, Jun Ding, Fei Ma

230-237 **Ultrasound-guided brachial plexus block at the clavicle level: A review.**
Zhimin Guo, Ming Zhao, Haihua Shu

Original Article

238-247 **Biosynthesis of copper oxide nanoparticles using *Caesalpinia sappan* extract: *In vitro* evaluation of antifungal and antibiofilm activities against *Candida albicans*.**
Mathurada Sasarom, Phenphichar Wanachantararak, Pisaisit Chaijareenont, Siriporn Okonogi

248-256 **LncRNA SNHG1 upregulates FANCD2 and G6PD to suppress ferroptosis by sponging miR-199a-5p/3p in hepatocellular carcinoma.**
Lin Zhou, Qing Zhang, Jiaxin Cheng, Xiandie Shen, Jing Li, Mingya Chen, Chang Zhou, Jianlin Zhou

257-269 **Effect of Chinese patent medicine Kunling Pill on endometrial receptivity: A clinical trial, network pharmacology, and animalbased study.**
Xinyao Pan, Qi Qing, Jing Zhou, Hongmei Sun, Lisha Li, Wenli Cao, Feijun Ye, Jun Zhu, Yan Sun, Ling Wang

270-278 **Apolipoprotein E deficiency attenuated osteogenesis *via* downregulating osterix.**
Qing Qi, Yingping Xu, Hongmei Sun, Jing Zhou, Lisha Li, Xinyao Pan, Jing Wang, Wenli Cao, Yan Sun, Ling Wang

279-288 **A single dose of ketamine relieves fentanyl-induced-hyperalgesia by reducing inflammation initiated by the TLR4/NF-κB pathway in rat spinal cord neurons.**
Xin Zhou, Qianyi Li, Quehua Luo, Le Wang, Jiaxin Chen, Ying Xiong, Guiyun Wu, Lu Chang, Pingping Liu, Haihua Shu

Brief Report

289-293 **Development of a simple high-performance liquid chromatography-ultraviolet method for sotorasib quantification in human plasma: Implications for therapeutic drug monitoring.**
Eri Hikita, Yoshito Gando, Hideo Chubachi, Mikio Shirota, Akifumi Kushiyama, Takeo Yasu

294-298 **Involvement of adaptive immune responses in a model of subacute colitis induced with dextran sulfate sodium in C57BL/6 mice.**
Jing Li, Fangzhou Dou, Shasha Hu, Jianjun Gao

299-303 **Higher serum AMH level is associated with better pregnancy outcomes of IVF/ICSI assisted pregnancy in infertile patients under 35 years old.**
Feijun Ye, Yan Du, Wenli Cao, Ruhe Jiang, Qing Qi, Hongmei Sun, Jing Zhou, Ling Wang

Review

DOI: 10.5582/ddt.2023.01013

Drug resistance and new therapies in gallbladder cancer

Yuxin Sun[1,§], Xiaoxuan Li[2,§], Haihong Cheng[1], Shouhua Wang[3], Di Zhou[3], Jun Ding[4,*], Fei Ma[1,5,*]

[1] Department of Oncology, Xinhua Hospital Affiliated to Shanghai Jiao Tong University School of Medicine, Shanghai, China;
[2] Qingdao University, Qingdao, Shandong, China;
[3] Department of General Surgery, Xinhua Hospital Affiliated to Shanghai Jiao Tong University School of Medicine, Shanghai, China;
[4] Department of Biliary and Pancreatic Surgery, Shanghai Shuguang Hospital Affiliated to Shanghai University of Traditional Chinese Medicine, Shanghai, China;
[5] Shanghai Institute for Pediatric Research, Shanghai, China.

SUMMARY Gallbladder cancer (GBC) is a highly aggressive malignancy, which poses significant challenges for timely diagnosis, resulting in a dismal prognosis. Chemotherapy serves as a primary treatment option in cases where surgery is not feasible. However, the emergence of chemoresistance poses a significant challenge to the effectiveness of chemotherapy, ultimately resulting in a poor prognosis. Despite extensive research on mechanisms of chemotherapeutic resistance in oncology, the underlying mechanisms of chemoresistance in GBC remain poorly understood. In this review, we present the findings from the last decade on the molecular mechanisms of chemotherapeutic resistance in GBC. We hope that these insights may provide novel therapeutic and experimental targets for further investigations into this lethal disease.

Keywords Gallbladder cancer, drug resistance, chemotherapy

1. Introduction

Gallbladder cancer (GBC) is a rare malignant neoplasm (*1*). The worldwide incidence of GBC is less than 2/100,000 individuals (*2*). The highest morbidity rates are found in Latin America, the Ganges Valley in Asia, and Poland, with incidence rates among females of 27.3/100,000, 21.5/100,000, and 14/100,000, respectively. The mortality rate of GBC has decreased worldwide but rising in Shanghai, China (*3*). Unfortunately, there has been no significant improvement in the effectiveness of treatment, and the five-year survival rate remains less than 5% (*4*). This is likely due to the difficulty in early detection and diagnosis, as there are no specific clinical symptoms. Moreover, the signs and symptoms that do occur are often masked by other conditions, such as cholecystitis or gallbladder stones. By the time most patients are diagnosed, the condition has progressed to a terminal stage (*5*), and radical surgical treatment, which is the only curative option, is no longer possible. Furthermore, patients who do receive surgery have a higher recurrence rate (*6*). Thus, adjuvant radiotherapy, chemotherapy, and immunotherapy play essential roles in improving the overall survival time of patients with GBC (*7*). Postoperative adjuvant radiotherapy has been shown to be therapeutic in improving patients' survival time (*8*). Chemotherapy is also critical, and the current regimen includes gemcitabine (GEM), 5-fluorouracil (5-FU) combined with cisplatin (DDP), and oxaliplatin (*7*). Recent advances in genome sequencing technology have led to the identification of potential genetic aberrations in patients with GBC, highlighting the increasing importance of targeted therapy in GBC treatment.

Given that only a small proportion of GBC patients are eligible for surgery, chemotherapy is typically the primary option for patients with unresectable or metastatic disease. GEM has demonstrated efficacy as a chemotherapy drug for GBC (*9*), with reported tumor response rates ranging from 10% to 30% and a median survival time of 8.1 months. However, GBC cells exhibit significant resistance to this drug and present a significant challenge for effective treatment. What's more, rapid drug resistance development has also become a bottleneck for other chemotherapy drugs like DDP. What's worse, the emergence of multidrug resistance (MDR) is particularly concerning (*10*), as it causes over 90% of deaths in cancer patients treated with traditional or novel chemotherapeutic drugs (*11*). Hence, research efforts must focus on overcoming drug resistance in GBC.

Tanweer Haider *et al.* provides a precise summary

of the mechanisms of chemotherapy resistance in tumors (*12*). The resistance was classified into intrinsic and extrinsic categories based on the involved factors. Intrinsic resistance refers to those specific elements present in the cancer cell or tissue itself before chemotherapy, which can reduce the effectiveness of chemotherapy drugs for particular cancers. Extrinsic drug resistance, also known as acquired drug resistance, is a complex mechanism involving the acquisition of gene mutations and activation of MDR-related signaling pathways. The mechanisms of drug resistance include various factors such as tumor microenvironmental (TME) factors, tumor heterogeneity, drug inactivation, reduced drug influx, increased drug outflow, changes in DNA repair and epigenetic effects, inhibition of apoptotic pathways and autophagy, epithelial-mesenchymal transformation (EMT), and changes in membrane lipids. The main causes of MDR include overexpression of ATP-binding cassette (ABC) superfamily membrane transporters such as p-glycoproteins (P-GP) and MDR-related proteins, inactivation of pathways associated with apoptosis inhibition, and enhancement of DNA self-repair ability. This review examines the mechanisms of chemotherapy resistance and summarizes the latest research advances in overcoming chemotherapy resistance in GBC over the past decade.

2. Research progress on the mechanism of chemotherapeutic resistance in GBC

2.1. TME

TME, consisting of multiple cell types (*e.g.*, endothelial cells, fibroblasts, immune cells) and extracellular components (*e.g.*, cytokines, growth factors, hormones, extracellular matrix), is a critical factor that affects the efficacy of chemotherapy (*13*). Changes in the TME could contribute to the development of drug resistance. Vascular endothelial growth factors (VEGFs) and fibroblast growth factors (FGFs) are key factors in TME that promote tumor growth and survival and have been implicated in chemotherapy resistance in cancer (*14*).

Leptin is an adipose-tissue-derived hormone that is involved in regulating glycometabolism, lipometabolism, and energy metabolism (*15*). Through the signal transducer and activator of transcription 3 (STAT3)/CCAAT/enhancer binding protein delta (CEBPD)/myeloid cell leukemia-1 (MCL1) axis, leptin has been found to induce mitochondrial fusion and inhibit GBC cell apoptosis induced by gemcitabine (*16*). In this signaling pathway, STAT3 acts as a leptin-regulated transcriptional activator, while CEBPD, a transcription factor of the C/EBP family, is inactivated in various cancers (*17*). *MCL1*, a target gene of CEBPD that responds to leptin, is overexpressed in various tumors (*18*). Research has shown that leptin can induce the phosphorylation of STAT3 in GBC cells, leading to increased expression of CEBPD and promoting the transcription of the MCL1 gene (*16*). This, in turn, enhances the anti-apoptotic ability and chemotherapy resistance of GBC cells by enabling mitochondrial fusion and promoting mitochondrial function. Therefore, increasing leptin secretion and promoting the CEBPD/MCL1 axis may enhance chemotherapy resistance in GBC (Figure 1). This study sheds light on the underlying mechanisms contributing to the poor prognosis of obese patients.

2.2. Anti-apoptosis effects

Apoptosis is a form of programmed cell death that plays a critical role in chemotherapy response (*19*). Resistance to chemotherapy can result from various factors that affect the expression of apoptotic cytokines (*11*). The caspase family and the B-cell lymphoma-2 (Bcl-2) family are the two factors typically involved in apoptosis. The caspase family is regarded as the primary mediator of apoptotic cell death, while the Bcl-2 family serves as a crucial regulatory component of the intracellular apoptotic pathway with varying effects on apoptosis (*20*). Bax, one of the pro-apoptotic Bcl-2 proteins, is a negative regulator of cell survival, while Bcl-2 proteins, also in the Bcl-2 family, play an inhibitory role in apoptosis. Numerous factors can affect apoptosis by regulating the expression of these molecules. For instance, estrogen can stimulate the expression of BCL-2, thereby promoting drug resistance in breast cancer (*21*).

Olfactomedin-4 (OLFM4) is a glycoprotein belonging to the OLFM family and is known to exhibit anti-apoptotic properties (*22,23*). Studies have revealed that OLFM4 expression is significantly increased during the progression of chronic cholecystitis to atypical hyperplasia and ultimately to GBC (*24*). Furthermore, genetic knockout of OLFM4 has been shown to result in a marked decrease in tumor proliferation and invasion (*25*). Additionally, cells cultured in the absence of

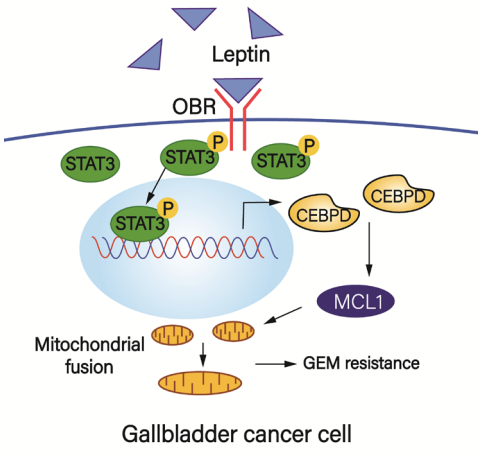

Figure 1. High expression of leptin promotes chemoresistance of GBC cells to GEM by activating the STAT3/CEBPD/MCL1 axis.

OLFM4 have been observed to exhibit reduced levels of ADP-ribosylation factor-like 6 interacting protein 1 (ARL6IP1), another anti-apoptotic cytokine. This implies that the OLFM4-ARL6IP1-caspase 3 axis plays a significant role in regulating chemotherapy resistance. Notably, the downregulation of OLFM4 has been found to increase the expression of caspase 3 and sensitize cells to chemotherapy with DDP, both *in vitro* and *in vivo*. Calreticulin (CRT), located in the endoplasmic reticulum, is another factor that activates anti-apoptotic effects (*26*). CRT is involved in various cellular metabolic processes, including calcium handling, cell adhesion, and migration (*27*). Upregulation of CRT has been observed in several cancers, including lung cancer, pancreatic cancer, and GBC, and it positively correlates with tumor size. Inhibition of CRT has been shown to induce apoptosis and suppress the activation of p-Akt, which enhances the anti-cancer efficacy of GEM (*28*). The PI3K/Akt pathway has previously been reported to increase cancer cell chemoresistance (*29*). Therefore, inhibiting OLFM4 and CRT may increase chemotherapeutic sensitivity and improve treatment efficacy.

MicroRNAs (miRNAs) are small, 20-22 nucleotide molecules that act as post-transcriptional regulators, playing a significant role in cancer development, including GBC (*30*). Among them, miR-125b-5p is a down-regulated miRNA in drug-resistant GBC cells. Recent research has revealed that miR-125b-5p down-regulates the expression of Bcl2, promoting apoptosis and enhancing the chemotherapy sensitivity of GBC cells to DDP (*31*). Hence, the downregulation of miR-125b-5p expression in GBC cells leads to chemotherapy resistance.

MiR-205-5p is another type of miRNA with potential as a diagnostic biomarker of cancer, capable of reducing tumor chemoresistance. Peripheral blood samples from GBC patients show reduced expression of miR-205-5p. Protein kinase C (PRKCE) is associated with tumor invasiveness and is upregulated in various cancers, including GBC. MiR-205-5p inhibits the expression of PRKCE, and its overexpression can promote GEM-induced apoptosis by increasing the sensitivity of GBC cells to GEM (*32*). Furthermore, increased expression of miR-205-5p and silencing of PRKCE can promote the expression of Bax and activate caspase 3. Therefore, the decreased expression of miR-205-5p leads to increased chemotherapy resistance in GBC cells (*33,34*).

MiR-31 is a miRNA that is down-regulated in DDP-resistant GBC cells. *Src* is a proto-oncogene (*35*) and a direct target of miR-31, whose expression is inhibited by miR-31. Akt, as one of the downstream kinases of Src, is implicated in the anti-apoptotic effect by disrupting the balance of Bcl-2 family proteins (*36*). The downregulation of miR-31 expression promotes the expression of activated p-Src and further increases the level of activated p-Akt. Ultimately, a decrease in Bax and an increase in Bcl-2 expression attenuate DDP-induced apoptosis (*37*). Therefore, the reduced expression of miR-31 leads to increased resistance to chemotherapy in GBC cells.

The acquisition of drug resistance in GBC is closely associated with anti-apoptotic effects (Figure 2). Studies investigating the mechanisms of apoptotic resistance have predominantly focused on traditional apoptotic pathways, such as Bax/Caspase3. However, these studies typically only describe a linear relationship between a gene and a downstream target protein. Apoptotic pathways are interconnected and form a complex network of structures. Thus, it is imperative that researchers integrate their studied genes into this intricate network of apoptotic pathways in order to more systematically explain how a series of linkage changes culminate in the development of apoptosis resistance in gallbladder cancer cells. Furthermore, imbalances in microRNA expression frequently arise during GBC development, which can influence cancer cell phenotype and elucidate the mechanism behind drug resistance. However, reversing these expression suppressions *in vivo* remains a significant challenge.

2.3. Autophagy effect

Recent studies have demonstrated that autophagy plays a dual role in tumor chemotherapy resistance and sensitization. Moderate autophagy can increase resistance to chemotherapeutic drugs, while excessive autophagy can prevent the formation of drug resistance, leading to accelerated cell death (*38*). Many factors are involved in cellular autophagy, including recombinant phosphoglycerate kinase 1 (PGK1), a critical enzyme that catalyzes glycolysis, and its activity has been linked to autophagy activation (*39*).

Long non-coding RNAs (lncRNAs) are a class of transcripts that are longer than 200 bases and lack protein-coding potential. These transcripts play vital roles in multiple biological processes of cancer progression, such as proliferation, apoptosis, epithelial-mesenchymal transition, and autophagy (*40*). Among the upregulated lncRNAs, lncRNA ENST00000425894, termed gallbladder cancer drug resistance-associated lncRNA1 (GBCDRlnc1), participates in the chemoresistance of gallbladder cancer cells (*41*). GBCDRlnc1 expression is increased in GBC tissues and can interact directly with PGK1, upregulating its protein level by inhibiting PGK1 ubiquitination in GBC cells *in vitro*, thereby inducing autophagy-related chemical resistance in GBC cells (*41*).

Although the mechanisms of autophagy are rarely studied in GBC, cellular autophagy plays a vital role in the development of drug resistance. For instance, GEM can cause protective autophagy by inhibiting the Akt/mTOR signaling pathway in various tumors, including GBC, resulting in tumor chemotherapy resistance (*42*). Moreover, enhanced autophagy activity in Doxorubicin (DOX)-resistant gallbladder carcinoma cells promotes

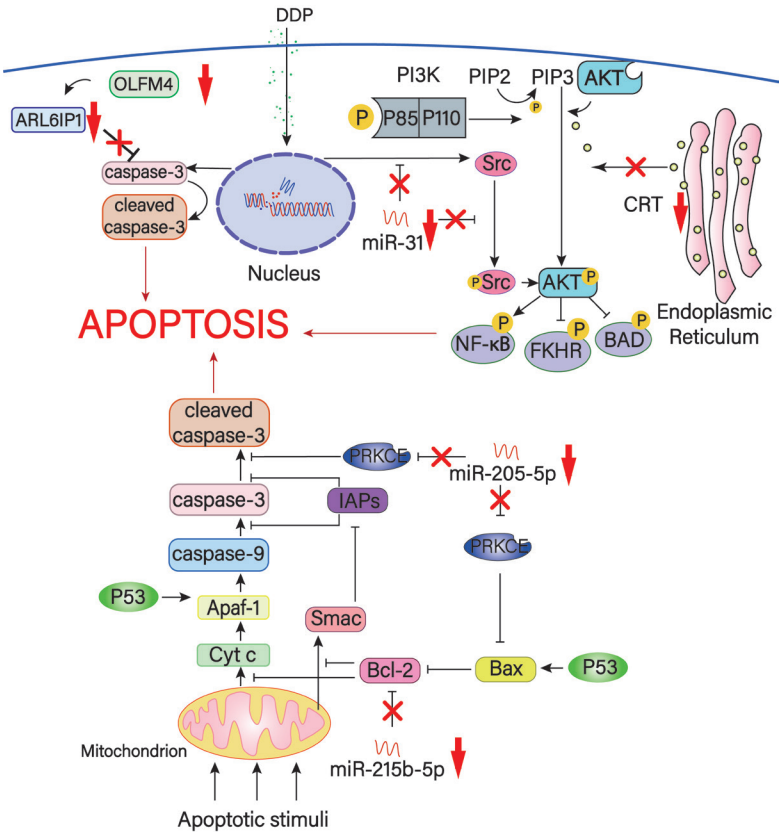

Figure 2. Molecular pathway diagram associated with apoptosis. (*i*) OLFM4 exerts its effect on cell apoptosis through the OLFM4-ARL6IP1-caspase 3 axis. (*ii*) CRT influences the apoptosis through the PI3K/AKT pathway. (*iii*) miR-125b-5p promotes cell apoptosis by affecting the expression of Bcl-2. (*iv*) miR-205-5p affects cell apoptosis through the PRKCE/Bax/caspase 3 pathway. (*v*) miR-31 influences cell apoptosis through the Src/Akt pathway.

drug resistance. Therefore, further research on cellular autophagy is necessary to develop strategies to combat drug resistance in GBC.

2.4. Drug efflux

The overexpression of membrane efflux pumps, such as P-GP, plays a crucial role in MDR, primarily through increased drug efflux (*43*). P-GP, a transmembrane transporter encoded by the multi-drug resistance gene 1 (MDR1), uses ATP-dependent mechanisms to transport drugs out of cells, thereby conferring resistance to cancer cells (*44*).

One miRNA that is significantly downregulated in GBC is miR-218-5p. It inhibits the activation of MDR1/P-GP by downregulating the expression of PRKCE. Therefore, decreased expression of miR-218-5p relieves the inhibitory effect on PRKCE, resulting in increased levels of MDR1/P-GP and drug outflow, ultimately promoting resistance of GBC cells to GEM and DDP.

Another downregulated miRNA in drug-resistant GBC cells is miR-145. MRP1, a critical component in developing chemoresistance, is a target of miR-145 (*45*). MiR-145 reduces the expression level of MDR1/P-GP by promoting the direct degradation of MRP1 mRNA, leading to increased drug efflux (*46*). Consequently, decreased expression of miR-145 leads to increased levels of MDR1/P-GP and enhanced resistance of GBC cells to GEM and DDP. Therefore, miRNAs play multiple roles in the development of gallbladder cancer, and it is important to investigate and reveal the functions of additional miRNAs in the mechanisms underlying GBC.

The deregulation of the mammalian target of rapamycin (mTOR), an atypical serine/threonine kinase, is implicated in the pathogenesis of GBC. mTOR plays a critical role in regulating cell proliferation, growth, differentiation, migration, and survival by modulating numerous cellular signaling pathways (*47*). Inhibition of the mTOR signaling pathway has been shown to suppress the synthesis of MDR1 induced by 5-FU and ultimately promote the chemosensitivity of GBC cells to 5-FU (*48*).

NADPH oxidase 1 (NOX1), a membrane-bound enzyme that is up-regulated in GBC, is a significant source of reactive oxygen species (ROS). Hypoxia-inducible factor 1a (HIF1a) is a master regulator of cellular responses to ROS and plays an essential role in tumorigenesis (*49*). Studies have demonstrated that increased expression of NOX1 can enhance intracellular ROS levels, which then activate the HIF-1A/MDR1 pathway. This leads to increased drug efflux and cisplatin

resistance in GBC cells (*50*).

This suggests that overexpression of P-GP plays a pivotal role in the acquisition of multidrug resistance in GBC (Figure 3). However, the regulation of P-GP expression is a complex and multifaceted process. Thus, developing a single agent that can effectively downregulate P-GP expression *in vivo* presents a significant challenge. Nonetheless, such an agent would be valuable in enhancing the efficacy of multiple chemotherapeutic agents used in combination therapy for GBC.

2.5. DNA repair alteration (DDR)

DDR is a critical mechanism for repairing direct or indirect DNA damage induced by chemotherapy. DDR can be activated to restore the dysfunctional pathway, thus increasing DNA repair activity and drug resistance (*51*). The robustness of the intracellular DDR is a critical determinant of chemotherapy sensitivity.

Long non-coding RNA myosin light chain kinase antisense RNA 1 (MYLK-AS1), which is upregulated in GBC (*52*), acts as a regulator in this process. Its target is the polycomb group (PcG) family member, zeste homologous enhancer 2 (EZH2). EZH2 is a critical regulator of cell cycle progression, autophagy, and apoptosis, promoting DNA repair and inhibiting cell senescence, thereby increasing the DNA repair capacity of cancer cells (*53*). Thus, overexpression of MYLK-AS1 targets miR-217, which increases the expression of EZH2, leading to increased DNA repair in GBC cells and ultimately promoting resistance to chemotherapy drugs.

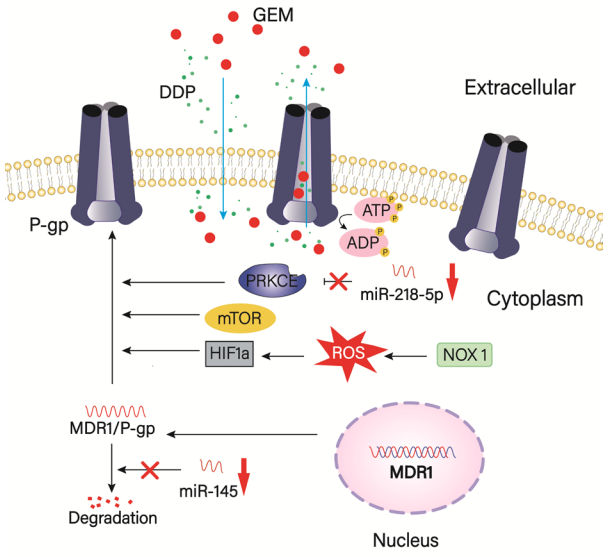

Figure 3. Diagram of cellular efflux mechanisms. (*i*) miR-218-5p inhibits the activation of MDR1/P-GP by downregulating the expression of PRKCE. (*ii*) miR-145 reduces the expression levels of MDR1/P-GP by directly degrading MRP1 mRNA. (*iii*) mTOR inhibits the synthesis of MDR1 induced by 5-FU. (*iv*) NOX1 increases intracellular ROS levels, thereby activating the HIF-1A/MDR1 pathway.

2.6. EMT

The EMT is a physiological process in which epithelial cells undergo transdifferentiation to form motile mesenchymal cells, playing an essential role in wound healing and cancer progression (*54*). Methyl-CpG binding domain protein 1 (MBD1), a transcriptional repressor that mediates DNA methylation, has also been implicated in tumor development and progression (*55*). Downregulation of MBD1 expression significantly increased the Gem sensitivity of gallbladder carcinoma cells (*56*). Furthermore, E-cadherin expression, an epithelial marker, was increased upon MBD1 knockdown, suggesting that MBD1 may promote EMT in GBC cells by suppressing e-cadherin expression. Hence, MBD1-mediated EMT may contribute to the development of chemotherapy resistance in GBC.

In conclusion, research on drug resistance mechanisms in gallbladder cancer was limited until 2010 due to the rarity of the disease and low diagnosis rates. However, with increased health awareness and clinical diagnoses, more patients with GBC receive chemotherapy, drawing attention to chemotherapy resistance in this malignancy. Among the various mechanisms studied, apoptosis and exocytosis are the primary focuses of research, providing insights for future clinical treatments. Additionally, investigating changes in the tumor microenvironment, cellular autophagy, and DNA repair mechanisms could enhance our understanding of chemotherapy resistance in GBC and lead to more effective treatment strategies.

3. Study of new agents and drugs against drug resistance

3.1. Agents at the basic experimental stage

Bufalin, a cardiotonic steroid (CTS) derived from traditional Chinese medicine toad venom, has been shown to exhibit multiple pharmacological activities including anti-tumor effects (*57*). One study demonstrated that bufalin can effectively downregulate Mcl-1, an important anti-apoptotic protein of the Bcl-2 protein family that helps cancer cells evade drug attacks. This downregulation leads to increased apoptosis of GBC cells and improved sensitivity of gallbladder cancer cells to chemotherapy drugs (*58*). Additionally, bufalin can suppress the proliferation and metastasis of tumor cells by impeding the MEK/ERK signaling pathway, reduce self-renewal and drug resistance of tumor stem cells by inhibiting the PI3K/Akt pathway, thus making it a promising candidate for treating patients with GBC resistant to conventional chemotherapy.

Maslinic acid (MA), a pentacyclic triterpene acid, has been shown to inhibit nuclear factor-κB (NF-κB) survival signaling pathways (*59*). By inhibiting NF-κB, MA is able to modulate the expression of regulatory factors for

cell proliferation (cyclin D1), apoptosis (Bax and Bcl-2), and metastasis (MMP-2 and MMP-9). Compared to treatment with GEM alone, the combination of MA and GEM resulted in significant downregulation of Cyclin D1 and Bcl-2 expression, while Bax expression was significantly increased, indicating that MA can inhibit cell proliferation, promote apoptosis, and enhance the sensitivity of GBC cells to chemotherapy (*60*).

Hispidulin, a flavonoid naturally occurring in the traditional Chinese medicinal herb *Salvia involucrate*, has been shown to increase caspase-3 activity and decrease BCL-2 expression while increasing Bax expression in GBC cells. Moreover, hispidulin can inhibit the HIF-1A/MDR1 pathway *via* AMPK signaling, resulting in decreased expression of P-GP and promoting the chemotherapy sensitivity of GBC cells (*61*).

Chloroquine, an autophagy inhibitor, has been found to enhance the induction of apoptosis and cell cycle arrest of GBC cells *in vitro* when used in combination with GEM. Furthermore, chloroquine can reduce the resistance of GBC cells to GEM by inhibiting autophagy and has also demonstrated enhanced tumor inhibition *in vivo* (*62*).

Cordycepin, a bioactive compound found in species of the genus *Cordyceps*, has shown promising results in promoting the sensitivity of GBC cells to chemotherapy drugs such as GEM and 5-FU by inhibiting the activation of mTORC1 and down-regulating the expression of MDR/HIF-1α *via* the AMPK signaling pathway (*63*).

Verapamil, a classical chemical sensitizer, has been shown to inhibit the transport function of P-GP by inhibiting the expression of MRP1. When combined with platinum-based therapy, cryotherapy with verapamil significantly increases the chemical sensitivity of GBC cells (*64*).

Tamoxifen is a commonly used anti-tumor drug with various beneficial effects. Research has demonstrated that tamoxifen can enhance the inhibition of cell activity and apoptosis induced by DDP (*65*). One crucial factor that determines GBC chemical resistance is the intracellular ROS level. Tamoxifen has been shown to induce ROS production and promote GBC apoptosis by inactivating the Nrf2 signal and increasing the expression of CYP.

Osi-027 is a novel ATP competitive inhibitor of mTORC1 and mTORC2 that can effectively inhibit the synthesis of MDR1, down-regulate the expression of MDR1 induced by 5-FU, and enhance the sensitivity of GBC cells to 5-Fu (*48*).

In general, most of these new agents are drugs that have shown antitumor effects in other cancer studies. The research results are only the antitumor phenomena observed in basic experiments and the superficial exploration of the anti-tumor mechanism. Few are used in clinical trials. What's more, the appropriate concentration, specificity, and toxicity of these small molecule drugs to normal tissues remain unknown. Only few agents are actually developed to combat resistance or have the significance to provide guidance for clinical drug use. The ultimate goal of scientific research is to use it to cure patients and benefit people's health. Therefore, there is a need to accelerate the pace of new drug development research.

3.2. The improvement of traditional chemotherapy drugs

NUC-1031 is a promising chemotherapy drug for the treatment of GBC, which has been developed through the application of ProTide technology to transform GEM into a phosphoramidate (*66*). Like GEM, NUC-1031's cytotoxic effect on cancer cells is largely attributed to the generation of the triphosphate form of the nucleotide analog (di-fluoro-deoxycytidine triphosphate [dFdCTP]). However, NUC-1031 can generate and maintain higher concentrations of dFdCTP inside the tumor cell than GEM due to its unique properties. Firstly, the phosphoramidate moiety enables NUC-1031 to enter the cancer cell, independent of the presence of nucleoside transporters. Secondly, once NUC-1031 has entered the cell, the protective group is cleaved off and releases an activated, monophosphorylated form of GEM (dFdCMP). This delivery of dFdCMP obviates the need for the activating enzyme, deoxycytidine kinase, which drives the rate-limiting phosphorylation of gemcitabine. dFdCMP is rapidly converted to di-fluoro-deoxycytidine diphosphate and then the key anticancer metabolite, dFdCTP. Thirdly, NUC-1031 is not subject to breakdown by cytidine deaminase (CDA), which is a key resistance mechanism in GBC. Due to its ability to overcome all three key resistance mechanisms, NUC-1031 achieves much higher levels of the active anticancer metabolite, dFdCTP, than GEM. This mechanism of action has been illustrated in previous publications on NUC-1031 (*67*). Furthermore, the agent has demonstrated safety and tolerability in phase 1 clinical trials and is currently being prepared for later clinical trials.

Capecitabine is an oral prodrug of 5-FU, which exerts its cytotoxic effects by inhibiting DNA synthesis, RNA processing, and protein synthesis. S-1 is another oral anticancer drug that consists of a combination of tegafur (a 5-FU prodrug), gimeracil, and oteracil potassium. Gimeracil acts as an inhibitor of dihydropyrimidine dehydrogenase, thereby increasing the concentration of fluorouracil in the blood and tumor tissue. Oteracil potassium reduces gastrointestinal toxicity by suppressing the phosphorylation of fluorouracil in the gastrointestinal tract. The BILCAP (compare capecitabine with observation following resection of biliary tract cancer) phase 3 trial conducted in the UK in 2019 demonstrated that capecitabine can improve overall survival after resection of biliary tract cancer when used as adjuvant chemotherapy following surgery (*68*). A phase 3 clinical trial (JCOG1202, ASCOT) was conducted in Japan in 2023, which compared adjuvant S-1 with observation in

resected biliary tract cancer. This study showed that S-1 as adjuvant therapy had a comparable survival effect to capecitabine but with fewer side effects for GBC (*69*).

These improvements to traditional chemotherapeutics are expected to be used in clinical applications and bring benefits to patients soon.

3.3. Molecular targeted therapy

Molecular targeted therapy represents a critical adjunct to conventional chemotherapy for advanced, chemotherapy-resistant GBC. Regorafenib is a multikinase inhibitor that targets several pathways, including angiogenesis *via* vascular endothelial growth factor receptors 1-3 and TIE2, oncogenesis by inhibiting the downstream pathways of KIT, RET, RAF1, and BRAF, modulation of the tumor microenvironment by blocking the activity of intracellular domains of platelet-derived growth factor receptor and fibroblast growth factor receptor, and activation of tumor immunity through colony-stimulating factor 1 receptor. In phase II trials (*70-72*), regorafenib was found to be active and significantly increased the median progression-free survival in patients with locally advanced/metastatic GBC that progressed after GEM/DDP-based chemotherapy. Additionally, other agents such as varlitinib, trastuzumab, surufatinib, lenvatinib, and others have also undergone phase 2 trials and demonstrated promising results in prolonging the survival time of GBC patients.

4. Conclusion and prospects

Patients diagnosed with GBC often miss the opportunity for surgery due to late detection, and thus chemotherapy becomes a crucial treatment option to prolong patient survival. The initial use of commonly used clinical chemotherapeutic agents such as gemcitabine and cisplatin has shown promising therapeutic effects. However, the development of chemoresistance has diminished the effectiveness of these agents and hindered their ability to provide long-term support for patients. Therefore, addressing chemotherapy resistance has become an important issue in extending patients' lives.

In the past decade, drug resistance in GBC has gained unprecedented attention, and researchers are addressing this challenge on two fronts. Firstly, efforts have focused on understanding the mechanisms underlying resistance. Alterations in apoptotic pathways and increased extracellular derivation have been identified as key contributors to drug resistance, while changes in miRNA expression seem to play a crucial role in the development of resistance. Secondly, researchers are investigating the development of new drugs that can overcome resistance in GBC cells, which arise when conventional chemotherapeutic agents are used.

To date, significant efforts have been dedicated to eliminating drug resistance as a therapeutic strategy and improving its efficacy. While studies have reported findings on various mechanisms that contribute to the development of drug resistance, there are limited in-depth and continuous studies available to systematically explain the mechanism of drug resistance in gallbladder cancer. Additionally, validation in large multicenter clinical trials is still challenging as gallbladder cancer is relatively rare and the number of patients with the disease per hospital is small. With regards to new small molecule drugs, although they have shown remarkable inhibitory effects on tumor cells in basic experiments, it is still a long road ahead before they can be clinically tested to benefit tumor patients. As such, further research and development are necessary to improve the understanding and management of drug resistance in gallbladder cancer.

In the future, further attention should be given to the following aspects: In basic research, emphasis should be placed on the mechanisms of drug efflux and apoptosis, with a particular focus on changes in various pathways during drug resistance, and systematic studies should be conducted to identify the key points of drug resistance. At present, correlation studies on MDR are too lacking to form a systematic study. Since the generation of MDRs is responsible for almost 90 percent, it should be the most important point for future basic research. The elucidations of the mechanisms and pathways of MDR can lead to the design of new drugs, targeted drugs and the most efficient way to benefit patients.

Funding: This work was supported by the National Natural Science Foundation of China (grant No.81802337), Shanghai Jiao Tong University (grant No.YG2017MS74), and the Shanghai Health Committee (grant No. 2020404447).

Conflict of Interest: The authors have no conflicts of interest to disclose.

References

1. Misra S, Chaturvedi A, Misra NC, Sharma ID. Carcinoma of the gallbladder. Lancet Oncol. 2003; 4:167-176.
2. Sharma A, Sharma KL, Gupta A, Yadav A, Kumar A. Gallbladder cancer epidemiology, pathogenesis and molecular genetics: Recent update. World J Gastroenterol. 2017; 23:3978-3998.
3. Hsing AW, Bai Y, Andreotti G, Rashid A, Deng J, Chen J, Goldstein AM, Han TQ, Shen MC, Fraumeni JF, Jr., Gao YT. Family history of gallstones and the risk of biliary tract cancer and gallstones: a population-based study in Shanghai, China. Int J Cancer. 2007; 121:832-838.
4. Goetze TO. Gallbladder carcinoma: Prognostic factors and therapeutic options. World J Gastroenterol. 2015; 21:12211-12217.
5. Hong D. Guidelines for diagnosis and treatment of gallbladder cancer. Journal of hepatopancreatobiliary Surgery. 2020; 32:664-666.
6. Patkar S, Ostwal V, Ramaswamy A, Engineer R, Chopra S, Shetty N, Dusane R, Shrikhande SV, Goel M. Emerging

role of multimodality treatment in gall bladder cancer: Outcomes following 510 consecutive resections in a tertiary referral center. J Surg Oncol. 2018; 117:372-379.
7. Zheng CJ, Zou H, Zhang XW. Progress in the comprehensive treatment of gallbladder carcinoma. J Mod Oncol. 2019; 27:2954-2957.
8. Mantripragada KC, Hamid F, Shafqat H, Olszewski AJ. Adjuvant therapy for resected gallbladder cancer: Analysis of the National Cancer Database. J Natl Cancer Inst. 2016; 109:djw202.
9. Nakamura M, Nakashima H, Abe T, Ensako T, Yoshida K, Hino K. Gemcitabine-based adjuvant chemotherapy for patients with advanced gallbladder cancer. Anticancer Res. 2014; 34:3125-3129.
10. Ding P, Gao Y, Wang J, Xiang H, Zhang C, Wang L, Ji G, Wu T. Progress and challenges of multidrug resistance proteins in diseases. Am J Cancer Res. 2022; 12:4483-4501.
11. Bukowski K, Kciuk M, Kontek R. Mechanisms of multidrug resistance in cancer chemotherapy. Int J Mol Sci. 2020; 21:3233.
12. Haider T, Pandey V, Banjare N, Gupta PN, Soni V. Drug resistance in cancer: Mechanisms and tackling strategies. Pharmacol Rep. 2020; 72:1125-1151.
13. Sethi T, Rintoul RC, Moore SM, MacKinnon AC, Salter D, Choo C, Chilvers ER, Dransfield I, Donnelly SC, Strieter R, Haslett C. Extracellular matrix proteins protect small cell lung cancer cells against apoptosis: a mechanism for small cell lung cancer growth and drug resistance *in vivo*. Nat Med. 1999; 5:662-668.
14. Sun Y. Tumor microenvironment and cancer therapy resistance. Cancer Lett. 2016; 380:205-215.
15. Zhang Y, Chua S, Jr. Leptin function and regulation. Compr Physiol. 2017; 8:351-369.
16. Wang WJ, Lai HY, Zhang F, Shen WJ, Chu PY, Liang HY, Liu YB, Wang JM. MCL1 participates in leptin-promoted mitochondrial fusion and contributes to drug resistance in gallbladder cancer. JCI Insight. 2021; 6:e135438.
17. Lai HY, Hsu LW, Tsai HH, Lo YC, Yang SH, Liu PY, Wang JM. CCAAT/enhancer-binding protein delta promotes intracellular lipid accumulation in M1 macrophages of vascular lesions. Cardiovasc Res. 2017; 113:1376-1388.
18. Brotin E, Meryet-Figuiere M, Simonin K, Duval RE, Villedieu M, Leroy-Dudal J, Saison-Behmoaras E, Gauduchon P, Denoyelle C, Poulain L. Bcl-XL and MCL-1 constitute pertinent targets in ovarian carcinoma and their concomitant inhibition is sufficient to induce apoptosis. Int J Cancer. 2010; 126:885-895.
19. Haider T, Tiwari R, Vyas SP, Soni V. Molecular determinants as therapeutic targets in cancer chemotherapy: An update. Pharmacol Ther. 2019; 200:85-109.
20. Czabotar PE, Lessene G, Strasser A, Adams JM. Control of apoptosis by the BCL-2 protein family: Implications for physiology and therapy. Nat Rev Mol Cell Biol. 2014; 15:49-63.
21. Teixeira C, Reed JC, Pratt MA. Estrogen promotes chemotherapeutic drug resistance by a mechanism involving Bcl-2 proto-oncogene expression in human breast cancer cells. Cancer Res. 1995; 55:3902-3907.
22. Zhang X, Huang Q, Yang Z, Li Y, Li CY. GW112, a novel antiapoptotic protein that promotes tumor growth. Cancer Res. 2004; 64:2474-2481.
23. Liu W, Liu Y, Li H, Rodgers GP. Olfactomedin 4 contributes to hydrogen peroxide-induced NADPH oxidase activation and apoptosis in mouse neutrophils. Am J Physiol Cell Physiol. 2018; 315:C494-C501.
24. Wang XY, Chen SH, Zhang YN, Xu CF. Olfactomedin-4 in digestive diseases: A mini-review. World J Gastroenterol. 2018; 24:1881-1887.
25. Lin Z, Yang S, Zhou Y, *et al*. OLFM4 depletion sensitizes gallbladder cancer cells to cisplatin through the ARL6IP1/caspase-3 axis. Transl Oncol. 2022; 16:101331.
26. Han Y, Liao Q, Wang H, Rao S, Yi P, Tang L, Tian Y, Oyang L, Wang H, Shi Y, Zhou Y. High expression of calreticulin indicates poor prognosis and modulates cell migration and invasion *via* activating Stat3 in nasopharyngeal carcinoma. J Cancer. 2019; 10:5460-5468.
27. Shi F, Shang L, Pan BQ, Wang XM, Jiang YY, Hao JJ, Zhang Y, Cai Y, Xu X, Zhan QM, Wang MR. Calreticulin promotes migration and invasion of esophageal cancer cells by upregulating neuropilin-1 expression *via* STAT5A. Clin Cancer Res. 2014; 20:6153-6162.
28. Ye J, Qi L, Du Z, Yu L, Chen K, Li R, Feng R, Zhai W. Calreticulin: A potential diagnostic and therapeutic biomarker in gallbladder cancer. Aging (Albany NY). 2021; 13:5607-5620.
29. Liu B, Liu Y, Zhao L, Pan Y, Shan Y, Li Y, Jia L. Upregulation of microRNA-135b and microRNA-182 promotes chemoresistance of colorectal cancer by targeting ST6GALNAC2 *via* PI3K/AKT pathway. Mol Carcinog. 2017; 56:2669-2680.
30. Chang Y, Liu C, Yang J, *et al*. MiR-20a triggers metastasis of gallbladder carcinoma. J Hepatol. 2013; 59:518-527.
31. Yang D, Zhan M, Chen T, Chen W, Zhang Y, Xu S, Yan J, Huang Q, Wang J. miR-125b-5p enhances chemotherapy sensitivity to cisplatin by down-regulating Bcl2 in gallbladder cancer. Sci Rep. 2017; 7:43109.
32. Zhang GF, Wu JC, Wang HY, Jiang WD, Qiu L. Overexpression of microRNA-205-5p exerts suppressive effects on stem cell drug resistance in gallbladder cancer by down-regulating PRKCE. Biosci Rep. 2020; 40:BSR20194509.
33. Lai X, Gupta SK, Schmitz U, Marquardt S, Knoll S, Spitschak A, Wolkenhauer O, Putzer BM, Vera J. MiR-205-5p and miR-342-3p cooperate in the repression of the E2F1 transcription factor in the context of anticancer chemotherapy resistance. Theranostics. 2018; 8:1106-1120.
34. Wang H, Zhan M, Xu SW, Chen W, Long MM, Shi YH, Liu Q, Mohan M, Wang J. miR-218-5p restores sensitivity to gemcitabine through PRKCE/MDR1 axis in gallbladder cancer. Cell Death Dis. 2017; 8:e2770.
35. Pelaz SG, Tabernero A. Src: coordinating metabolism in cancer. Oncogene. 2022; 41:4917-4928.
36. Hashemi M, Taheriazam A, Daneii P, Hassanpour A, Kakavand A, Rezaei S, Hejazi ES, Aboutalebi M, Gholamrezaie H, Saebfar H, Salimimoghadam S, Mirzaei S, Entezari M, Samarghandian S. Targeting PI3K/Akt signaling in prostate cancer therapy. J Cell Commun Signal. 2023; 17:423-443.
37. Bai J, Yang BJ, Luo X. Effects of 5-hydroxy-4'-nitro-7-propionyloxy-genistein on inhibiting proliferation and invasion *via* activating reactive oxygen species in human ovarian cancer A2780/DDP cells. Oncol Lett. 2018; 15:5227-5235.
38. White E. The role for autophagy in cancer. J Clin Invest. 2015; 125:42-46.
39. Qian X, Li X, Cai Q, *et al*. Phosphoglycerate kinase 1

phosphorylates Beclin1 to induce autophagy. Mol Cell. 2017; 65:917-931 e916.
40. Cai Q, Wang Z, Wang S, Weng M, Zhou D, Li C, Wang J, Chen E, Quan Z. Long non-coding RNA LINC00152 promotes gallbladder cancer metastasis and epithelial-mesenchymal transition by regulating HIF-1alpha *via* miR-138. Open Biol. 2017; 7:160247.
41. Cai Q, Wang S, Jin L, Weng M, Zhou D, Wang J, Tang Z, Quan Z. Long non-coding RNA GBCDRlnc1 induces chemoresistance of gallbladder cancer cells by activating autophagy. Mol Cancer. 2019; 18:82.
42. Chen C, Lu L, Yan S, Yi H, Yao H, Wu D, He G, Tao X, Deng X. Autophagy and doxorubicin resistance in cancer. Anticancer Drugs. 2018; 29:1-9.
43. Yalcin-Ozkat G. Molecular modeling strategies of cancer multidrug resistance. Drug Resist Updat. 2021; 59:100789.
44. Gottesman MM, Fojo T, Bates SE. Multidrug resistance in cancer: role of ATP-dependent transporters. Nat Rev Cancer. 2002; 2:48-58.
45. Hanssen KM, Haber M, Fletcher JI. Targeting multidrug resistance-associated protein 1 (MRP1)-expressing cancers: Beyond pharmacological inhibition. Drug Resist Updat. 2021; 59:100795.
46. Zhan M, Zhao X, Wang H, Chen W, Xu S, Wang W, Shen H, Huang S, Wang J. miR-145 sensitizes gallbladder cancer to cisplatin by regulating multidrug resistance associated protein 1. Tumour Biol. 2016; 37:10553-10562.
47. Hua H, Kong Q, Zhang H, Wang J, Luo T, Jiang Y. Targeting mTOR for cancer therapy. J Hematol Oncol. 2019; 12:71.
48. Li Q, Mou LJ, Tao L, Chen W, Sun XT, Xia XF, Wu XY, Shi XL. Inhibition of mTOR suppresses human gallbladder carcinoma cell proliferation and enhances the cytotoxicity of 5-fluorouracil by downregulating MDR1 expression. Eur Rev Med Pharmacol Sci. 2016; 20:1699-1706.
49. Semenza GL. HIF-1 mediates metabolic responses to intratumoral hypoxia and oncogenic mutations. J Clin Invest. 2013; 123:3664-3671.
50. Zhan M, Wang H, Chen T, Chen W, Yang L, He M, Xu S, Wang J. NOX1 mediates chemoresistance *via* HIF1alpha/MDR1 pathway in gallbladder cancer. Biochem Biophys Res Commun. 2015; 468:79-85.
51. Housman G, Byler S, Heerboth S, Lapinska K, Longacre M, Snyder N, Sarkar S. Drug resistance in cancer: An overview. Cancers (Basel). 2014; 6:1769-1792.
52. Li Y, Tian M, Zhang D, Zhuang Y, Li Z, Xie S, Sun K. Long non-coding RNA myosin light chain kinase antisense 1 plays an oncogenic role in gallbladder carcinoma by promoting chemoresistance and proliferation. Cancer Manag Res. 2021; 13:6219-6230.
53. Jones BA, Varambally S, Arend RC. Histone methyltransferase EZH2: A therapeutic target for ovarian cancer. Mol Cancer Ther. 2018; 17:591-602.
54. Holohan C, Van Schaeybroeck S, Longley DB, Johnston PG. Cancer drug resistance: An evolving paradigm. Nat Rev Cancer. 2013; 13:714-726.
55. Lopez-Serra L, Ballestar E, Fraga MF, Alaminos M, Setien F, Esteller M. A profile of methyl-CpG binding domain protein occupancy of hypermethylated promoter CpG islands of tumor suppressor genes in human cancer. Cancer Res. 2006; 66:8342-8346.
56. Wensheng L, Bo Z, Qiangsheng H, Wenyan X, Shunrong J, Jin X, Quanxing N, Xianjun Y, Xiaowu X. MBD1 promotes the malignant behavior of gallbladder cancer cells and induces chemotherapeutic resistance to gemcitabine. Cancer Cell Int. 2019; 19:232.
57. Sheng X, Sun X, Sun K, Sui H, Qin J, Li Q. Inhibitory effect of bufalin combined with Hedgehog signaling pathway inhibitors on proliferation and invasion and metastasis of liver cancer cells. Int J Oncol. 2016; 49:1513-1524.
58. Qian L, Su H, Wang G, Li B, Shen G, Gao Q. Anti-tumor activity of bufalin by inhibiting c-MET mediated MEK/ERK and PI3K/AKT signaling pathways in gallbladder cancer. J Cancer. 2020; 11:3114-3123.
59. Li C, Yang Z, Zhai C, Qiu W, Li D, Yi Z, Wang L, Tang J, Qian M, Luo J, Liu M. Maslinic acid potentiates the anti-tumor activity of tumor necrosis factor alpha by inhibiting NF-kappaB signaling pathway. Mol Cancer. 2010; 9:73.
60. Yu Y, Wang J, Xia N, Li B, Jiang X. Maslinic acid potentiates the antitumor activities of gemcitabine *in vitro* and *in vivo* by inhibiting NF-kappaB-mediated survival signaling pathways in human gallbladder cancer cells. Oncol Rep. 2015; 33:1683-1690.
61. Gao H, Xie J, Peng J, Han Y, Jiang Q, Han M, Wang C. Hispidulin inhibits proliferation and enhances chemosensitivity of gallbladder cancer cells by targeting HIF-1alpha. Exp Cell Res. 2015; 332:236-246.
62. Wang FT, Wang H, Wang QW, Pan MS, Li XP, Sun W, Fan YZ. Inhibition of autophagy by chloroquine enhances the antitumor activity of gemcitabine for gallbladder cancer. Cancer Chemother Pharmacol. 2020; 86:221-232.
63. Wu WD, Hu ZM, Shang MJ, Zhao DJ, Zhang CW, Hong DF, Huang DS. Cordycepin down-regulates multiple drug resistant (MDR)/HIF-1alpha through regulating AMPK/mTORC1 signaling in GBC-SD gallbladder cancer cells. Int J Mol Sci. 2014; 15:12778-12790.
64. Wang H, Li X, Chen T, Wang W, Liu Q, Li H, Yi J, Wang J. Mechanisms of verapamil-enhanced chemosensitivity of gallbladder cancer cells to platinum drugs: Glutathione reduction and MRP1 downregulation. Oncol Rep. 2013; 29:676-684.
65. Huang S, Wang H, Chen W, Zhan M, Xu S, Huang X, Lin R, Shen H, Wang J. Tamoxifen inhibits cell proliferation by impaired glucose metabolism in gallbladder cancer. J Cell Mol Med. 2020; 24:1599-1613.
66. Slusarczyk M, Lopez MH, Balzarini J, Mason M, Jiang WG, Blagden S, Thompson E, Ghazaly E, McGuigan C. Application of ProTide technology to gemcitabine: A successful approach to overcome the key cancer resistance mechanisms leads to a new agent (NUC-1031) in clinical development. J Med Chem. 2014; 57:1531-1542.
67. McNamara MG, Bridgewater J, Palmer DH, Faluyi O, Wasan H, Patel A, Ryder WD, Barber S, Gnanaranjan C, Ghazaly E, Evans TRJ, Valle JW. A phase Ib study of NUC-1031 in combination with cisplatin for the first-line treatment of patients with advanced biliary tract cancer (ABC-08). Oncologist. 2021; 26:e669-e678.
68. Primrose JN, Fox RP, Palmer DH, *et al*. Capecitabine compared with observation in resected biliary tract cancer (BILCAP): A randomised, controlled, multicentre, phase 3 study. Lancet Oncol. 2019; 20:663-673.
69. Nakachi K, Ikeda M, Konishi M, *et al*. Adjuvant S-1 compared with observation in resected biliary tract cancer (JCOG1202, ASCOT): A multicentre, open-label, randomised, controlled, phase 3 trial. Lancet. 2023;

401:195-203.
70. Demols A, Borbath I, Van den Eynde M, Houbiers G, Peeters M, Marechal R, Delaunoit T, Goemine JC, Laurent S, Holbrechts S, Paesmans M, Van Laethem JL. Regorafenib after failure of gemcitabine and platinum-based chemotherapy for locally advanced/metastatic biliary tumors: REACHIN, a randomized, double-blind, phase II trial. Ann Oncol. 2020; 31:1169-1177.
71. Kim RD, Sanoff HK, Poklepovic AS, Soares H, Kim J, Lyu J, Liu Y, Nixon AB, Kim DW. A multi-institutional phase 2 trial of regorafenib in refractory advanced biliary tract cancer. Cancer. 2020; 126:3464-3470.
72. Sun W, Patel A, Normolle D, Patel K, Ohr J, Lee JJ, Bahary N, Chu E, Streeter N, Drummond S. A phase 2 trial of regorafenib as a single agent in patients with chemotherapy-refractory, advanced, and metastatic biliary tract adenocarcinoma. Cancer. 2019; 125:902-909.

Received March 1, 2023; Revised July 15, 2023; Accepted August 8, 2023.

[§]These authors contributed equally to this work.

*Address correspondence to:
Fei Ma, Department of Oncology, Xinhua Hospital Affiliated to Shanghai Jiao Tong University School of Medicine, No. 1665 Kongjiang Road, Shanghai 200092, China.
E-mail: mafei@xinhuamed.com.cn

Jun Ding, Department of Biliary and Pancreatic Surgery, Shanghai Shuguang Hospital Affiliated to Shanghai University of Traditional Chinese Medicine, Shanghai 201203, China.
E-mail: doctording0916@126.com

Released online in J-STAGE as advance publication August 17, 2023.

Review

DOI: 10.5582/ddt.2023.01005

Ultrasound-guided brachial plexus block at the clavicle level: A review

Zhimin Guo[1], Ming Zhao[2], Haihua Shu[1,2,*]

[1] Guangdong Cardiovascular Institute, Guangdong Provincial People's Hospital, Guangdong Academy of Medical Sciences, Guangzhou, Guangdong, China;
[2] Department of Anesthesiology, Guangdong Provincial People's Hospital (Guangdong Academy of Medical Sciences), Southern Medical University, Guangzhou, Guangdong, China.

SUMMARY The supraclavicular block (SCB) and the infraclavicular block (ICB) are introduced to meet upper extremity surgery, where the transducer or the insertion point is placed superiorly and inferiorly at the approximate midpoint of the clavicle, respectively. These two approaches are highly appealing since they clearly exhibited each cord and its associated anatomy. In addition, it directed the needle accurately with real-time imaging by ultrasound guidance. Therefore, it brought higher success rates and fewer complications. Numerous trials have recently been conducted to examine the SCB and ICB regarding the new approach, injection techniques, block dynamics, and complication of hemidiaphragmatic paresis. It was found that both approaches could improve block effectiveness and postoperative analgesia for upper extremity surgery, according to recent studies at the level of the clavicular brachial plexus block. However, there is still a lack of work comparing the clinical performance and effectiveness of both approaches with ultrasonography. This review aims to outline the current available data from clinical trials along with case reports about these two approaches and to describe the findings published in the literature during the previous 5 years. Based on these findings, we attempt to determine whether there exists a one-size-fits-all approach that has the potential to meet upper extremity surgery.

Keywords Brachial plexus block, supraclavicular block, infraclavicular block, costoclavicular block, injection techniques, hemidiaphragmatic paresis, upper extremity surgery

1. Introduction

High-resolution ultrasound has been proven to identify the brachial plexus clearly, direct the needle to the target nerves precisely and visualize the pattern of local anaesthetic spread in real time (*1,2*). Various approaches to brachial plexus block with ultrasound guidance have been described elaborately, particularly recent well-recommended approaches of supraclavicular block (SCB) and infraclavicular block (ICB) at the level of the clavicle (*3,4*). Many trials have confirmed that SCB and ICB can be applied for upper extremity surgery (*5-8*). Compared with axillary block (AB) and/or interscalene block (ISB), SCB and ICB show faster onset times, higher block success rates and lower complication risks (*9,10*). However, how to flexibly choose and apply SCB and ICB in the clinical practice of upper extremity nerve block according to their respective advantages and disadvantages is still controversial (*11-15*). Recently, novel approaches have been reported around the clavicle to overcome these limitations, for example, the "corner pocket" approach in SCB and the costoclavicular approach in ICB (*1,16*). The performance of SCB and ICB may be accompanied with the risk of pneumothorax, yet it distinctly decreased when ultrasound was utilized (*3,4*).

Koscielniak-Nielsen ZJ *et al.* considered that ICB had a faster onset, better surgical effectiveness and fewer adverse events (*11*), but some recent trials indicated that similar block characteristics were both achieved in SCB and ICB, while adverse events were lower in ICB than in SCB (*12,13*). A systematic review indicated that the higher success rate of ICB may contribute to the double or triple injection technique, which accelerates anaesthetic spread (*17*). However, some trials demonstrated that there was no significant difference in the success rate by single or multiple injections, whether in SCB or ICB (*18,19*). Although multiple injections are safely and widely used to expand the block and shorten the onset time under ultrasound guidance, some

confusion still exists in these techniques (*15*).

Focusing on providing equivalent analgesia and reducing complications by the SCB, many studies have been performed to compare the effect of postoperative analgesia of SCB with ISB in patients undergoing shoulder surgery. It showed that SCB might achieve comparable analgesia without increasing the risk of hemidiaphragmatic paresis (HDP), a common complication of brachial plexus block (*20,21*). It was reported that the costoclavicular block (CCB), a kind of ICB current common clinically applied, could also provide effective postoperative analgesia for shoulder surgery and prevent the occurrence of HDP (*22*). Since the shoulder area is innervated by cervical nerves, where the SCB and ICB are not able to cover, SCB and ICB may be appropriate for postoperative analgesia but not for surgical anesthesia (*3,4*).

In general, current clinical trials at the level of the clavicular brachial plexus demonstrate that both approaches of SCB and ICB can achieve better block effectiveness anesthesia and postoperative analgesia for upper extremity surgery (*3,4*). The multiple injection technique is commonly used for its advantage of shorter onset time (*18,19*). CCB can perfectly circumvent the risk of HDP (*22*). We will introduce the new approaches, injection techniques, block dynamics, and HDP complications in the SCB and ICB (as shown in Tables 1 and 2).

2. Supraclavicular block

2.1. Clinical characteristics of different approaches

The SCB is a popular approach that has been approved for the brachial plexus for its greater safety due to real-time ultrasound guidance and better block dynamics known as the "spinal anesthesia of the arm" (*4,23*). Kapral *et al.* (*24*) first described the "proximal" approach with ultrasound guidance located approximately 3 cm superior at the midpoint of the clavicle, in which three trunks of the brachial plexus were clearly visualized, and complete block was achieved with a reduction in relative complications compared with axillary block (Table 1, online data, *https://www.ddtjournal.com/supplementaldata/150*). Targeting the neural cluster (confluence of trunks and divisions) in a transverse sectional view with a "distal" approach, the ultrasound probe was placed in the coronal oblique plane just above the supraclavicular fossa, where the cluster lateral to the subclavian artery lies on the top of the first rib (*25*). The success rate of this approach achieved 95% without pneumothorax using 20 mL of lidocaine 2% and 20 mL of bupivacaine 0.5% (Table 1, online data, *https://www.ddtjournal.com/supplementaldata/150*). For ultrasound-guided SCB in the distal approach (*1*), the needle tip advances to the corner bordered by the subclavian artery medially, the first rib inferiorly, and the divisions of the brachial plexus superior laterally, named the "corner pocket" technique, and is described as the optimal position for local anesthetic distribution, which provides a dense and complete block for the entire upper extremity within minutes. The authors found that this technique produced excellent success in achieving surgical anesthesia for the forearm and hand when administrating only as little as 15 mL of local anesthetic with ultrasound guidance (Table 1, online data, *https://www.ddtjournal.com/supplementaldata/150*).

Additionally, a new technique was named the intertruncal approach and claimed that it offers an

Table 2. Evidence of the risk of HDP in SCB and CCB

Article	Approach	Method	Analgesia effect	HDP
Aliste J[20]	ISB and SCB	20 mL of 0.5% levobupivacaine	Both groups displayed equivalent postoperative pain scores at 0.5, 1, 2, 3, 6, 12, and 24 hours.	ISB:SCB = 95% *vs.* 9%, $p < 0.001$.
Karaman T[21]	ISB and SCB	20 mL of 0.25% bupivacaine	No significant differences were found between the two groups for pain scores ($p = 0.34$).	/
Tran DQ[31]	SCB	Investigation using a modified "3+3" dose escalation design for exploring the dose-response relationship, 2:1 mixture of 1.5% mepivacaine and 0.5% bupivacaine.	/	All subjects demonstrated HDP at 15-20 min, and even with the lowest dose of 5ml, one of the three subjects occurred HDP at 15 min (33% incidence),suggesting that there is no clinically relevant dose at which HDP can be avoid.
Aliste J[22]	ISB and CCB	20 mL of levobupivacaine 0.5%.	CCB could provide comparable analgesia effect and shorter onset time (14.0 (5.0) *vs*. 21.6 (6.4) minutes, $p < 0.001$).	Avoiding the risk of HDP (CCB 0%:ISB 100%).
SivashanmugamT[40]	CCB and SCB	20 mL of mixture of 0.5% bupivacaine and 2% lidocaine.	/	CCB group is 5%, while in SCB group is 45%.

Note: Table 2 shows some evidence of the occurrence of HDP regarding SCB and CCB. Abbreviations: SCB, supraclavicular block; ISB, interscalene block; CCB, costoclavicular block.

advantage over the "intracluster" approach (*26*), as it purposefully avoids intraneural injection. It also offers advantages over the "corner pocket" approach, as it may help to avoid pneumothorax, by which local anesthetic is deposited in the two adipose tissue planes between the upper and middle trunks and the middle and lower trunks. It produced a shorter performing time within a few minutes and a rapid onset of action, similar to other injection techniques. Recently, a newest technique named "selective trunk block (SeTB)" (*27*) was performed as a "two-injection" peri-plexus technique with the first injection targeting the superior and middle trunk at the interscalene groove and the second injection targeting the inferior trunk at the corner pocket of the supraclavicular fossa. It has been demonstrated that nerve block with SeTB produces surgical anesthesia for the whole upper extremity undergoing intramedullary nailing of the humerus for a pathological fracture, except for the intercostobrachial nerve territory (the medial aspect of the upper arm) (*27*). The volume of local anesthetics (1:1 mixture of lidocaine 2% with 1:200,000 epinephrine and levobupivacaine 0.5%), targeting the superior and middle trunks, 8 mL and 7 mL, respectively, was administered at the interscalene groove, while 10 mL was injected into the inferior trunk at the corner pocket of the supraclavicular fossa (Table 1, online data, *https://www.ddtjournal.com/supplementaldata/150*) (*27*). The patient remained comfortable and required no additional analgesics during the perioperative period and first requested postoperative analgesics approximately 7 h after the block. There was no residual neurological deficit on postoperative day 1. The "SeTB" technique can produce sensory-motor blockade of the whole upper extremity, including the shoulder and arm. However, this is only a case report, and further study should be performed to evaluate the safety and efficacy in cohorts of patients with well-designed clinical trials.

2.2. Clinical characteristics of different injection points

The brachial plexus could be localized accurately with ultrasound guidance, and the needle was repositioned with a focus on local anesthetic spreading around the target nerves, intentionally making a second injection, but it remained unclear whether the double injection is necessary to guarantee complete anesthesia (*25*). A trial compared the clinical outcomes of single and double injections for upper extremity surgery with ultrasound-guided SCB (*28*). In the single-injection group, 35 mL of lidocaine 1.5% with epinephrine 5 μg/mL was administered at the junction of the first rib and subclavian artery (the "corner pocket"). In the double-injection group using the same mixture of local anesthetic, 25 mL was initially injected at the "corner pocket" site, and another 15 mL was injected superolateral to the subclavian artery. The double-injection technique resulted in a shorter onset time, but this group required a higher number of needle passes, and thus the total anesthesia-related times were similar (Table 1, online data, *https://www.ddtjournal.com/supplementaldata/150*). The double injection also resulted in a faster onset for sensory blockade of the musculocutaneous and radial nerves, a quicker motor block of the musculocutaneous nerve at the first 30 min and a higher rate of ulnar motor block at 10 min (Table 1, online data, *https://www.ddtjournal.com/supplementaldata/150*) (*28*). However, there were no differences in the success rate, procedural pain or adverse events between the groups. Further trials have been performed regarding the comparison between single injection and double or even triple injection using the corner pocket technique for ultrasound-guided SCB, but they presented similar overall success rates and offered no benefit over a single injection, which may be attributed to the higher volume of local anesthetics administered in their studies (*6,18,29*). A trial (*29*) showed a similar rate of complete sensory block at 15 min and similar surgical block success using 30 mL of mepivacaine 1.5% (Table 1, online data, *https://www.ddtjournal.com/supplementaldata/150*). Another trial (*6*) showed that the combined success of the sensory block was 20%~31% higher in the triple-injection group than in the single-injection group at 10, 15, and 20 min after injecting 30 mL of 1.5% lidocaine with epinephrine, but the overall success of surgical anesthesia did not differ significantly (Table 1, online data, *https://www.ddtjournal.com/supplementaldata/150*). Nitin Choudhary *et al.* (*18*) proposed that we should take full advantage of site-specific deposition of local anesthetic solution with the use of ultrasound in SCB to reduce the overall dose of the drugs and its overall adverse effects. In their trials, they limited their drug volume to 20 mL based on some proven studies and concluded that the double-injection group achieved a higher success rate with faster sensory and motor onset and a longer duration of sensory and motor block than the single-injection group (Table 1, online data, *https://www.ddtjournal.com/supplementaldata/150*) (*18*). Ten milliliters of 0.5% bupivacaine was injected into the superior cluster, and another 10 mL was injected into the corner pocket with the help of hydrodissection to ensure the correct direction in the double-injection group, while 20 mL was injected into the superior cluster in the single-injection group. Furthermore, Techasuk W *et al.* (*30*) compared the clinical outcomes of single and double injections in a novel targeted intracluster injection technique (TII), whereby 16 mL of lidocaine 1.5% was injected inside the main neural cluster and every single satellite (confluences of trunks and divisions of the brachial plexus). It demonstrated that the TII technique results in a shorter total anesthesia-related time due to quick onset (Table 1, online data, *https://www.ddtjournal.com/supplementaldata/150*) (*30*), but their sample size was too small to assess the safety of needle tip placement inside the neural cluster, though no neurological deficit

occurred in a month.

2.3. Complications

Since the development of the ultrasound-guided SCB technique, various approaches (*13,26,27*), including the intertruncal approach and the selective trunk block, have been introduced. The authors made many efforts to visualize accurately and inject exactly to the individual three cords (superior, middle and inferior) that were enough to produce complete sensorimotor blockage of the entire upper extremity (shoulder, arm, elbow, forearm and hand), except for the medial aspect of the upper arm (*27*). Further research is needed to confirm the application of these approaches for shoulder surgery. A trial (*20*) administered 20 mL of levobupivacaine 0.5% mixed with epinephrine and primarily examined the effect of analgesia and the incidence of HDP after arthroscopic shoulder surgery under ultrasound-guided ISB and SCB. Although the ISB resulted in a shorter onset time and a higher minimal composite score of 6 points at 30 min, it was definitely accompanied by a higher incidence of HDP than SCB (Table 2) (*20*). However, there are no intergroup differences in terms of performance time or intraoperative/postoperative opioid consumption, showing that small-volume SCB might achieve comparable anesthesia/analgesia without increasing the risk of HDP (*20*). Another trial (*21*) presented similar results that pain scores and analgesia requirements were not significantly different between SCB and ISB with 20 mL of 0.25% bupivacaine, concluding that SCB can be an alternative approach to ISB for postoperative pain management in shoulder surgery. Despite the lower incidence of HDP with the supraclavicular approach, the risk of this common adverse event should not be underestimated. The volume of local administration during SCB was determined to be essential for the occurrence of HDP following upper extremity surgery. The authors (*31*) conducted an investigation using a modified "3+3" dose escalation design for exploring the dose-response relationship and ipsilateral HDP in subjects undergoing ultrasound-guided SCB for surgeries on the right upper extremity. Dosing levels of 5, 10, 15, 20, 25, 30, 35 and 40 mL of the local anesthetic mixture (2:1 mixture of mepivacaine 1.5% and bupivacaine 0.5%) were administered in cohorts of three subjects per dose. Due to the 100% incidence of HDP at the starting dose of 35 mL, the dose of 40 mL was excluded. All subjects demonstrated HDP at 15-20 min, and even with the lowest dose of 5 mL, one of the three subjects experienced HDP at 15 min (33% incidence). It concluded that HDP occurred to some extent at all dose levels administered, suggesting that there is no clinically relevant dose at which HDP can be avoided, most likely due to the investment of the phrenic nerve and brachial plexus within the same prevertebral fascial sheath. It must be remembered that the optimal volume of local anesthetics has not yet been determined to decrease the complications without compromising the success rate of the brachial plexus block by various approaches.

3. Infraclavicular block

3.1. Clinical characteristics of different approach

Various ultrasound-guided ICB approaches have been reported. A trial (*32*) reported an approach as the lateral infraclavicular with the ultrasound transducer in the sagittal plane adducting the arm 90° inferiorly to the coracoid process. It showed excellent success without any supplemental anesthetics in 90.4% of the patients. However, all three cords are not always identifiable and close together lying deep to the pectoralis minor muscle. Another trial (*33*) compared the quality of surgical anesthesia in the lateral infraclavicular approach with the medial infraclavicular approach, which was performed at the apex of the delto-pectoral groove in the sagittal plane with the arm abducted 110°, where the cords are grouped close together, superior to the axillary artery. It demonstrated that the medial infraclavicular approach had better outcomes of onset time, ready imaging, closer to the surface and tolerance of tourniquet when compared with the lateral infraclavicular approach (Table 1, online data, *https://www.ddtjournal.com/supplementaldata/150*) (*33*). A novel approach, described by Karmakar (*16*), was named the costoclavicular approach and has been introduced. It was demonstrated that the costoclavicular space lying deep and posterior to the midpoint of the clavicle was bounded anteriorly by the subclavius and clavicular head of the pectoralis major muscle and posteriorly by the anterior chest wall, where the cords are relatively superficial, clustered together and share a consistent triangular relationship with one another laterally to the axillary artery. Their primary trial demonstrated that ultrasound-guided CCB using 20 mL local anesthetic produced a very rapid onset but decreased the risk of inadvertent vascular or pleural puncture, thereby concluding that CCB is a beneficial approach to ICB (*16*). There are significant variations in the position of the individual cords between the lateral approach and the costoclavicular approach (*34*). The former lying deep to the pectoral muscles (3-6 cm) around the second part of the axillary artery are rarely visualized in a single ultrasound window, while the latter lying between the posterior surface of the clavicle and the second rib around the first part of the axillary artery are clearly imaged laterally to the artery in a dense and consistent triangular arrangement. A study performed by Songthamwat *et al.* (*35*) demonstrated that ultrasound-guided CCB with 25 mL ropivacaine 0.5% could produce a faster overall sensory onset time, lower overall sensory score at 5 and 20 min, lower overall motor score at 10 min, complete sensory-motor blockade at 20 min, and faster ready time for surgery than the lateral approach

(Table 1, online data, *https://www.ddtjournal.com/supplementaldata/150*) (*35*). They concluded that the CCB had a promising future for upper extremity surgery with ultrasound guidance. Further research should be performed to ensure its safety, efficacy and reliability.

3.2. Clinical characteristics of different injection points

A trial (*36*) compared a single local anesthetic injection placed at the very posterior aspect of the axillary artery using 30 mL of mepivacaine 1.5% to triple injections placed at the posterior, lateral and medial sides of the artery during ultrasound-guided ICB. The rate of complete sensory block was comparable at 15 min and at each time interval up to 30 min, concluding that the success rate and the onset of complete sensory block are not enhanced by a triple injection (Table 1, online data, *https://www.ddtjournal.com/supplementaldata/150*) (*36*). Another similar trial (*19*) confirmed the effectiveness of a single injection at the optimal site posterior to the axillary versus triple injection ultrasound-guided ICB by the medial approach. Lidocaine 2% 30 mL was injected posteriorly to the artery in the single-injection group and in each brachial plexus spinal cord in the three-injection group. The single group produced a reduction in procedural time, a superior blockade at 20 min, and a higher success rate at 20 min for each individual nerve, especially for the ulna and radial nerves (Table 1, online data, *https://www.ddtjournal.com/supplementaldata/150*) (*19*). They concluded that the single injection technique demonstrated superiority and provided brachial plexus block as well as a triple injection. Tran *et al.* (*37*) also demonstrated a similar outcome: double injection provided no significant advantage compared with single injection, in which 35 mL of lidocaine 1.5% was injected at the 6-o'clock position of the axillary artery in the single group, while 15 mL and 20 mL were deposited at the 9-o'clock and 6-o'clock positions of the artery, respectively. There were no differences in imaging, needling, performance, onset and total anesthesia-related times or the rate of surgical anesthesia between the two groups (Table 1, online data, *https://www.ddtjournal.com/supplementaldata/150*) (*37*). Although the number of needle passes was also similar, the double-injection technique resulted in slightly less procedural discomfort (Table 1, online data, *https://www.ddtjournal.com/supplementaldata/150*) (*37*). However, there was a similarity among the above three trials (*19,36,37*) in that efforts were not made to identify the 3 cords of the brachial plexus around the artery. Since the costoclavicular space was discovered (*16*), CCB is thought to be a beneficial approach for ultrasound-guided ICB because all three cords of the brachial plexus are clustered together lateral to the axillary artery and are visualized clearly. A study (*38*) compared ultrasound-guided costoclavicular with lateral sagittal infraclavicular brachial plexus blocks and showed that sensorimotor onset was faster in the CC group, but there was no difference in the block performance times (Table 1, online data, *https://www.ddtjournal.com/supplementaldata/150*). Another trial (*39*) compared single and double injections using 35 mL of lidocaine 1%-bupivacaine 0.25% with epinephrine 5 µg/mL for ultrasound-guided CCB, by which the total volume of local anesthetic was injected between three cords of the brachial plexus in the single-injection group, while the first half of the volume was injected in this location, and the second half was deposited at the medial cord and the axillary artery in the double-injection group. It was proven that double injection provided a faster onset time and total anesthesia-related time but a similar success rate compared with single injection (Table 1, online data, *https://www.ddtjournal.com/supplementaldata/150*) (*39*). Luo *et al*. (*15*) confirmed that CCB and SCB resulted in similar block dynamics when the procedures were guided by ultrasound and verified by a nerve stimulator with 23 mL of local anesthetic. They proposed that the single-injection technique used commonly for the costoclavicular approach, with or without a peripheral nerve stimulator, has a high success rate (97%), which might be partially explained by the large LA volume used for the procedure (up to 35 mL). Studies on ultrasound guidance, whether in SCB or CCB, suggest that a single local anesthetic injection at the "corner pocket" or at the costoclavicular space as described above can provide sufficient and effective brachial plexus blockade and can become an alternative option.

3.3. Complications

A trial (*40*) aimed to compare the incidence of HDP between CCB and SCB using 20 mL of an equal mixture of bupivacaine 0.5% and lidocaine 2% with 5 µg/mL epinephrine. The authors found that the rate of HDP was 5% in the CCB group and 45% in the SCB group. When CCB is applied postoperatively for shoulder surgery compared with ISB with 20 mL of levobupivacaine 0.5% and epinephrine 5 µg/mL, it demonstrated that CCB could provide comparable analgesia effects at 0.5, 1, 2, 3, 6, 12, and 24 h, as well as avoiding the risk of HDP and a shorter onset time (Table 2) (*22*). There were no intergroup differences in the minimal composite scores of 6 points at 30 min, intraoperative/postoperative opioid consumption, side effects, or patient satisfaction at 24 h. The above trials seem to prove that CCB is a better choice for surgical anesthesia and analgesia with a reduction in the occurrence of HDP.

4. Cadaver evidence

Although the intracluster injection technique with ultrasound-guided SCB has been introduced for the advantage of faster onset time, one patient experienced numbness during the procedure and after surgery. It

spontaneously resolved in the follow-up 1 month; thus, the significance and safety of needle tip placement inside the neural clusters deserves special mention (*30*). One study performed by Susanne Retter (*41*) assessed the rate of subperineural needle placement with a single intracluster on ultrasound-guided SCB among 21 human cadavers using 0.2 mL black India ink. It demonstrated that Ink was extra-epineural in 13/41 (32%), sub-epineural but outside perineurium in 18/41 (44%), and sub-perineural in 10/41 sections (24%), which presented a high rate of sub-perineural injection with a single intracluster injection. Although an injection deep to the epineurium generally leads to reversible anesthesia, subperineural injections are associated with long-term nerve injury. An editorial (*42*) concerning the targeted intracluster for ultrasound guided SCB, which is too close for comfort. It mentioned that it is prudent to place the needle in the same interfascial plane toward the nerves, although it seems not to actually touch nerves with the widespread use of ultrasound guidance. Meanwhile, the occurrence of paraesthesias due to needle-nerve contact is accompanied by an increased risk for neurologic complications. The imaging of the compact region with the individual nerves under ultrasound revealed no advantages under this condition because there were no differences in the nerve elements, and it was difficult to identify separation among the epineurium when local anesthetic was injected into the intra- or intercluster. They concluded that it may not prevent injury even if each nerve fascicle is reliably identified. It aroused an awareness that is it worthy to achieve latency advantage but bring axonal disruption. Therefore, great efforts should be made to avoid subperineural placement of the needle and injection of local anesthetic.

5. Conclusion

During ultrasound-guided SCB, multiple injection techniques can achieve a faster onset time than single injection, but not the success rate. We might attribute this improvement to the discovery of the optimal injection site "corner pocket" with the large volume of local anesthetic. Compared with ISB, SCB could achieve equivalent surgical anesthesia and postoperative analgesia for shoulder surgery, but the rate of HDP should not be ignored or overestimated. Further study should focus on the optimal selection between various techniques with decreasing the volume of solution and the relative complication. Since the costoclavicular space has been discovered, in which the 3 cords tightly bundle together in a superficial location around the axillary artery and can be seen clearly, ultrasound-guided CCB would provide a better success rate even in a single injection. Compared with SCB and ISB, CCB seems to have great potential advantages in proving a better dynamic block effect, reducing relative complications, and performing more flexibility. However, there is no exact trial to prove that CCB alone is appropriate for shoulder surgery, despite better postoperative analgesia. Ultrasound-guided brachial plexus block at the level of the clavicle has recently been advocated for proximal extremity surgery, and SCB and CCB definitely demonstrate greater beneficial effects than ISB and axillary block. Although the incidence of postoperative nerve deficit is very low and major neurological complications are rare, continual caution should be made regarding the issue of intra-epineurial injection. Since the novel technique, selective trunk block, was introduced, many researchers have highly praised that this hybrid approach has great potential to meet upper extremity surgery. Numerous trials are needed to identify the safety and efficacy. Hence, all the approaches mentioned above could be an alternative for the clinical setting, but recent evidence did not determine which was the best or one-size-fits-all approach, and further research is required.

Funding: This project was supported by a grant from National Key R&D Program of China (2018YFC2001805).

Conflict of Interest: The authors have no conflicts of interest to disclose.

References

1. Soares LG, Brull R, Lai J, Chan VW. Eight ball, corner pocket: The optimal needle position for ultrasound-guided supraclavicular block. Reg Anesth Pain Med. 2007; 32:94-95.
2. Choi JJ, Kwak HJ, Jung WS, Chung SH, Lee MG. Sonographic guidance for supraclavicular brachial plexus blocks: Single *vs.* double injection cluster approach. Pain Physician. 2017; 20:529-535.
3. Williams LM, Singh K, Dua A, Singh A, Cummings A. Infraclavicular Nerve Block. In: StatPearls (StatPearls Publishing, Treasure Island (FL), 2023.
4. D'Souza RS, Johnson RL. Supraclavicular Block. In: StatPearls (StatPearls Publishing, Treasure Island (FL), 2023.
5. Lopez-Morales S, Moreno-Martin A, Leal del Ojo JD, Rodriguez-Huertas F. Ultrasound-guided axillary block versus ultrasound-guided infraclavicular block for upper extremity surgery. Rev Esp Anestesiol Reanim. 2013; 60:313-319.
6. Arab SA, Alharbi MK, Nada EM, Alrefai DA, Mowafi HA. Ultrasound-guided supraclavicular brachial plexus block: single versus triple injection technique for upper limb arteriovenous access surgery. Anesth Analg. 2014; 118:1120-1125.
7. Leurcharusmee P, Elgueta MF, Tiyaprasertkul W, Sotthisopha T, Samerchua A, Gordon A, Aliste J, Finlayson RJ, Tran DQH. A randomized comparison between costoclavicular and paracoracoid ultrasound-guided infraclavicular block for upper limb surgery. Can J Anaesth. 2017; 64:617-625.
8. Karmakar MK, Areeruk P, Mok LYH, Sivakumar RK. Ultrasound-guided selective trunk block to produce surgical anesthesia of the whole upper extremity: A case

report. A A Pract. 2020; 14:e01274.
9. Bharti N, Bhardawaj N, Wig J. Comparison of ultrasound-guided supraclavicular, infraclavicular and below-C6 interscalene brachial plexus block for upper limb surgery: A randomised, observer-blinded study. Anaesth Intensive Care. 2015; 43:468-472.
10. Stav A, Reytman L, Stav MY, Portnoy I, Kantarovsky A, Galili O, Luboshitz S, Sevi R, Sternberg A. Comparison of the supraclavicular, infraclavicular and axillary approaches for ultrasound-guided brachial plexus block for surgical anesthesia. Rambam Maimonides Med J. 2016; 7.
11. Koscielniak-Nielsen ZJ, Frederiksen BS, Rasmussen H, Hesselbjerg L. A comparison of ultrasound-guided supraclavicular and infraclavicular blocks for upper extremity surgery. Acta Anaesthesiol Scand. 2009; 53:620-626.
12. Gurkan Y, Hosten T, Tekin M, Acar S, Solak M, Toker K. Comparison of ultrasound-guided supraclavicular and infraclavicular approaches for brachial plexus blockade. Agri. 2012; 24:159-164.
13. Abhinaya RJ, Venkatraman R, Matheswaran P, Sivarajan G. A randomised comparative evaluation of supraclavicular and infraclavicular approaches to brachial plexus block for upper limb surgeries using both ultrasound and nerve stimulator. Indian J Anaesth. 2017; 61:581-586.
14. Dhir S, Brown B, Mack P, Bureau Y, Yu J, Ross D. Infraclavicular and supraclavicular approaches to brachial plexus for ambulatory elbow surgery: A randomized controlled observer-blinded trial. J Clin Anesth. 2018; 48:67-72.
15. Luo Q, Yao W, Chai Y, Chang L, Yao H, Liang J, Hao N, Guo S, Shu H. Comparison of ultrasound-guided supraclavicular and costoclavicular brachial plexus block using a modified double-injection technique: A randomized non-inferiority trial. Biosci Rep. 2020; 40:BSR20200084.
16. Karmakar MK, Sala-Blanch X, Songthamwat B, Tsui BCH. Benefits of the costoclavicular space for ultrasound-guided infraclavicular brachial plexus block: Description of a costoclavicular approach. Reg Anesth Pain Med. 2015; 40:287-288.
17. Park SK, Lee SY, Kim WH, Park HS, Lim YJ, Bahk JH. Comparison of supraclavicular and infraclavicular brachial plexus block: A systemic review of randomized controlled trials. Anesth Analg. 2017; 124:636-644.
18. Choudhary N, Kumar A, Kohli A, Wadhawan S, Siddiqui TH, Bhadoria P, Kamat H. Single-point versus double-point injection technique of ultrasound-guided supraclavicular block: A randomized controlled study. J Anaesthesiol Clin Pharmacol. 2019; 35:373-378.
19. Fredrickson MJ, Wolstencroft P, Kejriwal R, Yoon A, Boland MR, Chinchanwala S. Single versus triple injection ultrasound-guided infraclavicular block: confirmation of the effectiveness of the single injection technique. Anesth Analg. 2010; 111:1325-1327.
20. Aliste J, Bravo D, Fernandez D, Layera S, Finlayson RJ, Tran DQ. A randomized comparison between interscalene and small-volume supraclavicular blocks for arthroscopic shoulder surgery. Reg Anesth Pain Med. 2018; 43:590-595.
21. Karaman T, Karaman S, Asci M, Tapar H, Sahin A, Dogru S, Suren M. Comparison of ultrasound-guided supraclavicular and interscalene brachial plexus blocks in postoperative pain management after arthroscopic shoulder surgery. Pain Pract. 2019; 19:196-203.
22. Aliste J, Bravo D, Layera S, Fernandez D, Jara A, Maccioni C, Infante C, Finlayson RJ, Tran DQ. Randomized comparison between interscalene and costoclavicular blocks for arthroscopic shoulder surgery. Reg Anesth Pain Med. 2019.
23. Pester JM, Hendrix JM, Varacallo M. Brachial Plexus Block Techniques. In: StatPearls (StatPearls Publishing, Treasure Island (FL), 2023.
24. Kapral S, Krafft P, Eibenberger K, Fitzgerald R, Gosch M, Weinstabl C. Ultrasound-guided supraclavicular approach for regional anesthesia of the brachial plexus. Anesth Analg. 1994; 78:507-513.
25. Chan VWS, Perlas A, Rawson R, Odukoya O. Ultrasound-guided supraclavicular brachial plexus block. Anesth Analg. 2003; 97:1514-1517.
26. Siddiqui U, Perlas A, Chin K, Reina MA, Sala-Blanch X, Niazi A, Chan V. Intertruncal approach to the supraclavicular brachial plexus, current controversies and technical update: a daring discourse. Reg Anesth Pain Med. 2020; 45:377-380.
27. Sivakumar RK, Areeruk P, Karmakar MK. Selective trunk block (SeTB): A simple alternative to hybrid brachial plexus block techniques for proximal humeral fracture surgery during the COVID-19 pandemic. Reg Anesth Pain Med. 2021; 46:376-378.
28. Tran DQ, Munoz L, Zaouter C, Russo G, Finlayson RJ. A prospective, randomized comparison between single- and double-injection, ultrasound-guided supraclavicular brachial plexus block. Reg Anesth Pain Med. 2009; 34:420-424.
29. Roy M, Nadeau MJ, Cote D, Levesque S, Dion N, Nicole PC, Turgeon AF. Comparison of a single- or double-injection technique for ultrasound-guided supraclavicular block: a prospective, randomized, blinded controlled study. Reg Anesth Pain Med. 2012; 37:55-59.
30. Techasuk W, Gonzalez AP, Bernucci F, Cupido T, Finlayson RJ, Tran DQ. A randomized comparison between double-injection and targeted intracluster-injection ultrasound-guided supraclavicular brachial plexus block. Anesth Analg. 2014; 118:1363-1369.
31. Tedore TR, Lin HX, Pryor KO, Tangel VE, Pak DJ, Akerman M, Wellman DS, Oden-Brunson H. Dose-response relationship between local anesthetic volume and hemidiaphragmatic paresis following ultrasound-guided supraclavicular brachial plexus blockade. Reg Anesth Pain Med. 2020; 45:979-984.
32. Sandhu NS, Capan LM. Ultrasound-guided infraclavicular brachial plexus block. Br J Anaesth. 2002; 89:254-259.
33. Bigeleisen P, Wilson M. A comparison of two techniques for ultrasound guided infraclavicular block. Br J Anaesth. 2006; 96:502-507.
34. Li JW, Songthamwat B, Samy W, Sala-Blanch X, Karmakar MK. Ultrasound-guided costoclavicular brachial plexus block: Sonoanatomy, technique, and block dynamics. Reg Anesth Pain Med. 2017; 42:233-240.
35. Songthamwat B, Karmakar MK, Li JW, Samy W, Mok LYH. Ultrasound-guided infraclavicular brachial plexus block: Prospective randomized comparison of the lateral sagittal and costoclavicular approach. Reg Anesth Pain Med. 2018; 43:825-831.
36. Desgagnes MC, Levesque S, Dion N, Nadeau MJ, Cote D, Brassard J, Nicole PC, Turgeon AF. A comparison of a single or triple injection technique for ultrasound-

guided infraclavicular block: a prospective randomized controlled study. Anesth Analg. 2009; 109:668-672.
37. Tran DQ, Bertini P, Zaouter C, Munoz L, Finlayson RJ. A prospective, randomized comparison between single- and double-injection ultrasound-guided infraclavicular brachial plexus block. Reg Anesth Pain Med. 2010; 35:16-21.
38. Cesur S, Yayik AM, Das AN, Ahiskalioglu A. A randomized comparison between ultrasound-guided costoclavicular and infraclavicular block for upper extremity surgery. Turk J Med Sci. 2021; 51:1883-1888.
39. Layera S, Aliste J, Bravo D, Fernandez D, Garcia A, Finlayson RJ, Tran DQ. Single- versus double-injection costoclavicular block: a randomized comparison. Reg Anesth Pain Med. 2020; 45:209-213.
40. Sivashanmugam T, Maurya I, Kumar N, Karmakar MK. Ipsilateral hemidiaphragmatic paresis after a supraclavicular and costoclavicular brachial plexus block: A randomised observer blinded study. Eur J Anaesthesiol. 2019; 36:787-795.
41. Retter S, Szerb J, Kwofie K, Colp P, Sandeski R, Uppal V. Incidence of sub-perineural injection using a targeted intracluster supraclavicular ultrasound-guided approach in cadavers. Br J Anaesth. 2019; 122:776-781.
42. Gadsden J, Orebaugh S. Targeted intracluster supraclavicular brachial plexus block: Too close for comfort. Br J Anaesth. 2019; 122:713-715.

Received January 29, 2023; Revised May 3, 2023; Accepted August 8, 2023.

Address correspondence to:
Haihua Shu, Department of Anesthesiology, Guangdong Provincial People's Hospital, Guangdong Academy of Medical Sciences, 106 Zhongshan Second Road, Yuexiu District, Guangzhou, Guangdong 510080, P.R. China.
E-mail: shuhaihua@hotmail.com

Released online in J-STAGE as advance publication August 17, 2023.

Original Article

DOI: 10.5582/ddt.2023.01032

Biosynthesis of copper oxide nanoparticles using *Caesalpinia sappan* extract: *In vitro* evaluation of antifungal and antibiofilm activities against *Candida albicans*

Mathurada Sasarom[1], Phenphichar Wanachantararak[2], Pisaisit Chaijareenont[2,3], Siriporn Okonogi[1,3,*]

[1] Faculty of Pharmacy, Chiang Mai University, Chiang Mai, Thailand;
[2] Faculty of Dentistry, Chiang Mai University, Chiang Mai, Thailand;
[3] Center of Excellent inPharmaceutical Nanotechnology, Chiang Mai University, Chiang Mai, Thailand.

SUMMARY Synthesis of nanoparticles using natural organic substances has attracted more attention due to avoiding inorganic toxicity. This work aimed to synthesize copper oxide nanoparticles (CuONPs) using *Caesalpinia sappan* heartwood extract as a reducing agent. The effects of pH of synthesis reaction were investigated. The obtained CuONPs were characterized using UV-visible spectroscopy, Fourier transform infrared spectroscopy, scanning electron microscopy, and energy dispersive X-ray spectroscopy. Their particle size, size distribution, and zeta potential were determined using photon correlation spectrophotometry. *Candida albicans* is a major cause of chronic fungal infections due to its biofilms leading to severe drug resistance problems. In this study, *in vitro* antifungal and antibiofilm activities as well as killing kinetics of the synthesized CuONPs against *C. albicans* were investigated. Additionally, fungal biofilm was observed by using confocal laser scanning microscopy. The results showed that the pH of the synthesis reaction played an important role in the physicochemical properties and antifungal activities of the obtained CuONPs. CuONPs synthesized at pH 10 and 12 showed the relatively small and narrow size distribution with high negative zeta potential and time-dependent killing kinetics. Confocal laser scanning microscopy confirms obvious fungal biofilm reduction and increased fungal cell death after exposure to CuONPs. These findings suggest the optimal pH of CuONPs synthesis using *C. sappan* extract as a reducing agent. The results on antifungal and antibiofilm activities indicate that the obtained CuONPs can be a promising agent for treating fungal infection.

Keywords *Caesalpinia sappan*, green synthesis, copper oxide nanoparticles, antifungal activity, antibiofilm activity

1. Introduction

Candida albicans is a normal flora microorganism in humans. However, certain factors, *e.g.*, diet, medications, pH, and the human immune system, can modulate favorable conditions for its overgrowth and turn *C. albicans* into an insidious species and being the main cause of many fungal infections in humans and animals (*1*). Moreover, *C. albicans* can form biofilms that protect them from harmful substances and thus survive in various conditions and become resistant to antifungal drugs. Biofilm formation of *C. albicans* begins with the adherence of cells to a solid surface. The biofilms then develop from cell proliferation and early-stage filamentation of the adhered cells, resulting in a complex network of many layers. The developed biofilms consist of several types of cells encased in an extracellular matrix (*2*). Finally, the biofilms appear thick appearance to protect the microorganisms inside and make the treatment of these infections difficult (*3*). In the oral cavity, *C. albicans* biofilms formed on implanted medical devices can act as a reservoir for pathogenic cells (*4*). In denture-wearing patients, *C. albicans* is associated with denture acrylic surfaces to form biofilms (*5*). These biofilms can cause antimicrobial resistance and bloodstream infection leading to invasive systemic infections (candidemia). These infections have increased in modern clinical practice, especially in immunocompromised patients such as human immunodeficiency virus-infected patients and cancer patients who receive chemotherapy (*6*).

For this reason, the biofilm formation of *C. albicans* is a serious clinical effect as they can cause significant resistance to antifungal therapy by limiting the penetration of antibiotics and host immune response (*7*).

Nanotechnology is an important field of modern scientific research due to its wide range of applications. In the medical field, nanotechnology has been applied to the production and application of nanosized particles (nanoparticles) for diagnosis and therapeutics. Novel techniques and methods are continuously studied to produce different types of nanoparticles. Metal nanoparticles are one of those nanoparticles that are increasingly used in the biomedical field. (*8*). Among metal nanoparticles, copper oxide nanoparticles (CuONPs) have received great interest for many applications, including in the medical field due to their cost-effectiveness, economical attractiveness, promising nontoxicity, and easy preparation. They are used to manufacture electrical and electronic devices, catalysts in various chemical processes, cancer cell treatment applications and antimicrobial formulations (*9–12*). Furthermore, they show antimicrobial activity against various fungi, which are pathogenic for both agriculture and humans. Colonization of *Candida* spp. has been reported in many studies and some of them are resistant to antifungal agents (*13*). Interestingly, CuONPs have been reported to have a high potential to inhibit several strains of oral bacteria and fungi, especially *C. albicans* (*14*). Therefore, CuONPs can be a good candidate in various applications for health and safety issues.

The significant properties required for nanoparticles to be used in biological applications are high biocompatibility, bioactivity, bioavailability, and less toxicity as well as cost-effectiveness (*15*). However, these properties are rare in metal nanoparticles prepared from inorganic chemical-mediated synthesis. Therefore, there is a need for an environmentally and economically feasible way to synthesize these metal nanoparticles. Biosynthesis with the help of plant extracts, microorganisms, and algae, has attracted much attention (*16–18*). Among them, plant extracts have gained more selection than others for the biosynthesis of metal nanoparticles due to biocompatibility with biomedical applications, easy handling, accessibility, simplicity, environmentally friendly and nontoxic (*19,20*). In addition, phytochemical assisted synthesis of metal nanoparticles is an inexpensive and cost-effective approach (*21*). Different plant extracts have been used to prepare CuONPs (*22,23*). However, biosynthesis of CuONPs using *C. Sappan* extract has not been reported elsewhere.

C. Sappan is a plant of the Leguminosae family and distributed in Southeast Asia. The heartwood of *C. Sappan* is used as a coloring agent in food, beverages, cosmetics, and curative agents for treating arthritis, antidiabetic and skin infections (*24*). In many studies, the extract of *C. sappan* showed important biological activities such as antimicrobial (*25*), anti-inflammatory (*26*) and antioxidant activities (*27*). The heartwood of *C. sappan* consists of several phenolic components, including xanthone, coumarin, flavones, homoisoflavonoids, and brazilin (*28*). It has been reported that different phytochemicals in plant extracts play a significant role in the reduction process and capping of the synthesized metal nanoparticles (*29*). Since different plant extract consists of different phytochemicals, thus the physicochemical properties and activities of CuONPs obtained from different plant extract are different. In addition, synthesis-related factors such as pH and temperature also play an important role in controlling the quality and quantity of the nanoparticles (*18,30*). Therefore, it is challenging to investigate the physicochemical properties and antifungal activities against *C. albicans* of CuONPs synthesized using *C. sappan* extract as a reducing agent in various pH media.

2. Materials and Methods

2.1. Materials

C. albicans DMST 5815 was purchased from the National Institute of Health, Department of Medical Sciences, Ministry of Public Health, Thailand. Copper (II) sulfate pentahydrate salt ($CuSO_4 \cdot 5H_2O$) was purchased from Merck (Darmstadt, Germany). Sodium hydroxide (NaOH) and hydrochloric acid (HCl) were from RCI Labscan (Bangkok, Thailand). Sabouraud dextrose broth (SDB) and sabouraud dextrose agar (SDA) were purchased from Hime-dialabs (Mumbai, India). Tystatin (Nystatin) was from T.O. Pharma Co., LTD (Bangkok, Thailand). Other chemicals and solvents are of analytical grade.

2.2. Preparation of the extract

C. sappan was collected from the northern area of Thailand in January 2021. It was identified by a botanist in the botanical herbarium of the Faculty of Pharmacy, Chiang Mai University to obtain the reference voucher specimen (No. 002276). The heartwood of *C. sappan* was dried in an oven and ground to become a fine powder. To prepare a *C. sappan* aqueous extract, 5 g of the heartwood powder was mixed with 50 mL of water. Subsequently, the mixture was stirred at 500 rpm overnight. The extract was then filtered through Whatman's No.1 filter paper. The filtrate was centrifuged at 3000× *g* for 10 min to eliminate precipitations.

2.3. CuONPs synthesis

CuONPs were synthesized at 70°C using 1 mL aqueous extract of *C. sappan* and 19 mL of 10 mM $CuSO_4 \cdot 5H_2O$ solution under constant stirring at 500 rpm. To obtain suitable nanoparticles, an aqueous extract of *C. sappan* was added dropwise to the $CuSO_4 \cdot 5H_2O$ solution. After

30 min, the mixture was adjusted with 1 M NaOH or HCl to obtain pH 3, 6, 8, 10 and 12. Subsequently, the mixture was continuously reacted at 70°C for 2 h. The mixture was washed with Milli-Q water and any residual biological extract was removed by centrifugation at 8000× *g* for 30 min (three times). The obtained precipitate was dispersed in 10 mL of absolute ethanol and dried at 60°C for 8 h.

2.4. Characterizations of CuONPs

2.4.1. UV-visible spectroscopy

The dried powder of CuONPs was dispersed in Milli-Q water to obtain the concentration of 10 mg/mL. Then, 400 µL of this dispersion was diluted by adding 4 mL of Milli-Q water. The absorbance of this dilution was recorded from 200 to 800 nm using a UV-visible spectrophotometer (UV-2450 Shimadzu, Kyoto, Japan) to confirm the metal nanoparticles. Milli-Q water was used as a blank.

2.4.2. Fourier transform infrared (FTIR) spectroscopy

To explore the FTIR spectra of CuONPs, the dried powder of CuONPs was palletized with KBr. The obtained mixture was subjected to an FT-IR spectrometer (Thermo Nicolet/470FT-IR spectrometer, Nicolet Nexus, Madison, USA) in the range from 4000 to 500 cm^{-1} at a resolution of 16 cm^{-1}.

2.4.3. Particle size and zeta potential analysis

The particle size, size distribution and the zeta potential of the synthesized CuONPs were measured *via* photon correlation spectroscopy (PCS) analysis using a Zetasizer Nano ZS (Malvern Instruments Company, Worcestershire, UK). The dispersion of CuONPs in Milli-Q water was prepared to a concentration of 1 mg/mL. The dispersion was diluted up to 10 times with Milli-Q water and subjected to sonication for 30 min before measurement. The hydrodynamic size and size distribution of the synthesized CuONPs were measured at a fixed angle of 173. The particle size was expressed as the average diameter in nm, whereas the particle size distribution was expressed as the polydispersity index (PdI). The zeta potential of the synthesized CuONPs was analyzed and automatically calculated based on the Smoluchowski equation (*31*) using the Zetasizer (Malvern Instruments Company) software version 7.1. All experiments were performed in triplicate.

2.4.4. Morphology and element composition

The morphology of CuONPs was investigated using a field emission scanning electron microscope (FE-SEM) (JSM 6335 F, JEOL Ltd, Tokyo, Japan). The dried powder of CuONPs was mounted on a copper stub covered with carbon tape and sputter-coated with gold. The magnification was set at 30,000×. The shape and surface morphology of the particles were analyzed by secondary electron mode with an accelerating voltage of 0.3-30 kV. An energy-dispersive X-ray spectrophotometer (EDX) connected to the FE-SEM operated with a Si(Li) detector was used to analyze the CuONP composition and confirm the presence of copper.

2.5. Pathogenic strains and growth condition

In this study, *C. albicans* DMST 5815 was used as a pathogenic fungal strain. The strain was cultured in SDB at 37°C for 24-48 h. Fungal suspensions were prepared, and the cell concentration was adjusted to a turbidity of 0.5 McFarland standard using a McFarland densitometer (DEN-1 Biosan, Riga, Latvia).

2.6. Antifungal activity

The investigation of the antifungal activity of the synthesized CuONPs was performed by determining the minimum inhibitory concentration (MIC) and minimum fungicidal concentration (MFC) of the samples as follows. Stock dispersion of the synthesized CuONPs was prepared by dispersing dried powder of CuONPs in Milli-Q water to have a concentration of 12 mg/mL. Two-fold serial dilutions were prepared from the stock dispersion and 100 µL of each dilution was added to a 96-well microplate. Then, each well was added with 100 µL of *C. albicans* suspension in SDB at a concentration of 1×10^5 CFU/mL. Therefore, each well contained *C. albicans* at 0.5×10^5 CFU/mL and CuONPs at 6, 3, 1.5, 0.75, 0.375 and 0.187 mg/mL as final concentrations. The plate was incubated at 37°C for 24 h. The MIC is defined as the lowest concentration of CuONPs at which the microorganisms do not demonstrate visible growth. The turbidity in the well indicated the presence of microorganism growth. To determine MFC, the mixture in each well was streaked on each entire surface of SDA. Then, the agar plates were incubated in the same conditions as in the determination of MIC. After incubation, the lowest concentration of samples showing complete inhibition of *C. albicans* was recorded as MFC. All experiments were performed in triplicate. Nystatin solutions at concentrations of 0.012×10^{-4} - 2.5×10^{-3} mg/mL were used as positive controls.

2.7. Killing kinetics study

The study of killing kinetics of the synthesized CuONPs against *C. albicans* was conducted by adding 100 µL of CuONPs to a 96-well plate, followed by 100 µL of *C. albicans* suspension to obtain a final concentration of CuONPs at the lowest MFC and that of *C. albicans* concentration of 0.5×10^5 CFU/mL. The plates were

incubated at 37°C for 8 h. At time intervals of 0, 30 min, 1, 2, 4, and 8 h, the mixtures were withdrawn, and viable cell counts were determined by plating 20 µL of known dilutions of the culture samples on the entire surface of SDA. The cell count plates were subsequently incubated at 37°C for 24 h. The plates with 30 to 300 colonies were used for CFU counts. Log CFU/mL was plotted against time for constructing the killing kinetics curves. Nystatin at MFC concentration was used as a positive control. All assays were analyzed in triplicate.

2.8. Antibiofilm assay

2.8.1. Biofilm formation inhibition

The effect of CuONPs on the biofilm formation of *C. albicans* was investigated as follows. CuONPs dispersions in Milli-Q water were prepared for various concentrations of CuONPs. Aliquots of 100 µL of these dispersions were added into 96-well plates, followed by adding 100 µL of the culture suspension to obtain the final CuONPs concentrations of 1/4 MFC, 1/2 MFC, and MFC and that of *C. albicans* of 0.5×10^6 CFU/mL. Nystatin solution in Milli-Q water at a final concentration of 1/4 MFC, 1/2 MFC, and MFC was used as a positive control, whereas the well without a sample was a negative control. After incubation at 37°C for 24 h, the supernatants were discarded and washed three times with phosphate buffer solution pH 7.4 (PBS) to remove non-adherent planktonic cells. The formed biofilm was stained with 200 µL of 0.1% (w/v) crystal violet in a plate at room temperature for 30 min. Then, the plate was washed three times with PBS in each well. Then the plate was added with 100 µL of 30% (v/v) acetic acid to dissolve the dye and further incubated for 15 min at room temperature. The adherence biofilm was quantified by measuring the OD at 595 nm using a microplate reader (Model 680, Bio-Rad, Hercules, California, USA). All experiments were done in triplicate. The percentage of biofilm inhibition of CuONPs was calculated by the following equation. Inhibition of biofilm formation (%) = $1 - (OD_{sample}/OD_{control}) \times 100$.

2.8.2. Eradication effect

The eradication effect of CuONPs on the formed biofilm was examined as follows. Suspension of *C. albicans* was prepared, and 100 µL of the culture suspension was added to a 96-well plate, followed by 100 µL of SDB to obtain the final culture concentration of 0.5×10^6 CFU/mL. After incubation for 24 h, the medium in each well was discarded. Then, 100 µL of SDB and 100 µL of CuONPs dispersion in Milli-Q water were added to obtain the final CuONPs concentration of MFC, 2 MFC and 4 MFC mg/mL. Nystatin in Milli-Q water at the same concentrations was used as a positive control, whereas the well without sample solution was a negative control. The plates were further incubated at 37°C for 24 h. After incubation, the adherent candida cells were washed three times with PBS. The formed biofilm was stained with 200 µL of 0.1% (w/v) crystal violet for 30 min at room temperature. The plate was washed three times with PBS in each well. Then the plates were added 100 µL of 30% (v/v) acetic acid to dissolve the dye and incubated for 15 min at room temperature. The adherence biofilm was measured at 595 nm using a microplate reader (Model 680, Bio-Rad). The percentage of biofilm eradication was calculated by the following equation. Biofilm eradication (%) = $1 - (OD_{sample}/OD_{control}) \times 100$.

2.9. Confocal laser scanning microscopy (CLSM) analysis

The viable and dead cells in the biofilms were confirmed by CLSM (TCS SP8, Leica, Berlin, Germany). The suspension was prepared by mixing 1 mL of culture suspensions (1×10^6 CFU/mL) and 1 mL of SDB. The mixtures were added to six-well plates containing coverslips. The plates were incubated at 37°C for 48 h to allow the cells to form biofilms on the coverslips. After biofilm formation, the wells were rinsed with PBS. Then, 1 mL of SDB and 1 mL of CuONPs dispersion at the MFC concentration were added and the plates were further incubated at 37°C for 24 h. Nystatin in Milli-Q water at the MFC concentration was used as a positive control, whereas the well without sample was used as a negative control. After incubation, each well was washed 3 times with PBS to remove non-adherent *C. albicans*. Biofilm cell viability on the coverslips of each well was examined by a combination of fluorescent dyes mixed in a 1:1 volume ratio of 1.5 µM SYTO 9 for viable cells and 10 µM propidium iodide (PI) for dead cells. After incubation with the dye for 1 h, the coverslip was rinsed with PBS. The stained cell samples were examined with CLSM using λ ex/em = 488/543 nm for SYTO 9 and λ ex/em = 522/590 nm for PI.

2.10. Statistical analysis

Results were expressed as mean ± SDs. Data from the biofilm assay were statistically analyzed using ANOVA followed by Ducan's post hoc test. A p-value < 0.05 was considered statistically significant.

3. Results

3.1. Synthesis of CuONPs

To study the effects of pH on CuONPs synthesis, the proportion of the aqueous extract of *C. sappan* and copper sulfate solution was fixed at 1:19 (v/v). The reaction temperature and duration were fixed at 70°C and 2.5 h, respectively. The reaction pHs of 3, 6, 8, 10 and 12 were studied. It was noted that the color of the aqueous

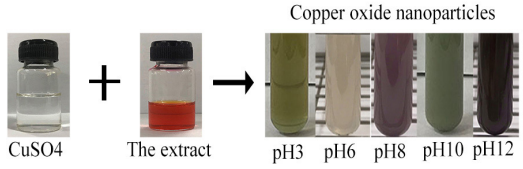

Figure 1. Photographs of CuONPs synthesized using *C. sappan* extract at different pH.

extract of *C. sappan* was orange, whereas that of copper sulfate solution was colorless. After adding the extract to the copper sulfate solution, the color of mixtures changed to gray. However, after adjusting the pH to 6, 8, 10, and 12, the mixtures changed to light purple, purple, light blue-green, and brownish black, respectively, as shown in Figure 1.

3.2. UV absorption and FTIR analysis

In the UV-visible spectroscopy analysis, the CuONPs synthesized at pH 6, 8, 10 and 12 exhibited a maximum absorbance peak of about 255 nm, as shown in Figure 2. It was found that the peak intensity increased while the pH increased. The CuONPs synthesized at pH 3 showed the small absorbance band at 224 nm. The FTIR spectra of the aqueous extract of *C. sappan* and the synthesized CuONPs are illustrated in Figure 3. The extract showed a broad peak at wave number region 3,500-3,300 cm^{-1}, which can be considered as OH stretching. Moreover, it showed the band in the region of 1,600-1,400 cm^{-1} which corresponds to C=O stretching of the carboxylic groups and the peak at 1,317 cm^{-1} which is due to C-O stretching. The FTIR spectra of the CuONPs synthesized at different pH showed different peak positions but in similar areas. The peaks at 3,479-3,387 cm^{-1} are considered for O-H stretching, the vibrations around 1,622-1,570 cm^{-1} are considered for C=O stretching, and around 1,131-1,121 cm^{-1} are for C-O vibration. In addition, the peaks at approximately 880-867 cm^{-1} are observed in the spectra of the CuONPs synthesized at pH 8, 10, and 12. These peaks are considered for aromatic Cu-O-H bonds. The peaks in the range of 520-623 cm^{-1} are considered for the expected cupric oxide and cuprous oxide vibrations.

3.3. Particle size and zeta potential analysis

The particle size of CuONPs synthesized at pH 6, 8, 10, and 12 was found in the range from approximately 255 to 458 nm with PdI range from 0.3 to 0.4, except for those synthesized at pH 3 that the obtained particles showed extremely large size and wide size distribution as shown in Table 1. The zeta potential of the synthesized particles at all pH values ranged from -13.93 to -25.0 mV, with pH 3 being the lowest and pH 10 and 12 being the highest values. It was noticed that the particle size and size distribution of CuONPs synthesized at pH 10 and 12 were significantly smaller and narrower than others.

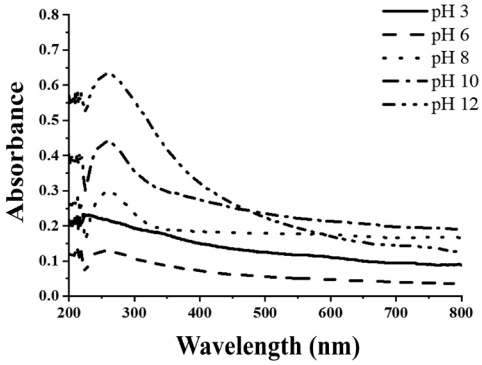

Figure 2. UV-visible spectra of CuONPs synthesized using *C. sappan* extract at different pH.

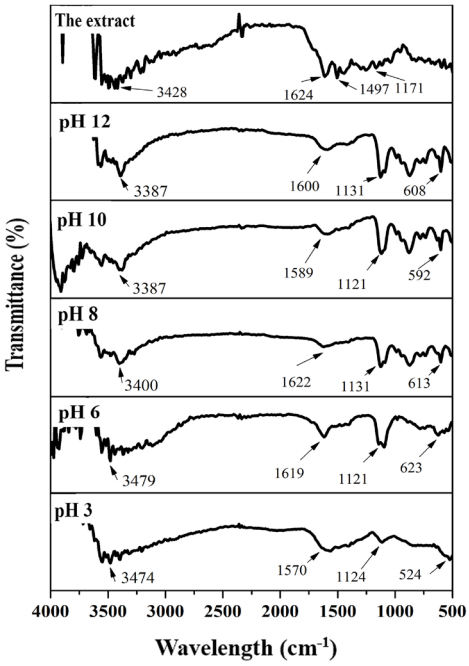

Figure 3. FTIR spectra of *C. sappan* extract and CuONPs synthesized using *C. sappan* extract at different pH.

Table 1. Particle size, size distribution, and zeta potential of the CuONPs synthesized at different pH of synthesis reaction

pH of synthesis reaction	Particle size (nm)	PdI	Zeta potential (mV)
pH 3	1322.3 ± 94.2^{d}	0.65 ± 0.11^{b}	-13.9 ± 0.2^{c}
pH 6	458.5 ± 6.9^{c}	0.38 ± 0.05^{a}	-15.7 ± 0.3^{b}
pH 8	369.4 ± 8.2^{b}	0.42 ± 0.02^{a}	-16.5 ± 0.1^{b}
pH 10	257.3 ± 8.4^{a}	0.32 ± 0.01^{a}	-24.8 ± 1.1^{a}
pH 12	255.6 ± 9.5^{a}	0.36 ± 0.06^{a}	-25.0 ± 0.2^{a}

Different letters indicate significant differences ($p < 0.05$) for particle size, PdI and zeta potential.

3.4. SEM and EDX

The morphology and chemical compositions of the

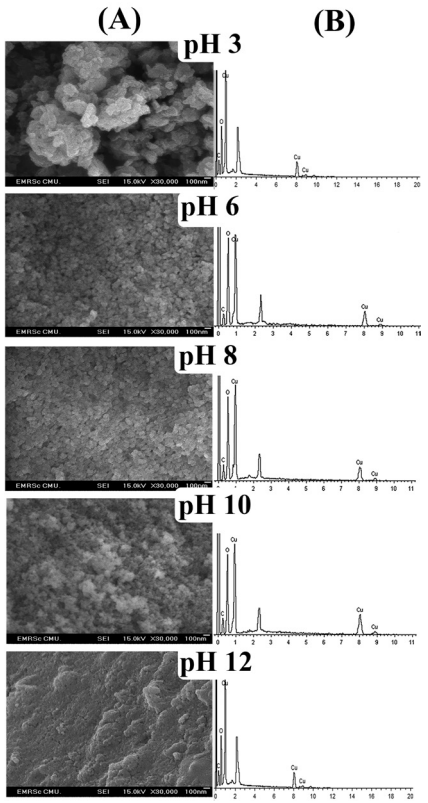

Figure 4. FESEM images (A) and EDX spectra (B) of CuONPs synthesized using *C. sappan* extract at different pH.

synthesized CuONPs investigated using SEM and EDX are shown in Figure 4. In the SEM images (Figure 4A), particle aggregation was observed in the CuONPs synthesized at pH 3, leading to extremely large particle sizes. Conversely, CuONPs synthesized at pH 6, 8, 10 and 12 had a spherical shape and overlapping of smaller particles. The EDX results (Figure 4B) of the CuONPs synthesized at all pH studied showed strong signals from elemental copper along with weak signals from other elements, such as oxygen and carbon.

3.5. Antifungal activity

The result of the antifungal test using the dilution method demonstrated that the CuONPs synthesized at various pH had antifungal activity but at different levels. As shown in Table 2, their MIC values ranged from 0.75-3 mg/mL, and MFC values were from 0.75 to more than 6 mg/mL. In the result, the MIC and MFC values of the CuONPs synthesized at pH 3 were the highest concentration, indicating the least antifungal effect on the pathogen. The MIC of the CuONPs synthesized at pH 8,10 and 12 against the pathogen was the same value of 0.75 mg/mL. However, the MFC of the CuONPs synthesized at pH 8 was significantly higher than those synthesized at pH 10 and 12. This result suggested that the CuONPs synthesized at pH 10 and 12 were the most effective against *C. albicans*. Nystatin showed antifungal activity with MIC and MFC values of 4.9×10^{-3} and 19.5×10^{-3} mg/mL, respectively.

Table 2. Antifungal activity of the CuONPs synthesized at different pH of synthesis reaction

pH of synthesis reaction	MIC (mg/mL)	MFC (mg/mL)
pH 3	3.00	> 6.00
pH 6	1.50	3.00
pH 8	0.75	1.5
pH 10	0.75	0.75
pH 12	0.75	0.75
Nystatin	4.9×10^{-3}	19.5×10^{-3}

3.6. Killing kinetics study

The microbial killing kinetics study measures the change in the *C. albicans* population within the time of specific exposure to the synthesized CuONPs. The growth curves of the samples compared to a negative control are presented in Figure 5. It was found that the growth curves of the pathogens after exposure to the CuONPs synthesized at pH 3, 6, and 8 were similar to that of the negative control. The reduction of viable cells could be found within 1-2 h, but after that the pathogen growth was significantly increased, whereas that synthesized at pH 10 and 12 could completely kill *C. albicans*. Interestingly, the CuONPs synthesized at pH 10 showed the completed killing of *C. albicans* within 1 h. The killing rate of these particles is as fast as that of nystatin, the positive control, and significantly faster than that synthesized at pH 12.

3.7. Antibiofilm assay

The result showed that the CuONPs synthesized in different pH could inhibit and eradicate biofilms of *C. albicans*, but at different levels, as shown in Figure 6. Furthermore, it was found that these effects depend on CuONPs concentration. For example, in Figure 6A, the inhibition effects of CuONPs synthesized at pH 3, 6, 8, 10, and 12 at 1/4 MFC were 8.95 ± 5.21%, 12.54 ± 9.93%, 27.55 ± 4.92%, 38.05 ± 0.87% and 40.15 ± 4.49%, respectively, while that of 1/2 MFC were 20.24 ± 0.36%, 48.46 ± 2.21%, 48.26 ± 3.11%, 69.99 ± 3.16% and 43.05 ± 5.93%, respectively. It was found that CuONPs synthesized at pH 6, 8, 10, and 12 at the MFC were able to inhibit biofilm formation by more than 70%. Interestingly, at this concentration, CuONPs synthesized at pH 10 and 12 showed the biofilm inhibition effect of 86.10 ± 1.10% and 87.68 ± 0.47%, respectively, significantly higher than that of nystatin at its MFC. In Figure 6B, the effects of the synthesized CuONPs on biofilm eradication are shown. The results showed that after exposure to the synthesized CuONPs, the formed biofilm of *C. albicans* was approximately 27.05 ± 4.25% to 79.28 ± 2.28% eliminated. The efficiency of the CuONPs synthesized at all tested pHs,

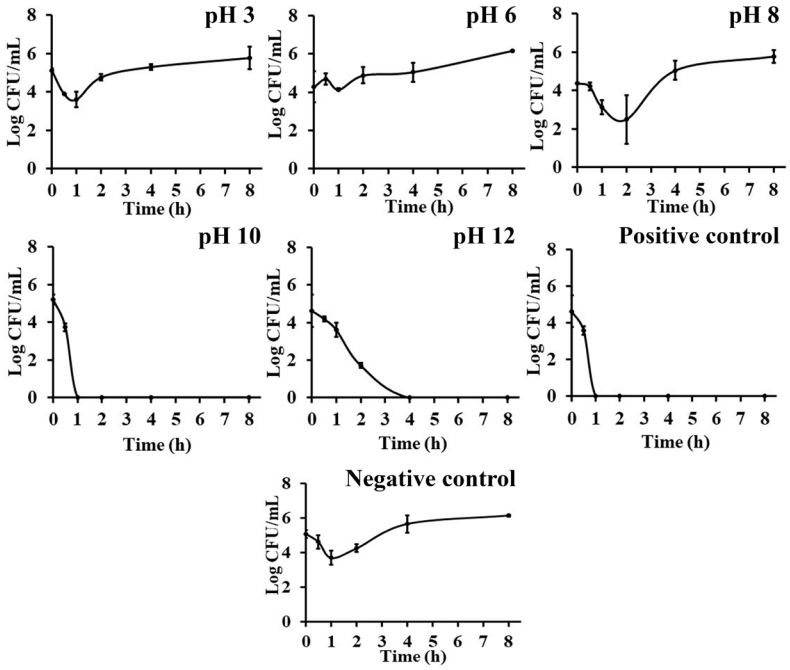

Figure 5. Time-killing kinetics against *C. albicans* of CuONPs synthesized using *C. sappan* extract at different pH in comparison with nystatin.

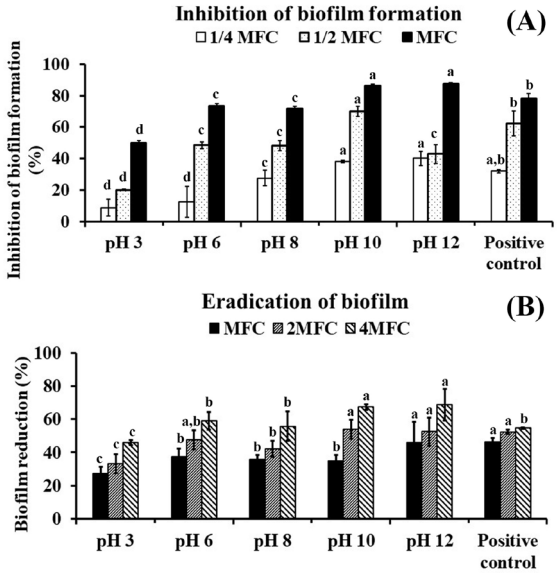

Figure 6. Effects of CuONPs synthesized using *C. sappan* extract at different pH in comparison with nystatin on inhibition of biofilm formation (A) and biofilm eradication (B). Different letters indicate significantly different ($p < 0.05$) for quantitative percentage of biofilm inhibition and biofilm eradication in the same sample concentration.

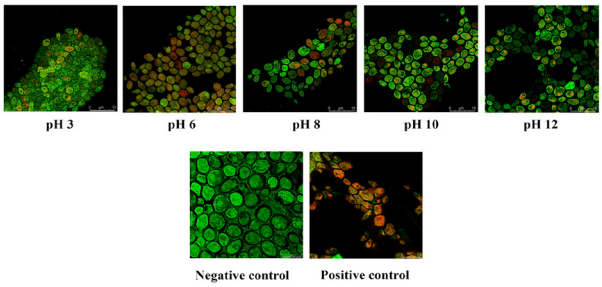

Figure 7. CSLM images of *C. albicans* biofilm treated with CuONPs synthesized using *C. sappan* extract at different pH in comparison with nystatin.

at MFC was less than 50%, while at 2 MFC, the biofilm eradication efficiency of the CuONPs synthesized at pH 10 and 12 was above 50% (53.88 ± 5.79% and 52.52 ± 8.63%, respectively). At the highest test concentration (4 MFC), the CuONPs synthesized at pH 6, 8, 10 and 12 showed a greater than 50% reduction in biofilm, whereas those synthesized at pH 3 showed only 46.03 ± 1.47% reduction. Based on these results, CuONPs synthesized at pH 10 and 12 were considered to have significantly higher potential for inhibition and removal of *C. albicans* biofilm than those synthesized at other pHs and nystatin.

3.8. CLSM analysis

CLSM images of *C. albicans* biofilms, as in Figure 7, showed the dead cells in red color and live cells in green color. The red cells stained with PI demonstrated that the number of cells after exposure to the synthesized CuONPs and the nystatin-positive control was higher than that of the negative control. After exposure to the CuONPs synthesized at all pH values and the nystatin-positive control, few green spots of viable cells were detected. After treatment with the synthesized CuONPs, the viable cell population was obviously lower than that of the negative control group. The population of *C. albicans* cells in the biofilms after exposure to the CuONPs synthesized at pH 10 and 12 was less than the others suggesting that most cells were dead and washed off the films.

4. Discussion

Many millions of people are affected by antimicrobial

resistance pathogens and many of them die every year (*32*). *C. albicans* represents the predominant cause of fungal infections and has the ability to develop biofilms that protect the pathogenic cells inside and increase their resistance to antifungal drugs (*1,2*). The use of metal nanoparticles is an effective alternative against antimicrobial-resistant pathogenic strains. We are interested in CuONPs because of its wide range of applications. It also has high antimicrobial activity against *C. albicans* and other pathogens (*33*).

Several methods such as electrochemical (*34*), radiation (*35*), photochemical (*36*), and by biological methods (*37*) have been used to synthesize metal nanoparticles. This study focuses on biological methods as it aims to reduce the use of inorganic substances. In this method, chemical reducing agents are replaced by high reducing power plant extract. *C. sappan* extract was used due to its high reducing activity (*38*). The different colors of the synthesized metal nanoparticles are due to the surface plasmon resonance excitation, a signal of nanoparticle formation (*39*). The surface plasmon resonance is due to the presence of free electrons, which is formed by conduction and valence bands, as they are close together in metals (*40*). Our results show different colors of the CuONPs system synthesized at different pH suggesting that pH affects the surface plasma resonance of the end products. Oligomeric clusters of copper can absorb at wavelength range 250-300 nm (*41*). Our results are in good agreement that the obtained CuONP particles absorb the wavelength range of 220-255 nm depending on the pH. The different absorption peaks of CuONPs synthesized at various pH values confirm the effect of pH on the surface plasma resonance absorbance of the obtained metal nanoparticles. It was found that the intensity of the absorbance peak of the obtained CuONP was increased by increasing the pH of the synthesis reaction. This might be related to the higher rate of formation of CuONPs in alkaline pH due to the ionization of the phenolic functional group present in the extract. The FTIR spectra of all CuONPs matched the FTIR spectra of the *C. sappan* extract. The obtained results reliably confirmed that the organic compounds of the *C. sappan* extract were responsible for the reduction of copper ions to CuONPs. The characteristic band at 528 cm^{-1} present in the FTIR spectra of CuONPs was considered to be that of cupric oxide (*42*). The negative value of zeta potential of the obtained CuONPs was attributed to a group of negatively charged compounds in the *C. sappan* extract. Our results showed that the small-size nanoparticles with high negative zeta potential could be synthesized only at pH 10 and 12. The size of the CuONPs synthesized at pH lower than 10 was large due to the low zeta potential, thus, leading to high particle aggregation. These can be confirmed by SEM images of CuONPs, showing minimal particle aggregation from the preparations at pH 10 and 12 and the highest particle aggregation from the preparation at pH 3. From the above findings, it can be concluded that the pH of the green synthesis reaction is an important factor for the characteristics of the obtained metal nanoparticles.

For antifungal activity, the smaller particles of CuONPs showed higher activity against *C. albicans* than larger particles. It has been reported that CuONPs involved in inactivation of *Escherichia coli* through membrane damage, intracellular ROS generation, and inactivation of fumarase enzyme (*43*). For the inhibition of *C. albicans*, we consider that CuONPs can destroy fungal membranes by the released Cu ion from the nanoparticles. In general, antifungal agents are classified as fungicidal and fungistatic according to the ratio of MFC to MIC. If the MFC/MIC ratio is ≤ 4, the agent is considered to have fungicidal activity. If the MFC/MIC ratio is > 4, the agent is fungistatic activity (*44*). From our results, the CuONPs synthesized at pH 6, 8, 10 and 12 possess fungicidal activity while the antifungal activity of those synthesized at pH 3 is fungistatic. This is considered that the smaller particle size has a more powerful antifungal effect.

The study of killing kinetics is to confirm the fungicidal activity of the agents and the results are more clinically useful than static MFC alone (*45*). It has been reported that fungicidal agent should be able to completely kill the test organisms within 24 h (*46*). In the present study, the CuONPs synthesized at different pH showed different killing efficiency. The CuONPs synthesized at pH 10 and 12 can completely kill *C. albicans* within less than 1 and 4 h, respectively, suggesting that these CuONPs are fungicidal agent.

Biofilms of human pathogens have been found to be highly associated with patient morbidity and mortality. It has been reported that the *Candida* spp. can form polymeric biofilms that can enhance the adherence of the pathogens to the surface (*47*). In addition, the extracellular polymeric substances secreted by *C. albicans* can prevent the diffusion of any agents into the cells, leading to high resistance to many antifungal drugs (*48*). Therefore, the prevention and eradication of biofilms are of great importance in the treatment of fungal infections. In this study, CuONPs synthesized at all pH exhibited a dose-dependent effects of inhibition of biofilm formation and removal of the formed biofilms of *C. albicans* but different levels. CuONPs synthesized at pH 10 and 12 showed the highest efficiency in these activities. The antibiofilm activities can be confirmed by CLSM analysis using florescent stains. Red fluorescence of PI indicates cells with damaged membranes and stains DNA of the dead cells, whereas green fluorescence of SYTO 9 indicates cells with intact membranes of viable cells. Our results in CLSM images show several viable cells in the biofilm of the untreated group. While viable cells were dramatically reduced in the synthesized CuONPs-treated biofilms. This indicates that CuONPs can effectively destroy *C. albicans*. These results are consistent with previous study where

CuONPs synthesized using leaf extracts of *Camellia japonica* showed a reduction in the number of colonies of *Pseudomonas aeruginosa* and *Klebsiella pneumoniae* (*49*). Our study also shows that many dead cells remain and can be clearly seen in the CLSM image of CuONPs synthesized at pH 3. However, for those synthesized at higher pH, especially at pH 10 and 12, only a small number of dead cells can be seen. This assumes that most dead cells are easily washed away.

In conclusion, the findings in this study confirmed that CuONPs biosynthesized using *C. sappan* extract at pH 10 and 12 possessed potent antifungal and antibiofilm activity. The results suggest that the obtained CuONPs may be a promising antifungal agent and are suitable for further study in animal models and clinical trials.

Acknowledgements

The authors greatly appreciate HISTOCENTER (Thailand) Co., Ltd. for providing us with CLSM analysis. We would like to thank the Center of Excellent in Pharmaceutical Nanotechnology of Chiang Mai University for facility support.

Funding: This work was supported by a grant from Thailand Research Fund through the Research and Researcher for Industry (RRi) Grant number PHD59I0076.

Conflict of Interest: The authors have no conflicts of interest to disclose.

References

1. Sandai D, Tabana YM, El Ouweini A, Ayodeji IO. Resistance of *Candida albicans* biofilms to drugs and the host immune system. Jundishapur J Microbiol. 2016; 9:1-7.
2. Eshima S, Kurakado S, Matsumoto Y, Kudo T, Sugita T. *Candida albicans* promotes the antimicrobial tolerance of *Escherichia coli* in a cross-kingdom dual-species biofilm. Microorganisms. 2022; 10:2179-2192.
3. Hawser SP, Douglas LJ. Resistance of *Candida albicans* biofilms to antifungal agents *in vitro*. Antimicrob Agents Chemother. 1995; 39:2128-2131.
4. Lalla RV, Latortue MC, Hong CH, Ariyawardana A, D'Amato-Palumbo S, Fischer DJ, Martof A, Nicolatou-Galitis O, Patton LL, Elting LS, Spijkervet FKL, Brennan MT. A systematic review of oral fungal infections in patients receiving cancer therapy. Support Care Cancer. 2010; 18:985-992.
5. Yoshijima Y, Murakami K, Kayama S, Liu D, Hirota K, Ichikawa T, Miyake Y. Effect of substrate surface hydrophobicity on the adherence of yeast and hyphal *Candida*. Mycoses. 2010; 53:221-226.
6. Garcia-Cuesta C, Sarrion-Pérez MG, Bagán JV. Current treatment of oral candidiasis: A literature review. J Clin Exp Dent. 2014; 6:576-582.
7. Gleiznys A, Zdanavičienė E, Žilinskas J. *Candida albicans* importance to denture wearers. A literature review. Stomatologija. 2015; 17:54-66.
8. Azharuddin M, Zhu GH, Das D, Ozgur E, Uzun L, Turner APF, Patra HK. A repertoire of biomedical applications of noble metal nanoparticles. Chem Commun. 2019; 5:6964-6996.
9. Dharmadasa R, Jha M, Amos DA, Druffel T. Room temperature synthesis of a copper ink for the intense pulsed light sintering of conductive copper films. ACS Appl Mater Interfaces. 2013; 5:13227-13234.
10. Gawande MB, Goswami A, Felpin FX, Asefa T, Huang X, Silva R, Zou X, Zboril R, Varma RS. Cu and Cu-based nanoparticles: Synthesis and applications in catalysis. Chem Rev. 2016; 116:3722-3811.
11. Sharma H, Mishra PK, Talegaonkar S, Vaidya B. Metal nanoparticles: A theranostic nanotool against cancer. Drug Discov Today. 2015; 20:1143-1151.
12. Ahamed M, Alhadlaq HA, Khan MAM, Karuppiah P, Al-Dhabi NA. Synthesis, characterization, and antimicrobial activity of copper oxide nanoparticles. J Nanomater. 2014; 2014:1-4.
13. Hardie JM. Oral microbiology: Current concepts in the microbiology of dental caries and periodontal disease. Br Dent J. 1992; 172:271-278.
14. Rahimi G, Khodavandi A, Yaghobi R. Antimycotic effect of copper oxide nanoparticles on *Candida albicans* biofilm. J Micro Nano Biomed. 2016; 1:7-12.
15. Tinkle S, Mcneil SE, Mühlebach S, Bawa R, Borchard G, Barenholz YC, Tamarkin L, Desai N. Nanomedicines: Addressing the scientific and regulatory gap. Ann N Y Acad Sci. 2014; 1313:35-56.
16. Nabila MI, Kannabiran K. Biosynthesis, characterization and antibacterial activity of copper oxide nanoparticles (CuO NPs) from actinomycetes. Biocatal Agric Biotechnol. 2018; 15:56-62.
17. Amin F, Fozia, Khattak B, Alotaibi A, Qasim M, Ahmad I, Ullah R, Bourhia M, Gul A, Zahoor S, Ahmad R. Green synthesis of copper oxide nanoparticles using *Aerva javanica* leaf extract and their characterization and investigation of *in vitro* antimicrobial potential and cytotoxic activities. Evid Based Complement Alternat Med. 2021; 2021:1-12.
18. Suwan T, Khongkhunthian S, Okonogi S. Silver nanoparticles fabricated by reducing property of cellulose derivatives. Drug Discov Ther. 2019; 13:70-79.
19. Mohanpuria P, Rana NK, Yadav SK. Biosynthesis of nanoparticles: Technological concepts and future applications. J Nanoparticle Res. 2008; 10:507-517.
20. Mittal AK, Chisti Y, Banerjee UC. Synthesis of metallic nanoparticles using plant extracts. Biotechnol Adv. 2013; 31:346-356.
21. Andra S, Balu SK, Jeevanandham J, Muthalagu M, Vidyavathy M, Chan YS, Danquah MK. Phytosynthesized metal oxide nanoparticles for pharmaceutical applications. Naunyn Schmiedebergs Arch Pharmacol. 2019; 392:755-771.
22. Mohamed EA. Green synthesis of copper & copper oxide nanoparticles using the extract of seedless dates. Heliyon. 2020; 6:1-6.
23. Siddiqui VU, Ansari A, Chauhan R, Siddiqi WA. Green synthesis of copper oxide (CuO) nanoparticles by *Punica granatum* peel extract. Mater Today Proc. 2019; 36:751-755.
24. Nirmal NP, Rajput MS, Prasad RGSV, Ahmad M. Brazilin from *Caesalpinia sappan* heartwood and its pharmacological activities: A review. Asian Pac J Trop Med. 2015; 8:421-430.

25. Srinivasan R, Selvam GG, Karthik S, Mathivanan K, Baskaran R, Karthikeyan M, Gopi M, Govindasamy C. *In vitro* antimicrobial activity of *Caesalpinia sappan* L. Asian Pac J Trop Biomed. 2012; 2:136-139.
26. Wu SQ, Otero M, Unger FM, Goldring MB, Phrutivorapongkul A, Chiari C, Kolb A, Viernstein H, Toegel S. Anti-inflammatory activity of an ethanolic *Caesalpinia sappan* extract in human chondrocytes and macrophages. J Ethnopharmacol. 2011; 138:364-372.
27. Badami S, Moorkoth S, Rai SR, Kannan E, Bhojraj S. Antioxidant activity of *Caesalpinia sappan* heartwood. Biol Pharm Bull. 2003; 26:1534-1537.
28. Nirmal NP, Rajput MS, Prasad RGS V, Ahmad M. Brazilin from *Caesalpinia sappan* heartwood and its pharmacological activities : A review. Asian Pac J Trop Med. 2015; 8:421-430.
29. Salayov A, Bedlovičová Z, Daneu N, Baláž M, Bujňáková ZL, Balážová L, Tkáčiková L. Green synthesis of silver nanoparticles with antibacterial activity using various medicinal plant extracts: Morphology and antibacterial efficacy. Nanomaterials. 2021; 11:1005-1025.
30. Patra JK, Baek KH. Green nanobiotechnology: Factors affecting synthesis and characterization techniques. J. Nanomater. 2014; 2014:1-12.
31. Rizvi SAA, Saleh AM. Applications of nanoparticle systems in drug delivery technology. Saudi Pharm J. 2018; 26:64-70.
32. Raut S, Adhikari B. The need to focus China's national plan to combat antimicrobial resistance. Lancet Infect Dis. 2017; 17:137-138.
33. Azam A, Ahmed AS, Oves M, Khan MS, Memic A. Size-dependent antimicrobial properties of CuO nanoparticles against Gram-positive and -negative bacterial strains. Int J Nanomedicine. 2012; 7:3527-3535.
34. Raja M. Production of copper nanoparticles by electrochemical process. Powder Metall Met Ceram. 2008; 47:402-405.
35. Hori T, Nagata K, Iwase A, Hori F. Synthesis of Cu nanoparticles using gamma-ray irradiation reduction method. Jpn J Appl Phys. 2014; 53:1-5.
36. Giuffrida S, Costanzo LL, Ventimiglia G, Bongiorno C. Photochemical synthesis of copper nanoparticles incorporated in poly(vinyl pyrrolidone). J Nanoparticle Res. 2008; 10:1183-1192.
37. Lee HJ, Song JY, Kim BS. Biological synthesis of copper nanoparticles using *Magnolia kobus* leaf extract and their antibacterial activity. J Chem Technol Biotechnol. 2013; 88:1971-1977.
38. Suwan T, Wanachantararak P, Khongkhunthian S, Okonogi S. Antioxidant activity and potential of *Caesalpinia sappan* aqueous extract on synthesis of silver nanoparticles. Drug Discov Ther. 2018; 12:259-266.
39. Sathiyavimal S, Vasantharaj S, Bharathi D, Saravanan M, Manikandan E, Kumar SS, Pugazhendhi A. Biogenesis of copper oxide nanoparticles (CuONPs) using *Sida acuta* and their incorporation over cotton fabrics to prevent the pathogenicity of Gram negative and Gram positive bacteria. J Photochem Photobiol B. 2018; 188:126-134.
40. Jana J, Ganguly M, Pal T. Enlightening surface plasmon resonance effect of metal nanoparticles for practical spectroscopic application. RSC Adv. 2016; 6:86174-86211.
41. Khatouri J, Mostafavi M, Amblard J, Belloni J. Radiation-induced copper aggregates and oligomers. Chem Phys Lett. 1992; 191:351-356.
42. Ethiraj AS, Kang DJ. Synthesis and characterization of CuO nanowires by a simple wet chemical method. Nanoscale Res Lett. 2012; 7:1-5.
43. Meghana S, Kabra P, Chakraborty S, Padmavathy N. Understanding the pathway of antibacterial activity of copper oxide nanoparticles. RSC Adv. 2015; 5:12293-12299.
44. Dudiuk C, Berrio I, Leonardelli F, Morales-Lopez S, Theill L, Macedo D, Yesid-Rodriguez J, Salcedo S, Marin A, Gamarra S, Garcia-Effron G. Antifungal activity and killing kinetics of anidulafungin, caspofungin and amphotericin B against *Candida auris*. J Antimicrob Chemother. 2019; 74:2295-2302.
45. Keepers TR, Gomez M, Celeri C, Nichols WW, Krause KM. Bactericidal activity, absence of serum effect, and time-kill kinetics of ceftazidime-avibactam against β-lactamase-producing *Enterobacteriaceae* and *Pseudomonas aeruginosa*. Antimicrob Agents Chemother. 2014; 58:5297-5305.
46. Pfaller MA, Sheehan DJ, Rex JH. Determination of fungicidal activities against yeasts and molds: Lessons learned from bactericidal testing and the need for standardization. Clin Microbiol Rev . 2004; 17:268-280.
47. Forsberg K, Woodworth K, Walters M, Berkow EL, Jackson B, Chiller T, Vallabhaneni S. *Candida auris*: The recent emergence of a multidrug-resistant fungal pathogen. Med Mycol. 2019; 57:1-12.
48. Chandra J, Mukherjee PK, Leidich SD, Faddoul FF, Hoyer LL, Douglas LJ, Ghannoum MA. Antifungal resistance of Candidal biofilms formed on denture acrylic *in vitro*. J Dent Res. 2001; 80:903-908.
49. Rajivgandhi G, Maruthupandy M, Muneeswaran T, Ramachandran G, Manoharan N, Quero F, Anand M, Song JM. Biologically synthesized copper oxide nanoparticles enhanced intracellular damage in ciprofloxacin resistant ESBL producing bacteria. Microb Pathog. 2019; 127:267-276.

Received May 11, 2023; Revised August 19, 2023; Accepted August 19, 2023.

*Address correspondence to:
Siriporn Okonogi, Center of Excellent in Pharmaceutical Nanotechnology, Faculty of Pharmacy, Chiang Mai University, Chiang Mai 50200, Thailand.
E-mail: okng2000@gmail.com

Released online in J-STAGE as advance publication August 24, 2023.

Original Article

DOI: 10.5582/ddt.2023.01035

LncRNA SNHG1 upregulates FANCD2 and G6PD to suppress ferroptosis by sponging miR-199a-5p/3p in hepatocellular carcinoma

Lin Zhou[1,§], Qing Zhang[1,2,§], Jiaxin Cheng[1], Xiandie Shen[1], Jing Li[1], Mingya Chen[1], Chang Zhou[1,*], Jianlin Zhou[1,*]

[1] State Key Laboratory of Developmental Biology of Freshwater Fish & Key Laboratory of Protein Chemistry and Developmental Biology of the Ministry of Education, College of Life Science, Hunan Normal University, Changsha, Hunan, China;
[2] Clinical Research Center for Reproduction and Genetics in Hunan Province, Reproductive and Genetic Hospital of CITIC-Xiangya, Changsha, Hunan, China.

SUMMARY Ferroptosis is a form of regulated cell death (RCD) triggered by iron-dependent lipid peroxidation and is closely associated with the occurrence and progression of hepatocellular carcinoma (HCC). The lncRNA SNHG1 (small nucleolar RNA host gene 1) has been shown to play an oncogenic role in HCC, but its function in RCD other than autophagy and apoptosis is still unknown. Here, we investigated the correlation between SNHG1 and 156 typical markers of five RCD types based on RNA sequencing data from The Cancer Genome Atlas database and showed the negative regulators of ferroptosis FANCD2 (Fanconi anemia complementation group D2) and G6PD (glucose-6-phosphate dehydrogenase) to be the most highly and fifth most highly correlating factors with SNHG1, respectively. A competitive endogenous RNA network of SNHG1 – miR-199a-5p/3p – FANCD2/G6PD was constructed bioinformatically. *In vitro* experiments showed that overexpression of the miR-199a precursor led to a decrease in expression of SNHG1, FANCD2, and G6PD, whereas knockdown of SNHG1 decreased expression of FANCD2 and G6PD but increased levels of miR-199a-5p and miR-199a-3p in HCC cells (Huh7 and HepG2). In addition, knockdown of SNHG1 increased erastin-mediated ferroptosis, iron accumulation, and lipid peroxidation. These results suggest that SNHG1 upregulates FANCD2 and G6PD by sponging miR-199a, thereby inhibiting ferroptosis in HCC. Moreover, a signature based on expression of SNHG1, FANCD2, and G6PD was identified as being associated with overall survival and the immunological microenvironment in HCC. Collectively, this study identified the SNHG1–miR-199a–FANCD2/G6PD axis in HCC, which is a potential marker for the prognosis and therapy of this tumor.

Keywords ferroptosis, FANCD2, G6PD, SNHG1, hepatocellular carcinoma

1. Introduction

Liver cancer is one of the most common and lethal types of cancers. According to global cancer statistics, the incidence and mortality of primary liver cancer ranked sixth and third, respectively, in 2020 (*1*). Hepatocellular carcinoma (HCC) and intrahepatic cholangiocarcinoma are the two major types of primary liver cancers, accounting for 75-85% and 10-15% of cases, respectively (*1*). Due to limited detection capabilities and the asymptomatic nature of HCC in early stages, most patients are diagnosed at a late stage and thus miss the chance of radical resection (*2*). The 5-year overall survival (OS) rate of HCC patients is only 19.5% (*3*). Hence, there is an urgent need to elucidate the molecular pathogenesis of HCC to improve the efficacy of diagnosis and treatment.

Recently, regulated cell death (RCD) has gained increasing attention from cancer researchers. RCD, also called programmed cell death, refers to a type of cell death that is regulated by genes and differs from uncontrolled and random cell death (*4,5*). The major types of RCD include apoptosis, autophagy, pyroptosis, necroptosis, PANoptosis, ferroptosis, and the newly discovered cuproptosis (*6*). Ferroptosis, a form of RCD induced by iron-dependent lipid peroxidation, was first discovered by Dixon *et al*. (*7*). Ferroptosis has been shown to be highly related to the occurrence and

progression of HCC and can be used as a therapeutic target and prognostic factor (*8, 9*).

The lncRNA SNHG1 plays an important role in various cancers, including HCC (*10*). Our previous study showed that SNHG1 (small nucleolar RNA host gene 1) acts as a competitive endogenous RNA (ceRNA) to regulate the cell cycle in HCC (*11*). However, its role in RCDs other than apoptosis and autophagy has not been investigated. In the present study, we performed coexpression analysis of SNHG1 and 156 RCD-related genes based on RNA sequencing (RNA-seq) data. According to the Pearson correlation coefficient, the ferroptosis-related genes *FANCD2* (Fanconi anemia complementation group D2) and *G6PD* (glucose-6-phosphate dehydrogenase) are the most highly and fifth most highly correlating factors with SNHG1, respectively. Therefore, we investigated the role and molecular mechanism of SNHG1 in ferroptosis and constructed a prognostic signature for predicting OS and response to immunotherapy in patients with HCC.

2. Materials and Methods

2.1. RNA-seq data acquisition

RNA-seq data and clinical information of patients with HCC were obtained from The Cancer Genome Atlas (TCGA) and International Cancer Genome Consortium (ICGC) databases. The TCGA cohort included 374 HCC tissues and 50 adjacent normal liver tissues. The ICGC cohort (LIRI-JP) included 243 HCC tissue samples and 202 adjacent nontumor liver tissue samples. In addition, microRNA (miRNA) expression RNA-seq data (371 HCC tissues and 49 adjacent normal liver tissues) were obtained from the TCGA database.

2.2. Cell lines, chemicals, and antibodies

The HCC cell lines HepG2 and Huh7 were obtained from American Type Culture Collection (ATCC) (Manassas, VA, USA) and cultured according to ATCC's instructions. All cell lines were free of mycoplasma and authenticated by Yubo Biological Technology (Shanghai, China) using short tandem repeat analysis. Erastin and FeRhoNox-1 (Fe^{2+} indicator) were purchased from Selleck (Houston, TX, USA) and MKBio (Shanghai, China), respectively. The antibodies used in this study were purchased from ABclonal (Wuhan, Hubei, China). MTT [3-(4,5-dimethylthiazol-2-yl)-2,5 diphenyl tetrazolium bromide] was purchased from Beyotime (Shanghai, China).

2.3. Lentivirus infection

Lentiviruses expressing SNHG1 shRNA or the microRNA-199a (miR-199a) precursor (hsa-mir-199a-1) were purchased from GeneChem (Shanghai, China). The target sequence of the SNHG1 shRNA was validated in our previous study (*11*). Lentivirus particles were transduced into cells according to the manufacturer's instructions. At 72 hours after transduction, the cells were cultured in fresh medium with hygromycin B to generate stable cell lines.

2.4. Western blotting

As previously described (*11*), total cellular proteins were extracted, separated, and transferred to a polyvinylidene fluoride (PVDF) membrane. After blocking, the membranes were cut into pieces and incubated separately with antibodies. Protein bands were visualized using the ChemiLucent ECL Detection System (Millipore, Billerica, MA, USA).

2.5. RNA isolation and reverse-transcription quantitative PCR (RT-qPCR)

Total RNA was isolated from cell lines using TRIzol reagent (Invitrogen, Carlsbad, CA, USA) and served as a template for the RT reaction. mRNAs were reverse-transcribed into cDNA using a First-Strand cDNA Synthesis Kit (GeneCopoeia, Guangzhou, Guangdong, China). Primers for 18S rRNA and SNHG1 have been described previously (*11*). The primers used for FANCD2 and G6P were as follows: FANCD2, 5′-ACATACCTCGACTCATTGTCAGT-3′ (forward) and 5′- TCGGAGGCTTGAAAGGACATC-3′ (reverse); G6PD, 5′- CGAGGCCGTCACCAAGAAC-3′ (forward) and 5′- GTAGTGGTCGATGCGGTAGA-3′ (reverse). For miRNA RT, miRNA was first polyA-tailed and reverse-transcribed using oligo-dT primers provided in miRNA First-Strand cDNA Synthesis Kit (GeneCopoeia). SYBR Green-based real-time PCR was performed using a qPCR kit (GeneCopoeia).

2.6. Analysis of erastin-mediated ferroptosis

Cells were plated in 96-well plates and treated with various concentrations of erastin for 48 h. Cell viability was determined by MTT assays as described previously (*11*).

2.7. Analysis of iron accumulation

Cells were seeded onto glass coverslips. After aspiration of the culture medium, the cells were washed twice with phosphate-buffered saline (PBS) and stained with FeRhoNox-1 (5 μmol/L) for 60 min at 37°C in a 5% CO_2 incubator. The cells were then observed under a fluorescence microscope.

2.8. Malondialdehyde (MDA) assay

Cells were incubated with thiobarbituric acid (TBA) at

95°C for 60 min and cooled in an ice bath for 10 min. The MDA concentration was quantified calorimetrically (OD = 532 nm).

2.9. Identification of SNHG1-associated typical RCD markers

Pearson correlation analysis was performed to investigate the coexpression relationship between SNHG1 and 156 typical markers of RCD from previous studies (*6,12*).

2.10. Construction of the ceRNA network

The ceRNA network was constructed as previously described (*11*). Differential expression of RNAs between HCC tissue and adjacent normal liver tissue was identified using the 'limma' package of R software (*https://www.r-project.org/*). StarBase (*https://starbase.sysu.edu.cn/index.php*) and the miRWalk database (*http://mirwalk.umm.uni-heidelberg.de/*) were used to predict potential lncRNA–miRNA and miRNA–mRNA pairs, respectively. The ceRNA network was visualized using the R package "ggalluvial."

2.11. Construction and validation of a prognostic signature

The TCGA cohort was used to construct a prognostic model, and the ICGC cohort was used to validate this model. Univariate and multivariate Cox regression analyses were performed to examine the correlation between gene expression with the R package "survival". The risk score for each patient was then calculated based on the coefficient of multivariate Cox regression analysis. A Kaplan–Meier (KM) survival curve was used to calculate survival difference between the high- and low-risk groups using the R packages "survival" and "survminer". Multivariate Cox regression analysis was performed to evaluate whether the risk score is an independent prognostic predictor of OS when other clinical factors (age, sex, stage, grade, T stage, N stage, and M stage) are considered. A receiver operating characteristic (ROC) curve was produced using the R package "timeROC" to evaluate the predictive power of the signature.

2.12. Comparison of immunity status between high- and low-risk groups

To evaluate the role of the risk model in the immunological microenvironment, we compared the proportions of 22 different immune cell types between patients with high- or low-risk score using CIBERSORT. CIBERSORT is an algorithm that uses a set of reference gene expression matrices to evaluate the proportions of immune cell types from bulk tumor sample expression data based on the principle of linear support vector regression (*13*). In addition, we compared differential expression of immune checkpoint genes between the high- and low-risk groups. Response to immune checkpoint inhibitor (ICI) immunotherapy in HCC patients was predicted using Tumor Immune Dysfunction and Exclusion (TIDE) (*http://tide.dfci.harvard.edu*) (*14*) and IMvigor210 (*15*) algorithms.

2.13. Statistical analysis

All statistical analyses were performed using R language. One-way analysis of variance (ANOVA) was used to assess differences between groups. Pearson's correlation test was used for correlation analysis. The log-rank test was used to evaluate the significance of differences in survival curves. Statistical significance was set at $p < 0.05$.

3. Results

3.1. SNHG1 correlates positively with the ferroptosis-related genes *FANCD2* and *G6PD*

We analyzed the coexpression relationship between SNHG1 and RCD markers based on RNA-seq data from TCGA (including 374 HCC tissue and 50 adjacent normal liver tissue specimens). According to previous literature (*6,12*), 156 typical markers of five RCD types, including ferroptosis, pyroptosis, necroptosis, PANoptosis, and cuproptosis, were selected for coexpression analysis. The negative regulators of ferroptosis FANCD2 and G6PD were found to correlate highly with SNHG1, with the first and fifth highest correlation coefficients (cor): cor (FANCD2, SNHG1) = 0.76, cor (G6PD, SNHG1) = 0.63 (Figure 1A). Similar to SNHG1(11), FANCD2 and G6PD were significantly overexpressed in HCC tissues (Figure 1B). These results suggest that SNHG1 is involved in ferroptosis.

3.2. Bioinformatic identification of a ceRNA network of SNHG1–miRNAs–FANCD2/G6PD

The above results showed that SNHG1 is coexpressed with FANCD2 and G6PD. According to the ceRNA hypothesis (*16*), SNHG1 is a potential ceRNA of FANCD2 and G6PD. Therefore, we constructed a ceRNA network of lncRNAs, miRNAs, and mRNAs. miRNAs targeting lncRNA SNHG1 and mRNA (FANCD2 and G6PD) were predicted using starBase and miRWalk software, respectively. A total of 87 common miRNAs targeting both lncRNA SNHG1 and mRNA (FANCD2 or G6PD) were identified (Figure 1C). In the ceRNA network, miRNAs correlate negatively with lncRNAs and mRNAs (*16*). Considering the lncRNA SNHG1 and mRNAs (FANCD2 or G6PD) to be overexpressed in HCC, we selected common miRNAs targeting both SNHG1 and FANCD2 (or G6PD) from

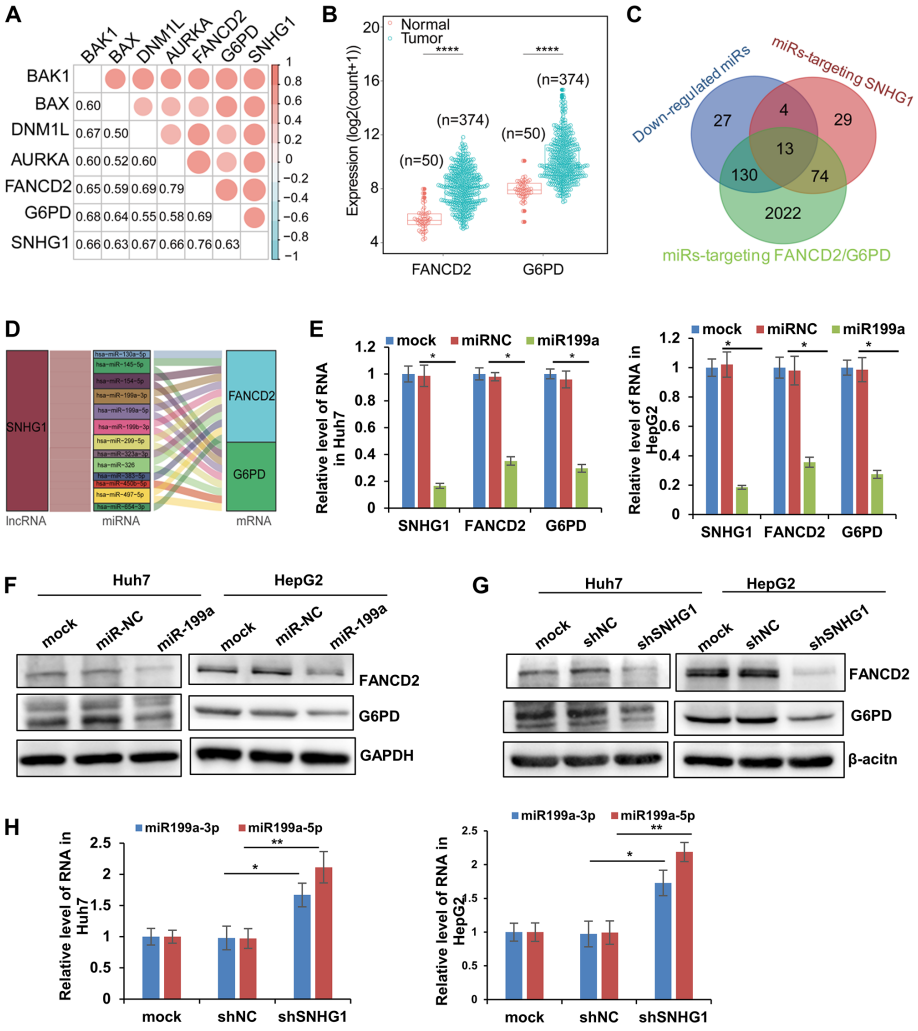

Figure 1. SNHG1 upregulates FANCD2 and G6PD as a ceRNA. (**A**) The coexpression relationship between SNHG1 and RCD markers was determined based on RNA-seq data from TCGA, and the top 7 genes with the highest coefficient are shown. (**B**) Differential expression of FANCD2 and G6PD between HCC and noncancerous liver tissues in TCGA cohorts. (**C**) Venn diagram showing the number of predicted miRNAs targeting FANCD2, G6PD and SNHG1 and downregulated miRNAs. (**D**) A ceRNA network of SNHG1–miRNAs–FACD2/G6PD. (**E-F**) The effect of miR-199a on expression of SNHG1, FANCD2, and G6PD. At 72 hours after infection with lentivirus particles expressing scrambled miRNA (miRNC) or premiR-199a (miR199a), the RNA and protein levels of SNHG1, FANCD2, and G6PD were detected by RT-qPCR (**E**) and western blotting (**F**), respectively. (**G-H**) The effect of SNHG1 on expression of FANCD2, G6PD and miR-199a-5p/3p. At 72 hours after infection with lentivirus particles expressing empty vector (shNC) or SNHG1 (shSNHG1), levels of FANCD2 and G6PD proteins and levels of miR-199a-5p and miR-199a-3p were detected by western blotting (**G**) and RT-qPCR (**H**), respectively. *$p < 0.05$, **$p < 0.01$.

the downregulated miRNAs (Figure 1C). As a result, 13 downregulated miRNAs met the criteria and were used to construct the ceRNA network (Figure 1D). These results suggest that SNHG1 regulates FANCD2 and G6PD by sponging 13 miRNAs.

3.3. Experimental validation of the SNHG1–miR-199a–FANCD2/G6PD axis

Interestingly, SNHG1, FANCD2, and G6PD were the common targets of miR-199a-5p and miR-199a-3p, which derive from the 5' and 3' arms of the same miRNA precursor, premiR-199a. Therefore, we transduced lentivirus particles expressing premiR-199a into HepG2 and Huh7 cells. The results of qPCR and western blotting analyses showed that overexpression of premiR-199a resulted in a decrease in expression of SNHG1, FANCD2, and G6PD (Figures 1E and 1F). This suggests that SNHG1, FANCD2, and G6PD are targets of miR-199a. Moreover, knockdown of SNHG1 decreased expression of FANCD2 and G6PD (Figure 1G) but increased levels of miR-199a-5p and miR-199a-3p (Figure 1H). These results indicate that SNHG1 increases expression of FANCD2 and G6PD by sponging miR-199a-5p/3p.

3.4. Suppression of SNHG1 promotes ferroptosis

The above results show that SNHG1 upregulates expression of FANCD2 and G6PD by sponging miR-199a-5p/3p, but FANCD2 and G6PD suppress ferroptosis (*17,18*). Therefore, we investigated whether

SNHG1 inhibits erastin-induced ferroptosis. As expected, SNHG1 knockdown increased erastin-mediated cytotoxicity in both Huh7 and HepG2 cells (Figures 2A and 2B), suggesting that SNHG1 protects HCC cells from ferroptosis. Ferroptosis is characterized by iron accumulation and lipid peroxidation (*19*). The effect of SNHG1 on iron accumulation and lipid peroxidation was determined using an Fe^{2+} indicator and MDA assay, respectively. The product of lipid peroxidation (Figures 2C and 2D) and the Fe^{2+} concentration (Figures 2E and 2F) increased in SNHG1-deficient cells with or without erastin treatment, suggesting that SNHG1 decreases iron accumulation and lipid peroxidation.

3.5. The prognostic value of a signature based on expression of SNHG1, FANCD2 and G6PD

Our previous study showed SNHG1 expression to act as a prognostic factor for OS in patients with HCC (*11*). Univariate and multivariate Cox regression analyses were performed to assess correlations between gene expression and OS. Based on univariate Cox regression analysis, both FANCD2 and G6PD are risk factors for HCC, similar to SNHG1 (Figure 3A). A three-gene signature was generated based on the multivariate Cox regression coefficient (Figure 3B), and the risk score of each patient was calculated using the following formula: risk score = 0.29873 × G6PD + 0.01513 × SNHG1 + 0.05200 × FANCD2.

To assess the prognostic significance of the risk model, we investigated the correlation between the risk score and clinical parameters. The patients in the TCGA and ICGC cohorts were divided into high- and low-risk groups according to the median risk score (cutoff value: 3.516333 in TCGA and 6.192844 in ICGC). Kaplan–Meier analysis showed that patients in the high-risk group had significantly worse survival than patients in the low-risk group in the TCGA (Figure 3C) and ICGC cohorts (Figure 3D). Moreover, time-dependent ROC analyses showed that this signature has high predictive ability. The area under the curve (AUC) of 1-year, 3-year, and 5-year survival in TCGA was 0.765, 0.666, and 0.633 (TCGA), respectively (Figure 3E). The AUCs of 1-year, 2-year, and 3-year survival in the ICGC cohort were 0.657, 0.706, and 0.765, respectively (Figure 3F). Multivariate Cox regression analysis showed that the risk

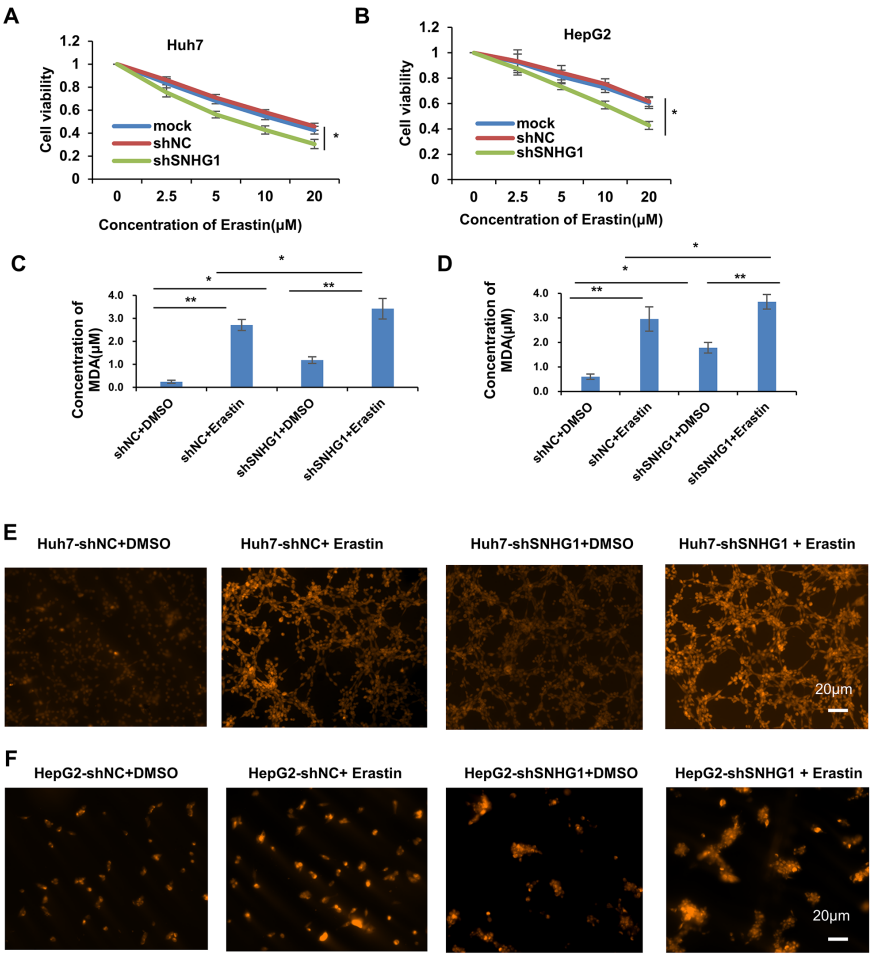

Figure 2. Suppression of SNHG1 promotes ferroptosis. Cells stably expressing empty vector (shNC) or SNHG1 (shSNHG1) were treated with different concentrations of erastin for 48 hours. (**A-B**) Cell viability was determined by MTT assays. (**C-D**) The MDA concentration was quantified by calorimetry. (**E-F**) The intracellular iron concentration was detected by the Fe^{2+} indicator FeRhoNox-1. *$p < 0.05$, **$p < 0.01$.

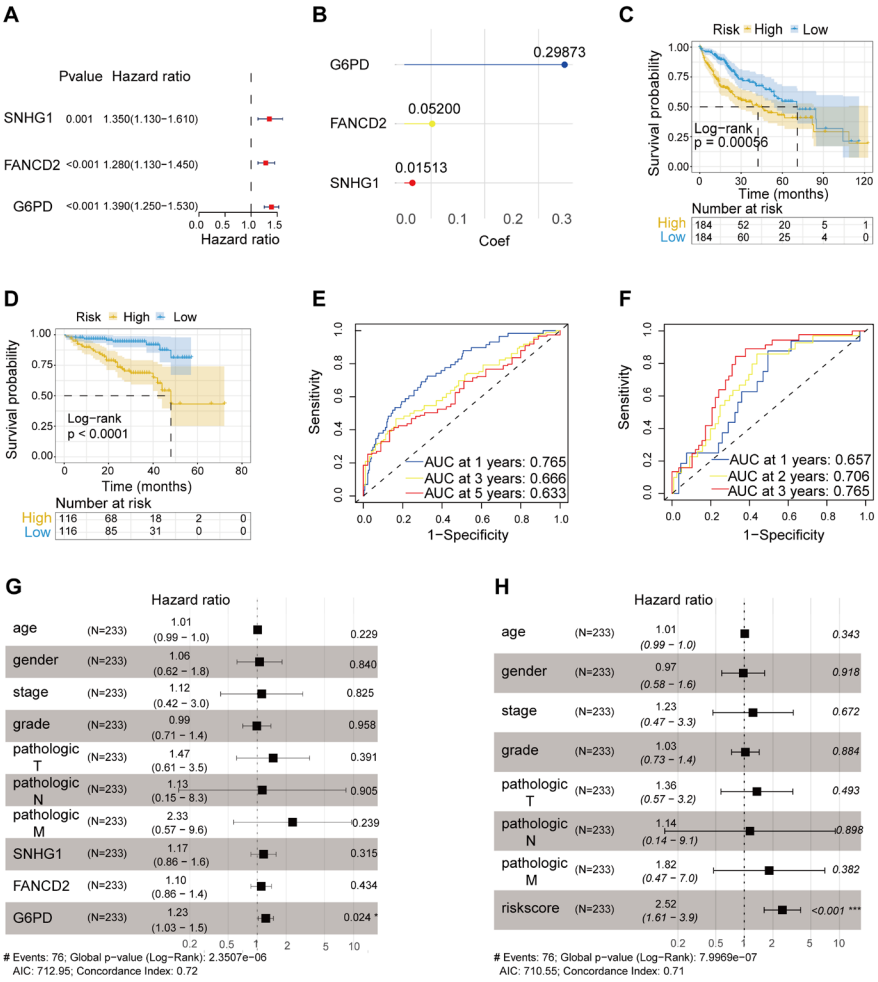

Figure 3. Construction and validation of a prognostic signature based on expression of SNHG1, FANCD2, and G6PD. (**A-B**) Univariate (**A**) and multivariate Cox regression (**B**) analyses were performed to assess the correlation between gene expression and overall survival. (**C-D**) Kaplan–Meier survival curves for low- and high-risk groups in TCGA (**C**) and ICGC cohorts (**D**). (**E-F**) Time-dependent ROC curve analyses of prediction models for survival in TCGA (**E**) and ICGC cohorts (**F**). **(G-H)** Multivariate analyses of factors associated with overall survival.

score and G6PD can serve as independent prognostic factors for patients with HCC when other clinical factors (age, sex, stage, grade, T stage, N stage, and M stage) are considered (Figures 3G-3H).

3.6. The value of the signature in predicting response to immunotherapy

To evaluate the role of the risk model in the immune microenvironment of HCC, the CIBERSORT algorithm was used to compare the 22 different immune cell types in HCC to evaluate the role of the risk model in the immune microenvironment of HCC. We found that 10 of these immune cell types were differentially expressed between the two risk groups. In patients with high risk scores, M2 macrophages, resting CD4 T cells, and resting mast cells were downregulated, whereas resting dendritic cells, M0 macrophages, activated CD4 T cells, and Treg cells were upregulated (Figure 4A). In addition, we determined whether there is a correlation between expression of inhibitory immune checkpoints and the risk score. Interestingly, expression levels of almost all checkpoints were significantly upregulated in the high-risk group (Figure 4B). Moreover, the high-risk group had a higher TIDE score than the low-risk group (Figure 4C). These results suggest that the risk score is associated with immune suppression. However, according to IMvigor210 analysis, the high-risk group had higher rates of complete response (CR) and partial response (PR) to ICI immunotherapy than the low-risk group (Figure 4D). This suggests that patients with high risk scores benefit more from ICI treatment.

4. Discussion

In the present study, we investigated the correlation between SNHG1 and typical markers of five RCD (ferroptosis, pyroptosis, necroptosis, PANoptosis, and cuproptosis). We found that SNHG1 correlated most strongly with the ferroptosis markers FANCD2 and G6PD. SNHG1 normally functions as a ceRNA for miRNAs in cancer (*10,11*). In the present study, a ceRNA network of SNHG1–miRNAs–FANCD2/G6PD was bioinformatically constructed, and the regulatory axis of

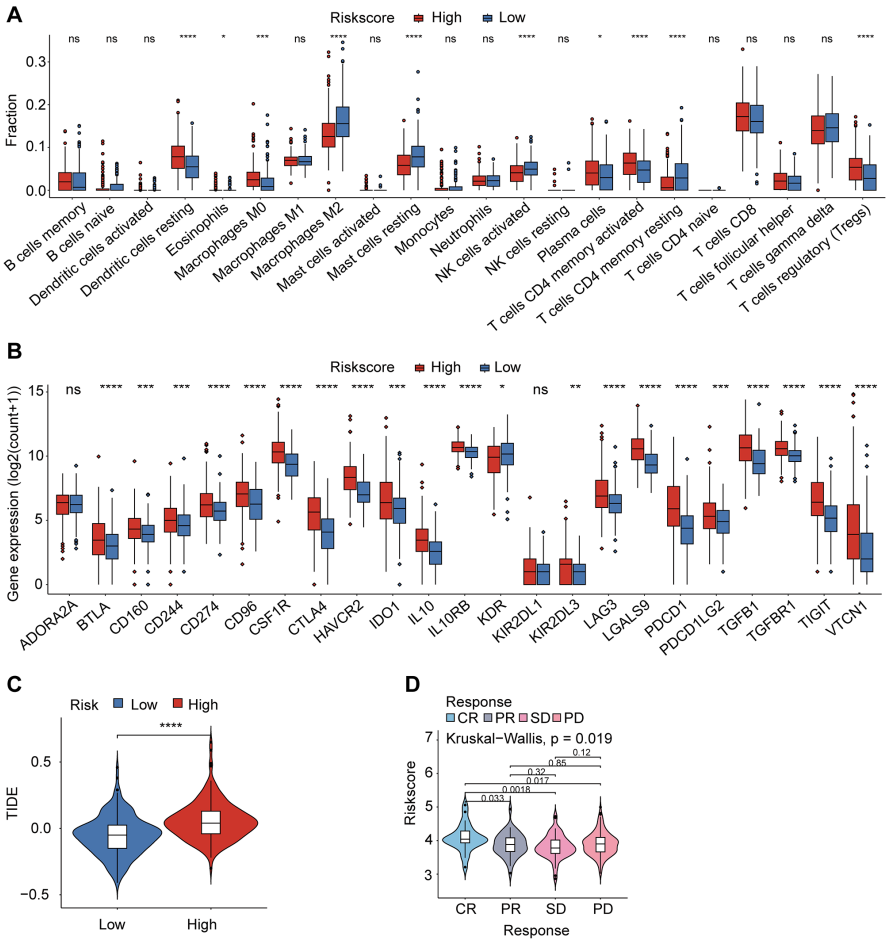

Figure 4. The gene signature based on expression of SNHG1, FANCD2, and G6PD is associated with the immune microenvironment. (**A**) The difference in the degree of immune infiltration of 22 immune cell types between the high- and low-risk groups, as assessed by the CIBERSORT algorithm. (**B**) The difference in expression of immune checkpoints between high- and low-risk groups. (**C-D**) Response to immunotherapy in HCC patients was estimated using TIDE (**C**) and IMvigor210 (**D**) algorithms. *$p < 0.05$, **$p < 0.01$, ***$p < 0.001$, ****$p < 0.0001$.

SNHG1–miR-199a–FANCD2/G6PD was experimentally validated. FANCD2 and G6PD are negative regulators of ferroptosis. FANCD2 inhibits ferroptosis by suppressing iron accumulation and lipid peroxidation (*17*). The repressive role of G6PD in ferroptosis is associated with the P450 metabolic pathway (*18*). We demonstrated that knockdown of SNHG1 or overexpression of premiR-199a decreased expression of FANCD2 and G6PD and that knockdown of SNHG1 enhanced erastin-induced ferroptosis in HCC cells. These results indicate that SNHG1 upregulates FANCD2 and G6PD by sponging miR-199a-5p/3p, thereby inhibiting ferroptosis. To our knowledge, this is the first report on involvement of SNHG1 in ferroptosis.

According to the miRBase database (*https://www.mirbase.org*), there are two miR-199a precursors: premir-199a-1 on chromosome 19 and premir-199a-2 on chromosome 1. Both precursors can be processed into mature miR-199a-5p and miR-199a-3p. Both miR-199a-5p and miR-199a-3p are known tumor suppressors in HCC (*20-22*). They regulate several cellular processes in cancer, including proliferation, apoptosis, migration, and invasion (*20-22*). Only two groups have reported the effects of miR-199a on ferroptosis; however, the results are conflicting. Lin *et al.* (*23*) reported that miR-199a-3p suppresses endothelial cell ferroptosis by targeting SP1. However, according to a study by Zhang *et al.*, miR-199a-5p stimulates ferroptosis-induced death of cardiomyocytes during ischemic/hypoxic injury by inhibiting the Akt/eNOS signaling pathway (*24*). It is possible that miR-199a exerts different effects by targeting different targets. However, it is unknown whether miR-199a regulates ferroptosis in cancer cells. Here, we report that overexpression of premiR-199a decreases expression of the negative regulators of ferroptosis FANCD2 and G6PD. This suggests that miR-199a exerts its antitumor activity by promoting ferroptosis.

Ferroptosis is a type of cell death induced by iron-dependent lipid peroxidation (*19*), and hepatocytes are the main cells involved in iron storage (*25*). Accumulating evidence has demonstrated that HCC cells can inactivate ferroptosis through multiple mechanisms and that activating ferroptosis is a

potential strategy for HCC cancer treatment (*26*). In addition, activation of ferroptosis can regulate the tumor immune microenvironment and sensitize cancer cells to immunotherapy (*27*). In the present study, we demonstrated that SNHG1, FANCD2 and G6PD are inhibitors of ferroptosis and constructed a signature based on SNHG1, FANCD2 and G6PD expression. The risk score calculated using this signature was an independent prognostic factor for OS in patients with HCC. Moreover, this risk score was associated with infiltration of immune cells and expression of immune checkpoints.

In conclusion, the present study demonstrates that SNHG1 upregulates FANCD2 and G6PD by sponging miR-199a-5p and miR-199a-3p, thereby inhibiting ferroptosis in HCC. Furthermore, a signature based on expression of SNHG1, FANCD2, and G6PD was identified as an independent prognostic marker for OS and associated with the proportion of infiltrating immune cell types, immune checkpoint expression, and response to immunotherapy. These findings are useful to further elucidate the pathogenesis of HCC and develop new strategies for clinical treatment and diagnosis.

Acknowledgements

The results published here are in part based upon data from The Cancer Genome Atlas (*https://portal.gdc.cancer.gov/*) and International Cancer Genome Consortium (*https://dcc.icgc.org*).

Funding: This work was supported by the National Natural Science Foundation of China (grant No. 82070155) and the Natural Science Foundation of Changsha (grant No. kq2202249).

Conflict of Interest: The authors have no conflicts of interest to disclose.

References

1. Sung H, Ferlay J, Siegel RL, Laversanne M, Soerjomataram I, Jemal A, Bray F. Global cancer statistics 2020: GLOBOCAN estimates of incidence and mortality worldwide for 36 cancers in 185 countries. CA Cancer J Clin. 2021; 71:209-249.
2. Rattanasupar A, Chartleeraha S, Akarapatima K, Chang A. Factors that affect the surveillance and late-stage detection of a newly diagnosed hepatocellular carcinoma. Asian Pac J Cancer Prev. 2021; 22:3293-3298.
3. Wang CY, Li S. Clinical characteristics and prognosis of 2887 patients with hepatocellular carcinoma: A single center 14 years experience from China. Medicine (Baltimore). 2019; 98:e14070.
4. Tang D, Kang R, Berghe TV, Vandenabeele P, Kroemer G. The molecular machinery of regulated cell death. Cell Research. 2019; 29:347-364.
5. Peng F, Liao M, Qin R, Zhu S, Peng C, Fu L, Chen Y, Han B. Regulated cell death (RCD) in cancer: Key pathways and targeted therapies. Signal Transduct Target Ther. 2022; 7:286.
6. Tsvetkov P, Coy S, Petrova B, *et al*. Copper induces cell death by targeting lipoylated TCA cycle proteins. Science. 2022; 375:1254-1261.
7. Dixon SJ, Lemberg KM, Lamprecht MR, Skouta R, Zaitsev EM, Gleason CE, Patel DN, Bauer AJ, Cantley AM, Yang WS, Morrison B 3rd, Stockwell BR. Ferroptosis: An iron-dependent form of nonapoptotic cell death. Cell. 2012; 149:1060-1072.
8. Wang W, Pan F, Lin X, Yuan J, Tao C, Wang R. Ferroptosis-related hub genes in hepatocellular carcinoma: Prognostic signature, immune-related, and drug resistance analysis. Front Genet. 2022; 13:907331.
9. Zhang B, Bao W, Zhang S, Chen B, Zhou X, Zhao J, Shi Z, Zhang T, Chen Z, Wang L, Zheng X, Chen G, Wang Y. LncRNA HEPFAL accelerates ferroptosis in hepatocellular carcinoma by regulating SLC7A11 ubiquitination. Cell Death Dis. 2022; 13:734.
10. Thin KZ, Tu JC, Raveendran S. Long non-coding SNHG1 in cancer. Clin Chim Acta. 2019; 494:38-47.
11. Zhou L, Zhang Q, Deng H, Ou S, Liang T, Zhou J. The SNHG1-centered ceRNA network regulates cell cycle and is a potential prognostic biomarker for hepatocellular carcinoma. Tohoku J Exp Med. 2022; 258:265-276.
12. Gong L, Huang D, Shi Y, Liang Z, Bu H. Regulated cell death in cancer: From pathogenesis to treatment. Chin Med J (Engl). 2023; 136:653-665.
13. Newman AM, Liu CL, Green MR, Gentles AJ, Feng W, Xu Y, Hoang CD, Diehn M, Alizadeh AA. Robust enumeration of cell subsets from tissue expression profiles. Nat Methods. 2015; 12:453-457.
14. Jiang P, Gu S, Pan D, *et al*. Signatures of T cell dysfunction and exclusion predict cancer immunotherapy response. Nat Med. 2018; 24:1550-1558.
15. Mariathasan S, Turley SJ, Nickles D, *et al.* TGFbeta attenuates tumour response to PD-L1 blockade by contributing to exclusion of T cells. Nature. 2018; 554:544-548.
16. Salmena L, Poliseno L, Tay Y, Kats L, Pandolfi Pier P. A ceRNA hypothesis: The rosetta stone of a hidden RNA language? Cell. 2011; 146:353-358.
17. Song X, Xie Y, Kang R, Hou W, Sun X, Epperly MW, Greenberger JS, Tang D. FANCD2 protects against bone marrow injury from ferroptosis. Biochem Biophys Res Commun. 2016; 480:443-449.
18. Cao F, Luo A, Yang C. G6PD inhibits ferroptosis in hepatocellular carcinoma by targeting cytochrome P450 oxidoreductase. Cell Signal. 2021; 87:110098.
19. Wu J, Wang Y, Jiang R, Xue R, Yin X, Wu M, Meng Q. Ferroptosis in liver disease: New insights into disease mechanisms. Cell Death Discov. 2021; 7:276.
20. Liu W, Zheng L, Zhang R, Hou P, Wang J, Wu L, Li J. Circ-ZEB1 promotes PIK3CA expression by silencing miR-199a-3p and affects the proliferation and apoptosis of hepatocellular carcinoma. Mol Cancer. 2022; 21:72.
21. Liu P, Xia P, Fu Q, Liu C, Luo Q, Cheng L, Yu P, Qin T, Zhang H. miR-199a-5p inhibits the proliferation of hepatocellular carcinoma cells by regulating CDC25A to induce cell cycle arrest. Biochem Biophys Res Commun. 2021; 571:96-103.
22. Li Z, Zhou Y, Zhang L, Jia K, Wang S, Wang M, Li N, Yu Y, Cao X, Hou J. microRNA-199a-3p inhibits hepatic apoptosis and hepatocarcinogenesis by targeting PDCD4. Oncogenesis. 2020; 9:95.

23. Li L, Wang H, Zhang J, Chen X, Zhang Z, Li Q. Effect of endothelial progenitor cell-derived extracellular vesicles on endothelial cell ferroptosis and atherosclerotic vascular endothelial injury. Cell Death Discovery. 2021; 7:235.
24. Zhang GY, Gao Y, Guo XY, Wang GH, Guo CX. MiR-199a-5p promotes ferroptosis-induced cardiomyocyte death responding to oxygen-glucose deprivation/reperfusion injury *via* inhibiting Akt/eNOS signaling pathway. The Kaohsiung J Med Sci. 2022; 38:1093-1102.
25. Brissot P, Ropert M, Le Lan C, Loreal O. Non-transferrin bound iron: A key role in iron overload and iron toxicity. Biochim Biophys Acta. 2012; 1820:403-410.
26. Casini A, Leone S, Vaccaro R, Vivacqua G, Ceci L, Pannarale L, Franchitto A, Onori P, Gaudio E, Mancinelli R. The emerging role of ferroptosis in liver cancers. Life (Basel). 2022; 12:2128.
27. Huang Y, Wang S, Ke A, Guo K. Ferroptosis and its interaction with tumor immune microenvironment in liver cancer. Biochim Biophys Acta Rev Cancer. 2022; 1878:188848.

Received June 1, 2023; Revised August 3, 2023; Accepted August 12, 2023.

[§]These authors contributed equally to this work.
**Address correspondence to:*
Chang Zhou, or Jianlin Zhou, College of Life Science, Hunan Normal University, 36 Lushan Road, Changsha, 410081, Hunan, China.
E-mail: zhouc@hunnu.edu.cn (Zhou C), jlzhou@hunnu.edu.cn (Zhou J)

Released online in J-STAGE as advance publication August 19, 2023.

Original Article

DOI: 10.5582/ddt.2023.01016

Effect of Chinese patent medicine Kunling Pill on endometrial receptivity: A clinical trial, network pharmacology, and animal-based study

Xinyao Pan[1,2,3,§], Qi Qing[1,2,3,§], Jing Zhou[1,2,3], Hongmei Sun[1,2,3], Lisha Li[1,2,3], Wenli Cao[4], Feijun Ye[4], Jun Zhu[5], Yan Sun[1,2,3,*], Ling Wang[1,2,3,*]

[1] Laboratory for Reproductive Immunology, Obstetrics and Gynecology Hospital of Fudan University, Shanghai, China;
[2] The Academy of Integrative Medicine of Fudan University, Shanghai, China;
[3] Shanghai Key Laboratory of Female Reproductive Endocrine-related Diseases, Shanghai, China;
[4] Reproductive Medicine Center, Zhoushan Maternal and Child Health Care Hospital, Zhoushan, Zhejiang, China;
[5] Department of Obstetrics and Gynecology, Wenling People's Hospital, Wenzhou Medical University, Wenling, Zhejiang, China.

SUMMARY Although pregnancy success rates are raised with assisted reproductive technology, it still cannot meet clinical demands. Kunling Pill (KLP), a traditional Chinese medicine, is widely used in various gynecological disorders, particularly in improving fertility and pregnancy rates. However, the underlying mechanism of how KLP affects pregnancy outcomes remains unclear. This study aimed to explore the effects and mechanisms of KLP on endometrial receptivity. Firstly, a retrospective trial was conducted to validate the efficacy of KLP on repeated implantation failure (RIF) patients. The result indicated a significant increase in the proportion of live birth in KLP group (30.56%) compared to the control group (16.89%). Secondly, network pharmacology methods predicted the active components and network targets of KLP. Endometrial receptivity is closely associated with the activation of inflammatory factors, predicting the function of KLP on the immune system. The estrogen and apoptotic signaling pathways were also highlighted in the gene ontology enrichment analysis. Thirdly, a decreased endometrial receptivity model was established by controlled ovarian hyperstimulation (COH) in female C57BL/6 mice, divided into the COH and KLP groups. Normal female mice are as control group. *In vivo*, KLP administration could increase endometrial thickness and the number of endometrial glands and pinopodes. In the endometrium, KLP supplementation upregulated the expressions of estrogen receptor α, progesterone receptor, endothelial nitric oxide synthase, and integrin αVβ3 in the murine uterus and reduced serum levels of estrogen and progesterone. KLP regulated the uterine immune cells and inhibited cell apoptosis in the ovary *via* Bcl-2/Bax/caspase-3 pathway. In conclusion, KLP administration raised the live birth rate in RIF patients to optimize medication regimens, mainly because KLP ameliorated impaired endometrial receptivity.

Keywords Kunling Pill, endometrial receptivity, implantation, apoptosis

1. Introduction

The success of *in vitro* fertilization (IVF) has increased dramatically (*1*); however, failures have become inadmissible for both providers and patients. Growing evidence highlights the importance of receptive endometrium in IVF and impaired endometrial receptivity is one of the key factors in low pregnancy rates and repeated implantation failure (RIF) (*2-4*). Moreover, as controlled ovarian hyperstimulation (COH) is commonly used in assisted reproductive technology (ART) nowadays, the adverse impact of COH on endometrial receptivity has become a major issue for patients. Small and undifferentiated endometrial glands were found in patients undergoing minimal stimulation with clomiphene citrate (*5*). Thus, the management of endometrial receptivity is a difficult and critical issue.

Receptive endometrium depends on the endocrine milieu, maternal immune system, hematologic factors, anatomic factors, *etc.* (*6*). Firstly, the proliferation and differentiation of the endometrium are regulated by steroid hormones, such as estrogen and progesterone, which are produced mainly by ovaries. Sex steroids act *via* their receptors to initiate the specific genes

and mediators' expression in the endometrium at the molecular level. Supraphysiologic estrogenic milieu during COH could result in desynchrony in the development of different cells and aberrations in the transcriptome of the endometrium, finally impairing endometrial receptivity (*7-8*). Secondly, there is a large amount of immune cell infiltration in the human endometrium at the window of implantation (WOI), including macrophages, T cells, and natural killer cells (*9*). Single-cell RNA sequencing confirms that endometrial immune profile disorders are associated with RIF at WOI (*3*), providing a deeper insight into the endometrial microenvironment disorder of RIF. Successful embryonic implantation requires a normal microenvironment. Integrin αVβ3 and endothelial nitric oxide synthase (eNOS) are of vital predictive values for endometrial receptivity in women with unexplained infertility, correlating to implantation failure (*10-11*). Although research has focused on improving endometrial receptivity, further research is needed to improve pregnancy outcomes for subfertile couples (*1,12*).

Traditional Chinese medicine (TCM) prescriptions have been widely accepted, and research has focused on their applications and mechanisms for treating infertility and gynecopathy in recent years in China (*13-15*). Kunling Pill (KLP), a Chinese patent medicine, is available to treat women with infertility and recurrent spontaneous abortion. KLP is composed of 31 kinds of Chinese herbs, and a total of 169 active ingredients were identified (*16*). KLP can help promote angiogenesis, regulate the balance of serum hormones, improve oocyte quality and diminished ovary reserve, and enhance endometrial receptivity (*16-18*). However, the underlying mechanism of how KLP affects RIF patients remains unclear.

This study was performed to determine the effect and possible mechanism of KLP on RIF. The effect of KLP on RIF patients was analyzed based on a retrospective study. Next, network pharmacology and a COH animal model were conducted to determine its possible mechanisms.

2. Materials and Methods

2.1. A clinical trial

2.1.1. Population

A retrospective study was carried out to evaluate the effect of KLP on patients with RIF at the Obstetrics and Gynecology Hospital of Fudan University between January 2021 and October 2022. The study received approval from the hospital's Ethics Committee (No. 2021-154-X1) and was conducted according to the Declaration of Helsinki 2002. The flowchart indicates the recruitment of patients (Figure 1).

RIF patients were selected following inclusion criteria: 1) at least three previous failures of IVF-ET therapy; 2) age 20 - 40 years old; 3) regular menstrual cycle; 4) negative autoimmune antibodies; 5) hysteroscopy or hysterosalpingogram indicating patency of at least one fallopian tube and normal cavity

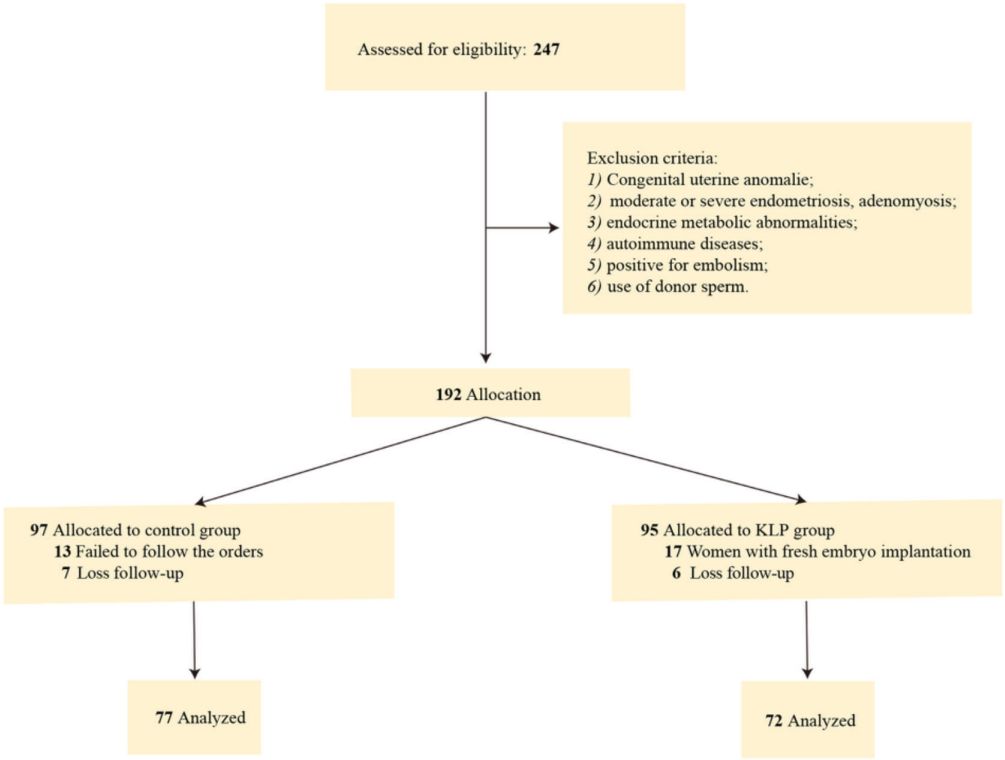

Figure 1. Flowchart of patients included in this study

morphology; 6) normal semen quality of male partner; 7) normal chromosomal karyotype of the couple; 8) voluntary participation in the study, willingness to take medication and follow up according to the treatment protocol. The exclusion criteria were: 1) congenital uterine anomalies; 2) moderate or severe endometriosis, adenomyosis; 3) endocrine metabolic abnormalities, such as polycystic ovary syndrome, diabetes mellitus, insulin resistance and hypothyroidism; 4) autoimmune diseases such as systemic lupus erythematosus, antiphospholipid syndrome, dry syndrome and scleroderma; 5) positive for embolism; 6) use of donor sperm.

2.1.2. Design and treatment

Patients were randomized into the control and KLP groups for embryo transfer in IVF cycles. For the control group, once the ovulation was confirmed by ultrasound and serum progesterone was examined, patients were given a trimodality therapy including estradiol valerate (DELPHARM Lille S.A.S., Lille, Lys-Lez-Lannoy Cedex, France) 1 mg bid po + progesterone injection (Zhejiang Xianju Pharmaceutical Co., Ltd., Xianju, Zhejiang, China) 60 mg qd im + dydrogesterone (Abbott Biologicals B.V., Veerweg, Zuid-Holland, Netherlands) 10 mg tid po. For the KLP group, patients were given KLP (Tasly Pharmaceutical Co., Ltd., Tianjin, China) 15 pills bid po from day 2 or day 3 of the menstrual cycle. Once the ovulation was confirmed, the following procedure was the same as the control group except for KLP supplementation. The embryo transfer of the two groups was conducted on day 4 of the trimodality therapy; KLP was stopped on the day before embryo transfer.

2.1.3. Outcome

The primary outcome measure of live birth was defined as the delivery of newborns ≥ 20 weeks of gestation. Positive pregnancy test (positive for urine human chorionic gonadotrophin (hCG) test), clinical pregnancy (presence of gestational sac on ultrasound at 6 weeks of gestation), and ongoing pregnancy (heartbeat activity confirmed by ultrasound at 8 weeks of gestation) were considered as secondary outcomes.

2.2. Network pharmacology

2.2.1. Selection of active ingredients by pharmacokinetic absorption, distribution, metabolism, and excretion prediction

Relevant components contained in KLP were collected on the Traditional Chinese Medicine Systems Pharmacology Database and Analysis Platform (TCMSP) (*https://tcmsp-e.com/*). We introduced drug likeness (DL) ≥ 0.18 and oral bioavailability (OB) ≥ 30% as screening conditions to collect the relevant compound components for preliminary screening. The potential targets of different compounds were further obtained and collated in the TCMSP database.

The UniProt database (*https://www.uniprot.org/*) was searched to obtain the validated human protein targets using "Homo sapiens" and "Reviewed" as screening criteria. Gene targets of each compound in the TCMSP database were matched with protein targets in the UniProt database to obtain the target information. The compound-target relationship network was analyzed by Cytoscape 3.8.2 (*http://cytoscape.org/*).

2.2.2. Target prediction and protein-protein interaction (PPI) network

"Endometrial receptivity" related disease targets were collected from GeneCards (*https://www.genecards.org/*) database. The intersection between KLP and endometrial receptivity targets was further imported into the String database (*http://string-db.org/*). Screening conditions of "Homo sapiens" and "confidence level > 0.4" were used to construct the PPI network. Cytoscape software was applied for re-editing the network in a color-based mode. The core 20 target genes were screened by the cytohuba plugin of Cytoscape after that.

2.2.3. Functional enrichment analysis and biological network construction

The obtained top 20 target genes were enriched for gene ontology (GO) and kyoto encyclopedia of genes and genomes (KEGG) pathway analysis by the Metascape platform (*https://metascape.org/gp/index.html*). KEGG enrichment analysis was used to identify core signaling pathways in endometrial receptivity regulated by KLP. GO enrichment analysis includes molecular function (MF), cellular component (CC), and biological process (BP) analysis. The pathways were regarded to be significantly enriched when $p < 0.05$. The Hiplot platform (*https://hiplot.com.cn/*) and Oebiotech platform (*https://cloud.oebiotech.cn/task/*) were adopted to visualize GO and KEGG pathway analysis in this study.

2.3. Reagents

Pregnant mare serum gonadotropin (PMSG) and hCG were purchased from ProSpec Technogene (Ness-Ziona, Central District, Israel) for COH treatment. KLP was obtained from Tasly Pharmaceutical Co., Ltd. and was dissolved in saline. DNase I, collagenase type IV, and Chicago sky blue dye were bought from Sigma-Aldrich, Inc. (St. Louis, MO, USA). Estradiol (E2) (Senxiong Biotech, Shanghai, China) and progesterone (P) (BioVendor, Brno, Moravian, Czech Republic) enzyme-linked immunosorbent assay (ELISA) kit were used for serum hormone measurement. Tissue RNA Purification

Kit and Color Reverse Transcription Kit were purchased from EZBioscience (Roseville, MN, USA). Hieff qPCR SYBR Green Master Mix was bought from Yeasen (Shanghai, China). Antibodies of estrogen receptor α (ERα) (Santa Cruz Biotechnology, Dallas, Texas, USA), eNOS (Abcam, Cambridge, Cambridgeshire, UK), integrin αVβ3 (Novus Biologicals, Centennial, CO, USA), and progesterone receptor (PR) (Santa Cruz Biotechnology) were used for immunohistochemistry (IHC). Live/Dead Cell Stain Kit and RPMI 1640 were purchased from Thermo Fisher Scientific, Inc. (Waltham, MA, USA). BV605-conjugated anti-mouse CD3e or Gr1, PE-conjugated anti-mouse CD8, APC-conjugated anti-mouse CD62L or F4/80, APC-Cy7-conjugated anti-mouse CD45, FITC-conjugated anti-mouse CD4 or CD11b, PerCP-Cy5.5-conjugated anti-mouse CD44, PE-Cy5.5-conjugated anti-mouse CD3 antibodies, and Fc receptor blocker were purchased from Biolegend (San Diego, CA, USA), Thermo Fisher Scientific, or BD Pharmingen (San Diego, CA, USA).

2.4. Animals and treatments

8-week-old female and male C57BL/6 mice were purchased from the Laboratory Animal Facility of the Chinese Academy of Sciences (Shanghai, China). Mice were habituated to housing conditions for seven days on a 12 h light and dark cycle following the Chinese Council for Animal Care guidelines. The animal experiments were approved by the experimental animal ethics committee of Fudan University (No. 202210034S).

Mice were divided into three groups: control (Ctrl), COH, and KLP; n =15 for each group. In the KLP group, mice were intragastrically administered 0.91 g/kg body weight (BW) KLP daily from the day of oestrus (*18*). Mice in control and COH groups received equivalent volumes of saline. After seven days of gavage and before mating, mice in COH and KLP groups were first treated with 5 IU/mouse PMSG by intraperitoneal injection and were injected with 5 IU/mouse hCG 48 h later. Mice in the Ctrl group accepted an equivalent volume of saline injection. After the final injection, all female and male mice were mated at a ratio of 2:1 overnight. The next morning vaginal plugs were examined to indicate successful mating (day 0.5 of pregnancy, PD 0.5). Pregnant female mice were sacrificed on PD 4.5 for sample collection.

2.5. Analysis of embryo implantation

Chicago sky blue dye solution (0.1 g/kg-BW) was intravenously injected on PD 4.5 to visualize implantation sites. Mice were sacrificed 10 minutes later, and the intact uterus was separated to evaluate the blue and enclosed implantation sites within the uterine wall.

2.6. Histology and immunostaining

Ovarian and uterine tissues were fixed in 4% formaldehyde for 24 h and embedded in paraffin. Sections (4 μm thick) were deparaffinized, ehydrated, and stained with hematoxylin and eosin (H&E). For immunostaining, sections were brought to boil using a microwave for antigen retrieval and quenched using 3% hydrogen peroxide (H_2O_2). Specimens were blocked for 30 min and then incubated overnight at 4℃ with eNOS, ERα, PR, and integrin αVβ3 primary antibodies, respectively. The next day, samples were incubated with a biotinylated secondary antibody for 50 min after being rinsed in buffer and followed by 3,3'-diamino-benzidine staining. The slides were then photographed under a light microscope (Nikon Instruments, Inc., Shanghai, China). The quantitative analysis of eNOS, ERα, PR, and αVβ3 was determined using Image-Pro Plus 6.0 software (Media Cybernetics, Bethesda, MD, USA).

2.7. Scanning electron microscopy

Uterine samples were fixed in 2.5% glutaraldehyde and post-fixed with 1% osmium tetroxide. After several washes in the buffer, tissues were dehydrated and subjected to critical point drying (Quorum, Laughton, East Sussex, UK). The samples were then mounted on the specimen holder, sputter coated with palladium gold using an ion sputter coater (Hitachi, Tokyo, Japan). Endometrial pinopodes were finally visualized under a scanning electron microscope (Hitachi).

2.8. Measurement of hormone concentration

Blood samples were quickly collected by cardiac puncture after isoflurane anesthesia and solidified at room temperature. Serum was prepared to determine hormone concentration by centrifugation at 3,000 rpm for ten min. According to the manufacturer's protocol, serum E2 and P concentrations were examined using ELISA kits.

2.9. RT-qPCR

Total tissue RNA was isolated from pregnant mice using Tissue RNA Purification Kit following the manufacturer's instructions. Total RNA was used to synthesize cDNA using the Color Reverse Transcription Kit. Quantitative real-time PCR was performed with qPCR SYBR Green Master Mix on a QuantStudio 6-Flex (Applied Biosystems, Waltham, MA, USA). The relative gene expression was compared to β-actin and calculated using $2^{-\Delta\Delta Ct}$ methods. The primers were synthesized by Sangon (Shanghai, China), and the sequences are shown in Table S1 (*http://www.ddtjournal.com/action/getSupplementalData.php?ID=151*).

2.10. Flow cytometric profiling of immune cells

Mice uterine fragments were prepared for single-cell

suspensions followed by continuous digestion in RPMI 1640 containing collagenase type IV (Sigma-Aldrich, Inc.) and DNase I (Sigma-Aldrich, Inc.) at 37°C in a gentle shaker. Once the fragments were dissociated (30 min), the cell suspension samples were passed through a 70 μm filter mesh and then resuspended in phosphate buffer solution (PBS) to count for further procedure. Single-cell suspensions were stained for 30 min at room temperature in the dark using a Live/Dead Cell Stain Kit and blocked with anti-CD16/CD32 mAb. Then the cell suspensions were stained with PE-anti-CD8, PE-Cy5.5-anti-CD3, PerCP-Cy5.5-anti-CD44, BV605-anti-CD3e, BV605-anti-Gr1, FITC-anti-CD4, FITC-anti-CD11b, APC-anti-CD62L, APC-anti-F4/80, APC-Cy7-anti-CD45. Flow cytometry was performed on CytoFLEX (Beckman Coulter, Brea, CA, USA), and data were analyzed with FlowJo software (Tree Star, Ashland, OR, USA).

2.11. TUNEL staining

Apoptosis in ovarian sections was detected by TUNEL Cell Apoptosis Detection Kit (Servicebio, Wuhan, Hubei, China). Paraffin sections were deparaffinized with xylene and rehydrated in graded alcohol series. The samples were washed in PBS and incubated with prepared Proteinase K working solution for 30 min at 37℃. After being quenched with 3% H_2O_2 for 20 min to inactivate the endogenous peroxidases, the samples were incubated with 50 μL Equilibration Buffer for 10 min and 56 μL TdT buffer at 37°C for 1 h, respectively. The slides were then rinsed with PBS and incubated with Streptavidin–HRP conjugate at 37°C for 30 min. Finally, samples were stained with diaminobenzidine and counterstained with hematoxylin. The slides were finally photographed and analyzed using Image-Pro Plus 6.0 software (Media Cybernetics).

2.12. Statistical analysis

Continuous variables were presented as mean ± standard deviation (SD), and the differences were compared by *t*-test or one-way ANOVA if normally distributed. Data that did not conform to normality were subjected to the Mann-Whitney or Kruskal-Wallis test. All the above analyses were two-sided, and a p value < 0.05 was considered statistically significant. All statistical analyses were conducted using GraphPad software (San Diego, CA, USA).

3. Results

3.1. KLP improved the pregnancy outcomes of RIF patients

A total of 247 patients were included, of whom 192 met the eligibility criteria, and 149 completed the follow-up. The demographic baseline characteristics of these individuals are presented in Table 1. Baseline characteristics of the Ctrl and KLP groups included age, body mass index (BMI), and the number of embryos previously transferred. No difference in baseline characteristics was found between the two groups. Both positive pregnancy test rates and clinical pregnancies had been improved in the KLP group versus the Ctrl group. We noted that all patients who achieved ongoing pregnancies resulted in live births. The KLP group showed ~2-fold higher ongoing pregnancy and live birth rates compared to the Ctrl group (Table 2).

3.2. Targets prediction and components identification of KLP

We use TCMSP to analyze the components of KLP. Two hundred and seventy-three active ingredients were predicted with the standard DL ≥ 0.18 and OB ≥ 30% in KLP. The most common active ingredients include β-sitosterol (in 14 herbs), stigmasterol (in 11 herbs), quercetin (in 10 herbs), and kaempferol (in 6 herbs). All the active ingredients were further screened for the corresponding targets in the TCMSP database and matched with 295 targets of the UniProt database. The target genes associated with the active compounds in KLP were analyzed by Cytoscape software. The compound-target network of KLP contains 273 compounds and 295 targets.

3.3. Network target analysis of KLP on endometrial receptivity

Based on the GeneCards and OMIM databases, 339 out of 678 target genes related to endometrial receptivity were collected and screened. Matching the 295 candidate targets of KLP on endometrial receptivity, 68 overlapping genes were considered hub targets in the drug-disease network. To further reveal the protein-protein interaction

Table 1. Descriptive baseline characteristics of patients with RIF

	Control group (n = 77)	KLP group (n = 72)
Age (years old)	33.4 ± 3.8	32.2 ± 4.2
BMI (kg/m^2)	21.2 ± 3.1	22.0 ± 2.7
No. of embryos previously transferred	4.3 ± 2.8	4.7 ± 3.1

KLP: Kunling Pill; BMI; body mass index.

Table 2. Pregnancy outcomes of patients

	Control group	KLP group
Positive pregnancy test rate (%)	25/77 (32.47)	29/72 (40.28)
Clinical pregnancy rate (%)	21/77 (27.27)	26/72 (36.11)
Ongoing pregnancy rate (%)	13/77 (16.89)	22/72 (30.56)*
Live birth rate (%)	13/77 (16.89)	22/72 (30.56)*

KLP: Kunling Pill. *p < 0.05.

relationship of these targets, the PPI network, which contains 68 nodes and 1150 edges, was constructed by the STRING database and re-edited by Cytoscape software (Figure 2A). The top 20 target genes including TP53, ESR1, EGFR, MAPK3, AKT1, TNF, STAT3, CTNNB1, IL6, HIF1A, MYC, FOS, PTGS2, MMP9, CCND1, IL1B, HSP90AA1, PTEN, CXCL8 and IL10 were screened using the cytohuba plug-in (Figure 2B, Table 3).

3.4. KEGG and GO enrichment analysis

Sixty-eight target genes were performed to explore the possible pathways of KLP in improving endometrial receptivity *via* the KEGG pathway and GO enrichment analysis. A total of 1445 significant GO terms were obtained. We found that the BP enrichment results were mainly related to gland development, response to the hormone or growth factor, regulation of apoptotic signaling pathway, cytokine production, and inflammatory response. MF processes were related to signaling receptor regulator activity, nitric-oxide synthase regulator activity, nuclear steroid receptor activity, integrin binding, hormone activity, *etc.* (Figure 3A). A total of 170 signaling pathways in KEGG enrichment analysis were screened out. The most significantly enriched pathways were presented in Figure 3B. The top-ranked pathways involved the estrogen signaling pathway, apoptosis, chemokine signaling pathway, progesterone-mediated oocyte maturation, cytokine-cytokine receptor interaction, p53 signaling pathway, ovarian steroidogenesis, *etc*.

3.5. Effect of KLP on PD4.5 murine embryo implantation and endometrium

Firstly, we observed embryo implantation in COH murine model after KLP treatment. As shown in Figure 4A, the implantation sites at PD4.5 can be scored visually by Chicago sky blue dye. COH model resulted in impaired implantation compared to the Ctrl group. In contrast, the KLP group ameliorated the compromised endometrial receptivity by increasing the counting of implantation sites to complete recovery (Figure 4B, $p < 0.001$). Murine endometrial morphology was then observed by optical microscope and scanning electron microscope. H&E staining showed that the uterine endometrium of the COH mice was thinner than control ones (Figures 4C-4D), with decreased endometrial glands and compact stroma (Figures 4E-4F). The orally given KLP thickened the endometrium and increased the endometrial glands of COH mice. The glandular lumen enlarged and contained secretory material. Vacuoles, which served as the dissolved ground substance of the glycogen particles, began to progress toward the glandular lumen. Meanwhile, the endometrial stroma became loose and edematous in KLP treated group. Pinopode formation at the top of the endometrial epithelium is well documented as a marker of endometrial receptivity. Compared to the Ctrl group, the absence of pinopodes in the COH group indicated damage to endometrial receptivity

Table 3. Top 20 target genes of KLP

Rank	Gene	Protein name	Score
1	*TP53*	Cellular tumor antigen p53	60
2	*EGFR*	Epidermal growth factor receptor	59
3	*ESR1*	Estrogen receptor	58
4	*MAPK3*	Mitogen-activated protein kinase 3	56
4	*TNF*	Tumor necrosis factor	56
4	*AKT1*	RAC-alpha serine/threonine-protein kinase	56
7	*CTNNB1*	Catenin beta-1	55
8	*HIF1A*	Hypoxia-inducible factor 1-alpha	54
8	*IL6*	Interleukin-6	54
8	*STAT3*	Signal transducer and activator of transcription 3	54
11	*FOS*	Proto-oncogene c-Fos	51
11	*MYC*	Myc proto-oncogene protein	51
11	*MMP9*	Matrix metalloproteinase-9	51
11	*PTGS2*	Prostaglandin G/H synthase 2	51
15	*CCND1*	G1/S-specific cyclin-D1	49
15	*IL1B*	Interleukin-1 beta	49
17	*PTEN*	Phosphatidylinositol-3,4,5-trisphosphate 3-phosphatase and dual-specificity protein phosphatase PTEN	48
18	*HSP90AA1*	Heat shock protein HSP 90-alpha	45
19	*CXCL8*	Interleukin-8	44
20	*RELA*	Transcription factor p65	42

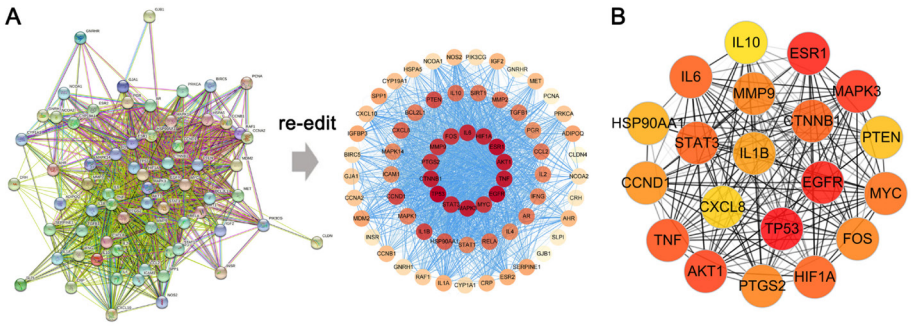

Figure 2. Identification of KLP's components and targets on endometrial receptivity. (A) PPI network showed the protein relationship between KLP and endometrial receptivity. The network was re-edited by Cytoscape. The node's color is marked from red to yellow according to the degree value in descending order. **(B)** Cytoscape showed the top 20 target genes. The higher the degree value, the deeper the color.

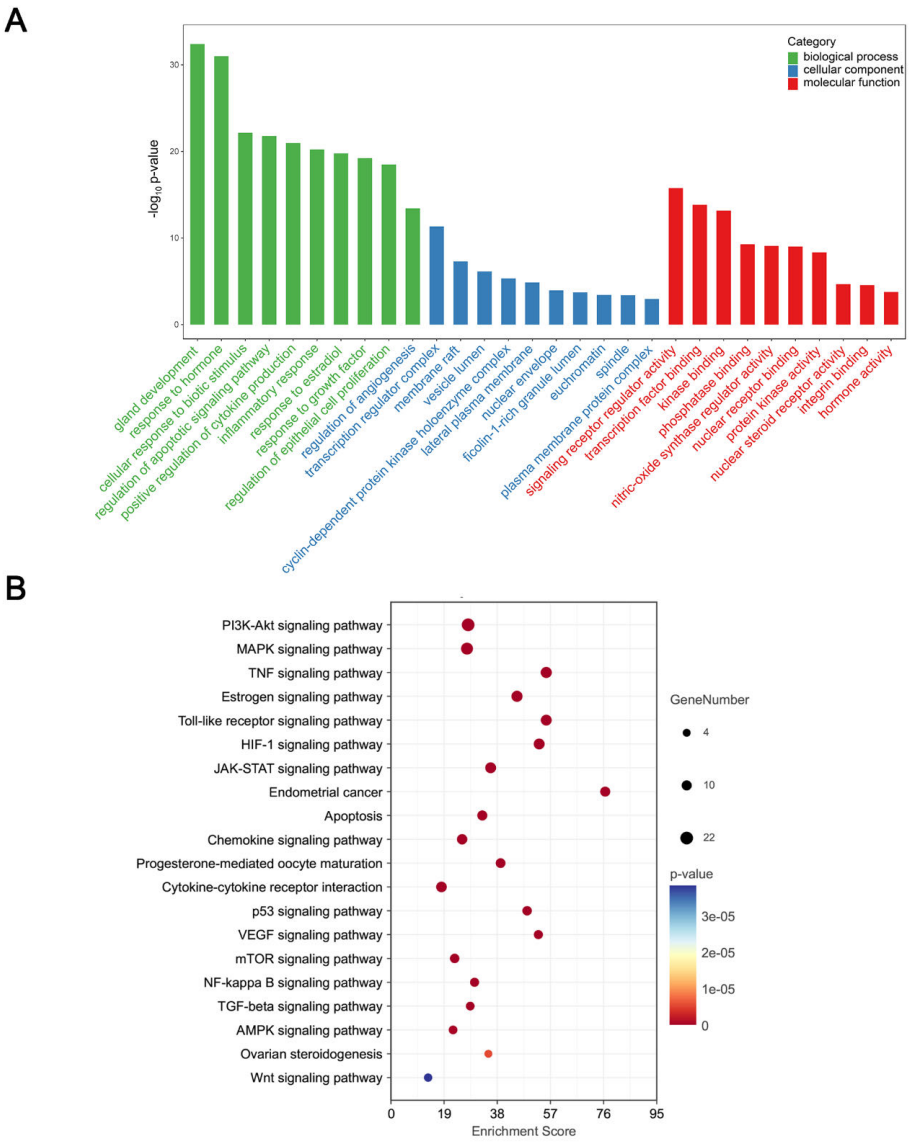

Figure 3. Enrichment analysis of KLP on endometrial receptivity. (A) The biological process, cellular component, and molecular function of GO analysis were shown. **(B)** KEGG pathway analysis showed the top 20 enrichment pathways.

caused by the intervention of COH (Figure 4G). After KLP treatment, pinopode morphology and coverage were significantly improved, consistent with increased quantities (Figure 4H, $p < 0.001$).

3.6. Effect of KLP on mice estrogen and progesterone activity

The serum hormone of estrogen was compared among different groups in PD4.5 mice. COH evokes supra-physiological serum levels of E2 and P, while KLP significantly attenuated their levels (Figures 5A-5B). The hormone receptors were further analyzed to explore changes in hormone signaling activation. Compared to the Ctrl group, RT-qPCR results suggested that *Erα* and *Pr* mRNA expression in the uterus was significantly downregulated in the COH mice (Figures 5C-5D), while KLP reversed it. A similar pattern was seen in protein level confirmed by IHC as KLP significantly repaired the decreased expression of ERα induced by COH intervention (Figures 5E-5F). We also examined progesterone activity as it collaborates with estrogen in successful implantation during WOI. IHC revealed that COH resulted in a significant drop in PR level, and KLP slightly elevated it (Figures 5G-5H).

3.7. Effect of KLP on endometrial receptivity and angiogenic activity in COH mice

Angiogenesis plays a crucial role in embryo implantation. We examined eNOS expression and found that eNOS was downregulated in the COH group and upregulated in the KLP group significantly, which suggests a potential target for KLP in angiogenesis (Figures 6A-6B). Integrin αVβ3 is a commonly used marker in assessing endometrial receptivity. We found that COH intervention

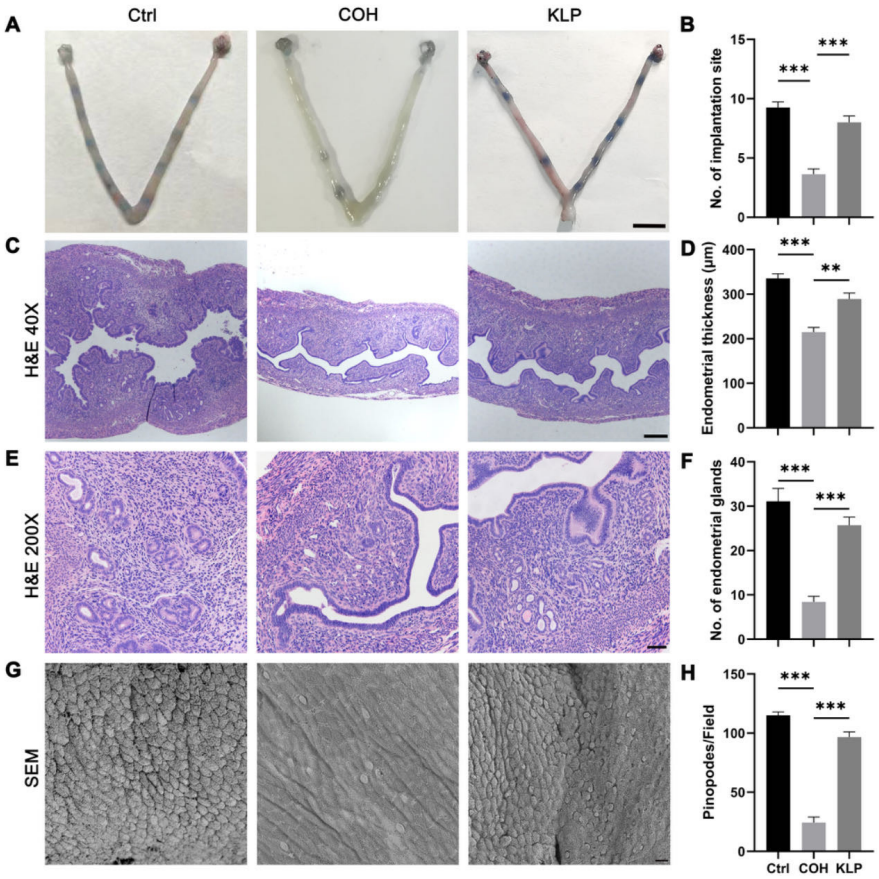

Figure 4. KLP treatment improved the successful implantation and endometrial development on PD 4.5 in COH mice. (A) Representative uteri with implantation sites determined by Chicago sky blue (blue bands) at PD 4.5. **(B)** The mean number of implantation sites on PD 4.5 in individual groups. **(C)** Representative H&E staining showed changes in murine endometrial thickness (40 ×). **(D)** The average endometrial thickness in each group. **(E)** Representative H&E staining showed changes in the morphology of uterine glands and stroma (200×). **(F)** The average number of uterine glands in each group. **(G)** The endometrial pinopode was observed using SEM (1000 ×). **(H)** Quantitation of pinopodes per field. Data are presented as the mean ± SEM. $^{**}p < 0.01$, $^{***}p < 0.001$. Scale bar, **(A)** 5 mm, **(C)** 200 μm, **(E)** 50 μm, and **(G)** 50 μm.

downregulated its expression, and KLP reversed it significantly (Figures 6C-6D), which indicates that KLP may improve endometrial receptivity by regulating the expression of integrin αVβ3.

3.8. Effect of KLP on immune cell populations of the murine uterus

To determine the cellular distribution and differentiation of uterine immune cells after KLP administration on COH mice, flow analysis of single cells in uterine tissue identified the proportion of T cells, myeloid cells of neutrophils, and macrophages in three groups. The ratio of $CD4^+/CD8^+$ T cells demonstrated a significant drop by COH intervention and a partial rise by KLP treatment (Figures 7A-7B). T cell activation status was further assessed using the classic CD44 and CD62L markers. Around 51% of cells in the Ctrl group had a $CD44^+CD62L^-$ effector phenotype. We found a 61% higher count of $CD44^+CD62L^-$ T cells after the COH process, with a drop to 52% by KLP supplementation (Figures 7C-7D). The proportion of uterine myeloid cells was also analyzed. Compared to the Ctrl group, $CD11b^+Gr1^+$ neutrophils increased in the COH group, and KLP supplementation could lower the proportion significantly (Figures 7E-7F). The functions of macrophages are crucial for establishing and maintaining pregnancy. The flow cytometry implicated a significant rise in $CD11b^+F4/80^+$ macrophage induced by COH, and KLP decreased the frequency (Figures 7G-7H).

3.9. Effect of KLP on ovarian cell apoptosis

Given that KLP could regulate serum E2 and P levels, we speculated that KLP might affect ovarian function. The ovary morphology in three groups was first studied by H&E staining (Figure 8A). Compared to the Ctrl group, mice in the COH group had ovaries with poor follicles and reduced corpus luteum (Figure 8B). Treatment with KLP reversed this damage, as more follicles and less corpus luteum were observed (Figure 8B). Moreover, TUNEL staining distinguished the apoptotic granulosa cells (Figure 8C). The mean density of apoptotic cells rose significantly in the COH group compared to the Ctrl group (Figure 8D). Treatment with KLP could significantly recover the apoptosis induced by COH in

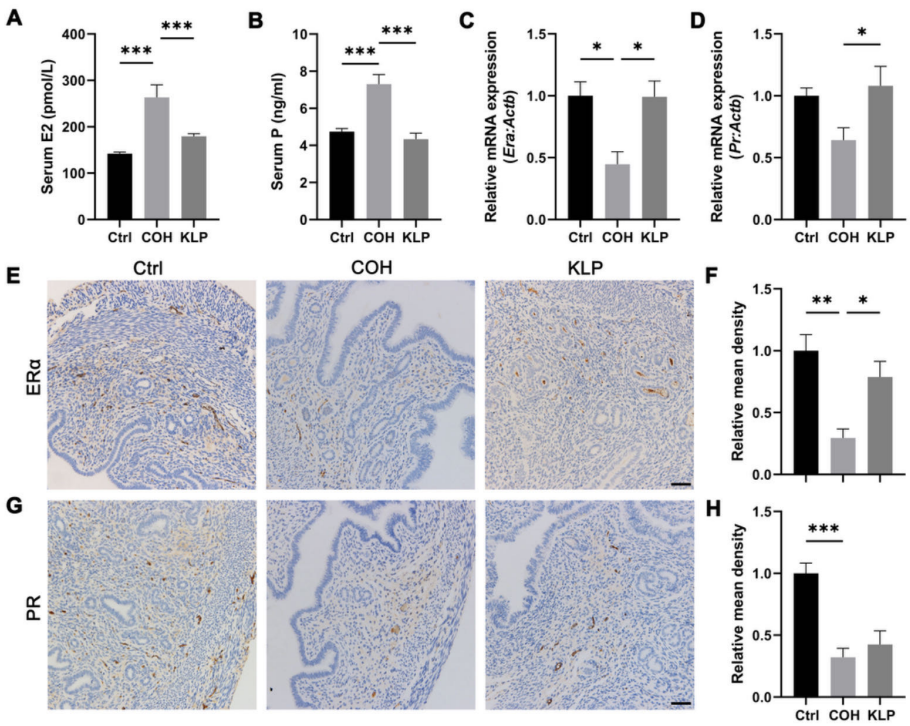

Figure 5. KLP treatment altered ovarian hormone activity impaired by COH. (A-B) ELISA determined serum levels of **(A)** estrogen and **(B)** progesterone. **(C-D)** mRNA expression of hormone receptor **(C)** *Erα* and **(D)** *Pr* in murine uterus. **(E-F)** Representative IHC staining pattern and quantitative analysis of ERα in murine uterus. **(G-H)** Representative IHC staining pattern and quantitative analysis of PR in murine uterus. Data are presented as the mean ± SEM. **p* < 0.05, ***p* < 0.01, ****p* < 0.001. Scale bar, 50 μm.

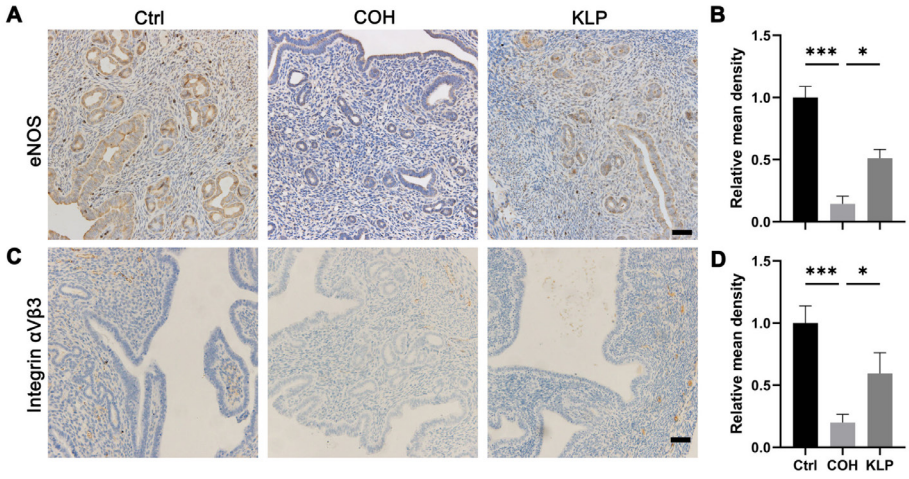

Figure 6. KLP ameliorated endometrial receptivity and angiogenic activity in COH mice. (A) Representative IHC staining of eNOS in the murine uterus from each group. **(B)** The expression of eNOS was quantified as relative mean density. **(C-D)** Representative IHC images and quantification of integrin αVβ3 in the murine uterus from each group. Data are presented as the mean ± SEM. **p* < 0.05, ****p* < 0.001. Scale bar, 50 μm.

the murine ovary. Thus, we further checked the related gene expression concerning apoptosis. mRNA expression of anti-apoptotic *Bcl-2* was downregulated in the COH model compared to the Ctrl group, and KLP significantly reversed the expression (Figure 8E). Mice in the model and Ctrl groups reached significant differences in apoptotic *Bax* and *Caspase 3* gene expression (Figures 8F-8G). After KLP administration, the expression of *Bax* and *Caspase 3* was significantly lower than that in the COH group (Figures 8F-8G), demonstrating the potential role of KLP in inhibiting apoptosis induced by COH intervention.

4. Discussion

In the present study, our results validated KLP as a

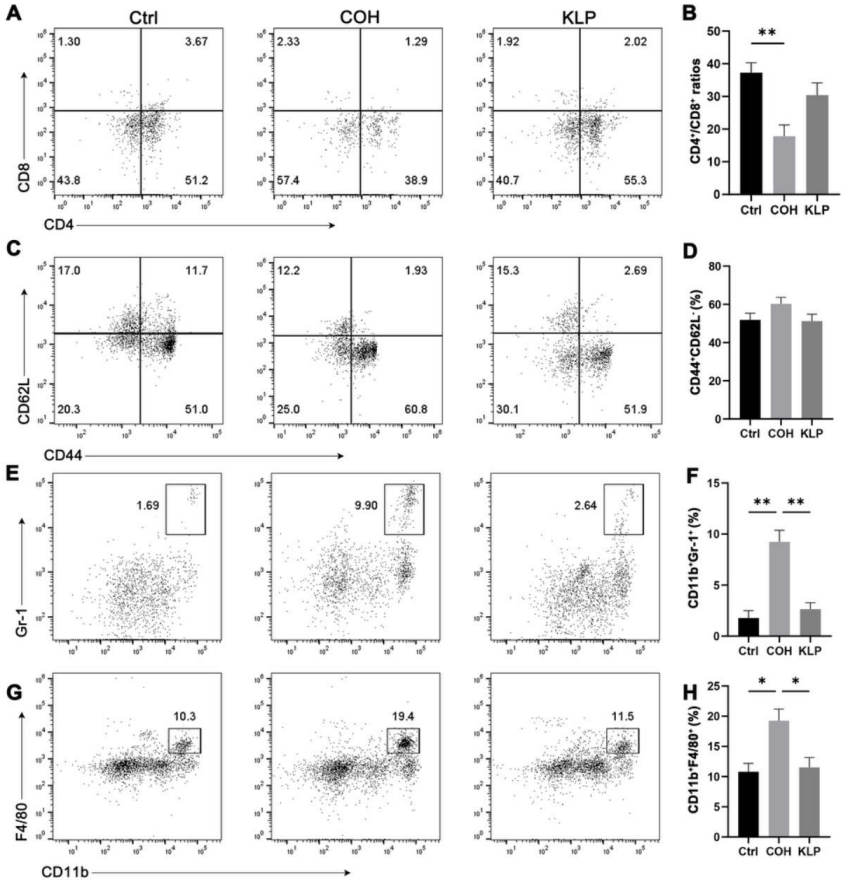

Figure 7. KLP affected uterine immune cell profiles of COH mice based on flow cytometry analysis. (A-B) The population of uterine $CD4^+$ T cell and $CD8^+$ T cell in mice. Data are plotted as $CD4^+/CD8^+$ ratio in T cells. **(C-D)** T cell activation status was detected using CD44 and CD62L markers. Data depict the percentages of $CD44^+CD62L^-$ T cells. The percentages of **(E-F)** neutrophil ($CD11b^+Gr\text{-}1^+$) and **G-H)** macrophage ($CD11b^+F4/80^+$) in the uterus. Data are presented as the mean ± SEM. *$p < 0.05$, **$p < 0.01$.

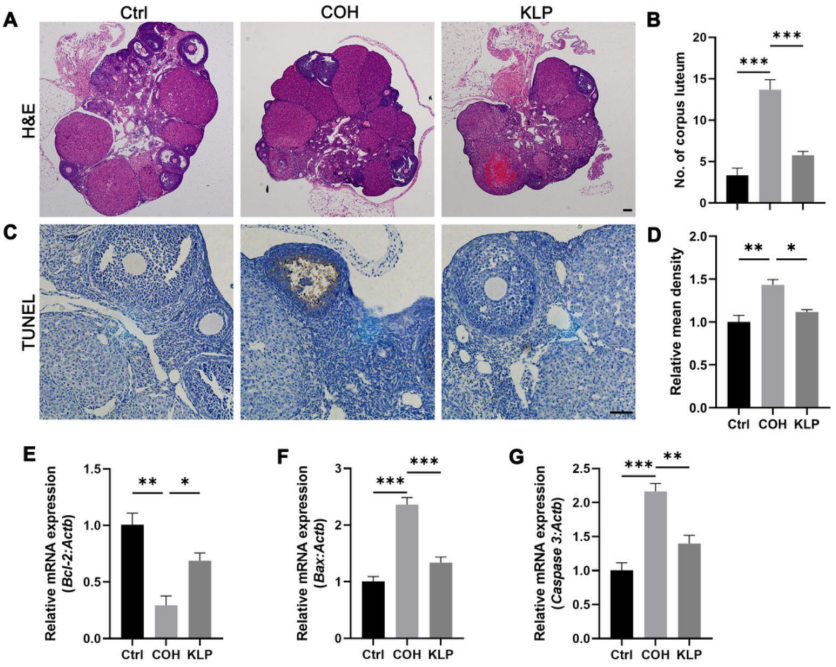

Figure 8. KLP inhibited ovarian apoptosis induced by COH. (A) Representative H&E staining showed ovarian morphology in each group. **(B)** The number of corpus luteum in the murine ovary was calculated. **(C)** Detection of apoptotic cells in the ovary by TUNEL staining. **(D)** TUNEL-positive cells were quantified as relative mean density. Expression of apoptosis-related genes **(E)** *Bcl-2,* **(F)** *Bax,* and **(G)** *Caspase 3* were examined by RT-qPCR. Data are presented as the mean ± SEM. *$p < 0.05$, **$p < 0.01$, ***$p < 0.001$. Scale bar, **(A)** 100 μm and **(C)** 50 μm.

beneficial assisting therapy for RIF firstly. Secondly, an integrated strategy was performed to explore and identify the components of KLP by integrating network pharmacology. Finally, we demonstrated that KLP improved impaired endometrial receptivity *via* Bcl-2/Bax/caspase-3 pathway in a COH model.

Successful pregnancy is a physiological process, which seems to be a silent "war" between the embryo and the mother (*2*). Approximately 12.7% of reproductive-age women seek infertility treatment each year, which is increasing yearly (*19*). Although success rates are raised with ART, it still cannot meet clinical demands. TCM, a complementary and alternative medical system, has been utilized widely in China. Given that KLP is a Chinese patent medicine for infertility, our clinical study in RIF patients indicated an increased pregnancy rate and live birth rate under a trimodality therapy with KLP application (30.56%), compared to the trimodality treatment (16.89%).

The composition of TCM is complex; all kinds of Chinese medicine often have some similar chemical components, so the search for the main effective components will help to analyze the key points of Chinese medicine in treating diseases and provide direction for the follow-up molecular mechanism. Network pharmacology, a biological system analysis approach, was utilized to uncover the relationship between multi-component medicines and the network target of diseases (*20-21*). The topological analysis found twenty key targets of KLP, including TP53, ESR1, EGFR, MAPK3, AKT1, TNF, STAT3, CTNNB1, IL6, HIF1A, MYC, FOS, PTGS2, MMP9, CCND1, IL1β, HSP90AA1, PTEN, CXCL8, and IL10. These 20 targets are closely related to endometrial receptivity. Studies have shown that endometrial receptivity is closely associated with inflammatory factors, such as IL6, IL1β, and CXCL8, predicting the function of KLP on the immune system. In GO enrichment analysis, the estrogen and apoptotic signaling pathways were highlighted. In brief, these results indicated a combination of mechanisms of KLP in suppressing inflammation, which was validated by flow cytometry analysis *in vivo*.

According to the research results of network pharmacology, we conducted an *in vivo* experiment at the animal level to verify the results from the bioinformatics analysis. KLP could ameliorate a pseudodecidual-like effect on murine uterine endometrium. Morphological changes carried out by KLP supplementation that coincident with the secretory phase reveal a receptive state of mice endometrium. Evaluation of sex steroids indicates that KLP may regulate endogenous hormones corresponding to the receptive endometrium. In our research, over secretion of E2 and P was induced by PMSG and hCG, which act as exogenous gonadotropin in COH mice. KLP helps in homeostasis by restoring hormones to normal levels.

There are two types of ER and PR in mice, ERα/β and PR-A/B. ERα and PR-A are the main receptors in the establishment of endometrial receptivity in knock-out mice (*22-24*). The maximal ERα and PR expression occurred in the menstrual cycle's mid-to-late proliferative phase (*25*). It was noted that elevated progesterone correlated with the under-expression of ERα in glandular epithelium (*26*). In our study, we detected a similar pattern where ERα decreased in COH mice, along with a high level of progesterone concentration. KLP supplementation raised the expression of endometrial ERα and PR, demonstrating the ameliorating effect of KLP on impaired endometrial receptivity through hormone receptors signals, consistent with the results of network pharmacology. In a normal pregnancy mice model, the expression of eNOS was found to be stood out on gestation day 5 and was higher in implantation sites compared to that inter-implantation sites (*27*). In idiopathic recurrent spontaneous miscarriage patients, eNOS down-regulation is associated with vascular dysfunction and impaired endometrial perfusion, possibly making the endometrium unreceptive (*28*). In cases of unexplained infertility, integrin αVβ3 is significantly lower in endometrium and has great predictive value for endometrial receptivity among biomarkers in the uterine fluid (*29-30*). *Cyperus Rotundus* L., one of the main components of KLP, enhances the adhesion of trophoblastic cells onto endometrial Ishikawa cells by upregulating leukemia inhibitory factor-dependent integrin αVβ3 expression (*31*). Our study showed that KLP could promote eNOS and integrin αVβ3 expression in mice endometrium, confirming the potential effect of KLP on ameliorating impaired endometrial receptivity.

GO enrichment analysis suggested that inflammatory response may be related to the efficacy of KLP. Since immune cells were involved in the inflammatory response during the peri-implantation period (*32*), flow cytometry was used to detect the proportion changes of uterine immune cells. A decrease in the ratio of $CD4^+$/$CD8^+$ T cells by COH intervention revealed a relative increase in cytotoxic $CD8^+$ T cells, which was partially reversed by KLP supplementation. Proportions of $CD11b^+Gr1^+$ neutrophils and $CD11b^+F4/80^+$ macrophage were significantly reduced in the KLP group implicating the immune regulation effect of KLP.

Apoptotic signaling pathways may play a role in the regulation of KLP, as indicated by KEGG and GO enrichment analysis. Therefore, we assessed the apoptosis of the murine ovary by TUNEL staining and qPCR. KLP ameliorated COH-induced ovarian apoptosis *via* upregulating *Bcl-2* expression and downregulating the expression of *Bax* and *Caspase 3*. High-level estrogen binds to phosphodiesterase 3A and induces apoptosis by blocking the endoplasmic reticulum-mediated translation of BCL-2 and other anti-apoptotic proteins (*33*). We speculated that KLP might partially exert its role through an anti-apoptotic action in COH mice by reducing the excessive hormone levels.

In conclusion, the present study demonstrated that KLP administration raised the live birth rate in RIF patients, improved the morphology of COH mice endometrium, and regulated the expression of endometrial receptivity biomarkers, serum hormones, and immune cells, which were due to that KLP ameliorated the impaired endometrial receptivity *via* Bcl-2/Bax/caspase-3 pathway.

Funding: This work was supported by grants from a project under the Scientific and Technological Innovation Action Plan of the Shanghai Natural Science Fund (grant No. 20ZR1409100 to L Wang), a project of the Chinese Association of Integration of Traditional and Western Medicine special foundation for Obstetrics and Gynecology-PuZheng Pharmaceutical Foundation (grant No. FCK-PZ-08 to L Wang), a project for hospital management of the Shanghai Hospital Association (grant No. X2021046 to L Wang), and a clinical trial project of the Special Foundation for Healthcare Research of the Shanghai Municipal Health Commission (grant No. 202150042 to L Wang).

Conflict of Interest: The authors have no conflicts of interest to disclose.

References

1. Tyler B, Walford H, Tamblyn J, Keay SD, Mavrelos D, Yasmin E, Al Wattar BH. Interventions to optimize embryo transfer in women undergoing assisted conception: A comprehensive systematic review and meta-analyses. Hum Reprod Update. 2022; 28:480-500.
2. Ashary N, Tiwari A, Modi D. Embryo implantation: War in times of love. Endocrinology. 2018; 159:1188-1198.
3. Lai ZZ, Wang Y, Zhou WJ, Liang Z, Shi JW, Yang HL, Xie F, Chen WD, Zhu R, Zhang C, Mei J, Zhao JY, Ye JF, Zhang T, Li MQ. Single-cell transcriptome profiling of the human endometrium of patients with recurrent implantation failure. Theranostics. 2022; 12:6527-6547.
4. Valdes CT, Schutt A, Simon C. Implantation failure of endometrial origin: It is not pathology, but our failure to synchronize the developing embryo with a receptive endometrium. Fertil Steril. 2017; 108:15-18.
5. Wu JL, Keller P, Kanchwala M, Xing C, Babayev SN, Carr BR, Bukulmez O, Word RA. Controlled ovarian stimulation protocols alter endometrial histomorphology and gene expression profiles. Reprod Sci. 2020; 27:895-904.
6. Franasiak JM, Alecsandru D, Forman EJ, Gemmell LC, Goldberg JM, Llarena N, Margolis C, Laven J, Schoenmakers S, Seli E. A review of the pathophysiology of recurrent implantation failure. Fertil Steril. 2021; 116:1436-1448.
7. Li R, Qiao J, Wang L, Li L, Zhen X, Liu P, Zheng X. MicroRNA array and microarray evaluation of endometrial receptivity in patients with high serum progesterone levels on the day of hCG administration. Reprod Biol Endocrinol. 2011; 9:29.
8. Horcajadas JA, Riesewijk A, Polman J, van Os R, Pellicer A, Mosselman S, Simón C. Effect of controlled ovarian hyperstimulation in IVF on endometrial gene expression profiles. Mol Hum Reprod. 2005; 11:195-205.
9. Robertson SA, Moldenhauer LM, Green ES, Care AS, Hull ML. Immune determinants of endometrial receptivity: A biological perspective. Fertil Steril. 2022; 117:1107-1120.
10. Wang L, Lv S, Mao W, Pei M, Yang X. Assessment of endometrial receptivity during implantation window in women with unexplained infertility. Gynecol Endocrinol. 2020; 36:917-921.
11. Shen M, Liu Y, Ma X, Zhu Q. Erbu Zhuyu decoction improves endometrial angiogenesis *via* uterine natural killer cells and the PI3K/Akt/eNOS pathway a mouse model of embryo implantation dysfunction. Am J Reprod Immunol. 2022; 89:e13634.
12. Holt-Kentwell A, Ghosh J, Devall A, Coomarasamy A, Dhillon-Smith RK. Evaluating interventions and adjuncts to optimize pregnancy outcomes in subfertile women: An overview review. Hum Reprod Update. 2022; 28:583-600.
13. Shepherd A, Brunckhorst O, Ahmed K, Xu Q. Botanicals in health and disease of the testis and male fertility: A scoping review. Phytomedicine. 2022; 106:154398.
14. Zhou SH, Deng YF, Weng ZW, Weng HW, Liu ZD. Traditional Chinese medicine as a remedy for male infertility: A review. World J Mens Health. 2019; 37:175-185.
15. Bai YL, Chen YH, Jiang C, Qian JH, Han LL, Lu HZ, Wang HZ, Sun YR. Efficacy and safety of traditional Chinese medicine in the treatment of immune infertility based on the theory of "Kidney Deficiency and Blood Stasis": A systematic review and meta-analysis. Evid Based Complement Alternat Med. 2021; 2021:9947348.
16. Guan F, Zhang S, Fan L, Sun Y, Ma Y, Cao C, Zhang Y, He M, Du H. Kunling Wan improves oocyte quality by regulating the PKC/Keap1/Nrf2 pathway to inhibit oxidative damage caused by repeated controlled ovarian hyperstimulation. J Ethnopharmacol. 2023; 301:115777.
17. Wang H, Cao D, Wang M, Shi Y, Wei B, Jiang S, Jiang Y, Lian H, Xue X, Ma Z, Li J. Proteomic analysis of human follicular fluid reveals the pharmacological mechanisms of the Chinese patent drug Kunling Pill for improving diminished ovarian reserve. Evid Based Complement Alternat Med. 2022; 2022:5929694.
18. Xu Y, Pan CS, Li Q, Zhang HL, Yan L, Anwaier G, Wang XY, Yan LL, Fan JY, Li D, Han JY. The ameliorating effects of Bushen Huatan Granules and Kunling Wan on polycystic ovary syndrome induced by dehydroepiandrosterone in rats. Front Physiol. 2021; 12:525145.
19. Carson SA, Kallen AN. Diagnosis and management of mnfertility: A Review. JAMA. 2021; 326:65-76.
20. Nogales C, Mamdouh ZM, List M, Kiel C, Casas AI, Schmidt HHHW. Network pharmacology: Curing causal mechanisms instead of treating symptoms. Trends Pharmacol Sci. 2022; 43:136-150.
21. Zhou J, Li L, Pan X, Wang J, Qi Q, Sun H, Li C, Wang L. The effect of a traditional Chinese quadri-combination therapy and its component quercetin on recurrent spontaneous abortion: A clinical trial, network pharmacology and experiments-based study. Front Pharmacol. 2022; 13:965694.
22. Lubahn DB, Moyer JS, Golding TS, Couse JF, Korach KS, Smithies O. Alteration of reproductive function but not prenatal sexual development after insertional disruption of the mouse estrogen receptor gene. Proc Natl Acad Sci U S

A. 1993; 90:11162-11166.
23. Lydon JP, DeMayo FJ, Funk CR, Mani SK, Hughes AR, Montgomery CA Jr, Shyamala G, Conneely OM, O'Malley BW. Mice lacking progesterone receptor exhibit pleiotropic reproductive abnormalities. Genes Dev. 1995; 9:2266-2278.
24. Mulac-Jericevic B, Mullinax RA, DeMayo FJ, Lydon JP, Conneely OM. Subgroup of reproductive functions of progesterone mediated by progesterone receptor-B isoform. Science. 2000; 289:1751-1754.
25. Lessey BA, Killam AP, Metzger DA, Haney AF, Greene GL, McCarty KS, Jr. Immunohistochemical analysis of human uterine estrogen and progesterone receptors throughout the menstrual cycle. J Clin Endocrinol Metab. 1988; 67:334-340.
26. Pereira G, Guo Y, Silva E, Bevilacqua C, Charpigny G, Lopes-da-Costa L, Humblot P. Progesterone differentially affects the transcriptomic profiles of cow endometrial cell types. BMC Genomics. 2022; 23:82.
27. Jia J, Gou J, Zhao X, Yi T, Li Z. Apolipoprotein A1 and heterogeneous nuclear ribonucleoprotein E1 implicated in the regulation of embryo implantation by inhibiting lipid peroxidation. Reprod Biomed Online. 2016; 33:635-645.
28. Banerjee P, Ghosh S, Dutta M, Subramani E, Khalpada J, Roychoudhury S, Chakravarty B, Chaudhury K. Identification of key contributory factors responsible for vascular dysfunction in idiopathic recurrent spontaneous miscarriage. PLoS One. 2013; 8:e80940.
29. Elnaggar A, Farag AH, Gaber ME, Hafeez MA, Ali MS, Atef AM. AlphaVBeta3 Integrin expression within uterine endometrium in unexplained infertility: A prospective cohort study. BMC Womens Health. 2017; 17:90.
30. Wang L, Lv S, Mao W, Pei M, Yang X. Assessment of endometrial receptivity during implantation window in women with unexplained infertility. Gynecol Endocrinol. 2020; 36:917-921.
31. Choi HJ, Chung TW, Park MJ, Jung YS, Lee SO, Kim KJ, Ha KT. Water-extracted tubers of Cyperus rotundus L. enhance endometrial receptivity through leukemia inhibitory factor-mediated expression of integrin αVβ3 and αVβ5. J Ethnopharmacol. 2017; 208:16-23.
32. Yang X, Tian Y, Zheng L, Luu T, Kwak-Kim J. The update immune-regulatory role of pro- and anti-inflammatory cytokines in recurrent pregnancy losses. Int J Mol Sci. 2022; 24:132.
33. Li D, Chen J, Ai Y, Gu X, Li L, Che D, Jiang Z, Li L, Chen S, Huang H, Wang J, Cai T, Cao Y, Qi X, Wang X. Estrogen-related hormones induce apoptosis by stabilizing schlafen-12 protein turnover. Mol Cell. 2019; 75:1103-1116.e1109.

Received March 19, 2023; Revised August 3, 2023; Accepted August 11, 2023.

[§]These authors contributed equally to this work.
*Address correspondence to:
Yan Sun, Laboratory for Reproductive Immunology, Obstetrics and Gynecology Hospital of Fudan University, 419 Fangxie Road, 200011 Shanghai, China.
E-mail: ysunsh@126.com

Ling Wang, Laboratory for Reproductive Immunology, Obstetrics and Gynecology Hospital of Fudan University, 419 Fangxie Road, Shanghai 200011, China.
E-mail: dr.wangling@fudan.edu.cn

Released online in J-STAGE as advance publication August 20, 2023.

Original Article

DOI: 10.5582/ddt.2023.01026

Apolipoprotein E deficiency attenuated osteogenesis *via* down-regulating osterix

Qing Qi[1,2,3,§], Yingping Xu[4,§], Hongmei Sun[1,2,3], Jing Zhou[1,2,3], Lisha Li[1,2,3], Xinyao Pan[1,2,3], Jing Wang[1,2,3], Wenli Cao[5], Yan Sun[1,2,3,*], Ling Wang[1,2,3,*]

[1] Laboratory for Reproductive Immunology, Obstetrics and Gynecology Hospital of Fudan University, Shanghai, China;
[2] The Academy of Integrative Medicine of Fudan University, Shanghai, China;
[3] Shanghai Key Laboratory of Female Reproductive Endocrine-related Diseases, Shanghai, China;
[4] Reproductive Medicine Center, Taizhou Hospital Affiliated to Wenzhou Medical University, Linhai, Zhejiang, China;
[5] Reproductive Medicine Center of Zhoushan Maternal and Child Health Care Hospital, Zhoushan, Zhejiang, China.

SUMMARY Apolipoprotein E (ApoE), a ligand for low-density lipoprotein receptors, is strongly induced during osteogenesis and has a physiologic role in regulating osteoblast function, but the mechanisms of its action are still unclear. The study aims to elucidate the influence and molecular mechanisms of *ApoE* on bone formation. An ovariectomy-induced osteoporotic model were conducted in *ApoE* knockout (*ApoE*$^{-/-}$) mice to study the effect of *ApoE* on the bone system. Bone quality were assessed through bone mineral density and histomorphometric analysis. To investigate the underlying role and mechanisms of *ApoE* during osteogenesis, primary osteoblasts from the calvariums of newborn *ApoE*$^{-/-}$ or wild-type (WT) mice were cultured in the osteoblastic differentiation medium *in vitro* for further research. Our animal experiment data showed that *ApoE*$^{-/-}$ mice exhibited bone loss, exacerbated by estrogen deprivation after ovariectomy. *ApoE* deficiency attenuated osteoblast activity and inhibited osteoblast osteogenesis, accompanied by decreased osterix expression. *ApoE* deficiency did not affect primary osteoblast viability and collagen-1 expression. Moreover, osteoprotegerin expression in *ApoE*$^{-/-}$ osteoblasts was reduced compared to WT controls. Our study demonstrated that *ApoE* gene deficiency contributed to bone loss and attenuated osteogenesis by down-regulating osterix expression.

Keywords apolipoprotein E, osteoblast, osteogenesis, osterix

1. Introduction

Osteoporosis and atherosclerosis are both prevalent diseases in postmenopausal women with bone and lipid metabolism disorders due to estrogen deficiency (*1*). Osteoporosis, characterized by decreased bone mass and density, could increase fracture risk, while atherosclerosis, characterized by dyslipidemia, is a syndrome affecting arterial blood vessels. Evidence notes that lipid metabolism is closely associated with bone metabolism. Recently, a study that included 1,116 Chinese female participants found that total cholesterol, low-density lipoprotein (LDL), and high-density lipoprotein (HDL) had a remarkable negative correlation with bone mass density at the lumbar spine (*2*). Another case-control study conducted with 150 individuals with metabolic syndrome has shown that vertebral fracture was a risk factor for coronary events (*3*). These studies imply that osteoporosis might share the same underlying pathogenesis as atherosclerosis.

Emerging evidence also shows that hyperlipemia might be a potent and important risk factor for osteoporosis (*4*). As we know, bone and fat originate from the same progenitor cell, multipotent mesenchymal stem cells (MSCs), which can differentiate into myoblasts or adipocytes under certain conditions (*5*). The products from LDL oxidation inhibit osteogenic differentiation and facilitate adipogenic differentiation of progenitor marrow stromal cells (*6,7*), resulting in osteoporotic bone loss. Oxidized lipids could regulate hyperlipidemia-induced parathyroid hormone resistance in bone anabolism in mice (*8*). Further on, in addition to their cholesterol-lowering effect, statins have been shown the bone anabolic action, indicating their protection against diseases such as osteoporosis (*9*). The pathogenesis of osteoporosis mainly results from the imbalance between osteoblasts and osteoclasts (*10,11*). Osteoblasts participate in bone formation while osteoclasts induce born absorption; bone formation could be hindered if disorders occur during osteoblasts' proliferation and

differentiation. Crosstalk between osteoblasts and osteoclasts is indispensable for maintaining the balance of bone metabolism (*11-13*). Osteoclastogenesis can be regulated by osteoblasts mainly through the receptor activator of the nuclear factor-κB (RANK) ligand (RANKL)/RANK/osteoprotegerin (OPG) axis (*14*).

Apolipoprotein E (ApoE), a significant plasma lipoprotein and a ligand for low-density lipoprotein receptors, is present in various tissues and expressed in different cells, including osteoblast, regulating the transportation and metabolism of lipids (*15*). Hyperlipidemia usually results from the gene mutations such as *ApoE*, which can be strongly induced during the mineralization of the primary osteoblasts *ex vivo* (*16*). Mice lacking *ApoE*, with a significant plasma cholesterol level, have displayed a high bone mass phenotype. In contrast, bone resorption was not affected due to an accelerated rate of bone formation (*16,17*). However, Hirasawa H *et al.* observed that *ApoE* knockout (*ApoE*$^{-/-}$) mice had reduced bone formation with a high-fat diet (*18*). Estrogen is a critical factor that could regulate both bone and lipid metabolisms. Estrogen decline during menopause causes lipid profile changes (*19*). Our previous study showed that estrogen could up-regulate the gene expression of *ApoE* receptors during osteoblast differentiation *in vitro* (*20*). The above observations indicated that *ApoE* might play a physiologic role in regulating osteoblast function, yet molecular mechanisms remained unclear.

In this work, *ApoE*$^{-/-}$ mice, which underwent ovariectomy or not, were conducted to probe the effect and underlying mechanisms of *ApoE* deficiency on the bone system. Bone mineral density (BMD) and histomorphometric parameters were analyzed to assess bone quality. To further investigate the relative mechanisms of bone metabolism regulated by *ApoE* deficiency, primary osteoblasts from newborn *ApoE*$^{-/-}$ and wild-type (WT) mice were cultured *in vitro*. Further experiments were carried out to explore mechanisms that *ApoE* deficiency regulates osteoblast-mediated osteoclastogenesis through RANKL/RANK/OPG axis.

2. Materials and Methods

2.1. Materials

The assay kits for total cholesterol (TC), LDL cholesterol, and HDL cholesterol were purchased from Nanjing Jiancheng Bioengineering Institute (Jiangsu, China). 4% paraformaldehyde (PFA) was purchased from Shanghai USEN Biological Technology Co., Ltd. (Shanghai, China). The tartrate-resistant acid phosphatase (TRAP) staining kit, calcein, β-glycerophosphate, ascorbate, dexamethasone, collagenase, 1α,25-$(OH)_2$ vitamin D_3 [1,25$(OH)_2D_3$], prostaglandin E2 (PGE2), and DMEM were obtained from Sigma-Aldrich, Inc. (St. Louis, MO, USA). Toluidine blue staining solution was commercially obtained from Leagene Biotech Inc. (Beijing, China). Alpha minimum essential medium (α-MEM) medium, fetal bovine serum (FBS), and lipofectamine 2000 were obtained from Thermo Fisher Scientific Inc. (CA, USA). Dispase was purchased from F. Hoffmann-La Roche, Ltd. (Basel, Schweiz). Oricell™ MSC osteogenic differentiation medium was bought from Cyagen Biosciences Inc. (Santa Clara, CA, USA). Penicillin, streptomycin, 5-bromo-4-chloro-3-indolyl-phosphate (BCIP)/nitroblue tetrazolium chloride (NBT), and MTT were obtained from Beyotime Biotech Inc. (Shanghai, China). The alkaline phosphatase (ALP) activity assay kit and Alizarin red S were purchased from GenMed Scientific Inc. (Shanghai, China). SYBR Premix Ex Taq II kits, RNAiso Plus, and PrimeScript RT Master Mix were commercially obtained from Takara Bio Inc. (Dalian, China). Si-*ApoE* and negative control (NC) were purchased from GenePharma Co., Ltd. (Shanghai, China). OPG was purchased from USCN Life Sciences Inc. (Wuhan, China). Primary antibodies against runt-related transcription factor 2 (Runx2), osterix, β-actin, and collagen-1 were purchased from Abcam Plc. (Cambridge, UK).

2.2. Animals

ApoE$^{-/-}$ and WT mice with C57BL/6 genetic background, aged 10-12 weeks, were commercially acquired from the Shanghai laboratory animal center of the Chinese Academy of Sciences (Shanghai, China). The mice were housed in a humidity-controlled (43 ± 8%) and temperature-controlled (23 ± 0.5°C) environment with a 12 h light and 12 h dark cycle. The Ethics Committee of Fudan University permitted the experimental protocols (approval number JS-020), which were carried out following the guidelines of Fudan University and the National Institutes of Health Guide for the Care and Use of Laboratory Animals.

Mice were mated with the same genotype, and newborn mice (2 days old) were used to isolate primary osteoblasts. *ApoE*$^{-/-}$ and WT mice (8 weeks old) were divided into four groups: ovariectomized (OVX) WT group, OVX *ApoE*$^{-/-}$ group, sham WT group, and sham *ApoE*$^{-/-}$ group (n = 6 for each group). Mice in the two OVX groups underwent ovariectomy through bilateral incisions, while mice in the two sham groups underwent the same surgical procedure without ovariectomy. After 12 weeks, murine blood, femur, and tibia sample were collected and analyzed.

2.3. Assessment of serum lipid profiles

Peripheral blood samples were collected from isoflurane-anesthetized mice by cardiac puncture to prepare the serum. Serum TC, LDL cholesterol, and HDL cholesterol were evaluated with a HITACHI-7080 automatic biochemical analyzer (Hitachi High-Tech Corporation,

Tokyo, Japan).

2.4. BMD and histomorphometric analysis

Dual-energy X-ray absorptiometry (DXA) was conducted to determine BMD with an animal PIXImus densitometer (Lunar; GE Corp., Fairfield, CT, USA), which the same technician performed. Uniformity was conducted by selecting consistent regions of interest from each sample for analysis. Bone structural parameters were detected with micro-computed tomography (micro-CT, Skyscan 1176, Bruker Corporation, Massachusetts, USA).

2.5. Immunohistochemistry

As previously described (*21*), after being fixed in 4% PFA, the murine tibiae were proceeded for decalcification with ethylenediaminetetraacetic acid, staining with TRAP for osteoclasts identification; the fixed murine tibiae were then stained with toluidine blue for analysis. Histological changes were observed using a microscope (Olympus, Tokyo, Japan).

2.6. Calcein labeling analysis

The bone formation sites were labeled with calcein referred to previous methods. Briefly, mice were administrated with calcein through intraperitoneal injection 7 and 2 days before the end of the experiment (*21*). Two nonconsecutive sections were collected from the tibia to measure bone formation rate (BFR) and mineral apposition rate (MAR) with a fluorescence microscopy (Olympus BX-60, Tokyo, Japan). The parameters, including BFR and MAR were analyzed referring to the previous protocols (*22*).

2.7. Primary osteoblasts isolation and differentiation

According to the genotype, primary osteoblasts were isolated from the calvaria of the newborn *ApoE*$^{-/-}$ and WT mice (*23*). Skull bones were digested five times (10 min each time) in α-MEM medium supplemented with 0.5% dispase and 0.1% collagenase. The first digestion was discarded; cells were collected from the remainder of the digestion and cultured in complete α-MEM for further study. The cell density in 24-well or 6-well culture plates is 5×10^4 per well or 1×10^5 per well, respectively. When cells reached 80% confluence, osteoblasts differentiation was induced in Oricell™ MSC osteogenic differentiation medium with ingredients from the kit as follows: MSC osteogenic differentiation basal medium supplemented with 10% MSC-qualified FBS, 1 M β-glycerophosphate, 20 mM ascorbate, and 1 mM dexamethasone.

2.8. ALP staining and activity analyses

Cells in 24-well plates were used for ALP staining, and cells in 6-well plates were used for ALP activity analyses after treating osteogenic differentiation medium for seven days. BCIP/NBT is the preferred staining substrate for ALP detection, and we performed ALP staining referring to the manufacturer's instructions. According to the protocol, an alkaline phosphatase activity assay kit was used to detect ALP activity in cell lysate. The pictures were obtained with a microscope (Nikon Corporation, Tokyo, Japan).

2.9. Alizarin red S staining

The calcium deposits of differentiated primary osteoblasts in 24-well culture plates were stained using Alizarin red S according to the provided protocol after osteogenic induction medium treatment for 21 days (*23*). Then the number of bone nodules was observed with a microscope (Nikon Corporation) and counted.

2.10. Proliferation analysis

1×10^3 per well primary osteoblasts were seeded into 96-well plates to perform MTT assay to monitor cell viability. The medium was exchanged with the MSC osteogenic differentiation medium when cells were fully adherent. 0.5 mg/mL MTT reagent was added separately after 12, 24, 48, and 96 h and incubated at 37°C for 4 h. The precipitation was dissolved in dimethyl sulfoxide after the supernatant was gently removed. Absorbance at 490 nm was determined with an enzyme-linked immunometric meter (Bio-Tek 800, Agilent Technologies, Inc., CA, USA).

2.11. RNA isolation and reverse transcription-quantitative PCR (qRT-PCR)

Primary osteoblasts were cultured in 6-well culture plates for 0, 3, 7, and 21 days, and then cells were collected to detect the gene expression. Primary osteoblasts were cultured for seven days and sequentially treated with or without 10^{-6} M $1,25(OH)_2D_3$ and 10^{-8} M PGE2 for 0, 1, and 2 days; the cells were used to detect the gene expression. Total RNA was extracted with an RNAiso Plus, referring to the provided protocol. Reverse transcription of total RNA was handled with a PrimeScript RT reagent kit. Quantitative PCR was conducted on Applied Biosystems 7900 HT (Thermo Fisher Scientific Inc.). Gene expression was analyzed with the $2^{-\Delta\Delta CT}$ method. The used primers are listed in Table 1.

2.12. Cell line MC3T3-E1 culture and transfection

MC3T3-E1, a mouse osteoblastic cell line, was commercially acquired from American Type Culture Collection (ATCC; Rockville, MD, USA) and cultured in DMEM with 10% FBS. For further research, MC3T3-E1

Table 1. The used primers are listed

Gene	Forward Primer	Reverse Primer
Runx2	GACAGTCCCAACTTCCTGTG	GCGGAGTAGTTCTCATCATTC
Osterix	GCTCGTAGATTTCTATCCTC	CTTAGTGACTGCCTAACAGA
Collagen-1	TGACTGGAAGAGCGGAGAGTA	GACGGCTGAGTAGGGAACAC
Opg	CCTTGCCCTGACCACTCTTAT	CGCCCTTCCTCACACTCAC
Rankl	CAAGATGGCTTCTATTACCTGT	TTGATGCTGGTTTTAACGAC
β-actin	CCTCTATGCCAACACAGT	AGCCACCAATCCACACAG

Opg: Osteoprotegerin; Rankl: Receptor activator of the nuclear factor-κB ligand; Runx2: Runt-related transcription factor 2.

was cultured in MSC osteogenic differentiation medium and transfected with si-*ApoE* or NC using Lipofectamine 2000. Cells were lysed to extract protein for western blot.

2.13. Western blot analysis

Cell protein samples were isolated, quantified, and denatured in sequence. The insoluble debris was removed by centrifugation, and the supernatant was retained for western blot analysis. Proteins were separated by electrophoresis on 10% sodium dodecyl sulfate polyacrylamide gels and transferred to a Hybond membrane. The membranes were blocked with non-fat milk, followed by incubation with primary antibodies against Runx2, osterix, collagen-1, and β-actin overnight at 4˚C. They are rinsed in a washing buffer three times and subsequently incubated with secondary antibodies. Signals were detected using a chemiluminescence system and displayed on an Amersham Imager 600 (GE Healthcare Life Sciences, MA, USA).

2.14. Enzyme-linked immunosorbent assay (ELISA)

Primary osteoblasts were cultured in the MSC osteogenic differentiation medium for seven days and then incubated with or without $1,25(OH)_2D_3$/PGE2 for 1 and 2 days. The culture supernatants were collected and used to detect the concentrations of OPG in accordance with the manufacturer's protocol.

2.15. Statistical analysis

Data were presented as the mean ± SEM. One-way ANOVA was performed followed by Bonferroni-Holm-adjusted *post-hoc* comparisons among three or more groups. The student's *t*-test was applied between two groups. $p < 0.05$ represented a significant difference.

3. Results

3.1. Bone loss was exacerbated in *ApoE*-deficient mice

Since deficiency of the *ApoE* gene is critical in cholesterol transport in mice, we first assessed serum lipid profiles. $ApoE^{-/-}$ mice showed a significantly increased serum TC and LDL cholesterol but reduced HDL cholesterol levels (Figure 1A), in accordance with a previous study (*18*). Ovariectomy did not affect serum levels of TC, LDL, and HDL (Figure 1A). To further explore femoral bone histomorphometric changes in *ApoE*-deficient mice, micro-CT analysis was performed to analyze bone properties. In the two sham groups, decreased BMD was observed in the bone trabecula of $ApoE^{-/-}$ mice but not WT mice (Figure 1B-1C left); in the two OVX groups, *ApoE* deprivation exacerbated the decrease in trabecular BMD compared to the WT mice (Figure 1B-1C left); OVX $ApoE^{-/-}$ mice had a lowest trabecular BMD in the four groups (Figure 1B, 1C left). Cortical BMD remained indistinguishable among the four groups, indicating ovariectomy or *ApoE* deficiency didn't affect cortical BMD (Figure 1B-1C right). Ovariectomy resulted in a decreased trabecular BMD, bone volume/tissue volume (BV/TV) ratio (Figure 1D), trabecular thickness (Tb.Th, Figure 1E), trabecular number (Tb.N, Figure 1G), and a remarkable increase in trabecular separation (Tb.Sp, Figure 1F), indicating a bone loss after estrogen deprivation through ovariectomy. Interestingly, *ApoE* deficiency aggravated the reduction of the BV/TV ratio, Tb.Th, and Tb.N and improved the Tb.Sp value (Figure 1C-G). OVX $ApoE^{-/-}$ mice had the lowest values of the BV/TV ratio, Tb.Th, and Tb.N and the highest Tb,Sp value in the four groups (Figure 1C-1G), showing *ApoE* deficiency aggravated bone loss.

To further explore the effects of *ApoE* deficiency on bone tissue homeostasis, we detected the static and bone dynamic histomorphometric parameters. The number of osteoblasts and osteoclasts were both increased in OVX mice, along with elevated BFR (Figure 1J, 1M) and MAR (Figure 1J, 1N), compared to the sham control mice; however, *ApoE* deficiency significantly reduced the number of osteoblasts (Figure 1H, 1K), BFR values (Figure 1J, 1M), and MAR values (Figure 1J, 1N). In contrast, the number of osteoclasts remained indistinguishable between WT and $ApoE^{-/-}$ mice (Figure 1I, 1L). These results indicated that *ApoE* deficiency resulted in osteopenia, possibly due to reduced osteoblastogenesis.

3.2. *ApoE* deficiency attenuated osteoblast activity and inhibited mineralization of differentiated primary osteoblasts

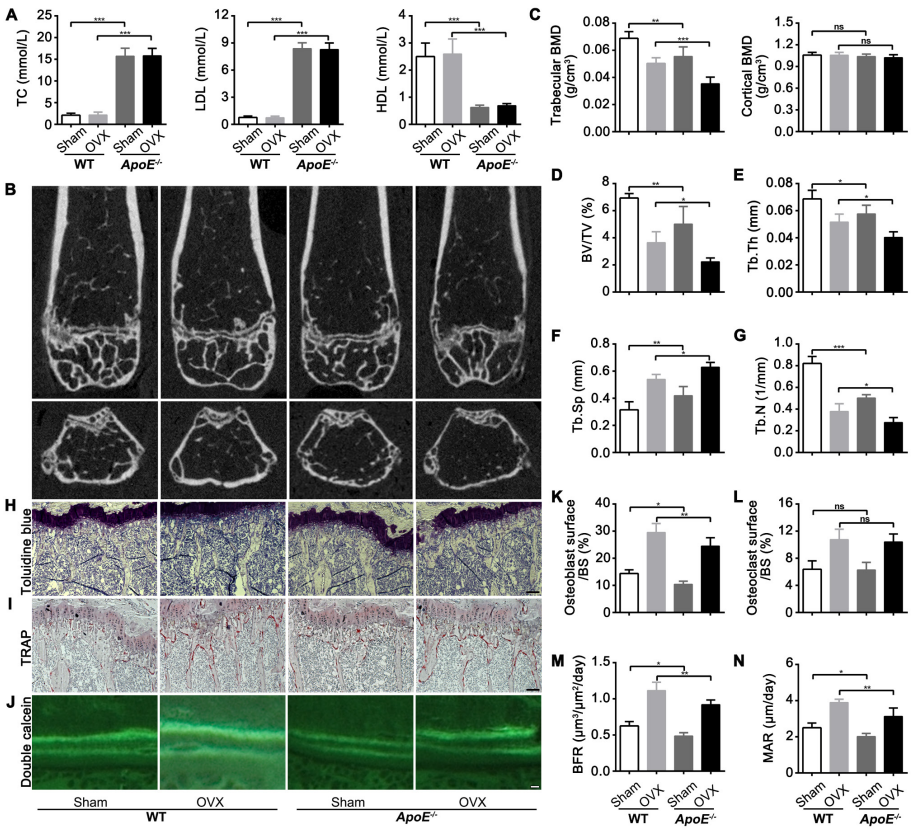

Figure 1. ***ApoE*** **deficiency enhanced ovariectomy-induced bone loss.** Eight-week-old mice underwent ovariectomy in OVX *ApoE*$^{-/-}$ and OVX WT groups; mice in sham *ApoE*$^{-/-}$ and sham WT groups underwent the same surgical procedure without ovariectomy. $n = 6$ for each group. After 12 weeks, all mice were sacrificed; serum and bone tissues were harvested for further investigation. **(A)** Serum levels of TC, LDL, and HDL. DXA was performed to measure trabecular and cortical BMD in each group. Micro-CT was used to determine the femoral phenotype in each group. **(B)** Micro-CT images. **(C)** Trabecular BMD and cortical BMD of femora. **(D)** BV/TV ratio, **(E)** Tb.Th, **(F)** Tb.Sp, and **(G)** Tb.N were measured. Histological analysis of the proximal tibiae in each group: **(H)** Toluidine blue staining, **(I)** TRAP staining, and **(J)** double calcein labeling. **(K)** Osteoblast surface/BS (%), **(L)** osteoclast surface/BS (%), **(M)** BFR, and **(N)** MAR were measured using the Osteo-Measure Histomorphometry System. **(H-I)** Scale bar represents 50 μm. **(J)** Scale bar represents 2 μm. Values are presented as the mean ± SEM. *$p < 0.05$, **$p < 0.01$, ***$p < 0.001$.

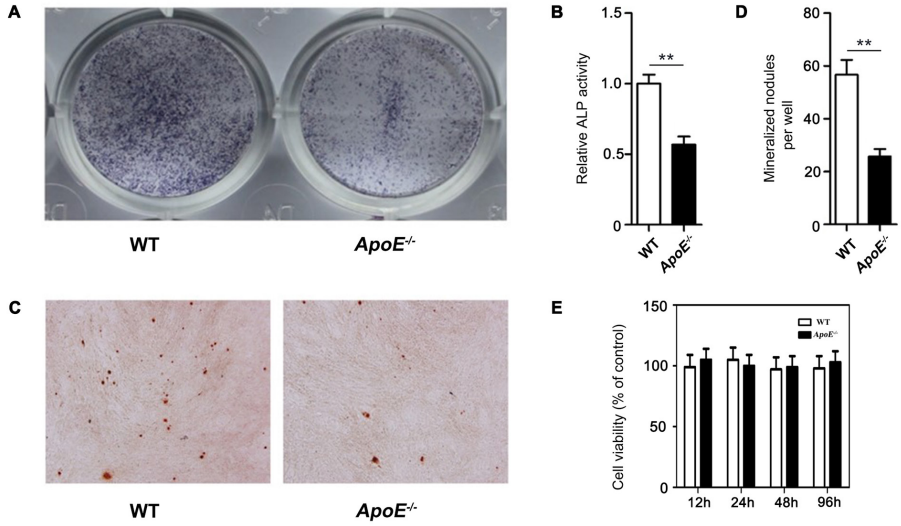

Figure 2. ***ApoE*** **deficiency attenuated osteoblast activity and inhibited the mineralization of differentiated osteoblasts.** Primary osteoblasts from *ApoE*$^{-/-}$ and WT mice were treated with an MSC osteogenic differentiation medium. After osteogenic induction for seven days, **(A)** ALP staining was used to evaluate osteoblast activity; **(B)** the quantitative analysis of ALP activity in cell lysate was determined using an ALP activity analysis kit. **(C)** Alizarin Red S staining was performed after osteogenic induction for 21 days, and **(D)** the number of mineralized nodules per well was calculated. **(E)** MTT assay was conducted to detect the cell viability of primary osteoblasts after being cultured with an osteogenic differentiation medium for 12, 24, 48, and 96 h. Values are presented as the mean ± SEM of at least three experiments. **$p < 0.01$.

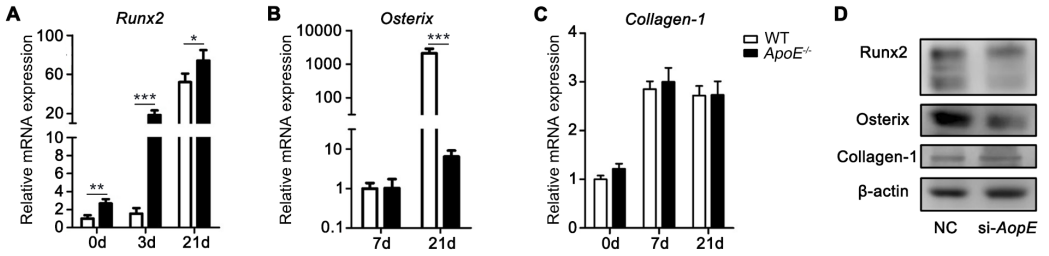

Figure 3. *ApoE* deficiency impaired the expression of osterix. Primary osteoblasts were cultured in an osteogenic induction medium for 0, 3, 7, and 21 days. Cells were harvested for total RNA extraction, and qRT-PCR was performed to analyze the gene expression. **(A)** *Runx2* mRNA expression. **(B)** *Osterix* mRNA expression. **(C)** *Collagen-1* mRNA expression. Values are presented as the mean ± SEM. **(D)** Western blot was performed to analyze protein levels of Runx2, osterix, and collagen-1 in mouse osteoblastic cell line MC3T3 after transfection with NC or si-*ApoE*. *$p < 0.05$, **$p < 0.01$, ***$p < 0.001$.

To explore mechanisms of *ApoE* deficiency affecting bone metabolism, primary osteoblasts from *ApoE*$^{-/-}$ and WT mice were cultured in MSC osteogenic differentiation medium. ALP staining was conducted to evaluate the ALP activity of osteoblasts. Fewer blue spots showed that the ALP activity of *ApoE*$^{-/-}$ osteoblasts decreased compared to the osteoblasts from WT mice (Figure 2A). Meanwhile, ALP activity in the cell lysate from *ApoE*$^{-/-}$ osteoblasts was also significantly reduced (Figure 2B). As shown in Figure 2C-2D, the number of osteoblastic calcium nodules in *ApoE*$^{-/-}$ osteoblasts was less than that in osteoblasts from WT controls, indicating that *ApoE* deficiency suppressed bone formation *in vitro*. In addition, to explore whether *ApoE* deficiency can affect the proliferation activity of the osteoblasts, an MTT assay was conducted to detect cell activity on the primary osteoblasts from WT and *ApoE*$^{-/-}$ mice *in vitro*. Data showed that *ApoE* deficiency had no noticeable impact on the cell viability of osteoblasts (Figure 2E).

3.3. *ApoE* deficiency inhibited the expression of osterix during the late stage of osteoblast differentiation *in vitro*

Osterix and Runx2 are key transcriptional factors during osteoblast differentiation; Runx2 is an early molecular regulator, whereas osterix is expressed in the late stage of osteoblast differentiation (*24,25*). Osteoblast differentiation was induced *in vitro* to assess the relative gene levels. Results demonstrated that the mRNA expression levels of *Runx2* in osteoblasts from *ApoE*$^{-/-}$ mice were higher on days 0, 3, and 21 compared to WT controls (Figure 3A). The *osterix* mRNA expression in osteoblasts from *ApoE*$^{-/-}$ mice was down-regulated on day 21, but there was no significant change on day 7 (Figure 3B). Meanwhile, the osterix protein expression in the si-*ApoE* group was reduced (Figure 3D), agreeing with the tendency of the reduced mRNA level. As shown in Figure 3C-3D, we didn't observe a noticeable difference in collagen-1 expression between *ApoE*$^{-/-}$ and WT osteoblasts.

3.4. *ApoE* deficiency down-regulated OPG expression and *Opg/Rankl* ratio

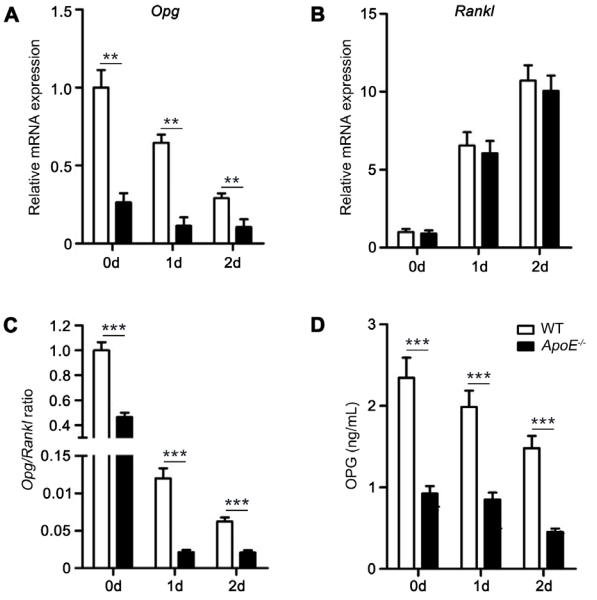

Figure 4. *ApoE* deficiency down-regulated OPG expression and *Opg/Rankl* ratio without affecting *Rankl* expression of osteoblasts *in vitro*. Primary osteoblasts cultured in the osteogenic differentiation medium were treated with or without $1,25(OH)_2D_3$/PGE2. After 0, 1, and 2 days, cells were harvested for total RNA extraction, and qRT-PCR was conducted to analyze the expression of **(A)** *Opg* and **(B)** *Rankl*. **(C)** The *Opg/Rankl* ratio. **(D)** Cell supernatant was used to test the protein level of OPG by ELISA analysis. Values are presented as the mean ± SEM of at least three experiments. **$p < 0.01$, ***$p < 0.001$.

Osteoblasts can regulate osteoclast differentiation by expressing OPG and RANKL through the RANKL/RANK/OPG system, a vital signaling pathway involved in osteoclastogenesis. Primary osteoblasts from *ApoE*$^{-/-}$ and WT mice were treated with $1,25(OH)_2D_3$/PGE2. A notable reduction in the *Opg* mRNA level was observed in osteoblasts from *ApoE*$^{-/-}$ mice (Figure 4A), whereas *ApoE* deficiency did not affect the *Rankl* mRNA level (Figure 4B). However, the ratio of *Opg/Rankl* significantly decreased in *ApoE*$^{-/-}$ osteoblasts compared to WT controls (Figure 4C). Moreover, the OPG protein level in the supernatant of *ApoE*$^{-/-}$ osteoblasts was remarkably reduced, indicating *ApoE* deficiency might affect the function of osteoblasts (Figure 4D).

4. Discussion

Our study focused on the role and related mechanisms of *ApoE* deficiency on bone metabolism at both animal and cellular levels. Results indicated that *ApoE*$^{-/-}$ mice showed a bone loss, which might be due to reduced osteogenesis. To investigate the underlying mechanisms, we used an osteoblastic differentiation culture system *in vitro* to explore the effect of *ApoE* deficiency. The result showed that *ApoE* deficiency attenuated osteogenesis *via* down-regulating osterix.

The ApoE component is a ligand for the LDL receptor, and *ApoE* deficiency increases the serum level of TC and LDL because of the failure of LDL receptor-mediated clearance (*26*). A further study proved that increased dietary lipids interfered with bone metabolism (*27*). We demonstrated osteopenia in *ApoE*$^{-/-}$ mice and further focused on the impact of *ApoE* deficiency on osteoblasts. Osteoblasts were derived from pluripotent MSCs that were the progenitors of multiple types of cells (*28,29*). The osteoblastic differentiation process includes cell proliferation, extracellular matrix formation and maturation, and mineralization (*30*). Osteoblasts secrete specific extracellular matrix proteins, including osteocalcin, ALP, and collagen-1, to form bone calcium nodules (*31,32*). Our results demonstrated an indistinguishable difference between *ApoE*$^{-/-}$ and WT primary osteoblasts in the proliferative activity and collagen-1 expression. Since *ApoE* did not impact osteoblast proliferation and extracellular matrix formation, we speculated that *ApoE* deficiency might hinder osteoblast differentiation or mineralization. Results showed decreased ALP activity and reduced bone calcium nodules in *ApoE*$^{-/-}$ osteoblasts, suggesting that *ApoE* deficiency attenuated cell activity and inhibited mineralization of differentiated primary osteoblasts.

Osteoblasts differentiation from MSCs depends on the transcription factors Runx2 and osterix (*24*). Runx2 is essential for the differentiation of osteoblasts and can stimulate the transcription of osteocalcin, collagen-1, osteopontin, and collagenase-3 during the differentiation process of MSCs into osteoblasts (*33*). *Osterix*, a bone morphogenetic protein-induced gene, is essential for transcriptional processes in osteoblasts (*25,34*). Although Runx2 and osterix are both crucial in osteoblast differentiation, the expression of the *osterix* gene could not be detected in *Runx2*$^{-/-}$ mice, indicating that osterix is downstream of Runx2 regulation and plays a vital role during the osteoblast differentiation (*24,25*). Although the mRNA level of *Runx2* in primary osteoblasts was enhanced, the mRNA expression of osterix was suppressed at the late stage of differentiation. The osterix protein level also decreased in *ApoE*$^{-/-}$ osteoblasts, indicating that the down-regulated expression of osterix might contribute to the impaired osteogenesis in *ApoE*-deficient osteoblasts. Given that osteoblasts lacking *ApoE* appeared to have less osteoblastic differentiation activity than WT osteoblasts due to reduced expression of osterix, *ApoE* may affect osterix gene expression through a Runx2 independent pathway. Further research is needed to explore the relationship between Runx2 and osterix when *ApoE* is absent and the potential mechanisms of *ApoE* regulating the osterix expression.

The interactions of osteoblasts and osteoclasts regulate bone formation and resorption (*35,36*). Communications between those two key players of bone metabolism are achieved through paracrine, direct cell-cell contact, or cell-bone matrix contact, especially the RANKL/RANK/OPG system (*35,37,38*). Osteoblasts can express OPG, a decoy RANKL receptor negatively regulating osteoclasts development (*39*). Moreover, RANKL secreted by osteoblasts can bind to RANK on the osteoclasts and stimulates osteoclastogenesis. *ApoE* deficiency did not affect *Rankl* gene expression; however, the OPG expression was down-regulated in *ApoE*$^{-/-}$ osteoblasts. In addition, a study indicated that reconstitution of *ApoE*$^{-/-}$*OPG*$^{-/-}$ mice with *ApoE*$^{-/-}$*OPG*$^{+/+}$ bone marrow could rescue atherosclerotic lesion progression and vascular calcification (*40*). As a vascular protective factor, reduced OPG expression may result in osteopenia and hyperlipemia in *ApoE*$^{-/-}$ mice. However, we cannot rule out the function of OPG on the two diseases in the *ApoE*-deficient mice now, and future experiments are required to analyze these mechanisms.

In the current study, bone loss was enhanced in *ApoE*-deficient mice after estrogen deprivation by ovariectomy, which might be due to the hindered osteogenesis *via* down-regulating osterix. The precise role of *ApoE* in the common pathomechanisms among estrogen, lipid metabolism, and bone metabolism would be an interesting question to be explored.

Acknowledgements

The authors wish to sincerely thank Peng Li and Suna Tian for their assistance in preparing the figures in this manuscript.

Funding: This work was supported by grants from a project under the Scientific and Technological Innovation Action Plan of the Shanghai Natural Science Fund (grant no. 20ZR1409100 to L Wang), a project of the Chinese Association of Integration of Traditional and Western Medicine special foundation for Obstetrics and Gynecology-PuZheng Pharmaceutical Foundation (grant no. FCK-PZ-08 to L Wang), a project for hospital management of the Shanghai Hospital Association (grant no. X2021046 to L Wang), a clinical trial project of the Special Foundation for Healthcare Research of the Shanghai Municipal Health Commission (grant no. 202150042 to L Wang), and a project under the science and technology programs of Zhoushan, Zhejiang (grant no. 2021C31055 to WL Cao).

Conflict of Interest: The authors have no conflicts of interest to disclose.

References

1. Tian L, Yu X. Lipid metabolism disorders and bone dysfunction - interrelated and mutually regulated (review). Mol Med Rep. 2015; 12:783-794.
2. Zhang Q, Zhou J, Wang Q, Lu C, Xu Y, Cao H, Xie X, Wu X, Li J, Chen D. Association between bone mineral density and lipid profile in Chinese women. Clin Interv Aging. 2020; 15:1649-1664.
3. Silva HC, Pinheiro MM, Genaro PS, Castro CH, Monteiro CM, Fonseca FA, Szejnfeld VL. Higher prevalence of morphometric vertebral fractures in patients with recent coronary events independently of BMD measurements. Bone. 2013; 52:562-567.
4. Yang Y, Liu G, Zhang Y, Xu G, Yi X, Liang J, Zhao C, Liang J, Ma C, Ye Y, Yu M, Qu X. Association between bone mineral density, bone turnover markers, and serum cholesterol levels in type 2 diabetes. Front Endocrinol (Lausanne). 2018; 9:646.
5. Frechette DM, Krishnamoorthy D, Pamon T, Chan ME, Patel V, Rubin CT. Mechanical signals protect stem cell lineage selection, preserving the bone and muscle phenotypes in obesity. Ann N Y Acad Sci. 2017; 1409:33-50.
6. Parhami F, Jackson SM, Tintut Y, Le V, Balucan JP, Territo M, Demer LL. Atherogenic diet and minimally oxidized low density lipoprotein inhibit osteogenic and promote adipogenic differentiation of marrow stromal cells. J Bone Miner Res. 1999; 14:2067-2078.
7. King S, Klineberg I, Brennan-Speranza TC. Adipose tissue dysfunction: Impact on bone and osseointegration. Calcif Tissue Int. 2022; 110:32-40.
8. Sage AP, Lu J, Atti E, Tetradis S, Ascenzi MG, Adams DJ, Demer LL, Tintut Y. Hyperlipidemia induces resistance to PTH bone anabolism in mice *via* oxidized lipids. J Bone Miner Res. 2011; 26:1197-1206.
9. Zhang Y, Bradley AD, Wang D, Reinhardt RA. Statins, bone metabolism and treatment of bone catabolic diseases. Pharmacol Res. 2014; 88:53-61.
10. Yang TL, Shen H, Liu A, Dong SS, Zhang L, Deng FY, Zhao Q, Deng HW. A road map for understanding molecular and genetic determinants of osteoporosis. Nat Rev Endocrinol. 2020; 16:91-103.
11. Langdahl BL. Overview of treatment approaches to osteoporosis. Br J Pharmacol. 2021; 178:1891-1906.
12. Eastell R, O'Neill TW, Hofbauer LC, Langdahl B, Reid IR, Gold DT, Cummings SR. Postmenopausal osteoporosis. Nat Rev Dis Primers. 2016; 2:16069.
13. Li SS, He SH, Xie PY, Li W, Zhang XX, Li TF, Li DF. Recent progresses in the treatment of osteoporosis. Front Pharmacol. 2021; 12:717065.
14. Martin TJ, Sims NA. RANKL/OPG; critical role in bone physiology. Rev Endocr Metab Disord. 2015; 16:131-139.
15. Bos MM, Noordam R, Blauw GJ, Slagboom PE, Rensen PCN, van Heemst D. The ApoE ε4 isoform: Can the risk of diseases be reduced by environmental factors? J Gerontol A Biol Sci Med Sci. 2019; 74:99-107.
16. Schilling AF, Schinke T, Münch C, Gebauer M, Niemeier A, Priemel M, Streichert T, Rueger JM, Amling M. Increased bone formation in mice lacking apolipoprotein E. J Bone Miner Res. 2005; 20:274-282.
17. Poznyak AV, Grechko AV, Wetzker R, Orekhov AN. In search for genes related to atherosclerosis and dyslipidemia using animal models. Int J Mol Sci. 2020; 21:2097.
18. Hirasawa H, Tanaka S, Sakai A, Tsutsui M, Shimokawa H, Miyata H, Moriwaki S, Niida S, Ito M, Nakamura T. ApoE gene deficiency enhances the reduction of bone formation induced by a high-fat diet through the stimulation of p53-mediated apoptosis in osteoblastic cells. J Bone Miner Res. 2007; 22:1020-1030.
19. Wang Q, Ferreira DLS, Nelson SM, Sattar N, Ala-Korpela M, Lawlor DA. Metabolic characterization of menopause: Cross-sectional and longitudinal evidence. BMC Med. 2018; 16:17.
20. Gui Y, Chu N, Qiu X, Tang W, Gober HJ, Li D, Wang L. 17-β-estradiol up-regulates apolipoprotein genes expression during osteoblast differentiation *in vitro*. Biosci Trends. 2016; 10:140-151.
21. Qi Q, Chen L, Sun H, Zhang N, Zhou J, Zhang Y, Zhang X, Li L, Li D, Wang L. Low-density lipoprotein receptor deficiency reduced bone mass in mice *via* the c-fos/NFATc1 pathway. Life Sci. 2022; 310:121073.
22. Parfitt AM, Drezner MK, Glorieux FH, Kanis JA, Malluche H, Meunier PJ, Ott SM, Recker RR. Bone histomorphometry: Standardization of nomenclature, symbols, and units. Report of the ASBMR Histomorphometry Nomenclature Committee. J Bone Miner Res. 1987; 2:595-610.
23. Li L, Zhou J, Xu Y, Huang Z, Zhang N, Qiu X, Wang L. C-C chemokine receptor type 6 modulates the biological function of osteoblastogenesis by altering the expression levels of osterix and OPG/RANKL. Biosci Trends. 2021; 15:240-248.
24. Chan WCW, Tan Z, To MKT, Chan D. Regulation and role of transcription factors in osteogenesis. Int J Mol Sci. 2021; 22:5445.
25. Nakashima K, Zhou X, Kunkel G, Zhang Z, Deng JM, Behringer RR, de Crombrugghe B. The novel zinc finger-containing transcription factor osterix is required for osteoblast differentiation and bone formation. Cell. 2002; 108:17-29.
26. Zhang SH, Reddick RL, Piedrahita JA, Maeda N. Spontaneous hypercholesterolemia and arterial lesions in mice lacking apolipoprotein E. Science. 1992; 258:468-471.
27. Li H, Gou Y, Tian F, Zhang Y, Lian Q, Hu Y, Zhang L. Combination of metformin and exercise alleviates osteoarthritis in ovariectomized mice fed a high-fat diet. Bone. 2022; 157:116323.
28. Wang C, Wang Y, Meng HY, Yuan XL, Xu XL, Wang AY, Guo QY, Peng J, Lu SB. Application of bone marrow mesenchymal stem cells to the treatment of osteonecrosis of the femoral head. Int J Clin Exp Med. 2015; 8:3127-3135.
29. Chamberlain G, Fox J, Ashton B, Middleton J. Concise review: Mesenchymal stem cells: Their phenotype, differentiation capacity, immunological features, and potential for homing. Stem Cells. 2007; 25:2739-2749.
30. Ponzetti M, Rucci N. Osteoblast differentiation and signaling: Established concepts and emerging topics. Int J Mol Sci. 2021; 22:6651.
31. Blair HC, Larrouture QC, Li Y, Lin H, Beer-Stoltz D, Liu L, Tuan RS, Robinson LJ, Schlesinger PH, Nelson DJ. Osteoblast differentiation and bone matrix formation *in vivo* and *in vitro*. Tissue Eng Part B Rev. 2017; 23:268-

280.
32. Lin X, Patil S, Gao YG, Qian A. The bone extracellular matrix in bone formation and regeneration. Front Pharmacol. 2020; 11:757.
33. Ducy P, Zhang R, Geoffroy V, Ridall AL, Karsenty G. Osf2/Cbfa1: A transcriptional activator of osteoblast differentiation. Cell. 1997; 89:747-754.
34. Zhang C. Transcriptional regulation of bone formation by the osteoblast-specific transcription factor Osx. J Orthop Surg Res. 2010; 5:37.
35. Yuan FL, Wu QY, Miao ZN, Xu MH, Xu RS, Jiang DL, Ye JX, Chen FH, Zhao MD, Wang HJ, Li X. Osteoclast-derived extracellular vesicles: Novel regulators of osteoclastogenesis and osteoclast-osteoblasts communication in bone remodeling. Front Physiol. 2018; 9:628.
36. Chen X, Wang Z, Duan N, Zhu G, Schwarz EM, Xie C. Osteoblast-osteoclast interactions. Connect Tissue Res. 2018; 59:99-107.
37. Li D, Liu J, Guo B, *et al*. Osteoclast-derived exosomal miR-214-3p inhibits osteoblastic bone formation. Nat Commun. 2016; 7:10872.
38. Xian L, Wu X, Pang L, *et al*. Matrix IGF-1 maintains bone mass by activation of mTOR in mesenchymal stem cells. Nat Med. 2012; 18:1095-1101.
39. Yao Z, Getting SJ, Locke IC. Regulation of TNF-induced osteoclast differentiation. Cells. 2021; 11:132.
40. Callegari A, Coons ML, Ricks JL, Yang HL, Gross TS, Huber P, Rosenfeld ME, Scatena M. Bone marrow- or vessel wall-derived osteoprotegerin is sufficient to reduce atherosclerotic lesion size and vascular calcification. Arterioscler Thromb Vasc Biol. 2013; 33:2491-2500.

Received April 23, 2023; Revised August 6, 2023; Accepted August 11, 2023.

[§]These authors contributed equally to this work.
**Address correspondence to:*
Yan Sun, Laboratory for Reproductive Immunology, Obstetrics and Gynecology Hospital of Fudan University, 419 Fangxie Road, 200011 Shanghai, China.
E-mail: ysunsh@126.com

Ling Wang, Laboratory for Reproductive Immunology, Obstetrics and Gynecology Hospital of Fudan University, 419 Fangxie Road, 200011 Shanghai, China.
E-mail: Dr.wangling@fudan.edu.cn

Released online in J-STAGE as advance publication August 17, 2023.

Original Article

DOI: 10.5582/ddt.2023.01029

A single dose of ketamine relieves fentanyl-induced-hyperalgesia by reducing inflammation initiated by the TLR4/NF-κB pathway in rat spinal cord neurons

Xin Zhou[1,2,§], Qianyi Li[3,4,§], Quehua Luo[1,2], Le Wang[2,5], Jiaxin Chen[2,6], Ying Xiong[2], Guiyun Wu[7], Lu Chang[2], Pingping Liu[2,8], Haihua Shu[1,2,9,*]

[1] Guangdong Cardiovascular Institute, Guangdong Provincial People's Hospital, Guangdong Academy of Medical Sciences, Guangzhou, Guangdong, China;
[2] Department of Anesthesiology, Guangdong Provincial People's Hospital (Guangdong Academy of Medical Sciences), Southern Medical University, Guangzhou, Guangdong, China;
[3] Guangzhou Kingmylab Pharmaceutical Research Co., Ltd., Guangzhou, Guangdong, China;
[4] Guangzhou KingMed Diagnostics Group Co., Ltd., Guangzhou, Guangdong, China;
[5] Department of Anesthesiology, Zhujiang Hospital, Southern Medical University, Guangzhou, Guangdong, China;
[6] School of Medicine South China University of Technology, Guangzhou, Guangdong, China;
[7] Department of Anesthesiology, Sun Yat-Sen Memorial Hospital, Sun Yat-Sen University, Guangzhou, Guangdong, China;
[8] The Second Affiliated Hospital of Guangzhou University of Chinese Medicine, Guangzhou, Guangdong, China;
[9] The Second School of Clinical Medicine, Southern Medical University, Guangzhou, Guangdong, China.

SUMMARY A large amount of clinical evidence has revealed that ketamine can relieve fentanyl-induced hyperalgesia. However, the underlying mechanism is still unclear. In the current study, a single dose of ketamine (5 mg/kg or 10 mg/kg), TAK-242 (3 mg/kg), or saline was intraperitoneally injected into rats 15 min before four subcutaneous injections of fentanyl. Results revealed that pre-administration of ketamine alleviated fentanyl-induced hyperalgesia according to hind paw-pressure and paw-withdrawal tests. High-dose ketamine can reverse the expression of toll-like receptor-dimer (d-TLR4), phospho- nuclear factor kappa-B (*p*-NF-κB, *p*-p65), cyclooxygenase-2 (COX-2), interleukin-1β (IL-1β), and tumor necrosis factor-α (TNF-α) 1 d after fentanyl injection in the spinal cord. Moreover, fentanyl-induced-hyperalgesia and changes in the expression of the aforementioned proteins can be attenuated by TAK-242, an inhibitor of TLR4, as well as ketamine. Importantly, TLR4, *p*-p65, COX-2, and IL-1β were expressed in neurons but not in glial cells in the spinal cord 1 d after fentanyl injection. In conclusion, results suggested that a single dose of ketamine can relieve fentanyl-induced-hyperalgesia *via* the TLR4/NF-κB pathway in spinal cord neurons.

Keywords fentanyl, hyperalgesia, ketamine, neuron, NF-κB, TLR4, COX-2, TNF-α

1. Introduction

Fentanyl has been widely used perioperatively as an analgesic since it was first synthesized in 1960. However, the use of high-dose fentanyl can induce hyperalgesia simultaneously from several hours to a few days after infusion (*1-4*). Fentanyl-induced hyperalgesia (FIH) decreases patients' quality of life and requires larger doses of fentanyl for pain relief, which increases adverse reactions such as nausea, vomiting, and respiratory depression. Thus, reducing FIH in patients is important.

For several decades, *N*-methyl-D-aspartate (NMDA) antagonists have been found to prevent opioid-induced hyperalgesia (OIH) and morphine tolerance (*5*). Ketamine, a nonselective NMDA antagonist, has clinically been used as an analgesic in acute pain, chronic pain, and cancer pain management (*6*). Ketamine was also found to play an effective role in decreasing remifentanil and fentanyl-induced hyperalgesia in many clinical trials (*7, 8*). In animal models of long-term hyperalgesia induced with chronic morphine injections (*9*) or acute repeated fentanyl injections (*10*), ketamine demonstrated significant preventive effects. However, there is still a lack of molecular evidence for a specific mechanism for the ability of ketamine to prevent FIH. Is only the NMDA receptor associated with its action? Or do other molecular mechanisms contribute to it?

Studies have demonstrated that TLR4 activation

contributed to opioid-induced tolerance and hyperalgesia and that the TLR4 antagonist LPS-RS can prevent OIH and tolerance. Recently, COX-2 and prostaglandin E2 (PGE2) in the spinal cord were found to be closely associated with FIH (*11*). Given the aforementioned findings, the current study investigated the effect of a single dose of ketamine on FIH and found that it alleviates FIH through the TLR4 receptor and its downstream pathway in the spinal cord.

2. Materials and Methods

2.1. Animals

Male Sprague Dawley (SD) rats weighing 200-220 g were purchased from the Laboratory Animal Center of Sun Yat-sen University. The rats were housed under conditions of a controlled temperature (24±1°C) and humidity (50-60%) with free access to sterile water and standard laboratory chow. Animals were kept under a 12 h:12h light /dark cycle.

2.2. Ethics

Ethical approval for this study was provided by the Ethical Committee of Guangdong Provincial People's Hospital, Guangdong, China (Chairperson Prof Hong, Tan) on November 29, 2021 (approval No.: KY-Q-2021-234-01). All data in the study were collected and analyzed between December 2021 and February 2023.

2.3. Drug administration

In accordance with a previous study (*12*), fentanyl (Yichang Humanwell Pharmaceutical Co., Ltd., Hubei, China) and ketamine (Heng Rui Pharmaceuticals, Jiangsu, China) were dissolved in saline. Ketamine 5 mg/kg or 10 mg/kg was respectively injected intraperitoneally into the rats, which were divided into a low-dose ketamine group (LK) and high-dose ketamine (HK). Control animals (Con) received the same volume of saline intraperitoneally.

Fentanyl was dissolved with saline to a concentration of 0.05 mg/mL and was injected subcutaneously 4 times at the dose of 60 μg/kg at 15-min intervals. Low-dose or high-dose ketamine was intraperitoneally injected 15 min before the fentanyl injection, and groups were designated low-dose ketamine + fentanyl (LKF) or high-dose ketamine + fentanyl (HKF). The fentanyl group was injected with the same volume of saline intraperitoneally 15 mins before the fentanyl injection. The control group received the same volume of saline subcutaneously and intraperitoneally.

TAK-242 (MedChemExpress, NJ, USA), a TLR4 inhibitor, was dissolved in 0.1% dimethyl sulfoxide (DMSO) with normal saline. Rats received 3 mg/kg TAK-242 intraperitoneally 15 mins before the fentanyl injection and were designated the TAK-242 + Fen group. The Fen group received the same volume of 0.1% DMSO intraperitoneally 15 mins before the fentanyl injection.

2.4. Experimental design

The experiment was conducted as shown in Figure 1. In part I, rats were randomly assigned to one of three groups to observe the influence of a single injection of ketamine: the LK group received an intraperitoneal injection of low-dose ketamine (5mg/kg) while the HK group received high-dose ketamine (10mg/kg). As a control, the Con group that was injected with saline intraperitoneally. The thermal hyperalgesia test and the Randall Selitto test were conducted 15 min, 30 min, 1 h, 2 h, 3 h, 4 h, and 1 d after the injection. The lumbar enlargement of the spinal cord (L4-L6) was harvested on day 1 for Western blotting.

To study the preventive effect of a single injection of ketamine on hyperalgesia induced by repeated subcutaneous injection of fentanyl, the rats were randomly assigned into four groups in part II: the Fen group was given four injections at 15-min intervals; the LKF group or HKF group received low-dose (5 mg/kg) or high-dose (10 mg/kg) ketamine 15 min before the first injection of fentanyl; and the Con group was given the same volume saline intraperitoneally and subcutaneously. The rats were subjected to the thermal hyperalgesia test and Randall Selitto test 15 min, 30 min, 1 h, 4 h, 1 d, and 7 d after the first administration of fentanyl. Western blotting and immunohistochemistry were performed on the rats on day 1 and day 7 after anesthesia.

Part III was to study whether blocking TLR4 signaling with TAK-242 could directly alleviate hyperalgesia and related proteins changes caused by fentanyl. TAK-242 was intraperitoneally 15 min before the fentanyl injection in the TAK-242 + Fen group while the Fen group received fentanyl. One day later, behavioral tests were conducted and molecules were detected.

2.5. Behavior test

In accordance with the method described previously (*13*), the thermal nociceptive test was conducted with a plantar test apparatus (IITC Life Science, CA, USA). In brief, rats were individually placed in a plexiglass chamber on a colorless transparent glass platform for 30-min for acclimation. A light beam was directed toward the middle plantar aspect of the left hind paw near the toes. The intensity of the light beam was 30 W and a 20-s cut-off time was used to avoid additional thermal injury. Three measurements were made per rat in each group with a 5-min interval. The paw withdrawal latency was recorded as the length of time (s) between projection of the light beam and paw withdrawal.

The mechanical pain threshold was measured with a mechanical pain threshold apparatus (UGO BASILE, Italy) and used as an indicator of mechanical nociception (*14, 15*). Stimulus in the form of mechanical pressure was applied to the midpoint of the right hind paw, and pressure was increased linearly. Three measurements were made per rat in each group with a 5-min interval. The pressure intensity (g) that caused an escape reaction was determined as the mechanical pain threshold.

2.6. Western blotting

Rats were euthanatized with 20% urethane (MACKLIN, Shanghai, China) 1.6 g/kg intraperitoneally. The lumbar enlargement of the spinal cord (L4-L6) was exposed by laminectomy. The dorsal half of the spinal cord was harvested in liquid nitrogen and then frozen at -80℃ until use. The cytoplasm and membrane protein were extracted following the protocol in the kit (Thermo Fisher Scientific, MA, USA). Cytoplasm protein was separated with TGX gel (Bio-rad, CA, USA), transferred onto a PVDF membrane (Merk Millipore, MA, USA), and incubated with antibodies against TLR4 (Novus Biologicals, USA), *p*-p65 (Cell Signaling Technology, MA, USA) COX-2 (Abcam, MA, USA), IL-1β (Abcam, MA, USA), TNF-α (Abcam, MA, USA), NaK (Abcam, MA, USA), β-action (CST, MA, USA), and GAPDH (CST, MA, USA). Blots were washed and incubated in HRP-linked anti-rabbit IgG antibody (KPL, MD, USA) and HRP-linked anti-mouse IgG antibody (KPL, MD, USA). Protein blots were visualized using Clarity ECL Substrates (Merk Millipore, MA, USA).

2.7. Immunohistochemistry

Rats were anesthetized with 20% urethane (MACKLIN, Shanghai, China) 1.6 g/kg intraperitoneally, and saline was perfused through the ascending aorta followed by 4% paraformaldehyde (PFA) (Sigma-Aldrich MO, USA). The lumbar enlargement of the spinal cord (L4-L6) was rapidly dissected and postfixed in 4% PFA. After dehydration in 30% sucrose, the samples were cut transversely and consecutively into slices of 20 μm and processed for immunohistochemistry with antibodies against TLR4, *p*-p65 (Affinity Bioscience, OH, USA), COX-2, IL-1β, NeuN (Merk Millipore, MA, USA), Iba-1 (Abcam, MA, USA), and GFAP (Abcam, MA, USA). Following incubation at 4℃ overnight, the slices were finally incubated with Cy-3-conjugated (Jackson Immunoresearch Laboratories, PA, USA), 488-conjugated (Invitrogen, CA, USA), and 647-conjugated (Invitrogen, CA, USA) secondary antibodies for 1 h at room temperature and then mounted on coverslips with Fluoromount-G with DAPI (Southern Biotech, Birmingham, AL). Images were captured with the LSM 780 confocal microscope (Zeiss, Germany).

2.8. Statistical analysis

All data were analyzed using GraphPad Prism 8 (GraphPad Software, USA) and are expressed as the mean ± SD. Nociceptive thresholds or latencies were quantified as direct measurement data and the area under the response time curve (AUC). Behavior test data and Western Blotting data were analyzed with one-way analysis of variance (ANOVA) or two-way ANOVA followed by Tukey's *post hoc* test. In all cases, $p < 0.05$ was considered to be a statistically significant difference.

3. Results

3.1. A single injection of ketamine relieves mechanical allodynia and thermal hyperalgesia induced by fentanyl

Ketamine is clinically used as an anesthetic, so to exclude the influence of a single low (5 mg/kg) or high dose (10 mg/kg) of ketamine on animals, hyperalgesia and allodynia were measured 15 min to 1 d after the ketamine injection (Figure 1A). As shown in Figure 2, both high and low doses of ketamine increased thermal hyperalgesia (Figure 2A) compared to the control group. The thermal pain threshold 30 min after injection (high dose: $p = 0.0384$ and low dose: $p = 0.0479$) and the mechanical pain threshold (Figure 2B) 15 min after injection (low dose: $p = 0.0433$ and high dose: $p < 0.001$) increased significantly, and the analgesic effect disappeared 1 h after injection. Western blotting revealed that ketamine had no effect on TLR4 (Figure 2C), *p*-p65 (Figure 2D), COX-2 (Figure 2E), IL-1β (Figure 2F), or TNF-α (Figure 2G) in the spinal cord on day 1. These results indicate that ketamine has a transient acute analgesic effect within 15-30 min but the animals' pain threshold returned to normal after 1 h, suggesting that ketamine has no significant long-term analgesic effect.

To determine if a single injection of ketamine is capable of reducing the hyperalgesia induced by fentanyl, mechanical and thermal pain thresholds were measured after the last injection of fentanyl (Figure 1B). The Hargreaves test (Figure 3A) revealed that the Fen ($p < 0.001$), LKF ($p < 0.001$), and HKF ($p < 0.001$) groups had a significantly increased paw withdrawal threshold 1-2 h after drug administration and returned to normal 4 h later. These may result from the rapid and strong analgesic effect of fentanyl. Importantly, the Fen group displayed thermal hyperalgesia from day 1 to day 2 compared to the control group (day 1: $p = 0.0478$, day 2: $p = 0.0254$), while the LKF (day 2: $p = 0.0065$) and HKF (day 2: $p = 0.0081$) groups displayed a higher paw withdrawal threshold compared to the Fen group and did not differ from the control group on day 2. Statistics indicated that the AUCs for the Fen ($p < 0.001$), LKF ($p < 0.001$), and HKF ($p < 0.001$) groups were larger than that for the control group 1 to 4 h after drug administration in the Hargreaves test (Figure 3B).

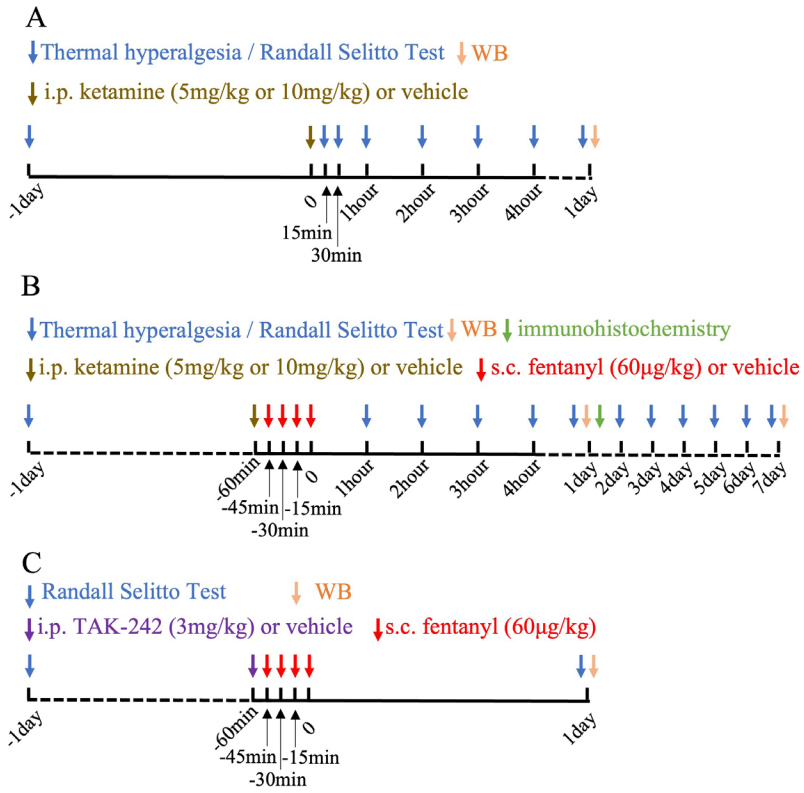

Figure 1. Timeline of the experiments. **(A)** One day after the behavior test for the baseline, low-dose and high-dose ketamine was injected into rats intraperitoneally. Then, behavior tests and WB were performed from 1 h to 1 d after the ketamine injection. **(B)** One d after the behavior test for the baseline, low-dose and high-dose ketamine was injected respectively 15 mins before 4 fentanyl injections at 15-min intervals. The behavior tests, WB, and immunohistochemistry were performed after the final ketamine injection. **(C)** One d after the behavior test for the baseline, TAK-242 was injected 15 mins before 4 fentanyl injections at 15-min intervals. Then, behavior tests and WB were performed 1 d after the final fentanyl injection.

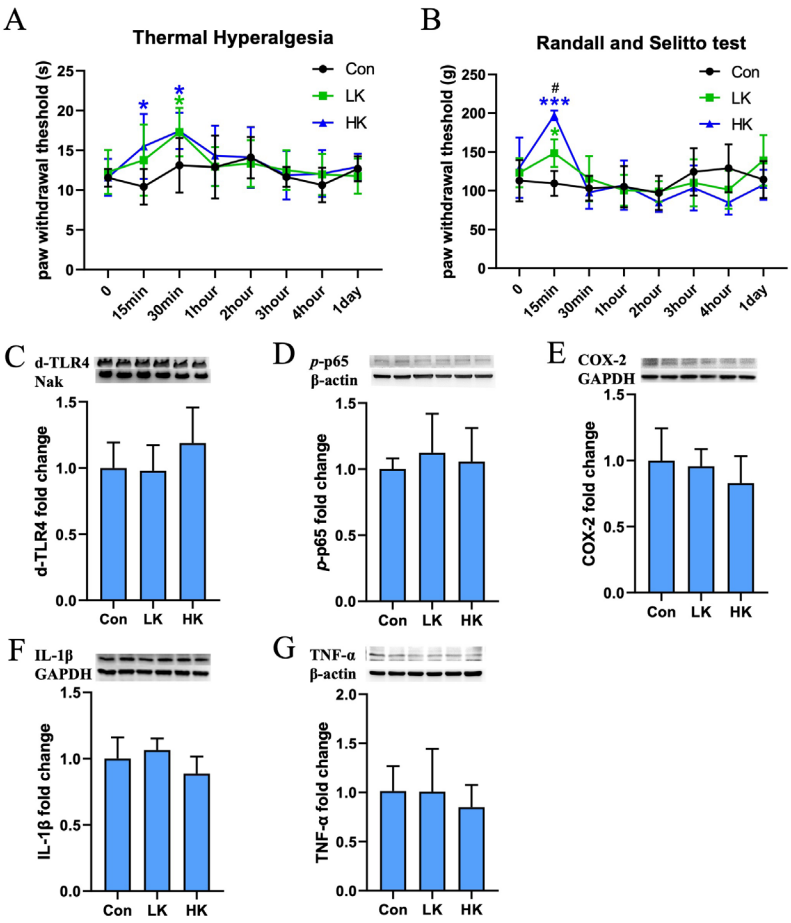

Figure 2. A single dose of ketamine had no long-term effects on naive rats. Ketamine 5 mg/mL or 10 mg/mL was injected into rats intraperitoneally. Thermal hyperalgesia **(A)** and allodynia **(B)** were determined from 15 min to 1 d after the injection (n = 6~8). The level of expression of d-TLR4 (n = 6) **(C)**, p-p65 (n = 6) **(D)**, COX-2 (n = 6) **(E)**, IL-1β (n = 6) **(F)**, and TNF-α (n = 6) **(G)** on day 1 after the ketamine injection was determined using Western Blotting. *$p < 0.05$, ***$p < 0.001$ *vs*. control group; $^{\#}p < 0.05$ *vs*. LK group. Data are expressed as the mean ± SD.

However, on days 1-7, the Fen group had a smaller AUC compared to the control group ($p < 0.001$) while the LKF ($p < 0.001$) and HKF ($p < 0.001$) groups had a higher AUC compared to the Fen group. The groups did not differ from the control group at the same time (Figure 3C).

The Randall-Selitto test was conducted to measure the mechanical pain threshold and yielded the same results as the Hargreaves test. The mechanical nociceptive threshold increased in the Fen group until 2 h (1 h: $p < 0.001$ and 2 h: $p < 0.001$) and in the HKF group until 3 h after drug injection (1 h: $p < 0.001$, 2 h: $p < 0.001$ and 3 h: $p = 0.0226$). However, the analgesic effect only lasted 2 h in the LKF group (1 h: $p < 0.001$ and $p = 0.0033$). The Fen group displayed a lower mechanical nociceptive threshold compared to the control group on day 1 to day 6 (day 1: $p = 0.0146$, day 2: $p = 0.0464$, day 3: $p = 0.003$, and day 6: $p = 0.0224$). The HKF (day 1: $p = 0.0439$ and day 4: $p = 0.0372$) group displayed a significant analgesic effect on day 1 and day 4 compared to the Fen group and did not differ from the control group (Figure 3D). Further calculation of AUCs revealed that the Fen ($p < 0.001$), LKF ($p < 0.001$), and HKF ($p < 0.001$) groups had a greater AUC than the control group in the first 4 h after the injection of fentanyl (Figure 3E). In contrast, the AUC for the Fen group on days 1 to 7 was significantly smaller than that for the control ($p < 0.001$), LKF ($p < 0.001$), and HKF ($p < 0.001$) groups (Figure 3F), indicating that the fentanyl-induced mechanical nociceptive threshhold was eliminated by ketamine.

Experimental results revealed significant hyperalgesia 1 to 4 d after fentanyl injection, and the animals' pain threshold returned to normal on day 7. Interestingly, a single injection of ketamine ahead of fentanyl can relieve mechanical allodynia and thermal hyperalgesia.

3.2. A single injection of ketamine in advance prevents the activation of the d-TLR4/ NF-κB pathway induced by fentanyl

To study the molecular mechanism by which ketamine prevents hyperalgesia induced by fentanyl, related protein expression was detected using Western blotting. Results suggested that d-TLR4 ($p = 0.0158$) (Figure 4A), *p*-p65 ($p = 0.0202$) (Figure 4B), COX-2 ($p = 0.0136$) (Figure 4C), IL-1β ($p = 0.0364$) (Figure 4D), and TNF-α ($p = 0.0314$) (Figure 4F) significantly increased in the spinal cord 1 d after fentanyl administration. The increased levels of d-TLR4 (Figure 4A) COX-2 (Figure 4C), and TNF-α (Figure 4E) induced by fentanyl can be reduced by a low dose of ketamine (d-TLR4: $p = 0.0262$, COX-2: $p = 0.0391$ and TNF-α: $p = 0.0229$), while a high dose of ketamine can reduce the levels of d-TLR4 ($p = 0.0015$) (Figure 4A), *p*-p65 ($p = 0.0030$) (Figure 4B), COX-2 ($p < 0.001$), IL-1β ($p < 0.001$) (Figure 4D), and TNF-α ($p = 0.0177$) protein expression.

Prior to day 7, there were no significant differences in levels of d-TLR4 (Figure 4F), *p*-p65 (Figure 4G), COX-2 (Figure 4H), IL-1β (Figure 4I), and TNF-α (Figure 4J) between the Fen group and the control group. Importantly, low or high doses of ketamine can reduce the levels of d-TLR4 (low dose: $p = 0.0032$ and high dose: $p = 0.0067$) (Figure 4F), COX-2 (low dose: $p = 0.0488$ and high dose: $p = 0.0397$) (Figure 4H), IL-1β (low dose: $p = 0.018$ and high dose: $p = 0.0083$) (Figure 4I), and TNF-α (low dose: $p < 0.001$ and high dose: $p < 0.001$) (Figure 4J) to various degrees but they do not alter the expression of *p*-p65 7 d after fentanyl injection (Figure 4G).

Immunohistochemical staining revealed that TLR4 (Figure 5A), *p*-p65 (Figure 5B), COX-2 (Figure 5C), and IL-1β (Figure 5D) co-localized with NeuN but not Iba-1 nor GFAP, indicating that TLR4, *p*-p65, COX-2, and IL-1β were expressed in neurons but not microglia nor astrocytes in the spinal cord on day 1 after fentanyl injection.

To sum up, the TLR4/NF-κ signaling pathway was activated 1 d after fentanyl injection and returned to normal 7 d later, which was consistent with behavioral results. A point worth noting is that a single injection of high-dose ketamine in advance alleviates the activation of TLR4/NF-κB better than low-dose ketamine on day 1. In addition, the combination of ketamine with fentanyl can still inhibit the TLR4/NF-κB/COX2 pathway on day 7.

3.3. Fentanyl-induced hyperalgesia and TLR4/NF-κB activation are prevented by inhibition of TLR4 with TAK-242

Thus far, results revealed that fentanyl injection led to hyperalgesia and activation of TLR4/NF-κB in the spinal cord, but causal links between TLR4/NF-κB activation and the abnormal behaviors in rats treated with fentanyl have not been established. To investigate this, the TLR4 inhibitor TAK-242 was injected 15 min before the first injection of fentanyl. Results indicated that TAK-242 substantially prevented the hyperalgesia induced by fentanyl ($p = 0.042$) (Figure 6A). Following the behavior tests, levels of TLR4, *p*-p65, COX-2, IL-1β, and TNF-α were measured using Western blotting, which revealed that the overexpression of TLR4 ($p = 0.0371$) (Figure 6B), *p*-p65 ($p = 0.0037$) (Figure 6C), COX-2 ($p = 0.0146$) (Figure 6D), IL-1β ($p = 0.0126$) (Figure 6E), and TNF-α ($p = 0.0422$) (Figure 6F) induced by fentanyl in the spinal cord was completely inhibited by TAK-242. These findings suggest that TLR4/NF-κB signaling in the spinal cord is essential for fentanyl-induced hyperalgesia.

4. Discussion

The current study found that the behavioral effects of thermal hyperalgesia in 1-2 d and mechanical allodynia

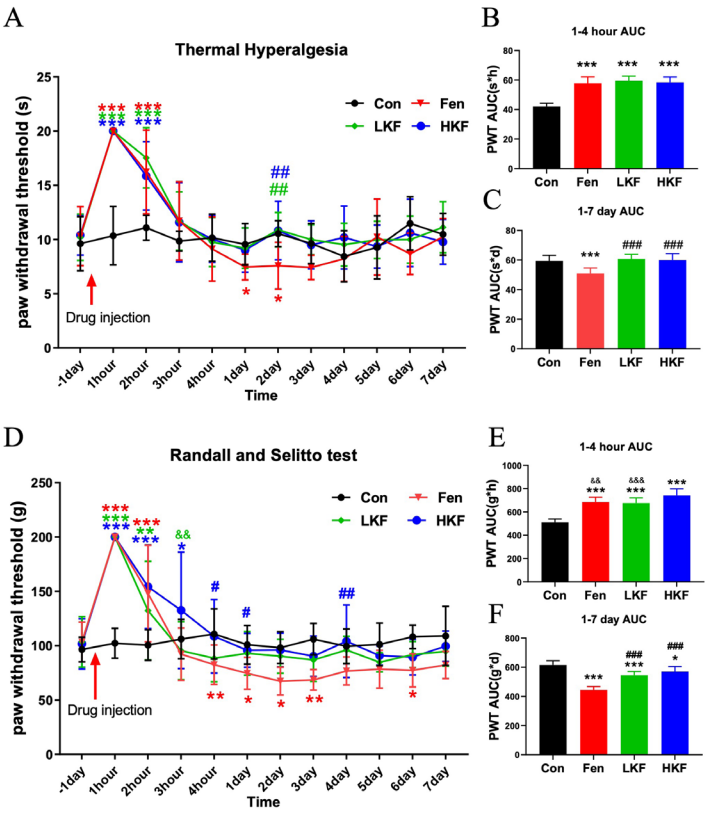

Figure 3. Pretreatment with ketamine reverses acute repeated fentanyl-induced hyperalgesia. Fentanyl 60 μg/kg was injected subcutaneously 4 times at 15-min intervals (Fen). Ketamine 5 mg/mL (LKF) or 10 mg/mL (HKF) was injected intraperitoneally 15 min before the fentanyl injection. Thermal hyperalgesia **(A)** and allodynia **(D)** were determined from 1 h to 7 d after drug injection. The AUC was calculated for hyperalgesia at 1-4 h **(B)**, hyperalgesia at 1-7 d **(C)**, allodynia at 1-4 h **(E)**, and allodynia at 1-7 d **(F)**. n = 9~12, *$p < 0.05$, **$p < 0.01$, and ***$p < 0.001$ *vs.* control group. $^{\#}p < 0.05$, $^{\#\#}p < 0.01$, and $^{\#\#\#}p < 0.001$ *vs.* fentanyl group, $^{\&\&}p < 0.01$ *vs.* HKF group. Data are expressed as the mean ± SD.

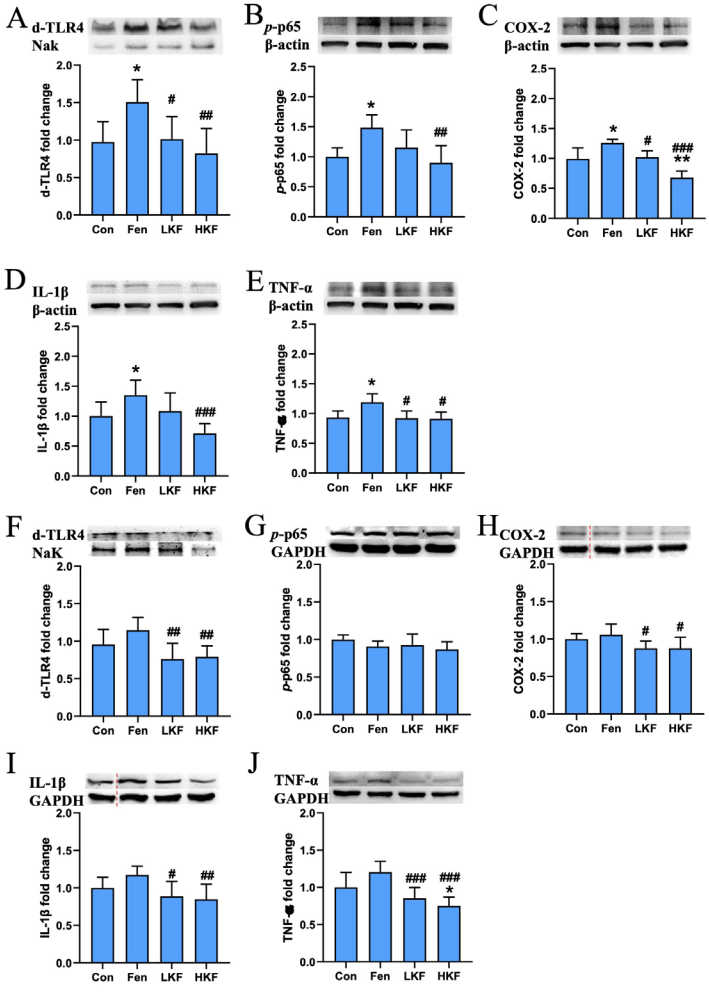

Figure 4. A single dose of ketamine can inhibit the high protein expression induced by acute repeated fentanyl injections on day 1 and its effect lasted for 7 d. One d after the drug injection following the drug injection protocol, the spinal cord was removed to determine the expression of TLR4 (n = 7) **(A)**, p-p65 (n = 6) **(B)**, COX-2 (n = 7) **(C)**, IL-1β (n = 8) **(D)**, and TNF-α (n = 6) **(E)** protein using Western Blotting. Fentanyl had no effect on the expression of TLR4 (n = 7) **(F)**, p-p65 (n = 4) **(G)**, COX-2 (n = 8) **(H)**, IL-1β (n = 8) **(I),** and TNF-α (n = 8) **(J)** protein expression on day 7. Ketamine decreased the expression of TLR4 **(F)**, COX-2 **(H)**, IL-1β **(I)**, and TNF-α **(J)** protein but not p-p65 **(G)** protein. *$p < 0.05$, **$p < 0.01$ *vs.* control group; $^{\#}p < 0.05$, $^{\#\#}p < 0.01$, and $^{\#\#\#}p < 0.001$ *vs.* fentanyl group. Data are expressed as the mean ± SD.

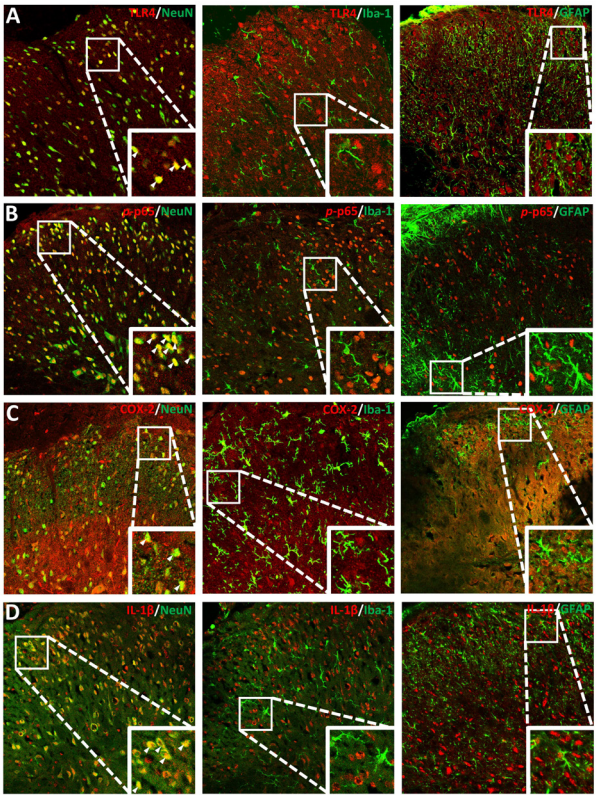

Figure 5. The localization of TLR4, *p*-p65, COX-2, and IL-1β in the spinal cord. One day after the fentanyl injection following the protocol, the spinal cord was removed to determine the localization of TLR4 **(A)**, *p*-p65 **(B)**, COX-2 **(C)**, and IL-1β **(D)**. TLR4, *p*-p65, COX-2, and IL-1β expressed in neurons (NeuN-positive cells) but not microglia (Iba-1-positive cells) nor astrocytes (GFAP-positive cells).

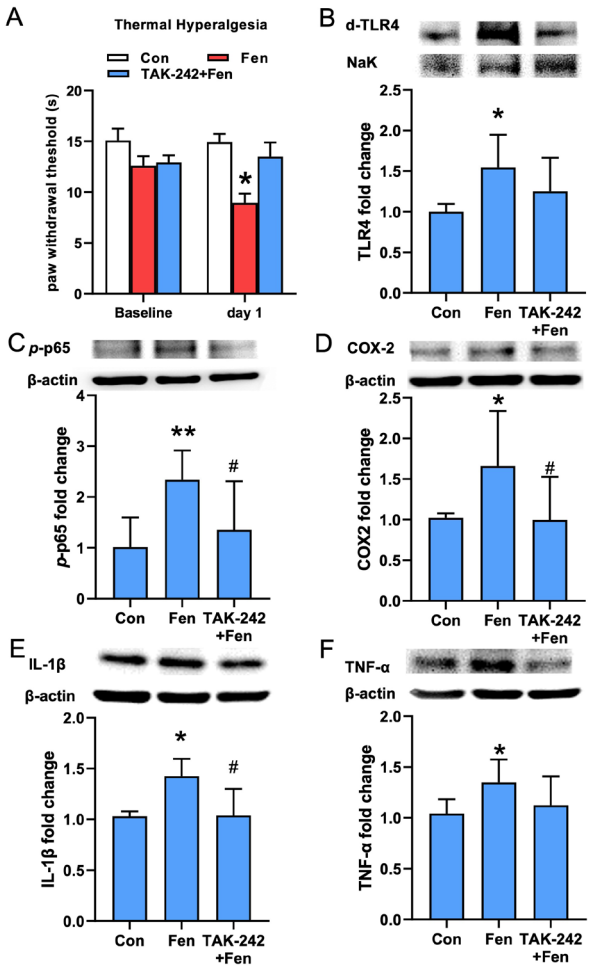

Figure 6. The TLR4 receptor contributed to fentanyl-induced-hyperalgesia. (A) The paw withdrawal threshold for rats before and one d after receiving fentanyl with/without TAK-242 (n = 7~9). The level of expression of d-TLR4 (n = 5~6). **(B)** The level of expression of *p*-p65 (n = 7~8) **(C)**, COX-2 (n = 8) **(D)**, IL-1β (n = 5) **(E)**, and TNF-α (n = 7~8) **(F)** on day 1 after the fentanyl and TAK-242 injection was determined using Western Blotting. $^{*}p < 0.05$ and $^{**}p < 0.01$ *vs.* control group; $^{\#}p < 0.05$ *vs.* fentanyl group. Data are expressed as the mean ± SD.

in 1-6 d induced by high doses of fentanyl in rats can be relieved by a single injection of ketamine in advance. This suggests that a single dose of ketamine had a significant effect at preventing fentanyl-induced hyperalgesia. In addition, the results of molecular experiments suggested that activation of the TLR4/NF-κB pathway was involved in fentanyl-induced hyperalgesia in spinal cord neurons and that ketamine reduced the activation of this pathway in a dose-dependent manner.

The current behavioral finding that a high dose of fentanyl can induce hyperalgesia is consistent with several clinical studies (*2, 4*) and animal studies (*11, 16*). However, other researchers (*3, 17*) have found that FIH lasted a few hours after injection. This difference in persistence over time may be due to the fentanyl dose. Interestingly, fentanyl-induced thermal hyperalgesia only lasts for 2 d while the mechanical nociceptive threshold can at least for up to 6 d. Some researcher have offered a few explanations for this phenomenon. One potential mechanism underlying mechanical allodynia is that Aβ fibers start to express some neuropeptides, which are usually expressed by small fibers (*18*). In some clinical studies, the ultra-lite components of heat-evoked potentials are described in the healthy after Aδ fiber blockade and C fiber sensitization (*19*). Different axon diameters and conduction velocities may lead to a different duration of allodynia and hyperalgesia in the current animal model.

The TRPV1 receptor (*20*), EphrinB receptor (*21*), and NMDA receptor (*9, 22-24*) are reported to be involved in OIH, which cannot comprehensively explain how ketamine reduces FIH. *p*-NF-κB in the spinal dorsal cord is reported to mediate morphine analgesic tolerance with increased TNF-α and IL-1β. The TLR4 inhibitor LPS-RS can alleviate morphine analgesic tolerance by reducing levels of *p*-NF-κB, TNF-α, and IL-1β (*25*). Hutchinson *et al.* found that the acute analgesic effects of morphine and oxycodone were significantly enhanced in TLR4 knockout rats (*26*). In a recent study, analgesic tolerance was prevented in TLR2 and TLR4 null mutant mice (*27*). In summary, the analgesic effect of opioids is enhanced

after TLR4 knockout, and the tolerance of opioids is alleviated. The current study found that TLR4/NF-κB mediated fentanyl-induced hyperalgesia. Therefore, the conjecture is that the enhanced analgesic effect of opioids after TLR4 knockout is due to reduced hyperalgesia. An important point to note is that, like the TLR4 inhibitor TAK-242, a single dose of ketamine can alleviate hyperalgesia and reduce the hyperactivation of TLR4/NF-κB induced by fentanyl. Studies have indicated that KC/GRO and TNF-α levels in male and female rats decreased 2 h after intravenous administration of ketamine, as did interleukin-6 (IL-6) levels in female rats and interleukin-10 (IL-10) levels in male rats (*28*). Low-dose ketamine inhibits neuroinflammation in PC12 cells by activating α7nAChR-mediated cholinergic anti-inflammatory pathways, such as the TLR4/MAPK/NF-κB signaling pathway (*29*), which suggests that ketamine may inhibit TLR4 expression in the same way.

The results from Figure 6 indicate that TLR4 may be one of the upstream proteins of COX-2, IL-1β, and TNF-α in fentanyl-induced-hyperalgesia. Bai *et al*. indicated that TLR4 was involved in morphine withdrawal-induced pain hypersensitivity by activating NF-κB, IL-1β, and TNF-α (*25*). In other pain models, such as arthritis hyperalgesia (*30*) and intraplantar-injected ceramide-induced-hyperalgesia (*31*), the inhibition of NF-κB can relieve hyperalgesia and decrease COX-2 expression. Moreover, morphine-3-glucoside (M3G), a morphine metabolite, can up-regulate TNF-α and COX2 mRNA expression and release prostaglandin E2 (PGE2) by activating the TLR4/NF-κB signaling pathway in central nervous system endothelial cells of rats (*32*). Interestingly, the current study found that repeated subcutaneous injections of fentanyl resulted in the overexpression of COX2, TNF-α, and IL-1β and that this can be inhibited by a single dose of ketamine or TAK-242. According to the aforementioned findings and the current findings, ketamine may relieve FIH by up-regulating inflammatory factors *via* the TLR4/NF-κB pathway.

Neurons mediate pain and densely innervate peripheral tissues through their nociceptors. A study has revealed that spinally projecting neurons were activated in the periaqueductal grey of adult mice after opioid injection (*33*). Ketamine is reported to act on neurons to reduce allodynia after injection of complete Freund's adjuvant (CFA) (*34*). Other researchers have even stated that the neurophysiological response of medullary pain-control neurons following chronic treatment with opioids is modulated by ketamine (*35*). Interestingly, the current study indicated that TLR4, NF-κB, COX-2, and IL-1β were co-localized with neurons, rather than astrocytes or microglia. Numerous studies have revealed that NF-κB is activated in neurons of the hippocampus, spinal cord, and dorsal root ganglion in models of chemotherapy-induced pain, while TNF-α and IL-1β are upregulated in neurons (*36, 37*). In addition, in ovariectomized and aged mice with chronic pain, TNF and Il-1β mRNAs were expressed in the neurons of DRGs and the spinal dorsal horn according to fluorescent in situ hybridization (FISH) (*38*). In a review, Roeckel *et al*. mentioned that neurons and glial cells activated by morphine will lead to OIH by producing cytokines such as IL-1β or TNF-α involved in LTP (*39*). Overall, these findings demonstrate that neurons in the central and peripheral nervous systems can modulate the production of proinflammatory cytokines, which may activate glial cells under pathological conditions. Neurons and glial cells interact with proinflammatory cytokines to produce continuous neuroinflammation and eventually lead to neuronal disease. The current study did not explore why TLR4, NF-κB, COX-2, and IL-1β are not expressed in glial cells 1 d after the fentanyl injection, so further research is needed to clarify this point. The neuron mechanisms found in the current study may have direct significance to clinical treatment of OIH.

In conclusion, results revealed that pretreatment with a single dose of ketamine relieved acute repeated FIH and increased levels of TLR4, NF-κB, COX-2, IL-1β, and TNF-α protein in spinal neurons. These results indicate an important role of the spinal neuron TLR4/NF-κB pathway in the manner in which ketamine relieves OIH. Preoperative or intraoperative administration of a single dose of ketamine may have a benefit on OIH and may improve the treatment of acute postoperative pain and even chronic post-surgical pain. Importantly, an early blockade of inflammation in spinal cord neurons rather than glial cells may interrupt the development of neuroinflammation, which may further prevent the activation of astrocytes and microglia and ultimately inhibit OIH initiated by neuroinflammation.

Acknowledgements

The authors wish to thank Professor Xian-Guo Liu from the Department of Physiology and Pain Research Center, Zhongshan School of Medicine, Sun Yat-sen University for supplying the research laboratory.

Funding: This work was supported by funding from the National Natural Science Foundation of China (Grant Number: 81870880), the National Key R&D Program of China (Grant Number: 2018YFC2001800), and the National Natural Science Foundation of Guangdong Province (Grant Number: 2016A030313827).

Conflict of Interest: The authors have no conflicts of interest to disclose.

References

1. Xuerong Y, Yuguang H, Xia J, Hailan W. Ketamine and lornoxicam for preventing a fentanyl-induced increase in postoperative morphine requirement. Anesth Analg. 2008;

107:2032-2037.
2. Yildirim V, Doganci S, Cinar S, Eskin MB, Ozkan G, Eksert S, Ince ME, Dogrul A. Acute high dose-fentanyl exposure produces hyperalgesia and tactile allodynia after coronary artery bypass surgery. Euro Rev Med Pharmaco Sci. 2014; 18:3425-3434.
3. Mauermann E, Filitz J, Dolder P, Rentsch KM, Bandschapp O, Ruppen W. Does fentanyl lead to opioid-induced hyperalgesia in healthy volunteers? A double-blind, randomized, crossover trial. Anesthesiology. 2016; 124:453-463.
4. Kalaydjian A, Farah F, Cheng Y, Acquadro MA, Gerges FJ. Opioid induced hyperalgesia with intrathecal infusion of high-dose fentanyl. Pain Pract. 2019; 19:222-223.
5. Trujillo KA, Akil H. Inhibition of morphine tolerance and dependence by the NMDA receptor antagonist MK-801. Science. 1991; 251:85-87.
6. Nowacka A, Borczyk M. Ketamine applications beyond anesthesia - A literature review. Eur J Pharmacol. 2019; 860:172547.
7. Garcia-Henares JF, Moral-Munoz JA, Salazar A, Del Pozo E. Effects of ketamine on postoperative pain after remifentanil-based anesthesia for major and minor surgery in adults: A systematic review and meta-analysis. Front Pharmacol. 2018; 9:921.
8. Bowers KJ, McAllister KB, Ray M, Heitz C. Ketamine as an adjunct to opioids for acute pain in the emergency department: A randomized controlled trial. Acad Emerg Med. 2017; 24:676-685.
9. Li X, Angst MS, Clark JD. A murine model of opioid-induced hyperalgesia. Molecular Brain Res. 2001; 86:56-62.
10. Laulin JP, Maurette P, Corcuff JB, Rivat C, Chauvin M, Simonnet G. The role of ketamine in preventing fentanyl-induced hyperalgesia and subsequent acute morphine tolerance. Anesth Analg. 2002; 94:1263-1269.
11. Li QB, Chang L, Ye F, Luo QH, Tao YX, Shu HH. Role of spinal cyclooxygenase-2 and prostaglandin E2 in fentanyl-induced hyperalgesia in rats. Br J Anaesth. 2018; 120:827-835.
12. Célèrier E, Rivat C, Jun Y, Laulin JP, Larcher A, Reynier P, Simonnet G. Long-lasting hyperalgesia induced by fentanyl in rats: Preventive effect of ketamine. Anesthesiology. 2000; 92:465-472.
13. Hargreaves K, Dubner R, Brown F, Flores C, Joris J. A new and sensitive method for measuring thermal nociception in cutaneous hyperalgesia. Pain. 1988; 32:77-88.
14. Randall LO, Selitto JJ. A method for measurement of analgesic activity on inflamed tissue. Archives Internationales de Pharmacodynamie et de Therapie. 1957; 111:409-419.
15. Miura T, Okazaki R, Yoshida H, Namba H, Okai H, Kawamura M. Mechanisms of analgesic action of neurotropin on chronic pain in adjuvant-induced arthritic rat: Roles of descending noradrenergic and serotonergic systems. J Pharmaco Sci. 2005; 97:429-436.
16. Wei X, Wei W. Role of gabapentin in preventing fentanyl- and morphine-withdrawal-induced hyperalgesia in rats. J Anesth. 2012; 26:236-241.
17. Mert T, Gunes Y, Ozcengiz D, Gunay I. Magnesium modifies fentanyl-induced local antinociception and hyperalgesia. Naunyn Schmiedebergs Arch Pharmacol. 2009; 380:415-420.
18. Nitzan-Luques A, Minert A, Devor M, Tal M. Dynamic genotype-selective "phenotypic switching" of CGRP expression contributes to differential neuropathic pain phenotype. Exp Neurol. 2013; 250:194-204.
19. Madsen CS, Johnsen B, Fuglsang-Frederiksen A, Jensen TS, Finnerup NB. The effect of nerve compression and capsaicin on contact heat-evoked potentials related to Adelta- and C-fibers. Neuroscience. 2012; 223:92-101.
20. Vardanyan A, Wang R, Vanderah TW, Ossipov MH, Lai J, Porreca F, King T. TRPV1 receptor in expression of opioid-induced hyperalgesia. J Pain. 2009; 10:243-252.
21. Xia WS, Peng YN, Tang LH, Jiang LS, Yu LN, Zhou XL, Zhang FJ, Yan M. Spinal ephrinB/EphB signalling contributed to remifentanil-induced hyperalgesia *via* NMDA receptor. Eur J Pain. 2014; 18:1231-1239.
22. Larcher A, Laulin JP, Celerier E, Le Moal M, Simonnet G. Acute tolerance associated with a single opiate administration: Involvement of *N*-methyl-D-aspartate-dependent pain facilitatory systems. Neurosci. 1998; 84:583-589.
23. Ohnesorge H, Feng Z, Zitta K, Steinfath M, Albrecht M, Bein B. Influence of clonidine and ketamine on m-RNA expression in a model of opioid-induced hyperalgesia in mice. PLoS One. 2013; 8:e79567.
24. Arout CA, Caldwell M, Rossi G, Kest B. Spinal and supraspinal *N*-methyl-D-aspartate and melanocortin-1 receptors contribute to a qualitative sex difference in morphine-induced hyperalgesia. Physiol Behav. 2015; 147:364-372.
25. Bai L, Zhai C, Han K, Li Z, Qian J, Jing Y, Zhang W, Xu JT. Toll-like receptor 4-mediated nuclear factor-kappaB activation in spinal cord contributes to chronic morphine-induced analgesic tolerance and hyperalgesia in rats. Neurosci Bull. 2014; 30:936-948.
26. Hutchinson MR, Northcutt AL, Hiranita T, *et al.* Opioid activation of toll-like receptor 4 contributes to drug reinforcement. J Neurosci. 2012; 32:11187-11200.
27. Thomas JHL, Lui L, Abell A, Tieu W, Somogyi AA, Bajic JE, Hutchinson MR. Toll-like receptors change morphine-induced antinociception, tolerance and dependence: Studies using male and female TLR and signalling gene KO mice. Brain Behav Immun. 2022; 102:71-85.
28. Spencer HF, Berman RY, Boese M, Zhang M, Kim SY, Radford KD, Choi KH. Effects of an intravenous ketamine infusion on inflammatory cytokine levels in male and female Sprague-Dawley rats. J Neuroinflam. 2022; 19:75.
29. Zhao J, Zhang R, Wang W, Jiang S, Liang H, Guo C, Qi J, Zeng H, Song H. Low-dose ketamine inhibits neuronal apoptosis and neuroinflammation in PC12 cells *via* alpha7nAChR mediated TLR4/MAPK/NF-kappaB signaling pathway. Int Immunopharmacol. 2023; 117:109880.
30. Luo JG, Zhao XL, Xu WC, Zhao XJ, Wang JN, Lin XW, Sun T, Fu ZJ. Activation of spinal NF-kappaB/p65 contributes to peripheral inflammation and hyperalgesia in rat adjuvant-induced arthritis. Arthritis Rheumatol. 2014; 66:896-906.
31. Doyle T, Chen Z, Muscoli C, Obeid LM, Salvemini D. Intraplantar-injected ceramide in rats induces hyperalgesia through an NF-kappaB- and p38 kinase-dependent cyclooxygenase 2/prostaglandin E2 pathway. FASEB J. 2011; 25:2782-2791.
32. Grace PM, Ramos KM, Rodgers KM, *et al*. Activation of adult rat CNS endothelial cells by opioid-induced toll-like receptor 4 (TLR4) signaling induces proinflammatory, biochemical, morphological, and behavioral sequelae.

Neuroscience. 2014; 280:299-317.
33. van den Hoogen NJ, Kwok CHT, Trang T. Identifying the neurodevelopmental differences of opioid withdrawal. Cell Mol Neurobiol. 2021; 41:1145-1155.
34. Zhou H, Zhang Q, Martinez E, Dale J, Hu S, Zhang E, Liu K, Huang D, Yang G, Chen Z, Wang J. Ketamine reduces aversion in rodent pain models by suppressing hyperactivity of the anterior cingulate cortex. Nat Commun. 2018; 9:3751.
35. Viisanen H, Lilius TO, Sagalajev B, Rauhala P, Kalso E, Pertovaara A. Neurophysiological response properties of medullary pain-control neurons following chronic treatment with morphine or oxycodone: Modulation by acute ketamine. J Neurophysiol. 2020; 124:790-801.
36. Xu T, Li D, Zhou X, Ouyang HD, Zhou LJ, Zhou H, Zhang HM, Wei XH, Liu G, Liu XG. Oral application of magnesium-L-threonate attenuates vincristine-induced allodynia and hyperalgesia by normalization of tumor necrosis factor-alpha/nuclear factor-kappaB signaling. Anesthesiology. 2017; 126:1151-1168.
37. Chen JL, Zhou X, Liu BL, Wei XH, Ding HL, Lin ZJ, Zhan HL, Yang F, Li WB, Xie JC, Su MZ, Liu XG, Zhou XF. Normalization of magnesium deficiency attenuated mechanical allodynia, depressive-like behaviors, and memory deficits associated with cyclophosphamide-induced cystitis by inhibiting TNF-alpha/NF-kappaB signaling in female rats. J Neuroinflammation. 2020; 17:99.
38. Zhang J, Mai CL, Xiong Y, Lin ZJ, Jie YT, Mai JZ, Liu C, Xie MX, Zhou X, Liu XG. The causal role of magnesium deficiency in the neuroinflammation, pain hypersensitivity and memory/emotional deficits in ovariectomized and aged female mice. J Inflamm Res. 2021; 14:6633-6656.
39. Roeckel LA, Le Coz GM, Gaveriaux-Ruff C, Simonin F. Opioid-induced hyperalgesia: Cellular and molecular mechanisms. Neuroscience. 2016; 338:160-182.

Received May 5, 2023; Revised July 27, 2023; Accepted August 5, 2023.

[§]These authors contributed equally to this work.
**Address correspondence to:*
Haihua Shu, Department of Anesthesiology, Guangdong Provincial People's Hospital (Guangdong Academy of Medical Sciences), Southern Medical University, 106# Zhongshan Second Road, Guangzhou, Guangdong, 510080, China.
E-mail: shuhaihua@hotmail.com

Released online in J-STAGE as advance publication August 9, 2023.

Brief Report

DOI: 10.5582/ddt.2023.01043

Development of a simple high-performance liquid chromatography-ultraviolet method for sotorasib quantification in human plasma: Implications for therapeutic drug monitoring

Eri Hikita[1,2], Yoshito Gando[1], Hideo Chubachi[3], Mikio Shirota[2,4], Akifumi Kushiyama[4,5], Takeo Yasu[1,2,4]

[1] Department of Medicinal Therapy Research, Pharmaceutical Education and Research Center, Meiji Pharmaceutical University, Tokyo, Japan;
[2] Department of Pharmacy, Tokyo Metropolitan Bokutoh Hospital, Tokyo, Japan;
[3] Department of Pharmacy, Shonan-Fujisawa Tokushukai Hospital, Kanagawa, Japan;
[4] Bokutoh Hospital-Meiji Pharmaceutical University Joint Research Center, Tokyo, Japan;
[5] Department of Pharmacotherapy, Meiji Pharmaceutical University, Tokyo, Japan.

SUMMARY Sotorasib, an oral small-molecule inhibitor, reportedly exerts promising activity against Kirsten rat sarcoma viral oncogene homolog (*KRAS)*-mutant tumors. However, the currently administered dose may fail to represent the optimal dose based on the therapeutic efficacy. Herein, we developed a simple and sensitive method using high-performance liquid chromatography with ultraviolet (HPLC-UV) to measure the sotorasib concentration in human plasma. The sotorasib calibration curve exhibited linearity across the concentration range of 0.10-20.0 μg/mL (r^2 = 0.9999). The coefficients of intra- and inter-day validation ranged between 0.79-9.75% and 3.01-6.13%, respectively. The assay accuracy ranged between –3.14 and 5.18%, with > 98.5% recovery. Subsequently, we applied the developed method to estimate sotorasib concentrations in a patient with *KRAS* G12C-mutated non-small cell lung cancer. We anticipate that our HPLC-UV method will be valuable for assessing the safety and efficacy of sotorasib in larger patient cohorts.

Keywords HPLC, sotorasib, therapeutic drug monitoring, KRASG12C mutation, non-small cell lung cancer

1. Introduction

Kirsten rat sarcoma viral oncogene homolog (*KRAS*) gene mutations have been frequently detected in patients with non-small cell lung cancer (NSCLC), colorectal cancer, pancreatic cancer, and other malignancies (*1,2*). Sotorasib is a small-molecule inhibitor that specifically inhibits *KRAS*. Preclinical studies have revealed that sotorasib can effectively suppress the phosphorylation of extracellular signal-regulated kinases, which serve as critical downstream effectors of *KRAS* (*3*). Consequently, sustained and complete tumor regression has been documented in murine models exhibiting *KRAS* G12C tumors (*4*). Importantly, sotorasib has been approved as the first targeted therapy for unresectable advanced or recurrent NSCLC with *KRAS* G12C mutation. However, treatment-related adverse events have necessitated dose modification (22.2%) and discontinuation of treatment (7.1%). The most common treatment-related adverse events that contribute to dose modification include diarrhea and elevated levels of aspartate aminotransferase (AST), alanine aminotransferase (ALT), and blood alkaline phosphatase (ALP) (*5*). Currently, sotorasib is administered at the maximum tolerated dose, as determined based on toxicity, although it does not necessarily reflect the optimal dose based on therapeutic efficacy (*6*).

Sotorasib is predominantly metabolized by cytochrome P450 (CYP)3A; hence, caution should be exerted when administering sotorasib concomitantly with CYP3A4 inducers and inhibitors. Furthermore, the absorption of sotorasib may be reduced when administered with antacids and proton pump inhibitors, potentially compromising treatment outcomes (*7*). Considering the pharmacokinetic profile, a daily dose of 960 mg sotorasib resulted in a coefficient of variation (CVs) of 98.3% for the maximum plasma concentration (C_{max}) (*8*), indicating substantial interindividual variability in blood concentrations. Therefore, careful consideration of blood sotorasib levels is warranted, emphasizing the importance of therapeutic drug monitoring (TDM) in

patients undergoing sotorasib therapy. The recommended sotorasib dose is 960 mg, with an initial dose reduction of 480 mg and a subsequent reduction of 240 mg suggested on encountering adverse reactions. However, comparable areas under the concentration-time curve from 0 h to 24 h ($AUC_{0–24h}$) and C_{max} values of sotorasib, ranging between 180 and 960 mg, have been documented following daily administration (*6*). During the dose escalation phase of a previous trial, low-dose sotorasib was found to afford overall response rates between 25 and 50% in patients with NSCLC, similar to the overall response rate achieved with 960 mg (*6*). Therefore, implementing sotorasib TDM to achieve a C_{max} equivalent to 960 mg may facilitate cost reduction in routine medical care.

To date, the sotorasib concentration in human plasma has only been measured using liquid chromatography-mass spectrometry (LC-MS/MS) (*9*). The LC-MS/MS system is expensive, and its introduction is limited to a few facilities. Conversely, high-performance liquid chromatography-ultraviolet (HPLC-UV) systems remain popular owing to their low initial cost and high utility in general hospitals. However, to the best of our knowledge, there have been no reports regarding the measurement of sotorasib concentrations in human plasma using HPLC-UV. Therefore, we developed a simple HPLC-UV method to estimate sotorasib concentrations in human plasma.

2. Methods

2.1. Instrumentation and reagents

The HPLC system consisted of a pump (PU-4180; Jasco, Tokyo, Japan), UV detector (UV-4075; Jasco), and autosampler (AS-4550; Jasco). Analysis was performed using an octadecylsilyl column (Capcell Pak C18 MG II; 250 mm × 4.6 mm; i.d., 5 μm; Osaka Soda, Osaka, Japan) equipped with a Capcell Pak C18 MG II guard column (10 mm × 4.0 mm; Osaka Soda). Sotorasib and bosutinib were acquired from Toronto Research Chemicals, Inc. (Ontario, Canada). The mobile phases comprised HPLC-grade acetonitrile, methanol, and water (Kanto Chemical Co., Inc., Tokyo, Japan) and KH_2PO_4 (Wako, Osaka, Japan).

2.2. Preparation of stock and working solutions

Stock solutions of sotorasib and bosutinib were prepared in acetonitrile and methanol, respectively, at a concentration of 1 mg/mL. The sotorasib stock solution was diluted in acetonitrile to obtain working solutions of 0.5, 1.25, 5.0, 12.5, 25.0, and 100.0 μg/mL. Bosutinib was diluted in methanol to obtain a 10 μg/mL working solution. Subsequently, the prepared stock and working solutions were stored at −80°C until use.

2.3. Assay procedure

A 10 μL working solution of sotorasib was vortexed with 50 μL of plasma in a 2.0 mL microtube (ClickFit 2.0 mL, Trerf Lab, Switzerland) for 10 s. Subsequently, 60 μL of sotorasib-spiked plasma, 10 μL of the internal standard (IS; 10 μg/mL bosutinib), and 130 μL of acetonitrile chilled to −20°C were added. The mixture was vortexed for 1 min and centrifuged at 15,000× *g* for 10 min at 4°C. The resulting supernatant (30 μL) was subjected to HPLC analysis. The detection wavelength was set to 230 nm, and the mobile phase comprised 0.5% KH_2PO_4 (pH 4.5) and acetonitrile (65:35, v/v) at a flow rate of 1.0 mL/min.

2.4. Calibration and validation

Calibration concentrations of sotorasib ranged from 0.10 to 20.0 μg/mL, and assay recovery and accuracy were determined at these concentrations. The assay precision was evaluated by analyzing five sets of control samples on the same day (intra-day) and on five different days (inter-day) at concentrations of 0.10, 0.25, 1.0, 2.5, 5.0, and 20.0 μg/mL.

2.5. Sample stability

Sotorasib stability in plasma samples was assessed at three different concentrations (0.10, 2.5, and 20.0 μg/mL). To establish benchtop stability, five samples (n = 5) stored at 25°C for 6 h were evaluated. Processed sample stability was evaluated by storing five samples (n = 5) at 4°C for 24 h. To determine long-term stability, five samples (n = 5) were stored at −60°C for four weeks and then assessed. Finally, freeze-and-thaw stability was determined by subjecting five samples (n = 5) to three cycles of freezing at −60°C and thawing.

2.6. Clinical application

Written informed consent was obtained from a patient with *KRAS* G12C-mutated NSCLC, and blood samples were collected for analysis. This case report measured the sotorasib blood levels of a single patient using our assay system. Samples were obtained at 2 h (C_{max}) after administering 960 mg of sotorasib on days 9, 13, 20, and 33. Plasma samples were obtained by centrifuging blood samples at 1,500× *g* for 15 min, which were subsequently stored at −80°C until analysis.

3. Results and Discussion

Figure 1a presents the chromatogram of the blank plasma sample, and Figure 1b shows the representative chromatogram of a plasma sample containing 0.10 μg/mL of sotorasib. The retention times for sotorasib and IS (bosutinib) were 14.5 and 10.8 min, respectively. The six-point sotorasib standard calibration curve exhibited linearity across the concentration range of 0.10-20.0 μg/

mL (r^2 = 0.9999). The lower limit of quantification for sotorasib was 0.10 μg/mL, with a recovery rate exceeding 95.8%. Considering this concentration range, the intra- and inter-day CVs ranged between 0.79-9.75% and 3.01-6.13%, respectively (Table 1). The assay accuracy ranged between –3.14-5.18%. The plasma stability of sotorasib was assessed under various conditions (Table 2). No significant sotorasib degradation was detected, and final concentrations were maintained within 91.43-108.05% of theoretical values.

In the present study, we developed a straightforward and highly sensitive HPLC-UV method to quantify plasma sotorasib concentrations in clinical settings. We believe this study makes a groundbreaking contribution to the management of patients receiving sotorasib therapy. The precision and accuracy of intra- and inter-assay variations and stability under diverse conditions adhered to the guidelines outlined by the Food and Drug Administration (*10*). Only one previous method for measuring sotorasib in human plasma samples has been reported, *i.e.*, an LC-MS/MS-based method, which requires a plasma volume of 20 μL for measurement (*9*). Conversely, the method developed in the present study allowed sotorasib quantification using minimal plasma volumes (as little as 10 μL); therefore, no further invasive procedures are required in addition to the usual blood collection.

Plasma concentrations of sotorasib were evaluated in samples collected from a male patient in his seventies, who was diagnosed with *KRAS* G12C-mutated NSCLC and undergoing second-line treatment with sotorasib. The patient had received sotorasib at a dose of 960 mg. Liver function tests revealed that the patient had AST, ALT, γ-glutamyl transpeptidase (γ-GTP), and ALP levels within the normal range prior to initiating sotorasib therapy. On day 33 following sotorasib administration, the patient exhibited an elevated γ-GTP level corresponding to grade 3, ALT level corresponding to grade 2, AST level corresponding to grade 1, and ALP level corresponding to grade 1, as per the Common Terminology Criteria for Adverse Events version 5.0. Consequently, sotorasib was discontinued on the following day. The plasma sotorasib concentrations on days 9, 13, 20, and 33 were 2.40 (Figure 1c), 4.55, 4.18, and 5.25 μg/mL, respectively. Figure 2 illustrates the trends in AST, ALT, γ-GTP, ALP, and C_{max} of sotorasib. The patient was concurrently taking vildagliptin, apixaban, hydrocortisone, metformin, risperidone, rosuvastatin, and yokukansan. Nine days after sotorasib discontinuation, elevated AST and ALT levels rapidly returned to normal.

In patients treated with sotorasib, the median (range) time to onset of grade 3 hepatotoxicity was found to be 9.1 (3.1-18.7) weeks (*11*). Considering our patient, the sudden onset of sotorasib-induced elevated γ-GTP, ALT, AST, and ALP levels was observed on day 33. Moreover, the C_{max} (5.25 μg/mL) of our patient on day 33 was similar to the C_{max} (5.39 μg/mL) previously reported for patients treated with 960 mg of sotorasib

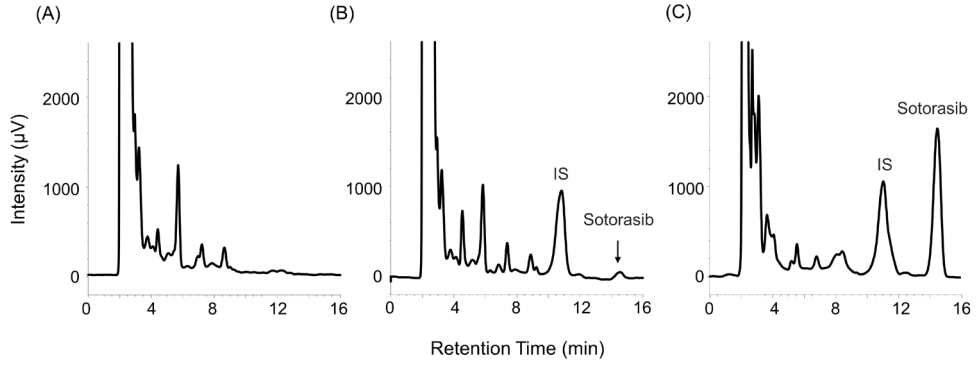

Figure 1. Chromatograms of (A) blank plasma sample, (B) plasma sample containing sotorasib 0.1 μg/mL, and (C) plasma sample from the patient receiving sotorasib 960 mg after 2 h on day 9 (2.40 μg/mL).

Table 1. Intra-day and inter-day accuracy and precision

Sotorasib added (μg/mL)	Intra-day (n = 5)			Inter-day (n = 5)			Recovery (%)
	Mean ± SD (μg/mL)	CV (%)	Accuracy (%)	Mean ± SD (μg/mL)	CV (%)	Accuracy (%)	
0.10	0.11 ± 0.01	9.75	5.18	0.10 ± 0.00	3.04	-0.68	95.83
0.25	0.25 ± 0.01	5.75	-1.91	0.25 ± 0.02	6.13	-0.43	106.92
1.0	0.97 ± 0.02	2.55	-2.79	0.99 ± 0.04	4.47	-1.42	101.18
2.5	2.45 ± 0.05	2.17	-2.17	2.48 ± 0.11	4.25	-0.71	100.84
5.0	4.95 ± 0.15	3.02	-0.98	4.98 ± 0.15	3.01	-0.39	101.51
20.0	19.22 ± 0.15	0.79	-3.88	19.37 ± 1.02	5.27	-3.14	102.32

CV, coefficient of variation; SD, standard deviation.

Table 2. Stability analyses under various conditions (n = 5)

Sotorasib added (μg/mL)	Stability condition (%)			
	Benchtop mean ± SD	Processed sample mean ± SD	Long-term 4 weeks mean ± SD	Freeze-and-thaw mean ± SD
0.10	108.05 ± 10.96	97.75 ± 6.14	100.76 ± 6.93	95.58 ± 4.60
2.5	96.26 ± 1.81	96.02 ± 2.07	92.27 ± 1.42	94.99 ± 4.19
20.0	91.43 ± 2.58	96.38 ± 2.25	91.90 ± 1.33	92.03 ± 2.96

SD, standard deviation.

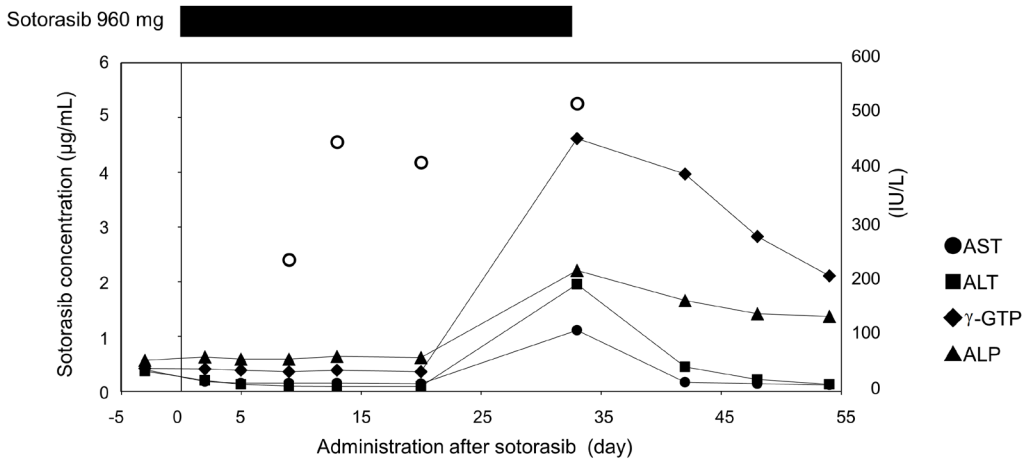

Figure 2. Trends for AST, ALT, γ-GTP, ALP, and the maximum concentration (C_{max}) of sotorasib. White circles indicate sotorasib C_{max}, black circles indicate AST, black squares indicate ALT, black diamonds indicate γ-GTP, and black triangles indicate ALP. AST, aspartate aminotransferase; ALT, alanine aminotransferase; γ-GTP, γ-glutamyl transpeptidase.

(*6*). Consequently, it is unlikely that the elevated levels of γ-GTP, ALT, AST, and ALP could be solely attributed to the high sotorasib C_{max}. No significant exposure-response relationships were identified for treatment-related adverse events (*12*). Conversely, the C_{max} value was 2.40 μg/mL on day 9 upon reaching a steady state, subsequently displaying an increasing trend to 4.55, 4.18, and 5.25 μg/mL after day 13. Moreover, elevated blood sotorasib concentrations have been reported in patients with hepatic dysfunction (*7*). Therefore, monitoring sotorasib C_{max} may facilitate the early detection of hepatotoxicity through changes in sotorasib C_{max} prior to the elevation of γ-GTP, ALT, AST, and ALP. Although our evaluation was limited to sotorasib C_{max} and GTP, ALT, AST, and ALP levels in a single patient, we plan to elucidate the relationship between altered sotorasib blood levels and hepatotoxicity in future studies using our developed HPLC-UV method.

Previous reports have failed to detect any correlation between the dose (180-960 mg) and steady-state drug exposure. Similarly, evidence suggesting a relationship between dose and response rate is lacking. Certain patients exhibit antitumor responses at lower than standard doses, suggesting that 960 mg could be deemed an excessive dose (*4*). Additionally, low-dose sotorasib may reduce gastrointestinal toxicity (*13*). Accordingly, TDM using the currently developed method to measure blood levels of sotorasib could help reduce the sotorasib dose and related gastrointestinal toxicity.

Nevertheless, the limitations of the present study should be considered. Firstly, we evaluated samples from only one patient. Consequently, it remains unknown whether sotorasib concentrations can be accurately measured in patients taking medications other than the seven drugs administered by the aforementioned patient. In future studies, we intend to employ the developed method to measure sotorasib in a larger cohort of patients to establish the accuracy of our sotorasib measurements.

Sotorasib has been assessed in clinical trials for pancreatic and colorectal cancer (*14,15*) and could be expanded to other indications in the future. Our method could be valuable for assessing the safety and efficacy of sotorasib in treating diverse cancers.

In conclusion, we developed a simple and sensitive HPLC-UV-based method for determining the concentration of sotorasib in a clinical setting. Further investigation utilizing our assay is warranted to elucidate the relationship between sotorasib blood levels and clinical efficacy, as well as adverse effects.

Funding: This research was funded by the Japan Society for the Promotion of Science (JSPS) KAKENHI [grant number JP20K16095].

Conflict of Interest: The authors have no conflicts of interest to disclose.

References

1. Román M, Baraibar I, López I, Nadal E, Rolfo C, Vicent S, Gil-Bazo I. *KRAS* oncogene in non-small cell lung cancer: Clinical perspectives on the treatment of an old target. Mol Cancer. 2018; 17:33.
2. Uras IZ, Moll HP, Casanova E. Targeting *KRAS* mutant non-small-cell lung cancer: Past, present and future. Int J Mol Sci. 2020; 21:4325.
3. Lito P, Solomon M, Li LS, Hansen R, Rosen N. Allele-specific inhibitors inactivate mutant KRAS G12C by a trapping mechanism. Science. 2016; 351:604-608.
4. Canon J, Rex K, Saiki AY, *et al*. The clinical KRAS(G12C) inhibitor AMG 510 drives anti-tumour immunity. Nature. 2019; 575:217-223.
5. Skoulidis F, Li BT, Dy GK, *et al*. Sotorasib for lung cancers with *KRAS* p.G12C mutation. N Engl J Med. 2021; 384:2371-2381.
6. Nakajima EC, Drezner N, Li X, *et al*. FDA approval summary: Sotorasib for *KRAS G12C*-mutated metastatic NSCLC. Clin Cancer Res. 2022; 28:1482-1486.
7. U.S. Food and Drug Administration, Drugs@FDA [database on the internet]. Sotorasib USPI. *https://www.accessdata.fda.gov/drugsatfda_docs/label/2021/214665s000lbl.pdf* (accessed June 1, 2023).
8. Hong DS, Fakih MG, Strickler JH, *et al*. $KRAS^{G12C}$ inhibition with sotorasib in advanced solid tumors. N Engl J Med. 2020; 383:1207-1217.
9. Wong P, Akrami A, Houk B, Vuu I, James CA. Validation of an LC-MS/MS method for the determination of sotorasib, a $KRAS^{G12C}$ inhibitor, in human plasma. Bioanalysis. 2022; 14:1281-1292.
10. US DHHS, FDA, CDER, CVM. Guidance for industry: Bioanalytical method validation. US Department of Health and Human Services, Food and Drug Administration, Center for Drug Evaluation and Research and Center for Veterinary Medicine, Rockville, MD, 2018.
11. Dy GK, Govindan R, Velcheti V, *et al*. Long-term outcomes and molecular correlates of sotorasib efficacy in patients with pretreated *KRAS* G12C-mutated non-small-cell lung cancer: 2-year analysis of CodeBreaK 100. J Clin Oncol. 2023; 41:3311-3317.
12. CDER application #214665Orig1s000 sotorasib. 2020. *https://www.accessdata.fda.gov/drugsatfda_docs/nda/2021/214665Orig1s000MultidisciplineR.pdf* (accessed June 1, 2023).
13. Ratain MJ, Tannock IF, Lichter AS. Dose optimization of sotorasib: Is the US Food and Drug Administration sending a message? J Clin Oncol. 2021; 39:3423-3426.
14. Strickler JH, Satake H, George TJ, *et al*. Sotorasib in *KRAS* p.G12C-mutated advanced pancreatic cancer. N Engl J Med. 2023; 388:33-43.
15. Fakih MG, Kopetz S, Kuboki Y, *et al*. Sotorasib for previously treated colorectal cancers with $KRAS^{G12C}$ mutation (CodeBreaK100): A prespecified analysis of a single-arm, phase 2 trial. Lancet Oncol. 2022; 23:115-124.

Received June 29, 2023; Revised August 2, 2023; Accepted August 12, 2023.

**Address correspondence to:*
Takeo Yasu, Department of Medicinal Therapy Research, Pharmaceutical Education and Research Center, Meiji Pharmaceutical University; 2-522-1, Noshio, Kiyose, Tokyo 204-8588, Japan.
E-mail: yasutakeo-tky@umin.ac.jp

Released online in J-STAGE as advance publication August 19, 2023.

Brief Report

DOI: 10.5582/ddt.2023.01015

Involvement of adaptive immune responses in a model of subacute colitis induced with dextran sulfate sodium in C57BL/6 mice

Jing Li[1,§], Fangzhou Dou[1,§], Shasha Hu[2,*], Jianjun Gao[1,*]

[1] Department of Pharmacology, School of Pharmacy, Qingdao University, Qingdao, Shandong, China;
[2] Department of Pathology, The Affiliated Hospital of Qingdao University, Qingdao, Shandong, China.

SUMMARY Inflammatory bowel disease (IBD) is a non-specific chronic intestinal inflammatory disorder. Pharmacotherapy serves as the main treatment strategy for IBD; however, the current medications have certain limitations, such as inefficacy and a tendency to induce tolerance, thereby requiring the development of innovative drugs to fulfill therapeutic requirements. A model of acute colitis induced with a solution of approx. 3% dextran sulfate sodium (DSS) has been widely used in preclinical drug development. Nevertheless, this model has some drawbacks, including rapid disease progression leading to mortality in some mice and disparities between the inflammatory characteristics of mice and the pathological features of human IBD. The current study found that mice freely consuming a lower concentration of a DSS solution (1-1.5%) for 10-15 days exhibited milder colitis symptoms. Continued consumption of the DSS solution for 15-20 days resulted in chronic inflammation in colon tissue, accompanied by a significant increase in the proportion of Th1 cells, indicating the involvement of adaptive immune responses. Subsequently, mice were treated with mesalazine or Centella triterpenes while concurrently consuming the DSS solution for 10 days. The treated mice had significant improvements in body weight and colon length compared to the control group. The advantages of this subacute model include minimal mortality among experimental mice and the fact that intestinal mucosal inflammation in mice resembles the pathological features of human IBD, enabling the assessment of drug efficacy against IBD.

Keywords inflammatory bowel disease (IBD), colitis, dextran sulfate sodium (DSS), Th1 cells, adaptive immune response

1. Introduction

Inflammatory bowel disease (IBD) is a non-specific chronic intestinal inflammatory disorder that mainly includes ulcerative colitis and Crohn's disease (*1*). The former mainly damages the colon and rectum, while the latter can damage any part of the gastrointestinal tract from the mouth to the anus, with the terminal ileum and colon often affected (*2,3*). Patients often present with symptoms such as abdominal pain, diarrhea, bloody stools, and weight loss (*2,3*). IBD is difficult to cure, prone to recur, and has a potential risk of cancer, seriously affecting the quality of life of patients (*4*). The etiology of IBD remains unclear, but it is associated with abnormal immune responses in the gastrointestinal tract (*5*). Drug therapy is the main treatment strategy for IBD, with commonly used drugs including mesalazine, corticosteroids, and biologics targeting inflammatory mediators (*6,7*). However, existing drugs have drawbacks such as inefficacy and the potential to induce tolerance, necessitating the development of new drugs to meet treatment needs (*8*).

A model of acute colitis induced with dextran sulfate sodium (DSS) is widely used in preclinical drug development (*9,10*). In this model, DSS is typically used at a concentration of approx. 3%, and mice exhibit obvious colitis symptoms such as diarrhea, rectal bleeding, and weight loss within 3-7 days (*11*). The advantages of this model lie in its convenience and rapidity, and it can respond to some commonly used anti-IBD drugs (*11*). However, this model also has some drawbacks, evident in the large individual differences among mice, with some showing mild or no obvious colitis symptoms while others exhibit severe symptoms such as significant rectal bleeding and weight loss. This can easily lead to death and result in missing data. Second, DSS-induced acute inflammation progresses rapidly, and it can heal on its own after DSS is discontinued. Therefore, preventive administration is generally used to evaluate the efficacy of compounds,

while it is seldom used to evaluate the efficacy of drugs in the disease model. Finally and most importantly, human IBD is a chronic inflammation that involves adaptive immune response that plays an important role in disease pathology (*5*). However, studies have shown that acute intestinal inflammation can still be induced in mice with defective adaptive immune responses, indicating that the pathological features of DSS-induced acute inflammation in mice differ from those of human IBD (*12*). Therefore, the mouse model of DSS-induced acute colitis needs to be improved to better evaluate the efficacy of compounds.

Reported here is a mouse model of subacute DSS-induced colitis in which mice was allowed free access to a low concentration of a DSS solution (1%-1.5%) for 40-45 days. This model is characterized by diarrhea in mice, adaptive immune response involvement, and generally no mortality during the experiment. It can be used to evaluate the therapeutic and/or preventive effects of drugs.

2. Materials and Methods

2.1. Agents and animals

DSS (M.W. 40,000) and mesalazine were purchased from Shanghai Aladdin Biochemical Technology Co., Ltd. (Shanghai, China). Centella triterpene tablets were manufactured by Shanghai Shyndec Pharmaceutical Co., Ltd. (Shanghai, China). Female C57BL/6 mice (8-10 weeks old, 18-22 g) were purchased from Beijing Vital River Laboratory Animal Technology Co., Ltd. (Beijing, China). The animals were housed under pathogen-free conditions. The research protocol was in accordance with the institutional guidelines of the Animal Care and Use Committee.

2.2. Histological processing and hematoxylin and eosin (H&E) staining

After mice were sacrificed, the entire colon and rectal segment were removed, rinsed thoroughly with pre-cooled normal saline, blot dried with filter paper, and visually inspected for macroscopic changes. The length of the colorectum was measured. One-cm sections of the colon were cut, fixed in 4% paraformaldehyde, and embedded in paraffin. Six-μm thick sections then prepared for H&E staining. Digital micrographs were taken with a Nikon N*i* microscope.

2.3. Extraction of mouse colorectal mucosal lymphocytes

After the mouse colon was washed with pre-cooled normal saline, the tissue was cut into approximately 0.5-1-cm fragments. An appropriate amount of separation solution was added (20 mL of a separation solution containing 18.52 mL of sterile calcium- and magnesium-free Hank's balanced salt solution, 1 mL of fetal calf serum, 200 μL of 100 mM dithiothreitol, 200 μL of 1 M HEPES, and 80 μL of 0.5 M EDTA). The tissue fragments were shaken (250 r/min) at 37°C for 15 min and then filtered through a 100-μm nylon mesh to obtain a filtrate containing intraepithelial lymphocytes and intestinal epithelial cells. The intestinal tissue fragments were then added to an appropriate amount of a digestion solution (10.5 mL of a digestion solution containing 500 μL of fetal calf serum, 15 mg of collagenase VIII, 10 mg of DNase I, and 10 mL of calcium- and magnesium-free PBS). The mixture was shaken (250 r/min) at 37°C for 45 min and then filtered through a 100-μm nylon mesh to obtain a filtrate containing lamina propria lymphocytes. The filtrate was centrifuged (860× *g*) at 4°C for 10 min, and the supernatant was discarded. The cell pellet was resuspended in 8 mL of 40% isotonic Percoll solution and slowly layered over 4 mL of 80% isotonic Percoll solution along the tube wall. After being left to stand for 10 min, the mixed liquid was subjected to density gradient centrifugation (1000× *g*) at 20°C for 20 min. The opaque cell layer between the two layers of the interface was aspirated and placed into a centrifuge tube, and PBS was added. After mixing, it was centrifuged (800× *g*) at 4°C for 8 min. The cell pellet was resuspended in 1 mL of RPMI 1640 medium containing 10% fetal calf serum, and then an intestinal mucosal lymphocyte suspension was obtained.

2.4. Determination of Th1/Th2/Th17 $CD4^+$ T cells

After resuspending the extracted intestinal mucosal lymphocytes in PBS, Fixable Viability Stain 780 (BD Biosciences, NJ, USA) was added to the suspension and incubated in the dark for 10-15 min. After the mixture was washed and centrifuged (350× *g*, 5 min), mouse BD Fc Block (BD Biosciences, NJ, USA) was added and incubated at 4°C for 5 min to block the Fc receptors of the cells. Then appropriate amounts of antibodies against CD3 (FITC anti-mouse CD3, BioLegend, CA, USA), CD4 (BB700 rat anti-mouse CD4, BioLegend, CA, USA), and CD25 (APC anti-mouse CD25, BioLegend, CA, USA) were added and incubated at 4°C in the dark for 30 min. After the mixture was washed and centrifuged (350× *g*, 5 min), 1 mL of 1× FIX/Perm was added to each tube, and the mixture was incubated at 4°C in the dark for 40 min. After the mixture was washed and centrifuged (450× *g*, 5 min), appropriate amounts of antibodies against IFN-γ (Brilliant Violet 650™ anti-mouse IFN-γ, BioLegend, CA, USA), IL-4 (PE/Cyanine7 anti-mouse IL-4, BioLegend, CA, USA), and IL-17A (Brilliant Violet 421™ anti-mouse IL-17A, BioLegend, CA, USA) were added to each tube. The mixture was incubated at 4°C in the dark for 45 min and then washed and centrifuged (450× *g*, 5 min). The cells were resuspended in 500 μL of staining buffer, filtered through a 300-mesh filter, and analyzed using flow

cytometry. Prior to flow cytometry, compensation beads (BD Biosciences, NJ, USA) were used to adjust the flow cytometer.

2.5. Statistical analysis

Data are expressed as the mean ± SEM and were analyzed using a one-way analysis of variance (ANOVA) followed by Dunnett's multiple range tests. The limit of statistical significance was $p < 0.05$. Statistical analysis was performed with the software SPSS/Win 16.0 (SPSS, Chicago, IL, USA).

3. Results and Discussion

3.1. Subacute colitis induced with DSS

Mice were allowed free access to a 1-1.5% DSS solution for about 40-45 days (Figure 1A). Their feces were examined daily for any changes and their weight was recorded every three days. On days 10-15, the mice exhibited diarrhea and were allowed to continue drinking the DSS solution until day 30. During day 15 to 30, the mice showed obvious symptoms of diarrhea, indicating the presence of colitis. During the first 30 days of the study, the mice maintained a relatively stable weight (Figure 1B). Starting on day 30, the mice were given therapeutic agents while still having access to the DSS solution for about 10-15 days.

3.2. Pathology of subacute colitis in C57BL/6 mice

Colon tissues of mice were collected at the beginning and on day 15, day 30, and day 40. After H&E staining, the pathological changes in the colon were examined (Figure 2). At the beginning, the colonic mucosa of mice had abundant and regularly arranged crypts (Figure 2A). Few white blood cells were observed in the mucosal layer. On day 15, mice developed diarrhea, and the quantity and quality of crypts decreased (Figure 2B). The number of goblet cells decreased, and the submucosa became thicker with leukocyte infiltration. On day 30, the number of crypts decreased further, and large amounts of leukocytes were observed in the mucosal and submucosal layers (Figure 2C). Isolated lymphoid follicles were also observed, indicating an adaptive immune response. On day 40, the number of crypts decreased significantly, and the mucosal and submucosal layers were infiltrated by a large number of plasma cells and lymphocytes (Figure 2D).

To further clarify the type of adaptive immune response in the colonic mucosa, on day 30 colonic mucosal lymphocytes were extracted from mice and analyzed for the Th subgroups of $CD4^+$ T cells using flow cytometry (Figure 3). The results indicated that the proportion of Th1 cells in the colonic mucosa of

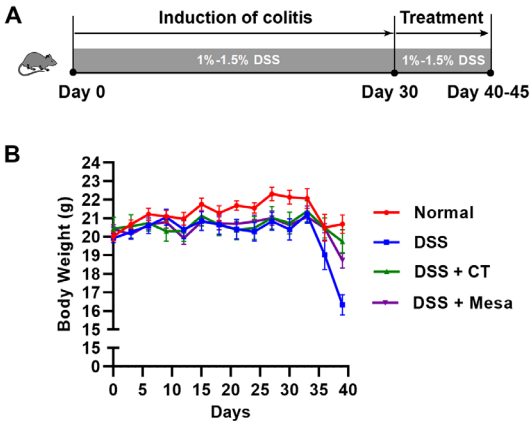

Figure 1. DSS (1%-1.5%)-induced subacute colitis in C57BL/6 mice. (**A**) The whole experiment could be divided into two phases. In phase 1, colitis was induced and maintained until day 30, when the colon mucosa exhibited chronic inflammatory characteristics. In phase 2, mice were treated with agents that have potential anti-colitis action. (**B**) The body weight of mice was monitored throughout the whole study. Body weight was stable during the first phase but tended to decrease during the second phase. CT, Centella triterpenes; Mesa, mesalazine.

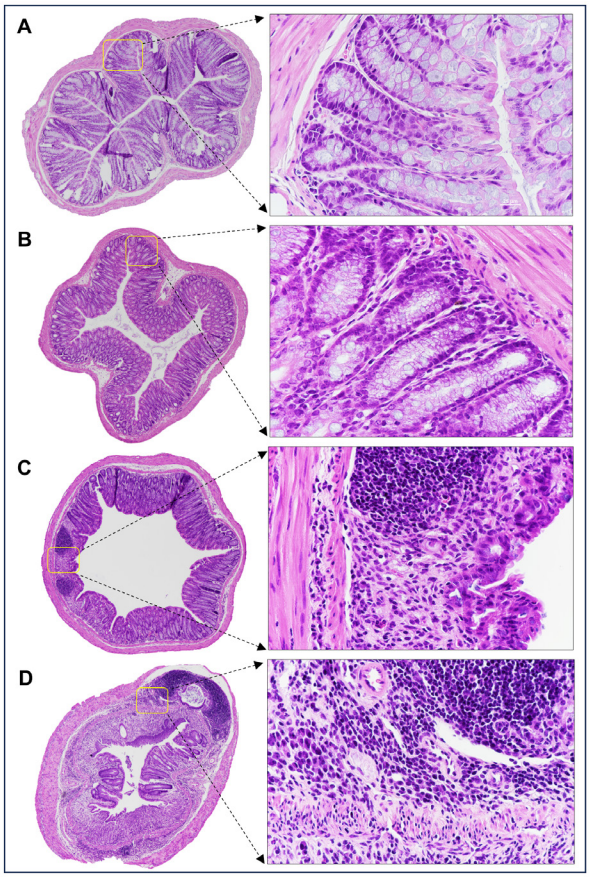

Figure 2. H&E staining of colon tissues removed on day 0, 15, 30, and 40 of the experiment. (**A**) Normal colon tissue on day 0. (**B**) Mild colitis on day 15, when the mice developed diarrhea. (**C**) The colon mucosa exhibited chronic inflammatory characteristics on day 30. (**D**) Colitis worsened on day 40, when a large number of leucocytes such as plasma cells and lymphocytes were observed in the mucosa and submucosa of colon tissue. Original magnification: 40× (left), 400× (right).

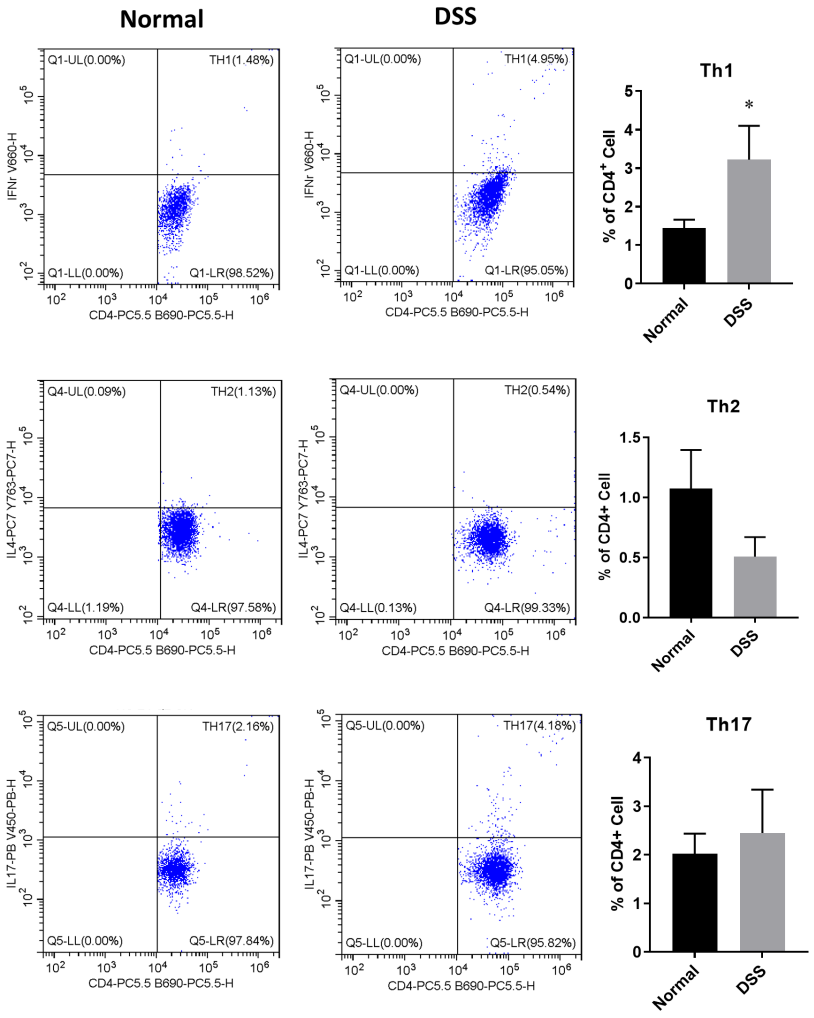

Figure 3. Alteration of Th cells in the mucosa of inflamed colon tissue. The mice were sacrificed on day 30 and the colon tissues were removed. Lymphocytes were extracted and subjected to flow cytometry. Cells that express both CD4 and IFN-γ were designated as Th1 cells, those that express both CD4 and IL-4 were designated as Th2 cells, and those that express both CD4 and IL-17A were designated as Th17 cells. The proportion of Th1 cells increased significantly in mice with DSS-induced colitis compared to that in normal mice. * $p < 0.05$.

mice with colitis increased significantly compared to that in normal mice, and the proportion of Th17 cells also tended to increase. Th1 and Th2 cells are generally believed to mediate the immune response in Crohn's disease and ulcerative colitis, respectively, while Th17 cells play an important role in both diseases (*13*). Therefore, this model of subacute colitis has certain prospects for use in the study of IBD.

3.3. Drug response in the model of subacute colitis

Mesalazine is an effective drug for treating IBD. The efficacy of mesalazine was noted in this model of subacute colitis. Starting on day 30, mice were orally administered mesalazine at a dose of 200 mg/kg twice daily for 10 days. At the end of the experiment, mice in the mesalazine treatment group had a significantly greater body weight and significantly longer colon length than those in the model group (Figure 4), indicating that mesalazine is effective at alleviating colitis in this model.

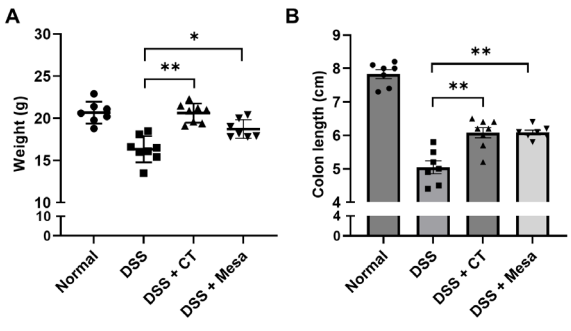

Figure 4. The body weight (A) and colon length (B) of mice at the end of the experiment. Starting on day 30, the mice were treated with Centella triterpenes or mesalazine for 10 days. Centella triterpenes and mesalazine markedly increased the body weight and colon length of mice compared to the vehicle. CT, Centella triterpenes; Mesa, mesalazine. * $p < 0.05$; ** $p < 0.01$.

Centella triterpenes mainly contain asiaticoside and madecassoside, which have anti-inflammatory

and wound healing action (*14*). Clinically, they are used to treat trauma, surgical wounds, burns, scars, and scleroderma in China. Studies have found that asiaticoside and madecassoside can alleviate the symptoms of acute colitis in a model at a dose of 50 mg/kg (*15*). In the current model, Centella triterpenes were orally administered at a dose of 1 mg/kg twice daily, significantly increasing the body weight and colon length of mice with colitis (Figure 4). Considering the conversion factor between mice and humans, this dose is close to the clinical dose of the drug, indicating that the mouse model of subacute colitis has advantages in evaluating the efficacy of drugs.

4. Conclusion

The use of a high-concentration DSS solution (approx. 3%) to induce acute colitis in mice in order to evaluate the efficacy of drugs has certain limitations. The current study found that mice, when freely consuming a lower concentration of a DSS solution (1-1.5%) for a duration of 10-15 days, exhibited milder symptoms of colitis. When intake of the DSS solution was continued for another 15-20 days, the mucosa of colon tissues exhibited characteristics of chronic inflammation, accompanied by a significant increase in the proportion of Th1 cells, indicating the involvement of an adaptive immune response. Subsequently, the mice were administered drug treatment for 10-15 days while consuming the DSS solution, allowing for the evaluation of the drug's efficacy against colitis. The advantages of this subacute model include minimal mortality of mice during the experimental process, the fact that the characteristics of murine intestinal mucosal inflammation resemble the pathological features of IBD in humans, and evaluating the efficacy of drugs to treat colitis in mice.

Funding: None.

Conflict of Interest: The authors have no conflicts of interest to disclose.

References

1. Annese V. Genetics and epigenetics of IBD. Pharmacol Res. 2020; 159:104892.
2. Ungaro R, Mehandru S, Allen PB, Peyrin-Biroulet L, Colombel JF. Ulcerative colitis. Lancet. 2017; 389:1756-1770.
3. Roda G, Chien Ng S, Kotze PG, Argollo M, Panaccione R, Spinelli A, Kaser A, Peyrin-Biroulet L, Danese S. Crohn's disease. Nat Rev Dis Primers. 2020; 6:22.
4. Wu Q, Wang X, Wu F, Peng D, Wu G, Yang L, Yuan L. Role of a multidisciplinary team (MDT) in the diagnosis, treatment, and outcomes of inflammatory bowel disease: A single Chinese center's experience. Biosci Trends. 2021; 15:171-179.
5. Geremia A, Biancheri P, Allan P, Corazza GR, Di Sabatino A. Innate and adaptive immunity in inflammatory bowel disease. Autoimmun Rev. 2014; 13:3-10.
6. Luo H, Cao G, Luo C, Tan D, Vong CT, Xu Y, Wang S, Lu H, Wang Y, Jing W. Emerging pharmacotherapy for inflammatory bowel diseases. Pharmacol Res. 2022; 178:106146.
7. Akram W, Garud N, Joshi R. Role of inulin as prebiotics on inflammatory bowel disease. Drug Discov Ther. 2019; 13:1-8.
8. Verstockt B, Ferrante M, Vermeire S, Van Assche G. New treatment options for inflammatory bowel diseases. J Gastroenterol. 2018; 53:585-590.
9. Katsandegwaza B, Horsnell W, Smith K. Inflammatory bowel disease: A review of pre-clinical murine models of human disease. Int J Mol Sci. 2022; 23:9344.
10. Wirtz S, Popp V, Kindermann M, Gerlach K, Weigmann B, Fichtner-Feigl S, Neurath MF. Chemically induced mouse models of acute and chronic intestinal inflammation. Nat Protoc. 2017; 12:1295-1309.
11. Chassaing B AJ, Malleshappa M, Vijay-Kumar M. Dextran sulfate sodium (DSS)-induced colitis in mice. Curr Protoc Immunol. 2014; 104:Unit-15.25.
12. Dieleman LA, Ridwan BU, Tennyson GS, Beagley KW, Bucy RP, Elson CO. Dextran sulfate sodium-induced colitis occurs in severe combined immunodeficient mice. Gastroentero. 1994; 107:1643-1652.
13. Jiang P, Zheng C, Xiang Y, Malik S, Su D, Xu G, Zhang M. The involvement of TH17 cells in the pathogenesis of IBD. Cytokine Growth Factor Rev. 2023; 69:28-42.
14. Sun B, Wu L, Wu Y, Zhang C, Qin L, Hayashi M, Kudo M, Gao M, Liu T. Therapeutic potential of *Centella asiatica* and its triterpenes: A review. Front Pharmacol. 2020; 11:568032.
15. Xu X, Wang Y, Wei Z, Wei W, Zhao P, Tong B, Xia Y, Dai Y. Madecassic acid, the contributor to the anti-colitis effect of madecassoside, enhances the shift of Th17 toward Treg cells *via* the PPARgamma/AMPK/ACC1 pathway. Cell Death Dis. 2017; 8:e2723.

Received March 14, 2023; Revised July 2, 2023; Accepted July 6, 2023.

[§]Both authors contributed equally to this work.
**Address correspondence to:*
Jianjun Gao, Department of Pharmacology, School of Pharmacy, Qingdao University, Qingdao, Shandong.
E-mail: gaojj@qdu.edu.cn

Shasha Hu, Department of Pathology, The Affiliated Hospital of Qingdao University, Qingdao, Shandong, China.
E-mail: huss0501@qdu.edu.cn

Released online in J-STAGE as advance publication July 12, 2023.

Brief Report

DOI: 10.5582/ddt.2023.01044

Higher serum AMH level is associated with better pregnancy outcomes of IVF/ICSI assisted pregnancy in infertile patients under 35 years old

Feijun Ye[1,§], Yan Du[2,3,§], Wenli Cao[1], Ruhe Jiang[2,3], Qing Qi[3,4,5], Hongmei Sun[3,4,5], Jing Zhou[3,4,5], Ling Wang[3,4,5,*]

[1] Reproductive Medicine Center, Zhoushan Maternal and Child Health Care Hospital, Zhoushan, Zhejiang, China;
[2] Clinical Research Unit, Obstetrics and Gynecology Hospital of Fudan University, Shanghai, China;
[3] Laboratory for Reproductive Immunology, Obstetrics and Gynecology Hospital of Fudan University, Shanghai, China;
[4] The Academy of Integrative Medicine, Fudan University, Shanghai, China;
[5] Shanghai Key Laboratory of Female Reproductive Endocrine-related Diseases, Shanghai, China.

SUMMARY This study aimed to investigate the effect of anti-Mullerian hormone (AMH) on the pregnancy outcome of infertility assisted by IVF/Micro-Insemination/Embryo Transfer Infertility Assistance (IVF/ICSI-ET). A total of 324 patients under the age of 35 who received IVF/ICSI-ET assistance in our center were included in this analysis. AMH levels of these patients were measured by chemiluminescence method and divided into clinical pregnancy group (175 cases) and non-pregnancy group (149 cases) according to the final pregnancy outcome. The relationship between the two groups' pregnancy outcomes and AMH levels was analyzed. The above association was re-evaluated after excluding patients with polycystic ovary syndrome. There was no significant difference in age, body mass index (BMI), follicle-stimulating hormone (FSH), and 2 pronucleus (PN) between clinical and non-clinical pregnancy groups. Compared with the clinical pregnancy group, the level of AMH in the non-pregnancy group was significantly lower ($p < 0.05$). A higher AMH level was closely related to better IVF/ICSI-ET assisted pregnancy outcome *in vitro*. After excluding AMH abnormalities, the AMH level was still significantly associated with pregnancy outcomes of *in vitro* IVF/ICSI-ET-assisted pregnancy. Our results show a correlation between AMH level and pregnancy outcome of *in vitro* IVF/ICSI-ET assisted pregnancy. For women under age 35, lower AMH levels may be one of the predictors of adverse pregnancy outcomes. For patients with low AMH level, it is suggested to strengthen monitoring to ensure the safety and smoothness of the pregnancy process.

Keywords infertility, *in vitro* fertilization-embryo transfer, pregnancy outcome, AMH

1. Introduction

"Infertility" refers to a couple's failed pregnancy after 12 months of unprotected sexual intercourse and pregnancy attempts. Infertility is increasing yearly, affecting about 15-20% of couples worldwide (*1*). About 85% of cases have a clear cause, such as ovulatory dysfunction, male infertility, or fallopian tube lesions. However, there are unexplained infertility cases where the cause is unknown.

It is important to note that lifestyle and environmental factors like smoking and obesity can negatively affect fertility (*2*). Aggravation of environmental pollution has particularly contributed to the occurrence of infertility. Exposure to perfluoroalkyl substances (PFAS) may be associated with decreased fertility. Higher PFAS exposure may lead to a decline in female fertility (*3*). Exposure to ambient air pollutants (such as sulfur dioxide) may potentially adversely affect male semen quality (*4*). In addition, ovarian reserve was negatively correlated with women's exposure to air pollutants (*5*).

For infertile patients, assisted reproductive technology (ART) has become their hope of becoming parents (*6*). ART, or *in vitro* fertilization and embryo transfer (IVF-ET), is an advanced reproductive technique that helps infertile individuals achieve pregnancy and treat fertility issues by facilitating the birth of healthy babies. The ART program includes processing eggs or embryos *in vitro* to promote fertilization and embryonic

development. The current ART process covers IVF and possible intracytoplasmic sperm injection (IVF/ICSI) (*7*).

Unfortunately, even with the help of IVF-ET technology, not all infertile people can achieve clinical pregnancy results for various reasons (*8*). Existing studies have shown that infertility is associated with adverse pregnancy outcomes, with or without fertility treatment (*9*). Certain lifestyle factors have also been found to impress the pregnancy outcomes of IVF/ICSI treatment. For example, women drinking > 84 grams/week were related to a lower pregnancy rate, while men drinking > 84 grams/week were linked to a lower live birth rate after IVF/ICSI treatment (*10*). The study also found that after age adjustment, the live birth rate decreased significantly as the duration of infertility increased from 1 year to 12 years. Fertility (that is, the possibility of becoming pregnant during a menstrual cycle) begins to decline significantly in the early thirties and even faster a few years later (around the age of 37) (*11,12*). However, our understanding of the factors affecting the success rate of *in vitro* pregnancy is still limited, which limits the optimization of IVF/ICSI treatment to improve the outcome of assisted pregnancy in infertile patients.

Anti-Mullerian hormone (AMH), a hormone produced by follicular granulosa cells, reflects the continuity of ovarian functional reserve, which can predict the response of ovary to gonadotropin stimulation and be used in individualized treatment strategy to improve the efficacy and safety of treatment (*13*). AMH is supposed to indicate the likelihood of success in controlled ovarian stimulation (COS) (*14*). AMH levels are utilized to evaluate ovarian reserves and aid in ovulation induction programs for women undergoing IVF cycles. However, the impact of AMH levels on pregnancy outcomes in IVF/ICSI is not fully understood. To address this, we conducted a retrospective analysis of the correlation between pre-pregnancy AMH levels and pregnancy outcomes in women less than 35 years of age who received IVF/ICSI-assisted pregnancy.

2. Materials and Methods

2.1. Study population

Three hundred seventy assisted pregnancy patients who met the indications of IVF-ET from January 2021 to December 2022 were screened, of which 324 were less than 35 years old. Patients were divided into two groups according to pregnancy outcome: clinical pregnancy group (confirmed to be pregnant by ultrasound); non-clinical pregnancy group (serum or urine examination indicated increased progesterone or human chorionic gonadotropin, but pregnancy was not confirmed by ultrasound; or patients who were not pregnant by biochemistry and ultrasound). The study was approved by the Institutional Review Board of Zhoushan Maternal and Child Health Hospital and followed the ethical guidelines of the 2000 Declaration of Helsinki. All the participants signed the informed consent document. Figure 1 is a flowchart of the study.

2.2. Data collection

AMH was detected on a model iFlash 3000 (Yahuilong Company, Shenzhen, Guangdong, China) using the chemiluminescence method, following the manufacturer's instructions. Follicle-stimulating hormone (FSH) and 2 pronucleus (PN) were extracted from medical records. Body mass index (BMI) was calculated as weight (kg)/ height $(m)^2$.

2.3. Determination of pregnancy

Clinical pregnancy was determined according to the results of ultrasound, which was performed using the GE Voluson E11 system (General Electric Medical Systems, Milwaukee, WI, USA). If the ultrasonic examination did not detect a pregnancy, and combined with human chorionic gonadotropin (hCG) < 7 U/mL, then it was judged as not a clinical pregnancy. hCG was determined using the hCG diagnostic reagent kits (Roche Diagnostic Reagent Co., Ltd. Marburg, Germany), according to the manufacturer's instructions. The detection method of hCG is electrochemiluminescence, using the Cobas e601 type electrochemiluminescence instrument (Roche Diagnostics, Indianapolis, IN, USA).

2.4. Statistical analyses

To compare the difference between the two groups, mean ± standard deviation (SD) was presented for normally distributed continuous variables, and *t*-test was used. Data were expressed as numbers and percentages for categorical variables, and the chi-square test was used. SPSS version 25.0 was utilized for the statistical analysis, with a significance threshold set at two-sided $p < 0.05$.

3. Results and Discussion

The BMI, FSH, and 2PN indexes remained indistinguishable between the clinical and non-clinical pregnancy group (Table 1). As shown in Figure 2, the average AMH level of the clinical pregnancy group (4.795 ± 3.12 ng/mL) notably increased compared to the non-pregnancy group (3.802 ± 2.13 ng/mL) ($p = 0.0025$).

As one of leading causes for female infertility worldwide, about 10% of patients with polycystic ovary syndrome (PCOS) seek ART (*15*).PCOS is an endocrine disease with metabolic abnormalities, and one of the characteristics of the disease is elevated levels of AMH (*16*). To rule out whether the increase of AMH in the two groups of our results is caused by subsequent diagnosis of PCOS patients, we performed subgroup analyses in non-PCOS patients.

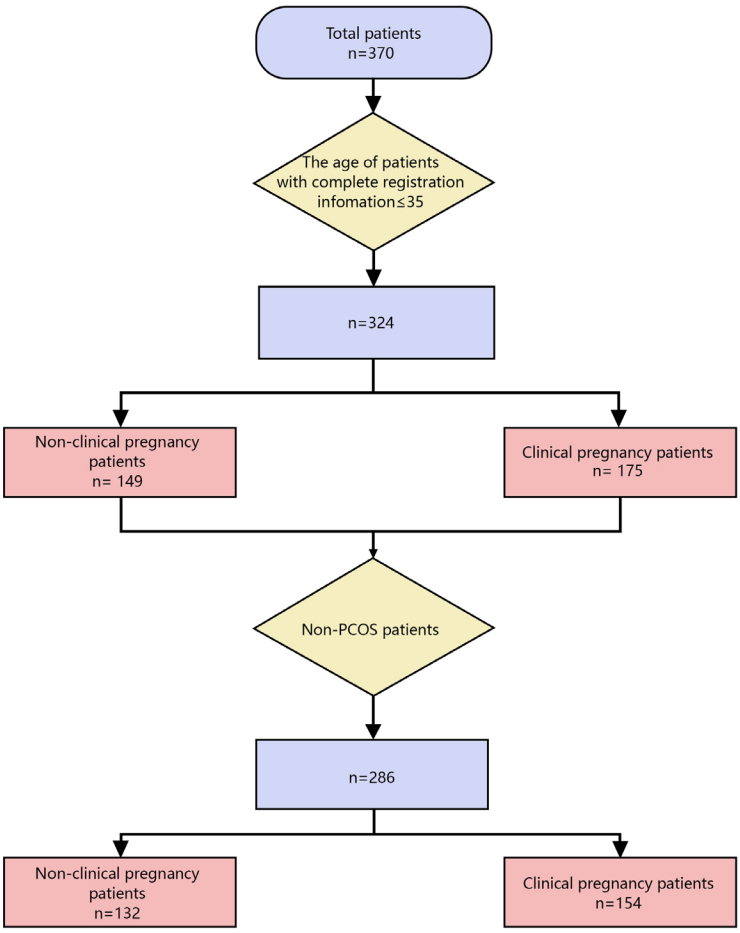

Figure 1. Study flowchart.

Table 1. Characteristics of non-clinical pregnancy *vs.* clinical pregnancy group

	Non-clinical pregnancy (n = 149)	Clinical pregnancy (n = 175)	p
Age	30.08 ± 2.80	30.70 ± 2.80	0.99
BMI	21.99 ± 3.30	22.32 ± 3.11	0.35
FSH	6.55 ± 2.06	6.41 ± 1.85	0.53
2PN	6.02 ± 3.24	5.36 ± 3.02	0.06
Years of infertility	3.31 ± 2.16	3.39 ± 2.48	0.92

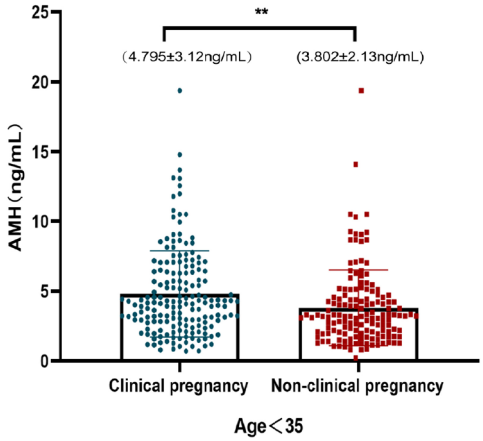

Figure 2. The level of AMH in patients under 35 years old, clinical pregnancy group (4.795 ± 3.12 ng/mL) *vs.* non-pregnancy group (3.802 ± 2.13 ng/mL). Each point represents a patient. The unit of AMH is ng/mL (**, p = 0.0025).

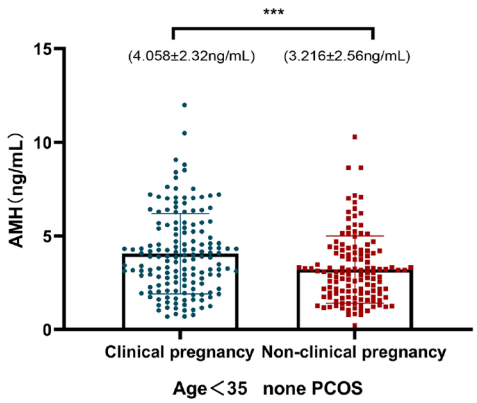

Figure 3. The level of AMH in patients under 35 years old without PCOS, clinical pregnancy group (4.058 ± 2.32 ng/mL) *vs.* non-pregnancy group (3.216 ± 2.56 ng/mL). Each point represents a patient. The unit of AMH is ng/mL (***, p = 0.0004).

In our study, 37 (11.4%) patients were later diagnosed with PCOS. After excluding these patients, the remaining 286 non-PCOS assisted pregnancies were used for subgroup analysis. As shown in Figure 3, the average AMH level of the clinically pregnant group (4.058 ± 2.32 ng/mL) was markedly higher than that of the non-pregnant group (3.216 ± 2.56 ng/mL) ($p < 0.05$).

The research on the pregnancy outcome of women using IVF-ET is still very limited. Therefore, it is of significant value to identify variables associated with the

pregnancy outcome and closely monitor them to improve the safety and smoothness of the pregnancy process. The current study focused on patients under 35 years of age receiving IVF/ICSI. The results showed obvious differences in AMH between the clinical pregnancy group with successful *in vitro* assisted pregnancy and those who failed to reach the clinical pregnancy stage. Specifically, AMH levels were positively correlated with successful clinical pregnancy assisted by IVF/ICSI. After excluding subsequent diagnosed PCOS patients, the high level of AMH was still positively related to the successful clinical pregnancy outcom*es* in *in vitro* assisted pregnancy, indicating that AMH may be a predictive index.

Recently, the research of AMH has made important progress in reproductive medicine. A retrospective cohort study found that serum AMH levels influenced pregnancy outcomes treated with gonadotropin-releasing hormone antagonists, indicating the positive role of AMH levels in predicting ovarian response and pregnancy outcomes (*17*). Another study revealed that AMH and antral follicle count (AFC) could forecast the final obtained egg number and the effect of embryo freezing during IVF cycles; high AMH and AFC were positively correlated with the number of collected oocytes (*18*). Furthermore, a cohort study found that young women with high AMH levels were more likely to experience an early miscarriage during their first IVF/ICSI procedure compared with women with intermediate AMH levels, suggesting that high AMH levels may be a risk factor of early miscarriage (*19*). A study discovered that young women with elevated AMH levels were more prone to early miscarriage during their initial IVF/ICSI treatment than those with moderate AMH levels. In young women, serum AMH levels were independently linked to the risk of early abortion after IVF-ET treatment (*20*). The results based on follicular fluid have shown that the AMH of follicular fluid matched by oocytes is a valuable index for predicting live birth after fresh single embryo transfer (*21*). However, whether there is any relationship between serum AMH and IVF/ICSI pregnancy outcome in infertile patients has not been fully evaluated.

In women, the production of AMH begins in the later stage of the fetus and continues into adulthood, then decreases steadily throughout the reproductive years until a severe decline during menopause, and finally to a level that cannot be detected (*22*). AMH is crucial in regulating various stages of follicular development and functions as a neuroendocrine hormone. Additionally, serum AMH levels are widely accepted as a dependable indicator of ovarian reserve, predicting the occurrence of PCOS and primary ovarian failure (*23*). Our study results suggest that the IVF/ICSI treatment regimen adjusted according to the level of AMH may improve the success rate of pregnancy and reduce the time and cost of treatment. For example, in women with lower levels of AMH, higher doses of ovulation-inducing drugs can stimulate follicular development to obtain more eggs and improve the pregnancy success rate. The relationship between the level of AMH as an indicator of ovarian reserve function and the clinical pregnancy rate of *in vitro* pregnancy is not fully understood. Further understanding of the mechanism of AMH in *in vitro* pregnancy outcomes can help adjust targeted assisted pregnancy program based on AMH levels to improve the success rate of out-of-vitro pregnancy in infertile patients.

Our research provides preliminary information for understanding AMH and *in vitro* pregnancy outcomes. However, considering our results are based on retrospective analysis from a single center, there may be biases and confounding factors influencing the study results. Due to the nature of the study design, we can only evaluate the association but not causal relationship. Studies are needed to determine the underlying mechanism to improve the clinical intervention of patients with low AMH and improve the *in vitro* pregnancy outcomes. In addition, future research could explore whether it can effectively improve the pregnancy success rate of low-AMH patients under the age of 35 by optimizing interventions for this population, such as supplementation with AMH (*24*).

To conclude, our results show that AMH levels were positively associated with clinical pregnancy outcomes of *in vitro* assisted pregnancy. To enhance the clinical pregnancy success rate of patients with low AMH assisted pregnancy and ensure the safety and smoothness of the pregnancy process, we need to carry out closer monitoring and adjust the intervention measures for low-AMH assisted pregnancy.

Funding: This work was supported by grants from a project under the Scientific and Technological Innovation Action Plan of the Shanghai Natural Science Fund (grant No. 20ZR1409100 to L Wang), a project of the Chinese Association of Integration of Traditional and Western Medicine special foundation for Obstetrics and Gynecology-PuZheng Pharmaceutical Foundation (grant No. FCK-PZ-08 to L Wang), a project for hospital management of the Shanghai Hospital Association (grant No. X2021046 to L Wang), a clinical trial project of the Special Foundation for Healthcare Research of the Shanghai Municipal Health Commission (grant No. 202150042 to L Wang), a project of the National Science Foundation of Gansu province (grant No. 23JRRG0009 to HM Sun), a project of the Innovation Foundation of Higher Education of Gansu Province (grant No. 2021B-239 to HM Sun), a project of the Chinese Association of Integration of Traditional and Western Medicine special foundation for Obstetrics and Gynecology (grant No. FCK-ZSYTW-04 to Q Qi) and a grant from Science and Technology Plan of Zhoushan City, Zhejiang Province (grant No. 2021C31055 to WL Cao).

Conflict of Interest: The authors have no conflicts of interest to disclose.

References

1. Harris E. Infertility affects 1 in 6 people globally. JAMA. 2023; 329:1443.
2. Carson SA, Kallen AN. Diagnosis and management of infertility: A review. JAMA. 2021; 326:65-76.
3. Cohen NJ, Yao M, Midya V, *et al*. Exposure to perfluoroalkyl substances and women's fertility outcomes in a Singaporean population-based preconception cohort. Sci Total Environ. 2023; 873:162267.
4. Zhang F, Li H, Xu W, *et al*. Sulfur dioxide may predominate in the adverse effects of ambient air pollutants on semen quality among the general population in Hefei, China. Sci Total Environ. 2023; 867:161472.
5. Lang M, Zhou M, Lei R, Li W. Comparison of pregnancy outcomes between IVF-ET pregnancies and spontaneous pregnancies in women of advanced maternal age. J Matern Fetal Neonatal Med. 2023; 36:2183761.
6. Schweizer S, Andrews JL, Grunewald K, Kumle L. Association of antenatal COVID-19-related stress with postpartum maternal mental health and negative affectivity in infants. JAMA Netw Open. 2023; 6:e232969.
7. Berntsen S, Söderström-Anttila V, Wennerholm UB, Laivuori H, Loft A, Oldereid NB, Romundstad LB, Bergh C, Pinborg A. The health of children conceived by ART: 'The chicken or the egg?'. Hum Reprod Update. 2019; 25:137-158.
8. Gaskins AJ, Zhang Y, Chang J, Kissin DM. Predicted probabilities of live birth following assisted reproductive technology using United States national surveillance data from 2016 to 2018. Am J Obstet Gynecol. 2023; 228:557.e551-557.e510.
9. Luke B, Gopal D, Cabral H, Stern JE, Diop H. Pregnancy, birth, and infant outcomes by maternal fertility status: The Massachusetts outcomes study of assisted reproductive technology. Am J Obstet Gynecol. 2017; 217:327.e321-327.e314.
10. Gilmore W, Chikritzhs T, Stockwell T, Jernigan D, Naimi T, Gilmore I. Alcohol: Taking a population perspective. Nat Rev Gastroenterol Hepatol. 2016; 13:426-434.
11. Broer SL, Broekmans FJ, Laven JS, Fauser BC. Anti-Müllerian hormone: Ovarian reserve testing and its potential clinical implications. Hum Reprod Update. 2014; 20:688-701.
12. Faddy MJ, Gosden RG, Gougeon A, Richardson SJ, Nelson JF. Accelerated disappearance of ovarian follicles in mid-life: Implications for forecasting menopause. Hum Reprod. 1992; 7:1342-1346.
13. Hou Y, Wang L, Li Y, Ai J, Tian L. Serum levels of anti-Müllerian hormone influence pregnancy outcomes associated with gonadotropin-releasing hormone antagonist treatment: A retrospective cohort study. Sci Rep. 2023; 13:2127.
14. Salama S, Sharaf M, Salem SM, Rasheed MA, Salama E, Elnahas T, Lotfy R. FSH versus AMH: Age-related relevance to ICSI results. Middle East Fertil Soc J. 2021; 26:27.
15. Joham AE, Norman RJ, Stener-Victorin E, Legro RS, Franks S, Moran LJ, Boyle J, Teede HJ. Polycystic ovary syndrome. Lancet Diabetes Endocrinol. 2022; 10:668-680.
16. Kotanidis L, Nikolettos K, Petousis S, Asimakopoulos B, Chatzimitrou E, Kolios G, Nikolettos N. The use of serum anti-Mullerian hormone (AMH) levels and antral follicle count (AFC) to predict the number of oocytes collected and availability of embryos for cryopreservation in IVF. J Endocrinol Invest. 2016; 39:1459-1464.
17. Liu X, Han Y, Wang X, Zhang Y, Du A, Yao R, Lv J, Luo H. Serum anti-Müllerian hormone levels are associated with early miscarriage in the IVF/ICSI fresh cycle. BMC Pregnancy Childbirth. 2022; 22:279.
18. Peuranpää P, Hautamäki H, Halttunen-Nieminen M, Hydén-Granskog C, Tiitinen A. Low anti-Müllerian hormone level is not a risk factor for early pregnancy loss in IVF/ICSI treatment. Hum Reprod. 2020; 35:504-515.
19. Tal R, Seifer CM, Khanimov M, Seifer DB, Tal O. High serum antimullerian hormone levels are associated with lower live birth rates in women with polycystic ovarian syndrome undergoing assisted reproductive technology. Reprod Biol Endocrinol. 2020; 18:20.
20. Dewailly D, Robin G, Peigne M, Decanter C, Pigny P, Catteau-Jonard S. Interactions between androgens, FSH, anti-Müllerian hormone and estradiol during folliculogenesis in the human normal and polycystic ovary. Hum Reprod Update. 2016; 22:709-724.
21. di Clemente N, Racine C, Pierre A, Taieb J. Anti-Müllerian hormone in female reproduction. Endocr Rev. 2021; 42:753-782.
22. La Marca A, Sunkara SK. Individualization of controlled ovarian stimulation in IVF using ovarian reserve markers: From theory to practice. Hum Reprod Update. 2014; 20:124-140.
23. Haddad-Filho H, Tosatti JAG, Vale FM, Gomes KB, Reis FM. Updates in diagnosing polycystic ovary syndrome-related infertility. Expert Rev Mol Diagn. 2023; 23:123-132.

Received July 11, 2023; Revised August 11, 2023; Accepted August 12, 2023.

[§]These authors contributed equally to this work.
**Address correspondence to:*
Ling Wang, Laboratory for Reproductive Immunology, Obstetrics and Gynecology Hospital of Fudan University, 419 Fangxie Road, Shanghai, China.
E-mail: dr.wangling@fudan.edu.cn

Released online in J-STAGE as advance publication August 17, 2023.

DD&T
Drug Discoveries & Therapeutics

Guide for Authors

1. Scope of Articles

Drug Discoveries & Therapeutics (Print ISSN 1881-7831, Online ISSN 1881-784X) welcomes contributions in all fields of pharmaceutical and therapeutic research such as medicinal chemistry, pharmacology, pharmaceutical analysis, pharmaceutics, pharmaceutical administration, and experimental and clinical studies of effects, mechanisms, or uses of various treatments. Studies in drug-related fields such as biology, biochemistry, physiology, microbiology, and immunology are also within the scope of this journal.

2. Submission Types

Original Articles should be well-documented, novel, and significant to the field as a whole. An Original Article should be arranged into the following sections: Title page, Abstract, Introduction, Materials and Methods, Results, Discussion, Acknowledgments, and References. Original articles should not exceed 5,000 words in length (excluding references) and should be limited to a maximum of 50 references. Articles may contain a maximum of 10 figures and/or tables. Supplementary Data are permitted but should be limited to information that is not essential to the general understanding of the research presented in the main text, such as unaltered blots and source data as well as other file types.

Brief Reports definitively documenting either experimental results or informative clinical observations will be considered for publication in this category. Brief Reports are not intended for publication of incomplete or preliminary findings. Brief Reports should not exceed 3,000 words in length (excluding references) and should be limited to a maximum of 4 figures and/or tables and 30 references. A Brief Report contains the same sections as an Original Article, but the Results and Discussion sections should be combined.

Reviews should present a full and up-to-date account of recent developments within an area of research. Normally, reviews should not exceed 8,000 words in length (excluding references) and should be limited to a maximum of 10 figures and/or tables and 100 references. Mini reviews are also accepted, which should not exceed 4,000 words in length (excluding references) and should be limited to a maximum of 5 figures and/or tables and 50 references.

Policy Forum articles discuss research and policy issues in areas related to life science such as public health, the medical care system, and social science and may address governmental issues at district, national, and international levels of discourse. Policy Forum articles should not exceed 3,000 words in length (excluding references) and should be limited to a maximum of 5 figures and/or tables and 30 references.

Case Reports should be detailed reports of the symptoms, signs, diagnosis, treatment, and follow-up of an individual patient. Case reports may contain a demographic profile of the patient but usually describe an unusual or novel occurrence. Unreported or unusual side effects or adverse interactions involving medications will also be considered. Case Reports should not exceed 3,000 words in length (excluding references).

Communications are short, timely pieces that spotlight new research findings or policy issues of interest to the field of global health and medical practice that are of immediate importance. Depending on their content, Communications will be published as "Comments" or "Correspondence". Communications should not exceed 1,500 words in length (excluding references) and should be limited to a maximum of 2 figures and/or tables and 20 references.

Editorials are short, invited opinion pieces that discuss an issue of immediate importance to the fields of global health, medical practice, and basic science oriented for clinical application. Editorials should not exceed 1,000 words in length (excluding references) and should be limited to a maximum of 10 references. Editorials may contain one figure or table.

News articles should report the latest events in health sciences and medical research from around the world. News should not exceed 500 words in length.

Letters should present considered opinions in response to articles published in *Drug Discoveries & Therapeutics* in the last 6 months or issues of general interest. Letters should not exceed 800 words in length and may contain a maximum of 10 references. Letters may contain one figure or table.

3. Editorial Policies

For publishing and ethical standards, *Drug Discoveries & Therapeutics* follows the Recommendations for the Conduct, Reporting, Editing, and Publication of Scholarly Work in Medical Journals issued by the International Committee of Medical Journal Editors (ICMJE, *https://icmje.org/recommendations*), and the Principles of Transparency and Best Practice in Scholarly Publishing jointly issued by the Committee on Publication Ethics (COPE, *https://publicationethics.org/resources/guidelines-new/principles-transparency-and-best-practice-scholarly-publishing*), the Directory of Open Access Journals (DOAJ, *https://doaj.org/apply/transparency*), the Open Access Scholarly Publishers Association (OASPA, *https://oaspa.org/principles-of-transparency-and-best-practice-in-scholarly-publishing-4*), and the World Association of Medical Editors (WAME, *https://wame.org/principles-of-transparency-and-best-practice-in-scholarly-publishing*).

Drug Discoveries & Therapeutics will perform an especially prompt review to encourage innovative work. All original research will be subjected to a rigorous standard of peer review and will be edited by experienced copy editors to the highest standards.

Ethical Approval of Studies and Informed Consent: For all manuscripts reporting data from studies involving human participants or animals, formal review and approval, or formal review and waiver, by an appropriate institutional review board or ethics committee is required and should be described in the Methods section. When your manuscript contains any case details, personal information and/or images of patients or other individuals, authors must obtain appropriate written consent, permission and release in order to comply with all applicable laws and regulations concerning privacy and/or security of personal information. The consent form needs to comply with the relevant legal requirements of your particular jurisdiction, and please do not send signed consent form to *Drug Discoveries & Therapeutics* to respect your patient's and any other individual's privacy. Please instead describe the information clearly in the Methods (patient consent) section of your manuscript while retaining copies of the signed forms in the event they should be needed. Authors should also state that the study conformed to the provisions of the Declaration of Helsinki (as revised in 2013, *https://wma.net/what-we-do/medical-ethics/declaration-of-helsinki*). When reporting experiments on animals, authors should indicate whether the institutional and national guide for the care and use of laboratory animals was followed.

Reporting Clinical Trials: The ICMJE (*https:// icmje.org/recommendations/browse/publishing-and-editorial-issues/clinical-trial-registration.html*) defines a clinical trial as any research project that prospectively assigns people or a group of people to an intervention, with or without concurrent comparison or control groups, to study the relationship between a health-related intervention and a health outcome. Registration of clinical trials in a public trial registry

at or before the time of first patient enrollment is a condition of consideration for publication in *Drug Discoveries & Therapeutics*, and the trial registration number will be published at the end of the Abstract. The registry must be independent of for-profit interest and publicly accessible. Reports of trials must conform to CONSORT 2010 guidelines (*https://consort-statement.org/consort-2010*). Articles reporting the results of randomized trials must include the CONSORT flow diagram showing the progress of patients throughout the trial.

Conflict of Interest: All authors are required to disclose any actual or potential conflict of interest including financial interests or relationships with other people or organizations that might raise questions of bias in the work reported. If no conflict of interest exists for each author, please state "There is no conflict of interest to disclose".

Submission Declaration: When a manuscript is considered for submission to *Drug Discoveries & Therapeutics*, the authors should confirm that 1) no part of this manuscript is currently under consideration for publication elsewhere; 2) this manuscript does not contain the same information in whole or in part as manuscripts that have been published, accepted, or are under review elsewhere, except in the form of an abstract, a letter to the editor, or part of a published lecture or academic thesis; 3) authorization for publication has been obtained from the authors' employer or institution; and 4) all contributing authors have agreed to submit this manuscript.

Initial Editorial Check: Immediately after submission, the journal's managing editor will perform an initial check of the manuscript. A suitable academic editor will be notified of the submission and invited to check the manuscript and recommend reviewers. Academic editors will check for plagiarism and duplicate publication at this stage. The journal has a formal recusal process in place to help manage potential conflicts of interest of editors. In the event that an editor has a conflict of interest with a submitted manuscript or with the authors, the manuscript, review, and editorial decisions are managed by another designated editor without a conflict of interest related to the manuscript.

Peer Review: *Drug Discoveries & Therapeutics* operates a single-anonymized review process, which means that reviewers know the names of the authors, but the authors do not know who reviewed their manuscript. All articles are evaluated objectively based on academic content. External peer review of research articles is performed by at least two reviewers, and sometimes the opinions of more reviewers are sought. Peer reviewers are selected based on their expertise and ability to provide quality, constructive, and fair reviews. For research manuscripts, the editors may, in addition, seek the opinion of a statistical reviewer. Every reviewer is expected to evaluate the manuscript in a timely, transparent, and ethical manner, following the COPE guidelines (*https://publicationethics.org/files/cope-ethical-guidelines-peer-reviewers-v2_0.pdf*). We ask authors for sufficient revisions (with a second round of peer review, when necessary) before a final decision is made. Consideration for publication is based on the article's originality, novelty, and scientific soundness, and the appropriateness of its analysis.

Suggested Reviewers: A list of up to 3 reviewers who are qualified to assess the scientific merit of the study is welcomed. Reviewer information including names, affiliations, addresses, and e-mail should be provided at the same time the manuscript is submitted online. Please do not suggest reviewers with known conflicts of interest, including participants or anyone with a stake in the proposed research; anyone from the same institution; former students, advisors, or research collaborators (within the last three years); or close personal contacts. Please note that the Editor-in-Chief may accept one or more of the proposed reviewers or may request a review by other qualified persons.

Language Editing: Manuscripts prepared by authors whose native language is not English should have their work proofread by a native English speaker before submission. If not, this might delay the publication of your manuscript in *Drug Discoveries & Therapeutics*.

The Editing Support Organization can provide English proofreading, Japanese-English translation, and Chinese-English translation services to authors who want to publish in *Drug Discoveries & Therapeutics* and need assistance before submitting a manuscript. Authors can visit this organization directly at *https://www.iacmhr.com/iac-eso/support.php?lang=en. IAC-ESO* was established to facilitate manuscript preparation by researchers whose native language is not English and to help edit works intended for international academic journals.

Copyright and Reuse: Before a manuscript is accepted for publication in *Drug Discoveries & Therapeutics*, authors will be asked to sign a transfer of copyright agreement, which recognizes the common interest that both the journal and author(s) have in the protection of copyright. We accept that some authors (*e.g.*, government employees in some countries) are unable to transfer copyright. A JOURNAL PUBLISHING AGREEMENT (JPA) form will be e-mailed to the authors by the Editorial Office and must be returned by the authors by mail, fax, or as a scan. Only forms with a hand-written signature from the corresponding author are accepted. This copyright will ensure the widest possible dissemination of information. Please note that the manuscript will not proceed to the next step in publication until the JPA Form is received. In addition, if excerpts from other copyrighted works are included, the author(s) must obtain written permission from the copyright owners and credit the source(s) in the article.

4. Cover Letter

The manuscript must be accompanied by a cover letter prepared by the corresponding author on behalf of all authors. The letter should indicate the basic findings of the work and their significance. The letter should also include a statement affirming that all authors concur with the submission and that the material submitted for publication has not been published previously or is not under consideration for publication elsewhere. The cover letter should be submitted in PDF format. For an example of Cover Letter, please visit: Download Centre (*https://www.ddtjournal.com/downcentre)*.

5. Submission Checklist

The Submission Checklist should be submitted when submitting a manuscript through the Online Submission System. Please visit Download Centre (*https://www.ddtjournal.com/downcentre)* and download the Submission Checklist file. We recommend that authors use this checklist when preparing your manuscript to check that all the necessary information is included in your article (if applicable), especially with regard to Ethics Statements.

6. Manuscript Preparation

Manuscripts are suggested to be prepared in accordance with the "Recommendations for the Conduct, Reporting, Editing, and Publication of Scholarly Work in Medical Journals", as presented at *http://www.ICMJE.org*.

Manuscripts should be written in clear, grammatically correct English and submitted as a Microsoft Word file in a single-column format. Manuscripts must be paginated and typed in 12-point Times New Roman font with 24-point line spacing. Please do not embed figures in the text. Abbreviations should be used as little as possible and should be explained at first mention unless the term is a well-known abbreviation (*e.g.* DNA). Single words should not be abbreviated.

Title page: The title page must include 1) the title of the paper (Please note the title should be short, informative, and contain the major key words); 2) full name(s) and affiliation(s) of the author(s), 3) abbreviated names of the author(s), 4) full name, mailing address, telephone/fax numbers, and e-mail address of the corresponding author; 5) author contribution statements to specify the individual contributions of all authors to this manuscript, and 6) conflicts of interest (if you have an actual or potential conflict of interest to disclose, it must be included as a footnote on the title page of the manuscript; if no conflict of interest

exists for each author, please state "There is no conflict of interest to disclose").

Abstract: The abstract should briefly state the purpose of the study, methods, main findings, and conclusions. For article types including Original Article, Brief Report, Review, Policy Forum, and Case Report, a one-paragraph abstract consisting of no more than 250 words must be included in the manuscript. For Communications, Editorials, News, or Letters, a brief summary of main content in 150 words or fewer should be included in the manuscript. For articles reporting clinical trials, the trial registration number should be stated at the end of the Abstract. Abbreviations must be kept to a minimum and non-standard abbreviations explained in brackets at first mention. References should be avoided in the abstract. Three to six key words or phrases that do not occur in the title should be included in the Abstract page.

Introduction: The introduction should provide sufficient background information to make the article intelligible to readers in other disciplines and sufficient context clarifying the significance of the experimental findings.

Materials/Patients and Methods: The description should be brief but with sufficient detail to enable others to reproduce the experiments. Procedures that have been published previously should not be described in detail but appropriate references should simply be cited. Only new and significant modifications of previously published procedures require complete description. Names of products and manufacturers with their locations (city and state/country) should be given and sources of animals and cell lines should always be indicated. All clinical investigations must have been conducted in accordance with the Declaration of Helsinki (as revised in 2013, *https://wma.net/what-we-do/medical-ethics/declaration-of-helsinki*). All human and animal studies must have been approved by the appropriate institutional review board(s) and a specific declaration of approval must be made within this section.

Results: The description of the experimental results should be succinct but in sufficient detail to allow the experiments to be analyzed and interpreted by an independent reader. If necessary, subheadings may be used for an orderly presentation. All Figures and Tables should be referred to in the text in order, including those in the Supplementary Data.

Discussion: The data should be interpreted concisely without repeating material already presented in the Results section. Speculation is permissible, but it must be well-founded, and discussion of the wider implications of the findings is encouraged. Conclusions derived from the study should be included in this section.

Acknowledgments: All funding sources (including grant identification) should be credited in the Acknowledgments section. Authors should also describe the role of the study sponsor(s), if any, in study design; in the collection, analysis, and interpretation of data; in the writing of the report; and in the decision to submit the paper for publication. If the funding source had no such involvement, the authors should so state.

In addition, people who contributed to the work but who do not meet the criteria for authors should be listed along with their contributions.

References: References should be numbered in the order in which they appear in the text. Citing of unpublished results, personal communications, conference abstracts, and theses in the reference list is not recommended but these sources may be mentioned in the text. In the reference list, cite the names of all authors when there are fifteen or fewer authors; if there are sixteen or more authors, list the first three followed by *et al*. Names of journals should be abbreviated in the style used in PubMed. Authors are responsible for the accuracy of the references. The EndNote Style of *Drug Discoveries & Therapeutics* could be downloaded at **EndNote** (*https://www.ddtjournal.com/examples/Drug_Discoveries_Therapeutics.ens*).

Examples are given below:

Example 1 (Sample journal reference):

Nakata M, Tang W. Japan-China Joint Medical Workshop on Drug Discoveries and Therapeutics 2008: The need of Asian pharmaceutical researchers' cooperation. Drug Discov Ther. 2008; 2:262-263.

Example 2 (Sample journal reference with more than 15 authors):

Darby S, Hill D, Auvinen A, *et al*. Radon in homes and risk of lung cancer: Collaborative analysis of individual data from 13 European case-control studies. BMJ. 2005; 330:223.

Example 3 (Sample book reference):

Shalev AY. Post-traumatic stress disorder: Diagnosis, history and life course. In: Post-traumatic Stress Disorder, Diagnosis, Management and Treatment (Nutt DJ, Davidson JR, Zohar J, eds.). Martin Dunitz, London, UK, 2000; pp. 1-15.

Example 4 (Sample web page reference):

World Health Organization. The World Health Report 2008 – primary health care: Now more than ever. *https://apps.who.int/iris/handle/10665/43949* (accessed September 23, 2022).

Tables: All tables should be prepared in Microsoft Word or Excel and should be arranged at the end of the manuscript after the References section. Please note that tables should not in image format. All tables should have a concise title and should be numbered consecutively with Arabic numerals. If necessary, additional information should be given below the table.

Figure Legend: The figure legend should be typed on a separate page of the main manuscript and should include a short title and explanation. The legend should be concise but comprehensive and should be understood without referring to the text. Symbols used in figures must be explained. Any individually labeled figure parts or panels (A, B, *etc*.) should be specifically described by part name within the legend.

Figure Preparation: All figures should be clear and cited in numerical order in the text. Figures must fit a one- or two-column format on the journal page: 8.3 cm (3.3 in.) wide for a single column, 17.3 cm (6.8 in.) wide for a double column; maximum height: 24.0 cm (9.5 in.). Please make sure that artwork files are in an acceptable format (TIFF or JPEG) at minimum resolution (600 dpi for illustrations, graphs, and annotated artwork, and 300 dpi for micrographs and photographs). Please provide all figures as separate files. Please note that low-resolution images are one of the leading causes of article resubmission and schedule delays.

Units and Symbols: Units and symbols conforming to the International System of Units (SI) should be used for physicochemical quantities. Solidus notation (*e.g*. mg/kg, mg/mL, mol/mm^2/min) should be used. Please refer to the SI Guide *www.bipm.org/en/si/* for standard units.

Supplemental data: Supplemental data might be useful for supporting and enhancing your scientific research and *Drug Discoveries & Therapeutics* accepts the submission of these materials which will be only published online alongside the electronic version of your article. Supplemental files (figures, tables, and other text materials) should be prepared according to the above guidelines, numbered in Arabic numerals (*e.g*., Figure S1, Figure S2, and Table S1, Table S2) and referred to in the text. All figures and tables should have titles and legends. All figure legends, tables and supplemental text materials should be placed at the end of the paper. Please note all of these supplemental data should be provided at the time of initial submission and note that the editors reserve the right to limit the size

and length of Supplemental Data.

7. Online Submission

Manuscripts should be submitted to *Drug Discoveries & Therapeutics* online at *https://www.ddtjournal.com/login*. Receipt of your manuscripts submitted online will be acknowledged by an e-mail from Editorial Office containing a reference number, which should be used in all future communications. If for any reason you are unable to submit a file online, please contact the Editorial Office by e-mail at *office@ddtjournal.com*

8. Accepted Manuscripts

Page Charge: Page charges will be levied on all manuscripts accepted for publication in *Drug Discoveries & Therapeutics* (Original Articles / Brief Reports / Reviews / Policy Forum / Communications: $140 per page for black white pages, $340 per page for color pages; News / Letters: a total cost of $600). Under exceptional circumstances, the author(s) may apply to the editorial office for a waiver of the publication charges by stating the reason in the Cover Letter when the manuscript online.

Misconduct: *Drug Discoveries & Therapeutics* takes seriously all allegations of potential misconduct and adhere to the ICMJE Guideline (*https://icmje.org/recommendations*) and COPE Guideline (*https://publicationethics.org/files/Code_of_conduct_for_journal_editors.pdf*). In cases of suspected research or publication misconduct, it may be necessary for the Editor or Publisher to contact and share submission details with third parties including authors' institutions and ethics committees. The corrections, retractions, or editorial expressions of concern will be performed in line with above guidelines.

(As of December 2022)

Drug Discoveries & Therapeutics
Editorial and Head Office
Pearl City Koishikawa 603,
2-4-5 Kasuga, Bunkyo-ku,
Tokyo 112-0003, Japan.
E-mail: office@ddtjournal.com